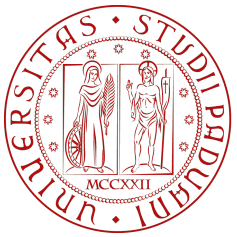

UNIVERSITÀ
DEGLI STUDI
DI PADOVA

HEAD OFFICE: Università degli Studi di Padova

DEPARTMENT: Physics and Astronomy "Galileo Galilei"

PH.D. COURSE IN: Physics

SERIES: XXXIV Cycle

BINARY NEUTRON STAR MERGER SIMULATIONS IN THE ERA OF MULTI-MESSENGER ASTROPHYSICS

Thesis written with the financial contribution of FONDAZIONE CARIPARO

PH.D. CANDIDATE: Jay Vijay Kalinani

SUPERVISOR: Dr. Riccardo Ciolfi

CO-SUPERVISOR: Prof. Jean Pierre Zendri

COORDINATOR: Prof. Franco Simonetto

FEBRUARY 2022

To Maa, Paa, and Einstein.

Acknowledgments

This Thesis would not have seen light without the tremendous help and support of so many people in so many ways.

I owe the deepest sense of gratitude to my supervisor and guru, Dr. Riccardo Ciolfi, for giving me the opportunity to work with him, for the insurmountable patience, persistent support, inspiration and understanding since day one, for believing in me while I continued to make numerous mistakes and for correcting them in the process, for encouraging me to participate in various conferences and workshops, and helping me with the talks, for dedicating countless number of hours for our discussions, for his excellent mentorship, for not only filling my gaps of knowledge but more importantly, showing ways to be a better human being. I thank him for his immense kindness, thoughtfulness and care, and for being there *always* throughout this journey, especially during the toughest of times. I am enormously indebted to him for helping me grow into the person I am today.

I profusely thank Prof. Bruno Giacomazzo for being the role model I would always look up to, for giving me the opportunity to be a part of the Spritz group, for hosting me in Trento, for his substantial help and profound insights during our various chats and discussions especially during the weekly Spritz calls, and for his continuous support, kindness and motivation.

I am also incredibly grateful to Dr. Wolfgang Kastaun for sharing his expertise and providing detailed explanations (including lengthy emails) during our interactions on various topics, for hosting me at the Albert Einstein Institute in Hannover, for including me in the development process of RePrimAnd and for helping me with coding, for his extreme patience and understanding throughout our collaboration.

I express my sincere thanks to Dr. Federico Cipolletta for encouraging me to get my hands dirty with the Spritz code, for his advice and suggestions during the development and testing of Spritz, and for the interesting conversations every time we met in person.

I also thank the various members of the Spritz group, Lorenzo Ennoggi, Lorenzo Sala, Edoardo Giangrandi, Beatrice Guidici, Alberto Ghedin, and Alice Gambaro, from whom I have learnt a great deal, and always enjoyed our exchanges.

I would also like to thank Andrea Pavan, colleague and friend, with whom I had fun working on the data hand-off to PLUTO.

I am also quite grateful to Prof. Carlos Palenzuela and collaborators, Ricard Aguilera-Miret, Federico Carrasco, Borja Miñano, Daniele Viganò for involving me in their project on BNS merger simulations.

I thank Erik Schnetter, Roland Haas, and other Einstein Toolkit members who provided timely and useful support with the toolkit.

I express my gratitude to Prof. Franco Simonetto and Mrs. Cristina Mazzucco for making the administrative and bureaucratic procedures seemingly easy for us PhD students. I also thank all the professors who taught me, and colleagues and students whom I interacted with during these past years, whose names I may have missed out.

Massive thanks goes to my friends from the Physics and Astronomy department, Dario, Achille, Davide, Andrea, Giovanni, Sarah, Andrea, Luca, Stefano and Alfredo, for all the good times we had, be it debates over physics, Mensa lunches, or even translating funny Italian idioms.

My sincere thanks to Prof. Jean Pierre Zendri for agreeing to be my co-supervisor.

I also thank the University of Padova for my enrolment, and the Cariparo Foundation for funding my PhD programme.

I am extremely thankful to Prof. Albino Perego and to Prof. Luca Del Zanna for carefully reading my Thesis, and providing their expert comments.

Huge thanks to my friends, Zlata(n), Sufi, Claudia, Harish, Alba, Dries, Sophie, Francesco, Francesca, Dimple, Sneha, Sara, Rishi, Eleonora, Elda, Beatrice, Unnati, and Alessia for their company and support during the various stages of this academic exploration.

I am eternally grateful to my parents, Priya and Vijay, for their constant presence, love, inspiration and support, without which, I wouldn't have had the courage to be here.

Abstract

The recent ground-breaking detection of gravitational waves (GW) from the merger of two neutron stars (NS), known as the GW170817 event, along with the observations of electromagnetic counterparts across the entire spectrum including a short gamma-ray burst (SGRB) and a radioactively powered kilonova, has given birth to the era of multimessenger astrophysics with GW sources. In order to probe the underlying physical mechanisms at play in such systems, it is necessary to employ fully general relativistic magnetohydrodynamic (GRMHD) simulations, including effects of magnetic fields and neutrino emission/reabsorption for a more realistic description. In the first part of this Thesis, we introduce our newly-developed GRMHD code `Spritz`, that solves the GRMHD equations in 3D Cartesian coordinates and on a dynamical spacetime. We present its salient features including the staggered formulation of the vector potential as well as support for any arbitrary equation of state (EOS), followed by a series of tests for code validation. We then describe the implementation of an approximate neutrino leakage scheme in `Spritz`, shedding some light on the involved equations, physical assumptions, and implemented numerical methods including higher order schemes, along with a large battery of general relativistic tests performed with and without magnetic fields and/or neutrino leakage. Since flux-conserving GRMHD codes like `Spritz` depend upon a technical algorithm to recover the fundamental 'primitive' variables from the evolved 'conserved' ones, which is often error-prone, we propose a new robust, accurate and efficient conservative-to-primitive variable recovery scheme named 'RePrimAnd', along with the proof of existence of a solution and its uniqueness. As a next natural step, we implemented this scheme in `Spritz` and performed a number of demanding GRMHD tests, including critical cases like a NS collapse to a black hole (BH) as well as the evolution of a BH-accretion disk system. The second part of the thesis focusses instead on the application of GRMHD codes to perform magnetized BNS merger simulations. In particular, using the `WhiskyMHD` code, we present a detailed study of BNS merger simulations forming a long-lived NS remnant and including long post-merger evolution. Exploring this 'magnetar scenario' allows us to address some of the open questions in the context of the SGRB and accompanying kilonova of the GW170817 event. Finally, we also discuss the results of the first magnetized BNS merger simulation performed with `Spritz` and the RePrimAnd scheme, concluding with an outlook on the next steps.

Contents

Publications

Part of this Thesis content has already led to six peer-review journal publications, plus two papers under review and one in preparation, which we list below:

Refereed Journals

JVK1 R. Ciolfi, W. Kastaun, **J.V. Kalinani**, & B. Giacomazzo (2019), *First 100 ms of a long-lived magnetized neutron star formed in a binary neutron star merger*, PRD 100, 023005, arXiv: 1904.10222.

JVK2 F. Cipolletta, **J.V. Kalinani**, B. Giacomazzo, & R. Ciolfi (2020), *Spritz: a new fully general-relativistic magnetohydrodynamic code*, CQG 37, 135010, arXiv: 1912.04794.

JVK3 R. Ciolfi & **J.V. Kalinani** (2020), *Magnetically driven baryon winds from binary neutron star merger remnants and the blue kilonova of August 2017*, ApJL 900 L35, arXiv: 2004.11298.

JVK4 W. Kastaun, **J.V. Kalinani**, & R. Ciolfi (2021), *Robust Recovery of Primitive Variables in Relativistic Ideal Magnetohydrodynamics*, PRD 103, 023018, arXiv: 2005.01821.

JVK5 F. Cipolletta, **J.V. Kalinani**, E. Giangrandi, B. Giacomazzo, R. Ciolfi, L. Sala, & B. Giudici (2021), *Spritz: General Relativistic Magnetohydrodynamics with Neutrinos*, CQG 38, 085021, arXiv: 2012.10174.

JVK6 A. Pavan, R. Ciolfi, **J.V. Kalinani**, & A. Mignone (2021), *Short gamma-ray burst jet propagation in binary neutron star merger environments*, MNRAS 506:3, 3483, arXiv: 2104.12410.

Submitted

JVK7 **J.V. Kalinani**, R. Ciolfi, W. Kastaun, B. Giacomazzo, F. Cipolletta, & L. Ennoggi (2021), *Implementing a new recovery scheme for primitive variables in the general relativistic magneto-hydrodynamic code Spritz*, submitted to PRD, arXiv:2107.10620.

JVK8 C. Palenzuela, R. Aguilera-Miret, F. Carrasco, R. Ciolfi, **J.V. Kalinani**, W. Kastaun, B. Minano, & D. Vigano (2021), *Turbulent magnetic field amplification in binary neutron star mergers*, submitted to PRD, arXiv:2112.08413.

In preparation

JVK9 **J.V. Kalinani**, R. Ciolfi, B. Giacomazzo, & L. Ennoggi (2022), in preparation.

List of Figures

List of Tables

Chapter 1

Introduction

About 130 million years ago, in a far away galaxy, two merging neutron stars (NS) performed a complex dance of whirling spirals around one another, generating cosmic quakes that shook the fabric of spacetime itself, and soon after merging, produced one of the most powerful bursts in the Universe. On August 17^{th}, 2017, near the end of their second observing run, the Advanced LIGO and Virgo observatories detected, for the first time ever, the gravitational wave (GW) signal from such a binary neutron star (BNS) merger event, named 'GW170817' [1]. This breakthrough detection was also accompanied by rich variety of electromagnetic (EM) counterparts including a short gamma-ray burst (SGRB) [2] and an ultraviolet/optical/infrared transient consistent with a radioactively powered kilonova [3] (named GRB 170817A and AT2017gfo, respectively), drenching the entire EM spectrum from gamma-rays to radio [4]. Followed by the most extensive world-wide campaign that led to these observations, the GW170817 event kick-started the era of multi-messenger astrophysics with GW sources, opening a new window to look at our Universe.

BNS merger events present a rich phenomenology with the potential to answer some long standing puzzles in physics and astrophysics. For instance, the GW170817 observations offered crucial insights on the behaviour of matter at supranuclear densities by placing new constraints on the NS equation of state (EOS) [5–8]. Morever, this event provided the smoking-gun evidence revealing that BNS mergers constitute at least a fraction of the progenitors of SGRBs [2, 9–11] (see also [12] for a review) and also serve as ideal sites for r-process nucleosynthesis [3, 13, 14]. GW170817 also allowed to independently estimate the Hubble constant [15], and aided as a testbed for general relativity [16]. Most certainly, the plethora of science extracted from this event has been unprecedented.

Along with a number of key discoveries, the GW170817 event also left behind some open questions regarding the merger process as well as the mechanisms that produced the SGRB and the accompanying kilonova. For example, the GW170817 merger most likely resulted in a metastable (hypermassive or supramassive) NS which ultimately collapsed to a BH. However, the survival time of the massive NS remnant before collapse, remains poorly constrained. This further casts uncertainty on the nature of the central engine that powered the tightly collimated,

relativistic jet responsible for the SGRB, which could have been either the rapidly rotating strongly magnetized massive NS remnant ('magnetar scenario') or a spinning BH surrounded by a magnetized accretion disk ('BH-disk scenario'; see e.g., [17] for a review). Moreover, the question of how such remnants can launch jets is an unsolved problem.

Another enduring mystery concerns the proper interpretation of the accompanying kilonova. The AT2017gfo lightcurve strongly suggested that its source consisted of at least two distinct ejecta components, an early 'blue kilonova', peaking ~ 1 day after merger at ultraviolet/blue wavelengths, and a following 'red kilonova', peaking ~ 1 week after merger in the infrared band (e.g., [3, 14, 18, 19]). However, the physical origin and properties of these two components are still a matter of debate (see e.g., [20–24], and also [25, 26] for reviews).

In order to address such open questions, general relativistic magnetohydrodynamic (GRMHD) simulations represent a key tool, including magnetic field effects as a fundamental element (e.g., [27, 28] and refs. therein). In the past decade, various numerical relativity groups have successfully performed stable BNS simulations using state-of-the-art GRMHD codes currently available in the market such as `GRHydro` [29], `IllinoisGRMHD` [30] and `WhiskyMHD` [31, 32], covering a growing range of the parameter space, and adding more and more key physical ingredients including temperature and composition dependent tabulated EOS, neutrino radiation, and/or NS spin (e.g., [28, 33–40] and refs. therein). Following this trend, we have developed `Spritz`, a new numerical code that solves the GRMHD equations in three spatial dimensions and on a dynamical spacetime. Inheriting a number of basic features from its parent code `WhiskyMHD`, `Spritz` is designed to serve as an astrophysical laboratory to study the physics of compact objects.

This Thesis is composed of two parts. In the first, we focus on the development of `Spritz`, and a new technical scheme for GRMHD codes. In Chapter 2, we give a brief overview of the '3+1' formalisms describing the equations for the evolution of spacetime as well as the conservative formulation of the GRMHD equations. We also outline state-of-the-art numerical techniques including the high resolution shock capturing methods which are commonly adopted to solve the aforementioned equations on a numerical grid. In Chapter 3, we introduce our new numerical code `Spritz`. The code has been extensively tested against a number of 1D, 2D and 3D tests including the study of magnetized NSs. The results of these tests are also described. This first version of `Spritz` did not include any neutrino treatment. Inclusion of neutrino effects is crucial, for instance, to accurately model the BNS merger ejecta and their composition, which are in turn responsible for the kilonova emission. In Chapter 4, we present details of the implementation of an approximate neutrino leakage scheme in `Spritz`, based on the `ZelmaniLeak` code [41] which follows a ray-by-ray approach. This second `Spritz` version also includes support for microphysical tabulated EOS, as well as incorporation of higher order schemes. We also report the full set of tests that were performed in order to check the implementation of the new infrastructure for the neutrino leakage scheme as well as higher order methods. Modern flux-conservative GRMHD codes like `Spritz`, numerically evolve a set of conservative equations based on 'conserved' variables which then need to be converted back into the fundamental ('primitive') variables. The corresponding conservative-to-primitive variable recovery procedure, based on root-finding algorithms, constitutes one of

the core elements of such GRMHD codes. In Chapter 5, we introduce a new robust, accurate and efficient recovery scheme called RePrimAnd, and demonstrate its ability to always converge to a unique solution via a mathematical proof. We also talk about the fine-grained error policies provided by the scheme, derive analytical bounds for the error of primitive variables, and also present the results of the testsuite performed on the stand-alone version of the scheme. Later, we focus on the technical aspects of implementing the RePrimAnd scheme into `Spritz`, and report a number of GRMHD tests in 3D, including critical cases such as a NS collapse to a BH as the evolution of a BH-accrection disk system, which were performed to validate our implementation.

The second part of the Thesis concentrates on the application of GRMHD codes `WhiskyMHD` and `Spritz` to perform magnetized BNS merger simulations in order to address some of the aforementioned open problems. For instance, the 'BH-disk' scenario is predominantly explored in present magnetohydrodynamics simulations supporting magnetic fields as the main driver behind jet formation (e.g., [42–44]), whereas the 'magnetar scenario' remains poorly studied. In the first part of Chapter 6, we extend the first systematic investigations of [35] to explore the latter case through magnetized BNS merger simulations with long post-merger evolution. Here, we describe our findings on the evolution of magnetic fields and their topology, NS remnant structure and its rotation profile, GW signal, and implications on jet formation by such systems. The second half of the Chapter is devoted to address the origin of the blue component of the GW170817 kilonova. This component is associated with ejecta properties which constitute low opacities $\simeq 0.5\,\mathrm{cm}^2/\mathrm{g}$, relatively high mass $\simeq 0.015-0.025\,M_\odot$ and velocities as high as $\simeq 0.2-0.3\,c$ (e.g., [3, 14, 18, 19]). Source candidates such as shock-driven dynamical ejecta typically have relatively low mass (e.g., [45–47], but see also [23]), whereas, post-merger baryon winds launched by the accretion disk surrounding a BH remnant have limited velocities $\sim 0.1\,c$ (e.g., [21]). Here, we explore a third promising candidate, which considers the magnetically driven baryon winds arising from the massive NS remnant prior to its eventual collapse to a BH (if any). Chapter 7 presents the first magnetized BNS merger simulation performed using the `Spritz` code along with RePrimAnd C2P. Here, we study instead the standard 'BH-disk' scenario, focussing on the prospects of jet formation by this system. Finally, in Chapter 8, we collect our conclusions and the directions for future work.

Contribution

Below, I briefly summarize my contribution to the research work which led to the different publications mentioned in this Thesis:

JVK1 In this work, I analyzed the data generated by the binary neutron star merger simulation reported in the paper, produced some of the figures, and contributed to the interpretation of results and paper writing.

JVK2 My main contribution was in extensively testing of the `Spritz` code. For this, I added code to setup the tests and performed the respective simulations. I also wrote part of the paper and produced some of the figures.

JVK3 Here, I focussed on the data analysis of the binary neutron star merger simulation and produced some of the figures reported in the manuscript. I also contributed to the interpretation of results and paper writing.

JVK4 I developed code for testing the new numerical scheme reported in the paper and performed the corresponding simulations. I also produced some of the figures and wrote parts of the manuscript text.

JVK5 I gave a substantial contribution to the various tests presented in the paper, including setup, running the respective simulations, analysing the results, and producing the figures. I was in particular responsible for all tests involving magnetic fields. I also contributed to paper writing.

JVK6 The binary neutron star merger simulation performed by me using the `WhiskyMHD` code was used as the initial data for performing the jet simulations with `PLUTO` code. I also helped in the critical/novel step of importing data between the two codes.

JVK7 I led the work, developing the code necessary for implementing the scheme introduced in JVK4 into the `Spritz` code, and setting up and performing all the test simulations mentioned in the paper. I also led the paper-writing and produced all the plots.

JVK8 I generated the initial data which was used to perform the binary neutron star merger simulations reported in the paper. I also contributed to the interpretation of results.

JVK9 This is an upcoming work led by me, for which I already performed the first binary neutron star merger simulation using the `Spritz` code along with the newly implemented scheme of JVK4 and JVK7. Additional simulation and analysis to complete the work will also be performed by me. Finally, I will lead the paper-writing.

Notation

We adopt the spacelike signature as $(-,+,+,+)$, and use a system of units in which $c = G = M_\odot = 1$. Greek indices run from 0 to 3, whereas Latin indices from 1 to 3, and we adopt the standard Einstein's convention for the summation over repeated indices. The 3-vectors are indicated with an arrow, while we use bold letters to denote 4-vectors and tensors.

Computational resources

All the numerical simulations discussed in this Thesis were performed on the clusters GALILEO and MARCONI at CINECA (Bologna, Italy). We acknowledge the CINECA awards under ISCRA and MoU INAF-CINECA initiatives, for the access to high performance computing resources and various support grants. Part of the numerical computations have been made possible through a CINECA-INFN agreement, by means of the allocations for TEONGRAV and VIRGO groups.

Chapter 2

Mathematical and numerical background

The non-linear nature of the coupled Einstein's field equations render them difficult to solve analytically for systems such as compact binary mergers. Numerical relativity represents a fundamental approach to recast these equations along with magnetohydrodynamical ones in order to solve them on a numerical grid. In this chapter, we first describe the *3+1 decomposition* approach adopted to arrive at numerical solutions of the Einstein's equations. For this, the equations are treated as an *initial value problem* (also called as a *Cauchy problem*), and require evolving spatial hypersurfaces forward in time, starting from the *initial data* in hand. Later, we describe the 3+1 formulation of general relativistic magnetohydrodynamics (GRMHD) equations adopted for matter evolution. The final section of this chapter focuses on various state-of-the-art numerical techniques required to solve both spacetime and matter equations on a computer.

2.1 3+1 foliation of spacetime

The geometry of the 4-dimensional spacetime manifold $\mathcal{M}$ is governed by the Einstein's equations,

$$G_{\mu\nu} \equiv R_{\mu\nu} - \frac{1}{2} g_{\mu\nu} R = 8\pi T_{\mu\nu} \ , \tag{2.1}$$

where $G_{\mu\nu}$ is the Einstein tensor, $R_{\mu\nu} \equiv R^{\rho}_{\mu\rho\nu}$ is the Ricci tensor, $R \equiv R^{\mu}_{\mu}$ is the Ricci scalar, $T_{\mu\nu}$ is the stress-energy tensor, and $g_{\mu\nu}$ is the metric tensor. In order to solve these equations numerically, the 3+1 decomposition formalism involves foliating the 4-dimensional spacetime into 3-dimensional spacelike hypersurfaces, which are then evolved forward in time with a fixed timestep. Particularly, the spatial field quantities are first defined on an initial time-slice which is a spatial hypersurface. The coupled spatial and matter equations are then evolved from one time-slice to another.

Considering the 4-dimensional spacetime manifold $\mathcal{M}$ to be globally hyperbolic in nature, we foliate it into a family of non-intersecting, 3-dimensional spacelike hypersurfaces Σ_t parameterized by the global time function $t \in \mathcal{R} : \mathcal{M} = \mathcal{R} \times \Sigma_t$. We then define $\mathbf{n}$ as the unit 4-vector orthonormal to the hypersurfaces Σ_t such that it is proportional to the gradient of t as $n = -\alpha \nabla t$, where α is set following the normalization $\mathbf{n} \cdot \mathbf{n} = -1$. Now, considering a coordinate basis $\mathbf{e}_\mu = \{\mathbf{e}_0, \mathbf{e}_i\}$ of 4-vectors, with the timelike coordinate basis $\mathbf{e}_0$ chosen such that $\mathbf{e}_0 \cdot \nabla t = 1$ and other three spacelike basis 4-vectors tangent to the hypersurfaces such that $\mathbf{n} \cdot \mathbf{e}_i = 0$, then $\mathbf{n}$ can be decomposed as

$$\mathbf{n} = \frac{\mathbf{e}_0}{\alpha} + \frac{\boldsymbol{\beta}}{\alpha} \,, \tag{2.2}$$

where α and $\boldsymbol{\beta} = \beta^i \boldsymbol{e}_i$ are called the *lapse* function and *shift* vector respectively. The lapse function α represents the rate of advancement of the physical proper time ($\alpha \Delta t$) between two neighbouring spatial hypersurfaces Σ_t and $\Sigma_{t+\Delta t}$ along the timelike unit normal vector $\mathbf{n}$. Whereas, the shift vector $\boldsymbol{\beta}$ is purely spatial and determines the change in the coordinates of a spatial point when transporting from hypersurface Σ_t to $\Sigma_{t+\Delta t}$. We can also define a time vector as

$$t^\mu = \alpha n^\mu + \beta^\mu \,. \tag{2.3}$$

The geometrical representation of the lapse function and the shift vector are shown in Figure 2.1. The spatial part of the spacetime 4-metric $g_{\mu\nu}$ can be defined as $\gamma_{\mu\nu} \equiv g_{\mu\nu} + n_\mu n_\nu$ where

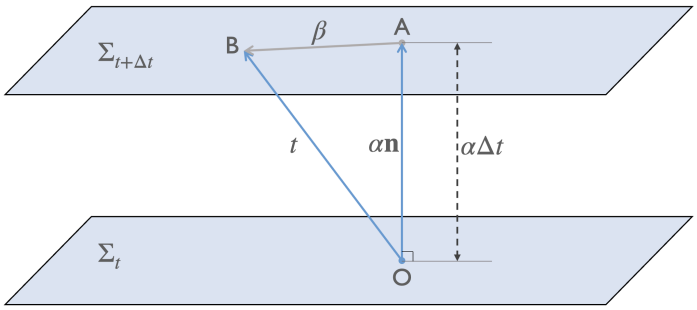

Figure 2.1: Foliation of spacetime in 3+1 formalism. Between the two neighboring hypersurfaces Σ_t and $\Sigma_{t+\Delta t}$, the proper time ($\alpha \Delta t$) is computed using the *lapse* function along the normal from point O to A, while the *shift* or the difference in the spatial coordinates is determined using the shift vector, which is the difference between the vectors OA and OB.

$\boldsymbol{\gamma}$ is the projector orthogonal to $\mathbf{n}$, satisfying $\boldsymbol{\gamma} \cdot \boldsymbol{n} = 0$. Using γ_{ij} as the spatial 3-metric of the hypersurface, the line element can then be decomposed into the 3+1 form as

$$\begin{aligned} \mathrm{d}s^2 &= g_{\mu\nu} \mathrm{d}x^\mu \mathrm{d}x^\nu \\ &= -\alpha^2 dt^2 + \gamma_{ij} (\mathrm{d}x^i + \beta^i \mathrm{d}t)(\mathrm{d}x^j + \beta^j \mathrm{d}t) \end{aligned} \,, \tag{2.4}$$

where $\alpha = 1/\sqrt{-g^{00}}$, $\beta_j = g_{0j}$, $\beta_i = \gamma_{ij}\beta^j$ and $\beta^\mu = \big(0, \beta^i\big)$. The spacetime metric components can then be written in the matrix form as

$$g_{\mu\nu} = \begin{pmatrix} -\alpha^2 + \|\beta\|^2 & \beta_j \\ \beta_i & \gamma_{ij} \end{pmatrix} , \tag{2.5}$$

and the determinant of $g_{\mu\nu}$, i.e. g, can be written in terms of the determinant of $\gamma_{\mu\nu}$, i.e. γ as

$$\det(g) = \det(-\alpha^2\gamma). \tag{2.6}$$

For developing a covariant formulation with respect to the spatial metric $\gamma_{\mu\nu}$, which is a dynamical variable, we require a 3-dimensional covariant derivative associated with $\gamma_{\mu\nu}$. To do so, all the indices of the 4-dimensional covariant derivative ∇_σ is projected onto Σ_t as

$$D_\mu T^\nu_\rho \equiv \gamma^\sigma_\mu \gamma^\nu_\lambda \gamma^\delta_\rho \nabla_\sigma T^\lambda_\delta \ , \tag{2.7}$$

where T^λ_δ is considered as an arbitrary tensor on the spatial hypersurface Σ_t. One can show that the covariant derivative of spatial metric vanishes as $D_\mu \gamma_{\nu\rho} = 0$. Using this property, the spatial connection coefficients (or the so called *Christoffel symbols*) can be computed as

$$\Gamma^\tau_{\mu\nu} = \frac{1}{2}\gamma^{\tau\sigma}(-\gamma_{\mu\nu,\sigma} + \gamma_{\sigma\mu,\nu} + \gamma_{\nu\sigma,\mu}) \ . \tag{2.8}$$

And the spatial Riemann tensor associated with spatial metric $\gamma_{\mu\nu}$ can then be written as

$$R^\sigma_{\mu\nu\rho}\phi_\sigma = (D_\mu D_\nu - D_\nu D_\mu)\phi_\rho \ , \tag{2.9}$$

where ϕ^μ is defined as a spatial vector field on hypersurfaces Σ_t. In order to compute the spatial components of the Riemann tensor, we use the Christoffel symbols as

$$R^\sigma_{\mu\nu\rho} = \Gamma^\sigma_{\mu\rho,\nu} - \Gamma^\sigma_{\nu\rho,\mu} + \Gamma^\delta_{\mu\rho}\Gamma^\sigma_{\nu\delta} - \Gamma^\delta_{\nu\rho}\Gamma^\sigma_{\mu\delta} \ , \tag{2.10}$$

and the spatial Ricci tensor can be computed by the contraction of this Riemann tensor as $R_{\mu\rho} = R^\nu_{\mu\nu\rho} = R_{\mu\nu\rho\sigma}\gamma^{\nu\sigma}$ and the 3-dimensional scalar curvature as $R = R^\mu_\mu$. The 3-dimensional Riemann tensor $R^\sigma_{\mu\nu\rho}$ represents the *intrinsic curvature* of the hypersurface Σ_t.

To understand the embedding of the 3-dimensional hypersurface Σ_t in the 4D spacetime manifold $\mathcal{M}$, we introduce the concept of the *extrinsic curvature*. Extrinsic curvature is the covariant 'time-derivative' of the spatial 3-metric, and is given by the Lie derivative $\mathcal{L}_n$ of the 3-metric with respect to the normal vector n^μ as

$$K_{\mu\nu} \equiv -\gamma^\tau_\mu \nabla_\tau n_\nu = -\frac{1}{2}\mathcal{L}_n \gamma_{\mu\nu} \ , \tag{2.11}$$

where γ^τ_μ is the projection operator defined as $\gamma^\tau_\mu \equiv \delta^\tau_\mu + n^\tau n_\mu$. After a few steps of calculations, the following expression can be deduced

$$\mathcal{L}_n \gamma_{\mu\nu} \equiv n^\tau \nabla_\tau \gamma_{\mu\nu} + \gamma_{\mu\tau}\nabla_\nu n^\tau + \gamma_{\nu\tau}\nabla_\mu n^\tau = 2\gamma^\tau_\mu \nabla_\tau n_\nu \ . \tag{2.12}$$

By construction, the extrinsic curvature tensor is a symmetric spatial tensor which fulfils the relations $K_{\mu\nu} = K_{\nu\mu}$ and $K_{\mu\nu}n^\nu = 0$, and gives a measure of bending of the hypersurface Σ_t. $K_{\mu\nu}$ can also be expressed in terms of 'acceleration' as

$$K_{\mu\nu} = -n_\mu a_\nu - \nabla_\mu n_\nu \ , \tag{2.13}$$

where $a_\nu \equiv n^\tau \nabla_\tau = D_\nu \ln \alpha$.

This gives us all the necessary ingredients required to derive the equations for the dynamic variables $\gamma_{\mu\nu}$ and $K_{\mu\nu}$ in terms of the spacetime Ricci tensor. Using its symmetry properties, one can project $R_{\mu\nu\rho\sigma}$ in three different ways. The *Gauss equation* is obtained when all its four indices are projected into Σ_t, yielding

$$R_{\mu\nu\rho\sigma} + K_{\mu\rho}K_{\nu\sigma} - K_{\mu\sigma}K_{\nu\rho} = \gamma^\alpha_\mu \gamma^\beta_\nu \gamma^\gamma_\rho \gamma^\delta_\sigma \ R_{\alpha\beta\gamma\delta} \ . \tag{2.14}$$

The *Codazzi equation* can be derived with three spatial projections and a contraction with n^μ, giving

$$D_\mu K_{\nu\rho} - D_\nu K_{\mu\rho} = \gamma^\gamma_\nu \gamma^\alpha_\mu \gamma^\beta_\rho n^\delta \ R_{\gamma\alpha\beta\delta} \ . \tag{2.15}$$

And finally, one can arrive at the the *Ricci equation* with two spatial projections and two contractions as

$$\mathcal{L}K_{\mu\nu} = n^{\sigma\rho}\gamma^\beta_\mu \gamma^\gamma_\nu \ R_{\gamma\sigma\beta\rho} - \frac{1}{\alpha} D_\mu D_\nu \alpha - K^\rho_\nu K_{\mu\rho} \ . \tag{2.16}$$

The above equations can then be used to derive the *Arnowitt-Deser-Misner* (ADM) formulation after a few steps of calculation.

2.1.1 Arnowitt-Deser-Misner formulation

The ADM formulation introduced by R. Arnowitt, S. Deser, and C. W. Misner [48] was the first successful attempt towards the 3+1 decomposition, linking the 3D curvature quantities with projections of the stress-energy tensor. To arrive at the ADM equations, we first begin with the following useful relation

$$D_\mu V^\nu = \gamma^\rho_\mu \nabla_\rho V^\mu + K_{\mu\rho} V^\rho n^\nu \ , \tag{2.17}$$

where V^μ represents any spatial vector. Contracting (2.14) twice with the spatial metric, we get

$$2n^\mu n^\nu \ G_{\mu\nu} = R + K^2 - K_{\mu\nu}K^{\mu\nu} \ . \tag{2.18}$$

Considering the total energy density measured by a normal observer defined as $\rho \equiv n^\mu n^\nu T_{\mu\nu}$ and using (2.1), we can arrive at the equation for the Hamiltonian constraint after a few steps of computation as

$$R + K^2 - K_{ij}K^{ij} = 16\pi\rho \ . \tag{2.19}$$

Similarly, the equations for the momentum constraint can be derived by contracting (2.15), giving

$$D_j K^j_i - D_i K = 8\pi j_i \ , \tag{2.20}$$

where $j_\mu \equiv -\gamma^\nu_\mu n^\rho T_{\nu\rho}$ is called momentum density measured by a normal observer n^μ. Then, the evolution equation for the spatial metric can be simplified as

$$\partial_t \gamma_{ij} = -2\alpha K_{ij} + D_i\beta_j + D_j\beta_i \ , \tag{2.21}$$

and the simplified evolution equation for the extrinsic curvature can be written as

$$\begin{aligned} \partial_t K_{ij} = &-D_i D_j \alpha + \alpha(R_{ij} - 2K_{ik}K^k_j + KK_{ij}) - 8\pi\alpha(S_{ij} - \frac{1}{2}\gamma_{ij}(S-\rho) \\ &+\beta^k D_k K_{ij} + K_{ik}D_j\beta^k + K_{kj}D_i\beta^k) \ , \end{aligned} \tag{2.22}$$

where $S_{\mu\nu} \equiv \gamma_{\mu\rho}\gamma_{\nu\sigma}T^{\rho\sigma}$ is the momemtum density as measured by an observer moving normal to the spacelike hypersurfaces, and its trace is given as $S \equiv \gamma^{\mu\nu}S_{\mu\nu}$. Equations (2.19), (2.20), (2.21), (2.22) are collectively known as the *ADM equations*. The four constraint equations (2.19) and (2.20) define the conditions to be satisfied on each hypersurface Σ_t, and along with the six evolution Equations (2.21) and (2.22), they make a set of ten equations for the components of $g_{\mu\nu}$. Due to the lack of robustness and stability properties needed for long-term simulations, this formalism is not generally used in the state-of-the-art numerical codes. However, it provided the first fundamental stepping stone towards the development of modern day algorithms like the BSSN formulation, which we discuss below.

2.1.2 BSSNOK formulation

In recent years, there had been a considerable effort by several groups in developing a new formulation of the Einstein's equations as a extension to the ADM formulation in order to achieve long-term stability. In late 1980s, a conformal traceless reformulation of the ADM equations was proposed, which was subsequently shown to be promising in terms of robustness and stability for long-term numerical simulations incorporating different classes of spacetime including NSs and BHs. The most commonly used version of this formulation is known as the BSSNOK (or BSSN) formulation [49–51], coined using the initials of its authors (Baumgarte, Shapiro, Shibata, Nakamura, Oohara and Kojima). Unlike the weakly hyperbolic[1] nature of the ADM equations, the BSSN formulation is strongly hyperbolic, which introduces auxiliary variables to construct a well-posed system of equations. To briefly provide an outline of this formulation (but more information on how it is implemented in numerical codes can be found in [55, 56]), we first consider the conformal transverse-traceless decomposition of the ADM equations with conformal three-metric given as

$$\tilde{\gamma}_{ij} = \phi^2\gamma_{ij} \qquad and \qquad \tilde{\gamma}^{ij} = \phi^{-2}\gamma^{ij} \ , \tag{2.23}$$

where $\tilde{\gamma} \equiv det\,(\tilde{\gamma}_{ij}) = 1$ and the *conformal factor* ϕ is defined as

$$\phi \equiv [det\,(\gamma_{ij})]^{-1/6} = \gamma^{-1/6} \ . \tag{2.24}$$

[1]Hyperbolicity is related to the concept of 'well-posedness' for a set of partial differential equations. Well-posed system of equations have solutions which depend continuously on the initial data, such that any small change in the initial data leads to only small variation in the solutions. For further details on hyperbolicity, see [52–54].

Similarly, using the same conformal decomposition technique, the trace-free conformal extrinsic curvature tensor can be written as $\tilde{A}_{ij} = \phi^2 A_{ij}$ where

$$A_{ij} \equiv K_{ij} - \frac{1}{3}\gamma_{ij}K \ . \tag{2.25}$$

We now introduce $\tilde{\Gamma}$ such that the conformal coefficients (or conformal connection functions) $\tilde{\Gamma}^i$ are defined as

$$\tilde{\Gamma}^i \equiv \tilde{\gamma}^{jk}\tilde{\Gamma}^i_{jk} = \tilde{\gamma}^{ij}\tilde{\gamma}^{kl}\partial_l\tilde{\gamma}^{jk} \ , \tag{2.26}$$

wherethe Christoffel symbols $\tilde{\Gamma}^i_{jk}$ of conformal three-metric can be written as

$$\begin{aligned}\tilde{\Gamma}^i_{jk} &= \Gamma^i_{jk} - \frac{1}{3}\left(\delta^i_j\Gamma^n_{kn} + \delta^i_k\Gamma^n_{jn} - \gamma_{jk}\gamma^{il}\Gamma^n_{ln}\right) \\ &= \Gamma^i_{jk} + 2\left(\delta^i_j\partial_k \ln\phi + \delta^i_k\partial_j \ln\phi - \gamma_{jk}\gamma^{il}\partial_l \ln\phi\right) \ .\end{aligned} \tag{2.27}$$

This is computed using the relation $\partial_i \ln\phi = -\frac{1}{6}\partial_i \ln\gamma = -\frac{1}{3}\Gamma^n_{in}$. The three dimensional Ricci tensor can be conformally decomposed in a similar way as $R_{ij} = \tilde{R}_{ij} + \tilde{R}^{\phi}_{ij}$, such that

$$\tilde{R}_{ij} \equiv -\frac{1}{2}\tilde{\gamma}^{ln}\partial_l\partial_n\tilde{\gamma}_{ij} + \tilde{\gamma}_{k(}\partial_{j)}\tilde{\Gamma}^k + \tilde{\Gamma}^k\tilde{\Gamma}_{(ij)k} + \tilde{\gamma}^{ln}\left(2\tilde{\Gamma}^k_{l(i}\tilde{\Gamma}_{j)kn} + \tilde{\Gamma}^k_{in}\tilde{\Gamma}_{kjl}\right) \ , \tag{2.28}$$

$$\tilde{R}^{\phi}_{ij} \equiv \frac{1}{\phi^2}\left[\phi\left(\tilde{D}_i\tilde{D}_j\phi + \tilde{\gamma}_{ij}\tilde{D}^k\tilde{D}_k\phi\right) - 2\tilde{\gamma}_{ij}\tilde{D}^k\phi\tilde{D}_k\phi\right] \ , \tag{2.29}$$

where $\tilde{D}_i$ is the covariant derivative related to the conformal metric $\tilde{\gamma}$. Having defined all the necessary ingredients, we can now recast the ADM equations using the conformal decomposition for the evolution of variables such as $\tilde{\Gamma}^i$, ϕ and K, in order to obtain the following formulation after a few steps of computation

$$\partial_t\tilde{\gamma}_{ij} = -2\alpha\tilde{A}_{ij} + 2\tilde{\gamma}_{k(i}\partial_{j)}\beta^k - \frac{2}{3}\tilde{\gamma}_{ij}\partial_k\beta^k + \beta^k\partial_k\tilde{\gamma}_{ij} \tag{2.30}$$

$$\partial_t\tilde{A}_{ij} = \phi^2\left[-D_iD_j\alpha + \alpha\left(R_{ij} - 8\pi S_{ij}\right)\right]^{TF} + \beta^k\partial_k\tilde{A}_{ij} + 2\tilde{A}_{k(i}\partial_{j)}\beta^k + \alpha\left(\tilde{A}_{ij}K - 2\tilde{A}_{ik}\tilde{A}^k_j\right) - \frac{2}{3}\tilde{A}_{ij}\partial_k\beta^k \tag{2.31}$$

$$\partial_t\phi = \frac{1}{3}\phi\alpha K - \frac{1}{3}\phi\partial_i\beta^i + \beta^k\partial_k\phi \tag{2.32}$$

$$\partial_t K = -D^iD_i\alpha + \alpha\left[\tilde{A}_{ij}\tilde{A}^{ij} + \frac{1}{3}K^2 + 4\pi\left(\rho + S\right)\right] + \beta^i\partial_i K \tag{2.33}$$

$$\partial_t\tilde{\Gamma}^i = \tilde{\gamma}^{jk}\partial_j\partial_k\beta^i + \frac{1}{3}\tilde{\gamma}^{ik}\partial_k\partial_j\beta^j + \frac{2}{3}\tilde{\Gamma}^i\partial_j\beta^j - \tilde{\Gamma}^j\partial_j\beta^i - 2\tilde{A}^{ij}\partial_j\alpha + \beta^j\partial_j\tilde{\Gamma}^i + 2\alpha\left(\tilde{\Gamma}^i_{jk}\tilde{A}^{jk} - 3\tilde{A}^{ij}\partial_j \ln\phi - \frac{2}{3}\tilde{\gamma}^{ij}\partial_j K\right) - 16\pi\alpha\tilde{\gamma}^{ij}S_j \ , \tag{2.34}$$

where $T^{\rm TF}_{ij}$ is the trace-free part of the 3-dimensional second rank tensor T_{ij}, i.e. $T^{\rm TF}_{ij} \equiv T_{ij} - \gamma_{ij}T^k_k/3$. In addition to the constraint equations (2.19) and (2.20), the Equations (2.30 -2.34) together make the standard *BSSN formulation*. Note that we have moved from evolving

12 variables (i.e., γ_{ij}, K_{ij}) in the ADM formulation to first-order-in-time, second-order-in-space system for 17 evolved variables (i.e., $\tilde{\gamma}_{ij}$, $\tilde{A}_{ij}$, ϕ, K, $\tilde{\Gamma}^i$) in this formulation which is equivalent to a hyperbolic system [57–59], guaranteeing the robustness and stability in numerical simulations.

The improved properties of this conformal traceless formulation of the Einstein equations were discussed and compared to the ADM system in [55, 60]. Particularly, [60] reported numerical tests of a number of strongly gravitating systems with convergent high-resolution shock-capturing (HRSC) methods with total-variation-diminishing (TVD) schemes using the equations from [61]. These tests included relativistic stars, black holes, boson stars, along with analysis for gravitational waves. The results showed no numerical instabilities for sufficiently long times when using this formulation for the evolution of the various strongly gravitating systems. However, it was also reported that this formulation requires higher grid resolution than the ones needed in the ADM formulation in order to achieve the same accuracy. Since the most desirable property in any long simulation is a small error growth-rate and error accumulation, the BSSN equations based on the conformal traceless formulation is widely adopted as the state-of-the-art form for the evolution of the field equations.

2.1.3 Gauge conditions

In 3+1 decomposition formalisms, we can decide how to slice the 4-dimensional spacetime and choose the coordinate system that fits best for our simulations in order to sustain stability and at the same time, reduce the computational costs. Particularly, we can have different gauge choices for the lapse function α and the shift vector β^i, implying *gauge freedom*. For each hypersurface Σ_t, we use a *slicing condition* for the lapse function and a *spatial shift condition* for the shift vector. One should set the gauge conditions optimally so that (i) singularities in spacetime could avoided, (ii) coordinate distortions taking place on the spatial grid are counteracted, and (iii) computational costs are minimal. Below, we describe the possible choices for α and β^i.

2.1.3.1 Slicing conditions

For the simplest choice, the *geodesic slicing* condition sets the lapse function to be unity, that is:

$$\alpha = 1 \tag{2.35}$$

which implies that for the Eulerian observers, the worldlines are timelike geodesics with acceleration $a = 0$, and the proper time along the worldlines is equal to the coordinate time. In such a case, the spacetime metric takes the form

$$g_{\mu\nu}\mathrm{d}x^\mu \mathrm{d}x^\nu = -\mathrm{d}t^2 + \gamma_{ij}\mathrm{d}x^i\mathrm{d}x^j \ . \tag{2.36}$$

One major drawback of using this condition is that in non-uniform gravitational fields, it allows the worldlines to converge and cross, leading to a coordinate singularity, which could be undesirable for numerical simulations. Alternatively, we can foliate spacetime in such a way that

$$K = 0, \qquad \partial_t K = 0 \ , \tag{2.37}$$

where the trace of the extrinsic curvature is set to zero and also does not change with time, giving a vanishing mean curvature for the hypersurfaces Σ_t. This condition is called as the *maximal slicing condition* since in such a case, the volume of any bounded portion defined on the hypersurface tends to maximum [62]. For this condition, even if the extrinsic curvature grows, the free-falling Eulerian observers do not focus, thus avoiding singular points. Therefore, this condition is also called as the *singularity-avoiding slicing condition*. Utilizing the evolution equations (2.21), (2.22) and the Hamiltonian constraint (2.19), in combination with the maximal slicing condition, we get an elliptic equation

$$D^i D_i \alpha = \alpha \left[K_{ij} K^{ij} + 4\pi(\rho + S) \right] \ , \tag{2.38}$$

where $D^2 \equiv \gamma^{ij} \partial_i \partial_j$ is the three-metric Laplacian. However, solving this elliptic equation for each hypersurface makes it computationally demanding, and thus deems this gauge condition as an impractical choice. Current numerical codes implement rather a hyperbolic K-driver slicing condition called as the *Bona-Masso slicing* [63], which has a generic form given as

$$\partial_t \alpha - \beta^k \partial_k \alpha = -f(\alpha) \alpha^2 (K - K_0) \ , \tag{2.39}$$

where $K_0 \equiv K(t = 0)$ and $f(\alpha) > 0$. This form is a generalization of many well-known slicing conditions. Keeping $f = 1$, we get the *harmonic slicing condition*, while by setting $f = q/\alpha$, we recover the generic *'1+log' slicing condition* where q is an integer (with value $+2$ as a usual choice for most simulations discussed in this thesis) and $\alpha = h(x^i) + \ln \gamma^{q/2}$ with $h(x^i)$ defined as a positive arbitrary time-independent function.

2.1.3.2 Shift conditions

For the simplest condition, the shift vector can be set to zero, i.e.,

$$\beta^i = 0 \ . \tag{2.40}$$

This setting might work for simple configurations but could encounter difficulties when dealing with rotation leading to large values of the metric coefficients γ_{ij}, or be inefficient when evolving blackhole spacetimes.

Using a similar approach for defining the slicing conditions, we can define elliptical, parabolic and hyperbolic shift-conditions. The most commonly adopted are the *Gamma driver* shift conditions which essentially act in order to drive $\tilde{\Gamma}^i$ to be constant. For example, the *Gamma-freezing prescription* suggests to keep $\tilde{\Gamma}^i$ constant in time, imposing $\partial_t \tilde{\Gamma}^i = 0$, leading to an elliptic equation for the shift vector. Whereas, the *parabolic Gamma driver* proposed by Alcubierre and Brügmann [64] is given as

$$\partial_t \beta^i = k \partial_t \tilde{\Gamma}^i \ , \tag{2.41}$$

where k is a positive term. As the name suggestions, this condition leads to parabolic equation for the shift vector. The *hyperbolic Gamma driver* introduced by Alcubierre *et al* [56], is given as

$$\partial_t^2 \beta^i = k \partial_t \tilde{\Gamma}^i - (\eta - \partial_t k) \partial_t \beta^i \ , \tag{2.42}$$

where η is a dissipation term which helps to avoid strong oscillations in the shift vector due to rapid and large gauge variations. This condition gives a hyperbolic equation for the shift vector.

The '1+log' slicing condition (2.39) together with the 'hyperbolic Gamma-driver' shift condition (2.42) are the most commonly used settings in modern-day numerical relativity simulations.

2.2 Relativistic hydrodynamics

Analogous to the 3+1 decomposition of 4D spacetime, we require a 3+1 formulation to evolve the matter field equations involving magnetic fields. In this Section, we first discuss the basic relativistic hydrodynamic (RHD) equations, followed by the GRMHD formulation implemented in the numerical codes such as `WhiskyMHD` and `Spritz`.

2.2.1 General equations

Considering a perfect fluid, we first define the 4-dimensional rest-mass density current and the energy-momentum tensor as

$$J^{\mu} = \rho u^{\mu} \tag{2.43}$$

$$T^{\mu\nu} = (\rho + \rho\epsilon + p)u^{\mu}u^{\nu} + pg^{\mu\nu} = h\rho u^{\mu}u^{\nu} + pg^{\mu\nu} \ , \tag{2.44}$$

where p stands for gas pressure, ρ for rest-mass density, u^{μ} the four velocity of the fluid, ϵ for specific internal energyand $h = 1 + \epsilon + p/\rho$ is specific relativistic enthalpy. The equation for the conservation of matter current density i.e., the continuity equation, and for the conservation of energy-momentum can be written respectively as

$$\nabla_{\mu} J^{\mu} = \nabla_{\mu} \left(\rho u^{\mu}\right) = 0 \tag{2.45}$$

$$\nabla_{\mu} T^{\mu\nu} = \nabla_{\mu} \left[h\rho u^{\mu}u^{\nu} + pg^{\mu\nu}\right] = 0 \ . \tag{2.46}$$

In the past years, the numerical solutions of the RHD equations have been derived through different approaches such as the non-conservative formulation from 1970s to the most recent robust (conservative) formulation implemented in current numerical codes, which is discussed in the following section.

2.2.2 Conservative formulation

In a generic first order form, a system of partial differential equations for relativistic hydrodynamics can be written as

$$\partial_t \mathbf{U} + \mathbf{A} \cdot \nabla \mathbf{U} = \mathbf{S} \ , \tag{2.47}$$

where $\mathbf{U} \equiv (u^{\mu}, \epsilon, s)$ with s as specific entropy, $\mathbf{A} = \mathbf{A}(\mathbf{U})$ and $\mathbf{S}$ as the source term. The equation yields a hyperbolic system if the matrix of coefficients of $\mathbf{A}$ is diagonalisable to construct an eigen-value equation. If the matrix $\mathbf{A}(\mathbf{U})$ is the Jacobian of the *flux vector* $\boldsymbol{F(U)}$ with

respect to the state vector $\mathbf{U}$, i.e. $\mathbf{A}(\mathbf{U}) \equiv \partial\mathbf{F}/\partial\mathbf{U}$, the homogeneous version of (2.47) can be written in a *conservative form*, giving

$$\partial_t \mathbf{U} + \nabla \mathbf{F}(\mathbf{U}) = 0 \ , \tag{2.48}$$

with U as the vector of conserved variables.

A quasi-linear system of equations is be said to be *hyperbolic* if the matrix $\mathbf{A}$ has N real eigenvalues (where the dimension of the matrix is $N \times N$) and admits a complete set of eigenvectors. If all the eigenvalues are real and distinct, the system is said to be *strictly hyperbolic*.

In order to better appreciate the importance of a quasi-linear hyperbolic system, we start with the one-dimensional linear advection equation, which can be considered as the simplest conservative and hyperbolic equation:

$$\partial_t U + a\partial_x U = 0 \ , \tag{2.49}$$

with initial conditions

$$U(x, t = 0) = U_0(x) \ . \tag{2.50}$$

The solution of this equation can be easily computed and is given as

$$U(x, t) = U_0(x - at) \tag{2.51}$$

for $t \geq 0$. Here, the initial data moves unaltered with velocity a either to the left (if $a < 0$) or to the right (if $a > 0$), and the solution $U(x, t)$ remains constant along the line $x - at = x_0$, which is called as the *characteristics* of the equation. When differentiating $U(x, t)$ along one of the curves $x'(t) = dx/dt$ to get

$$\begin{aligned} \frac{dU(x(t), t)}{dt} &= \frac{\partial U}{\partial t} + \frac{\partial U}{\partial x} x'(t) \\ &= \frac{\partial U}{\partial t} + a\frac{\partial U}{\partial x} \\ &= 0 \ , \end{aligned} \tag{2.52}$$

showing that U is constant along the characteristics. We could extend this notation to a system of equations like, for e.g., (2.47) with $S = 0$. For a hyperbolic system with a full set of eigenvectors $\mathbf{R}^l$ where $l = (1, ..., N)$, and representing the $N \times N$ matrix (having columns as $\mathbf{R}^l$) with $\mathbf{Q}$, we have

$$\mathbf{\Lambda} = \boldsymbol{Q}^{-1}\boldsymbol{A}\boldsymbol{Q} \tag{2.53}$$

where $\mathbf{\Lambda} = \mathrm{diag}(\lambda_1, ..., \lambda_N)$. Defining the *characteristic variables* as

$$\boldsymbol{V} = \boldsymbol{Q}^{-1}\boldsymbol{U} \ , \tag{2.54}$$

Equation (2.47) in 1-dimension with $S = 0$ becomes

$$\frac{\partial \boldsymbol{V}}{\partial t} + \mathbf{\Lambda}\frac{\partial \boldsymbol{V}}{\partial x} = 0 \ . \tag{2.55}$$

This equation can be split into N independent scalar equations since Λ is diagonal,

$$\frac{\partial V_l}{\partial t} + \lambda_l \frac{\partial V_l}{\partial x} = 0 \ , \ l = 1, ..., N \ . \tag{2.56}$$

having the solutions given as

$$V_l(x,t) = V_l(x - \lambda_l t, 0) \ . \tag{2.57}$$

By inverting Equation (2.54) as $\mathbf{U} = \mathbf{QV}$, we have the solution of original Equation (2.47) in 1-dimension (with $S = 0$), which can be broken down into components as

$$\mathbf{U}(x,t) = \sum_{l-1}^{N} V_l(x - \lambda_l t, 0) A^l \ . \tag{2.58}$$

This solution can be viewed as the superposition of N waves, each propagating without any distortions with a speed given by its corresponding eigenvalue.

Another approach in integral form which admits non-smooth solutions for the partial differential equation such as (2.48) considers multiplying (2.48) with a smooth function ϕ providing compact support in space. For one spatial dimension case of (2.48), the integral form can be written as

$$\int_0^{\infty} \int_{-\infty}^{+\infty} [\phi \, \partial_t U + \phi \, \partial_x F] \, dxdt = 0 \ , \tag{2.59}$$

which, after integration by parts, gives

$$\int_0^{\infty} \int_{-\infty}^{+\infty} [U \partial_t \phi + F \partial_x \phi] \, dxdt = - \int_{-\infty}^{+\infty} \phi(x,0) U(x,0) dx \ , \tag{2.60}$$

which is known as the *weak formulation* with U as a *weak solution* for all ϕ. This allows the solutions for discontinuities to be admitted as weak solutions for the conservation equations.

The *Lax-Wendroff theorem* (1960) highlights the need for the conservative formalism, stating: *numerical schemes based on conservative formalism, if convergent, do converge to the weak solution of the problem* [65]. Whereas, the *Hou-LeFloch theorem* (1994) states that: *non-conservative schemes do not converge to the correct solution if a shock-wave is present in the flow* [66]. These statements strongly support implementation of flux-conservative formulations for hydrodynamic equations in numerical simulations for obtaining convergence to correct solutions. We emphasize more on the concept of convergence in Section 2.3.2.

2.2.3 General relativistic hydrodynamics

In the conservative form, the set of Equations (2.43)-(2.44) can be written in the following hyperbolic, first-order and flux-conservative form

$$\frac{1}{\sqrt{-g}} \{ \partial_t [\sqrt{\gamma} \boldsymbol{F}^0(\boldsymbol{U})] + \partial_i [\sqrt{-g} \boldsymbol{F}^{(i)}(\boldsymbol{U})] \} = \boldsymbol{S}(\boldsymbol{U}) \ , \tag{2.61}$$

where $\mathbf{F}^{(i)}(\mathbf{U})$ stands for the flux-vector in the i-direction, $\mathbf{S}(\mathbf{U})$ are the source terms [67], and $\sqrt{-g} = \alpha\sqrt{\gamma}$. Except for the dependence on stress-energy tensor, the source terms depend only

on the metric and its derivatives. In order to recast Equations (2.43)-(2.44) into a conservative form, the *primitive* hydrodynamical variables $\mathbf{U} \equiv (\rho, v^i, \epsilon)$ are mapped into a set of conserved variables $\mathbf{F}^0(\mathbf{U}) \equiv (D, S_i, \tau)$ which are defined in the following way:

$$D \equiv \rho W \ , \tag{2.62}$$

$$S_i \equiv \rho h W^2 v_i \ , \tag{2.63}$$

$$\tau \equiv \rho h W^2 - p - D \ , \tag{2.64}$$

where v^i is the fluid 3-velocity as measured by an Eulerian observer, $W \equiv (1 - \gamma_{ij} v^i v_j)^{-1/2}$ is the Lorentz factor, and ϵ is the specific internal energy. And the flux vectors and the source terms in the final form are written as

$$\boldsymbol{F}^{(i)} = [D(v^i - \beta^i/\alpha), S_j(v^i - \beta^i/\alpha) + p\delta^i_j, \tau(v^i - \beta^i/\alpha) + pv^i]^T \ , \tag{2.65}$$

$$\boldsymbol{S} = [0, T^{\mu\nu}(\partial_\mu g_{\nu j} + \Gamma^\delta_{\mu\nu} g_{\delta j}), \alpha(T^{\mu 0}\partial_\mu \ln\alpha - T^{\mu\nu}\Gamma^0_{\nu\mu})]^T \ . \tag{2.66}$$

Along with Equations (2.62)-(2.66), we require an equation of state (EOS) which relates the pressure to the rest-mass density ρ and to the specific internal energy ϵ, in order to close the system of equations for hydrodynamics. In Section 2.2.6, we describe in detail the different EOS adopted in numerical codes. For more details on this formulation, we refer to [67, 68]. In order to solve these equations on a computer, one needs to employ powerful numerical methods, in particular high resolution shock-capturing (HRSC) schemes based on Riemann solvers. Such methods are a fundamental tool for correctly representing shocks which are expected in various astrophysical scenarios. We also need to employ a root-finding algorithm in order to recover the primitive variables from the evolved conserved ones, which is not a trivial step as it may be subjected to numerical inaccuracies and could be computationally expensive. We discuss such schemes in detail in Sections 3.1.3 and 4.2.3. However, the Valencia formulation proves to be one of the favorable ones in terms of robustness and stability, and is widely used in modern numerical codes.

2.2.4 General relativistic magnetohydrodynamics

In order to include the effect of electric and magnetic fields in the GRHD formalism, we start with the Faraday electromagnetic tensor $F^{\mu\nu}$ and its dual ${}^*F^{\mu\nu} = (1/2)\eta^{\mu\nu\sigma\delta}F_{\sigma\delta}$, which are written as

$$F^{\mu\nu} = U^\mu E^\nu - U^\nu E^\mu - \eta^{\mu\nu\lambda\delta} U_\lambda B_\delta \ , \tag{2.67}$$

$${}^*F^{\mu\nu} = \frac{1}{2}\eta^{\mu\nu\lambda\delta}F_{\lambda\delta} = U^\mu B^\nu - U^\nu B^\mu - \eta^{\mu\nu\lambda\delta} U_\lambda E_\delta \ , \tag{2.68}$$

where E^μ stands for the electric field, B^μ is the magnetic field, U^μ a generic observer's four–velocity, and $\eta^{\mu\nu\lambda\delta} = \frac{1}{\sqrt{-g}}[\mu\nu\lambda\delta]$ is the Levi-Civita pseudo-tensor which represents the volume element. Equations governing the evolution of electromagnetic fields are the well-known Maxwell's equations, given as

$$\nabla_\nu {}^*F^{\mu\nu} = 0 \ , \tag{2.69}$$

$$\nabla_\nu F^{\mu\nu} = 4\pi \mathcal{J}^\mu \ , \tag{2.70}$$

where $\mathcal{J}^\mu$ is the charge-current four-vector which is expressed using Ohm's law as

$$\mathcal{J}^\mu = q u^\mu + \sigma F^{\mu\nu} u_\nu \ , \tag{2.71}$$

where q is the proper charge density and σ represents the electrical conductivity. Under the assumption of ideal MHD which considers a perfectly conducting fluid such that $\sigma \to \infty$ and $F^{\mu\nu}u_\nu = 0$ (implying that the comoving observer measures no electric field), the electromagnetic tensor and the Maxwell equations can be re-written solely in terms of the magnetic field b measured in the comoving frame, as

$$F^{\lambda\delta} = \eta^{\mu\nu\lambda\delta} b_\mu u_\nu, \qquad {}^*F^{\mu\nu} = b^\mu u^\nu - b^\nu u^\mu = \frac{u^\mu B^\nu - u^\nu B^\mu}{W} \ , \tag{2.72}$$

$$\nabla_\nu {}^*F^{\mu\nu} = \frac{1}{\sqrt{-g}} \partial_\nu \left[\sqrt{-g} \left(b^\mu u^\nu - b^\nu u^\mu \right) \right] = 0 \ , \tag{2.73}$$

where b is the magnetic field measured by a comoving observer, which can be written in terms of the magnetic field measured by an Eulerian observer B in the following way:

$$b^0 = \frac{W B^i v_i}{\alpha}, \quad b^i = \frac{B^i + \alpha b^0 u^i}{W}, \quad b^2 \equiv b^\mu b_\mu = \frac{B^2 + \alpha^2 (b^0)^2}{W^2} \ , \tag{2.74}$$

with $B^2 \equiv B^i B_i$. Considering $\tilde{B}^i \equiv \sqrt{\gamma} B^i$ where γ is the determinant of γ_{ij}, and $\tilde{v}^i \equiv \alpha v^i - \beta^i$, Equation (2.73) can be separated into time and spatial components, with the time component giving the *divergence-free condition* as

$$\partial_i \tilde{B}^i = 0 \ , \tag{2.75}$$

while the spatial component giving the magnetic-field *induction equations* as

$$\partial_t \tilde{B}^i = \partial_j (\tilde{v}^i \tilde{B}^j - \tilde{v}^j \tilde{B}^i) \ , \tag{2.76}$$

Including the magnetic field contribution, the stress-energy tensor can be redefined as

$$T^{\mu\nu} = \left(\rho h + b^2 \right) u^\mu u^\nu + \left(p + p_{\rm mag} \right) g^{\mu\nu} - b^\mu b^\nu \ , \tag{2.77}$$

where p represents the gas pressure, $p_{\rm mag} \equiv \frac{b^2}{2}$ is the magnetic pressure, and $h = 1 + \epsilon + p/\rho$ stands for the relativistic specific enthalpy.

The final expressions of the GRMHD equations in the flux-conservative form as described by Equation (2.61) can be written as

$$\boldsymbol{F}^0 = \begin{pmatrix} D \\ S_j \\ \tau \\ B^k \end{pmatrix}, \qquad \boldsymbol{F}^i = \begin{pmatrix} D\tilde{v}^i/\alpha \\ S_j \tilde{v}^i/\alpha + (p + b^2/2)\delta^i_j - b_j B^i/W \\ \tau \tilde{v}^i/\alpha + (p + b^2/2) v^i - \alpha b^0 B^i/W \\ B^k \tilde{v}^i/\alpha - B^i \tilde{v}^k/\alpha \end{pmatrix} \ , \tag{2.78}$$

$$\boldsymbol{S} = \begin{pmatrix} 0 \\ T^{\mu\nu}(\partial_\mu g_{\nu j} - \Gamma^{\delta}_{\nu\mu} g_{\delta j}) \\ \alpha(T^{\mu 0}\partial_\mu \ln\alpha - T^{\mu\nu}\Gamma^{0}_{\nu\mu}) \\ 0^k \end{pmatrix} , \tag{2.79}$$

where $0^k = (0,0,0)^T$ and

$$D \equiv \rho W \tag{2.80}$$
$$S_j \equiv (\rho h + b^2) W^2 v_j - \alpha b^0 b_j \tag{2.81}$$
$$\tau \equiv (\rho h + b^2) W^2 - (p + b^2/2) - \alpha^2 (b^0)^2 - D \ . \tag{2.82}$$

As mentioned earlier, to complete this set of equations, we also need to add the EOS encoding the behavior of matter at microphysical level.

2.2.5 Electromagnetic gauge conditions

In order to ensure the divergence-free constaint (2.75), one common approach is to evolve the electromagnetic vector potential in a numerical code instead of magnetic field variables. To do so, we first express magnetic field $\mathbf{B}$ in terms of the vector potential $\mathbf{A}$ Considering ∇ as a purely spatial operator, we can write

$$\mathbf{B} = \nabla \times \mathbf{A} \, . \tag{2.83}$$

Taking the divergence of $\mathbf{B}$, we get

$$\nabla \cdot \mathbf{B} = \nabla \cdot (\nabla \times \mathbf{A}) = 0 \ . \tag{2.84}$$

Therefore, by construction, evolving the vector potential $\mathbf{A}$ automatically satisfies (2.75).

We now introduce the four-vector potential as

$$\mathcal{A}_\nu = n_\nu \Phi + A_\nu \, , \tag{2.85}$$

where A_ν is the purely spatial vector potential, whereas Φ stands for the scalar potential. The magnetic field as measured by an Eulerian observer, can then be written as

$$B^i = \epsilon^{ijk} \partial_j A_k \, , \tag{2.86}$$

and the induction equations (2.76) can be re-written in terms of A_i as

$$\partial_t A_i = -E_i - \partial_i \left(\alpha\Phi - \beta^j A_j \right) , \tag{2.87}$$

where $\epsilon^{ijk} = n_\nu \epsilon^{\nu ijk}$ is the 3-dimensional spatial Levi-Civita tensor.

However, the gauge freedom admitted by Maxwell's equations renders the choice of the four-vector potential $\mathcal{A}^\nu$ as not unique, and allows to set a suitable gauge.

2.2.5.1 Algebraic gauge

The numerical codes that first employed vector potential evolution equations to perform GRMHD simulations considered using the *algebraic* gauge [69, 70], where the scalar potential satisfies the following condition

$$\Phi = \frac{1}{\alpha}\left(\beta^j A_j\right). \tag{2.88}$$

This choice leads to a much simplified version of (2.87), reducing it to

$$\partial_t A_i = -E_i\,, \tag{2.89}$$

and therefore, does not necessitate the evolution of the scalar potential Φ.

2.2.5.2 Lorenz gauge

The *Lorenz* gauge is another choice that has been recently adopted in GRMHD simulations [69], which is based on the constraint

$$\nabla_\nu \mathcal{A}^\nu = 0\,, \tag{2.90}$$

which serves as an advection equation for $\mathcal{A}$. In order to impose this constaint, this gauge condition also requires to solve the following evolution equation for the scalar potential

$$\partial_t\left(\sqrt{\gamma}\Phi\right) + \partial_i\left(\alpha\sqrt{\gamma}A^i - \sqrt{\gamma}\beta^i\Phi\right) = 0. \tag{2.91}$$

The Lorenz gauge has proven to be advantageous over the algebraic gauge in GRMHD simulations which utilize adaptive mesh refinement (AMR), for e.g., BNS and NSBH merger simulations [69]. The use of algebraic gauge in such simulations with AMR leads to generation of static gauge modes which then cause interpolation errors at the refinement boundaries, producing spurious magnetic fields near the boundary regions (see [69] for more details), rendering this gauge choice completely unsuitable for BNS or NSMH merger simulations, and more generally, for all simulations which involve magnetised matter crossing refinement boundaries. A more robust gauge choice has been introduced in [71] with the name of *generalized Lorenz* gauge, which considers

$$\nabla_\nu \mathcal{A}^\nu = \xi n_\nu \mathcal{A}^\nu\,, \tag{2.92}$$

where $\xi n_\nu \mathcal{A}^\nu$ acts like a damping term in the advection equation for $\mathcal{A}$. When employing this gauge choice, the evolution equation for the scalar potential becomes

$$\partial_t\left(\sqrt{\gamma}\Phi\right) + \partial_i\left(\alpha\sqrt{\gamma}A^i - \sqrt{\gamma}\beta^i\Phi\right) = -\xi\alpha\sqrt{\gamma}\Phi\,. \tag{2.93}$$

2.2.6 Equation of state

To close the set of GRMHD equations, we require an equation of state (EOS) which provides the relation between the gas pressure p, the rest-mass density ρ and the specific internal energy ϵ. In numerical codes, depending on the (astro)physical problem in hand, various types of

EOS are employed, such as analytical ones which describe the behaviour of an 'ideal fluid' or a 'polytropic' gas [72], to more complex ones which include finite-temperature and composition dependence which come in tabulated forms [73].

One of the major challenges in the field of astrophysics is to understand the behavior of matter in extremely high densities ($\sim 10^{15}$ g cm^{-3} or higher), such as in the core of NSs, which are not reproducible in Earth laboratories. But NSs themselves serve as excellent laboratories for studying the behaviour of high-density nuclear matter. The EOS of nuclear matter in the outer and inner crust of NSs below saturation density ρ_0, is well-constrained as described in the models suggested by Baym, Pethick and Sutherland (1971) [74] and Negele and Vautherin (1975) [75], which are also tested and verfied by the terrestrial experiments. Conversely, the theoretical EOS models for supranuclear densities in the core are only partially constrained by the empirical data, as currently the experiments cannot probe the the extreme conditions of the NS core (see [76–78] for a review). Astrophysical measurements of NS radii, masses, tidal effects and moments of inertia have the potential to provide information about the EOS properties, and the distribution of pressure with respect to the nuclear density. Therefore, it is essential for any GRMHD code to be able to handle various types of EOS with distinct compositions as well as different treatments of nucleon interactions, in order to probe various theoretical models, and support comparison studies between theoretical models and observations.

2.2.6.1 Polytropic EOS

The NS EOS models can be divided into *soft*, *moderate* and *stiff*, depending on the pressure at a given density. Usually, *stiffer* EOS are characterized by higher pressure for a given density, while the opposite are deemed as *softer*. As the pressure is higher in the case of a stiffer EOS model, it results in a NS with larger radius and lower central density as compared to the one derived from a soft EOS having the same mass. A parametrized EOS based on specifying the stiffness of the star at different density intervals measured by the adiabatic index $\Gamma = d\log P/d\log\rho$, can accurately represent many realistic EOS tables [79]. When Γ is taken as a constant, the EOS is called as a *polytrope*, and consequently, the parametrized EOS becomes *piecewise-polytropic*.

A parameterized piecewise polytropic EOS has a generic form

$$p(\rho) = K_i \rho_i^{\Gamma_i} \qquad for \quad \rho_i \leq \rho \leq \rho_{i+1} \ , \tag{2.94}$$

where $\Gamma = 1 + 1/N$ is the adiabatic exponent with N as the adiabatic index, and K is the polytropic constant. Depending on the prescribed composition in the NS model, we define each threshold density ρ_i and accordingly set the parameters of the EOS, i.e., Γ_i and K_i. By the first law of thermodynamics, the energy density $e = \rho(1+\epsilon)$ satisfies the relation

$$\mathrm{d}\frac{e}{\rho} = -p\mathrm{d}\frac{1}{\rho} \ . \tag{2.95}$$

Thus, for $\Gamma \neq 1$, and after a few steps of algebra, we have

$$e(\rho) = (1+w_i)\rho + \frac{K_i}{\Gamma_i - 1}\rho^{\Gamma_i} \ , \tag{2.96}$$

where

$$w_i = \frac{e(\rho_i - 1)}{\rho_i - 1} - 1 - \frac{K_i}{\Gamma_i - 1}\rho_{\rho_i - 1}^{\Gamma_i} \ . \tag{2.97}$$

For each density interval with ρ_{i-1} being the dividing density between zones $i-1$ and i, the expression for the specific enthalpy h is given by

$$h(\rho) = \frac{e + p}{\rho} = 1 + w_i + \frac{\Gamma_i}{\Gamma_i - 1} K_i \rho^{\Gamma_i - 1} \ , \tag{2.98}$$

and the internal energy $e_{\rm int}$ is given by

$$e_{\rm int}(\rho) = \frac{e}{\rho} - 1 = w_i + \frac{K_i}{\Gamma_i - 1}\rho^{\Gamma_i - 1} \ , \tag{2.99}$$

and finally, the sound velocity v_s is written as

$$v_s(\rho) = \sqrt{\frac{\mathrm{d}p}{\mathrm{d}e}} = \sqrt{\frac{\Gamma_i p}{e + p}} \ . \tag{2.100}$$

Such an EOS allows the treatment of NS matter as relativistic, degenerate, quantum Fermi gases at *zero temperature*, and thus, is often referred to as a *cold* NS EOS. Also, due to its isentropic nature, the evolution equation for τ need not be solved when adopting this EOS for numerical evolution.

2.2.6.2 Ideal gas EOS

Another standard EOS adopted in numerical simulations is the *classical ideal gas* EOS which derives its name from the assumption that matter behaves like a classical (non-quantum), ideal (considering only elastic, contact interactions, while long-range interactions are neglected) fluid, which is given by the equation

$$p(\rho, \epsilon) = (\Gamma - 1)\,\rho\epsilon \ , \tag{2.101}$$

which is also alternatively referred to as the *gamma-law* EOS. This is a two-parameter EOS since it depends on both ρ and ϵ. Also, this EOS allows non-isentropic changes to occur, and thus, one needs to solve the evolution equation for τ when considering this EOS for numerical evolution.

2.2.6.3 Hybrid EOS

It is also a common practice to hybridize an EOS, which consists of a cold part and a simple thermal part, given as

$$p(\rho, \epsilon) = p_{\rm cold}(\rho) + (\Gamma_{\rm th} - 1)\,\rho(\epsilon - \epsilon_{\rm cold}(\rho) \ , \tag{2.102}$$

$$\epsilon_{\rm min} = \epsilon_{\rm cold}(\rho) \ . \tag{2.103}$$

This hybridized type of EOS, which includes a thermal component to describe matter evolution, is often used in numerical relativity simulations.

Apart from the above, there also exist finite-temperature composition dependent 3-parameter EOS which we describe in detail in Section 4.1.2.

2.3 Numerical methods

The non-linear nature of the relativistic hydrodynamic equations make them very difficult to solve in an analytical way except for very few (simple) special cases. In particular, the entire set of GRMHD equations consists of more than twenty first-order coupled non-linear equations, for which deriving a general, analytical solution is almost unfeasible. Therefore, we turn to the numerical approaches to find their approximate solutions instead. In this section, we discuss a few important numerical techniques, focusing on grid-based methods and schemes. We begin with a basic introduction of the discretization method, and importance of stability and convergence, followed by a brief description of the finite difference scheme. Furthermore, we discuss the high-resolution shock capturing (HRSC) methods, which have proven to be accurate and efficient when dealing with shocks and discontinuities, and are most employed in state-of-the-art GRMHD codes.

2.3.1 Discretization

For grid-based methods, we require a transition from the continuum initial-value problem to the discrete one. Thus, in this case, we discretize the spacetime along with the hydrodynamical variables, as well as the operators that act on them. In Figure 2.2, we show a schematic representation of such a discretization method. The discretization for spacetime is done separately

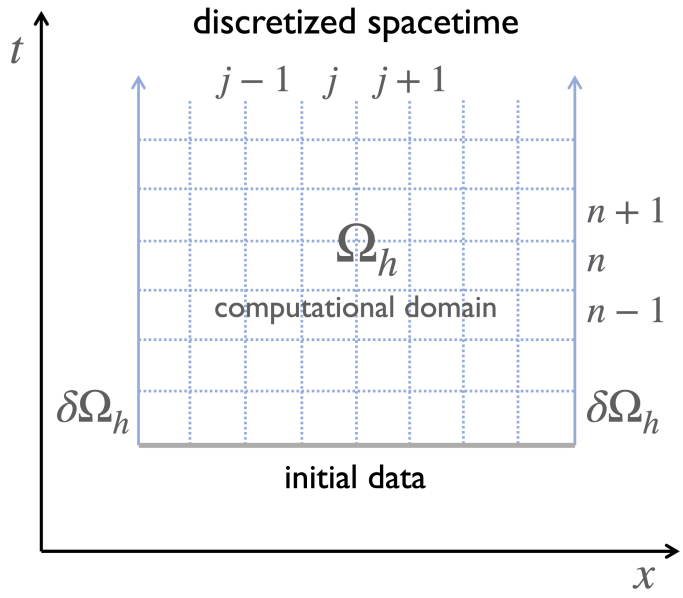

Figure 2.2: Schematic representation of the discretization of spacetime for a initial value problem with solutions Ω_h with boundaries defined by $\partial\Omega_h$.

for space and for time after foliation, in the following way:

$$t^n \equiv t^0 + n\Delta t, \qquad n = 0, 1, \ldots, N_t \tag{2.104}$$

$$x_j \equiv x_0 + j\Delta x, \qquad j = 0, 1, \ldots, J \ , \tag{2.105}$$

where Δt is the separation between two spacelike slices, Δx is the grid mesh width while x_j represents the gridpoints. Similarly, a continuous function $U(x,t)$ can be discretized into a set of approximated values U_j^n as

$$\boldsymbol{U}(x,t) \approx U(x_j^n) = U(x_j, t^n) \equiv U_j^n \ . \tag{2.106}$$

For the continuous differential operator, say L, we discretize as

$$\boldsymbol{L}(\boldsymbol{U}) \to L_h(U_j^n) \ . \tag{2.107}$$

2.3.2 Stability, consistency and convergence

In order to achieve *convergence* to a solution, the numerical scheme must first satisfy the consistency and stability criteria. For a partial differential equation (PDE) of a generic form

$$\boldsymbol{L}(\boldsymbol{U}) = \boldsymbol{F} \ , \tag{2.108}$$

where $\mathbf{F}$ is a function of $\mathbf{U}$ alone, such that it could be discretized to the form

$$L_h(U_j^n) = F_h \ , \tag{2.109}$$

a numerical scheme is considered to be *consistent* [80] if it satisfies

$$\lim_{h\to 0} \epsilon_j^{(h)} \equiv \left[L_h(U_j^n) - F_h\right] - \left[\boldsymbol{L}(\boldsymbol{U}) - \boldsymbol{F}\right] \to 0 \ , \tag{2.110}$$

where $\epsilon_j^{(h)}$ is called as the *truncation error* (or residual error). Therefore, in the limit of vanishing grid-spacing, if the truncation error goes to zero, the scheme is said to be consistent, and solutions computed by the scheme will approach the true PDE's solutions. For the scheme considering $L_h(U_j^n) = 0$ with a discretized two-norm given by

$$\|U(t^n)\|_2 = \left(\frac{1}{J}\sum_{j=0}^{J}(U_j^n)^2\right)^{1/2} \ , \tag{2.111}$$

the *stability* criteria is given as

$$\|U^n\|_2 \leq C\left\|U^0\right\|_2 , \qquad for \quad 0 \leq n\Delta t \leq T;\ \Delta x, \Delta t \to 0 \ . \tag{2.112}$$

Stability ensures that the errors decay with subsequent increase in time-steps. Finally, L_h is said to satisfy the global convergence criterion if

$$\lim_{h\to 0} Ch^p = 0 \ , \tag{2.113}$$

where p is the global convergence order. In summary, the solutions obtained through the discretization process should pass the consistency and stability conditions in order to obtain convergence.

2.3.3 Finite difference schemes

In order to find the solutions of non-trivial PDEs in GRMHD, we have a variety of approximate approaches in the market, amongst which the finite difference (FD) schemes play an important role and are most commonly adopted. After discretization, consider a differential equation for the function $u(x_j, t^n)$ defined at position x_j and time t^n. We can then express the solution of this equation as a Taylor expansion around (x_j, t^n) such that the derivatives in the expansion are computed from the difference equations that evaluate differences in the neighboring grid-points. This is the basic concept followed in the grid-based FD methods.

2.3.3.1 Courant-Friedrichs-Lewy condition

Before describing the different approaches in FD schemes, let us first shed some light on an important criterion required to ensure the convergence of an FD scheme. In particular, to have stabilitiy, we must choose an appropriate time-step interval Δt for evolution. To understand the physical perspective, imagine a wave moving across the spatial grid and say we need to compute its amplitude after each time step. In this case, the computation speed, or in other words, propagation speed of the solutions to the PDE, should be less than the characteristive wave speed defined by the grid spacing $\Delta x/\Delta t$. The *Courant-Friedrichs-Lewy* (CFL) condition [81] defines this constraint as

$$\nu \frac{\Delta t}{\Delta x} \leq C_{\rm CFL} \ , \tag{2.114}$$

where $C_{\rm CFL}$ is a constant factor usually set to a value less than 1, and ν is the characteristic speed of the equations. In Figure 2.3, we show a comparison between the CFL-stable and CFL-unstable schemes.

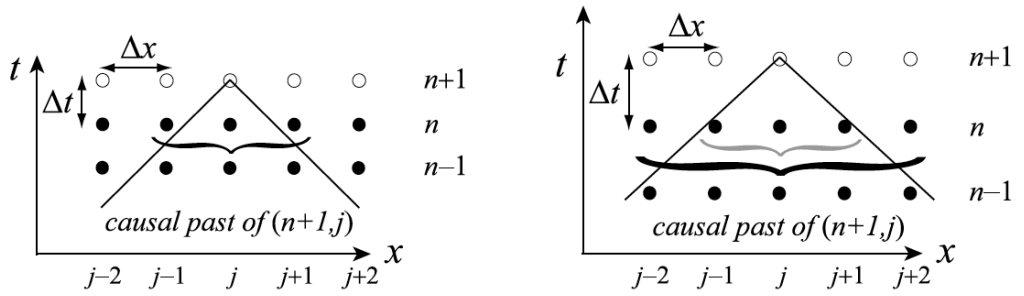

Figure 2.3: Schematic representation of the CFL criterion. *Left:* Stable time integration is enabled as $\Delta t/\Delta x$ is small enough. *Right:* $\Delta t/\Delta x$ is too large for stable time integration performed for points $j-1$, j and $j+1$, but is small enough for stable time integration performed for points $j-2$ upto $j+2$ (with unit step increase). Figure taken from [68].

2.3.3.2 Forward, backward and centered difference schemes

Consider the spatial and temporal grid spacings represented as $\Delta x \equiv x_{j+1} - x_j$ and $\Delta t \equiv t^{n+1} = t^n$ respectively. The Taylor expansion (in first order) along the spatial direction can then be written as

$$u(x_{j+1}, t^n) = u(x_j, t^n) + \partial_x u(x_j, t^n) + \mathcal{O}(\Delta x^2) \ , \tag{2.115}$$

$$u(x_{j-1}, t^n) = u(x_j, t^n) - \partial_x u(x_j, t^n) + \mathcal{O}(\Delta x^2) \ , \tag{2.116}$$

Using these equations, we can define the *forward* and *backward* Euler schemes respectively as

$$\partial_x u(x_j, t^n) = \frac{u(x_{j+1}, t^n) - u(x_j, t^n)}{\Delta x} + \mathcal{O}(\Delta x) \ , \tag{2.117}$$

$$\partial_x u(x_j, t^n) = \frac{u(x_j, t^n) - u(x_{j-1}, t^n)}{\Delta x} + \mathcal{O}(\Delta x) \ , \tag{2.118}$$

Considering Equations (2.115) and (2.116) up to second order expansion, we have

$$u(x_{j+1}, t^n) = u(x_j, t^n) + \Delta x \, \partial_x u(x_j, t^n) + \frac{\Delta x^2}{2} \partial_x^2 u(x_j, t^n) + \mathcal{O}(\Delta x^3) \ , \tag{2.119}$$

$$u(x_{j-1}, t^n) = u(x_j, t^n) - \Delta x \, \partial_x u(x_j, t^n) + \frac{\Delta x^2}{2} \partial_x^2 u(x_j, t^n) + \mathcal{O}(\Delta x^3) \ , \tag{2.120}$$

and subtracting (2.120) from (2.119), we get

$$\partial_x u(x_j, t^n) = \frac{u(x_{j+1}, t^n) - u(x_{j-1}, t^n)}{2\Delta x} + \mathcal{O}(\Delta x^2) \ , \tag{2.121}$$

which represents a *centered* difference scheme. Similarly, in this way, one can compute the higher-order approximation of such derivatives.

2.3.3.3 Upwind scheme

Another first order scheme for computations in the temporal direction from which the characteristic information propagates, is called upstream or *upwind* scheme. Consider again a one-dimensional scalar advection equation of the form similar to (2.49)

$$\partial_t u + \lambda \partial_x u = 0 \ , \tag{2.122}$$

with λ as the advection velocity and $u = u_0(x - \lambda t)$ as the general solution, the Taylor expansion of this solution around (x_j, t^n) can be written as

$$u(x_j, t^n + \Delta t) = u(x_j, t^n) + \partial_t u(x_j, t^n) \Delta t + \mathcal{O}(\Delta t^2) \ , \tag{2.123}$$

which after discretization, becomes

$$u(x_j, t_{n+1}) = u(x_j, t_n) + \partial_t u(x_j, t_n) \Delta t + \mathcal{O}(\Delta t^2) \ . \tag{2.124}$$

One can isolate the time and spatial derivative of this equation, obtaining the first-order FD approximation of the time derivative as

$$\partial_t u(x_j, t_n) = \frac{u(x_j, t_{n+1}) - u(x_j, t_n)}{\Delta t} + \mathcal{O}(\Delta t) \ , \tag{2.125}$$

while the spatial derivative can be written using either Equation (2.117) or (2.118). While the approximation for the spatial derivative encounters slight ambiguity, the time derivative, which can be resolved thinking that the each point in the initial solution translates to a new one $x + \lambda \Delta t$ with time interval Δt. Then, depending on the direction, and the sign of the advection velocity λ, we can consequently write (2.122) as

$$\frac{u(x_j, t_{n+1}) - u(x_j, t_n)}{\Delta t} = -\lambda \left(\frac{u(x_j, t_n) - u(x_{j-1}, t_n)}{\Delta x} \right) + \mathcal{O}(\Delta t, \Delta x) \quad for \ \lambda > 0 \ , \tag{2.126}$$

$$\frac{u(x_j, t_{n+1}) - u(x_j, t_n)}{\Delta t} = -\lambda \left(\frac{u(x_{j+1}, t_n) - u(x_j, t_n)}{\Delta x} \right) + \mathcal{O}(\Delta t, \Delta x) \quad for \ \lambda < 0 \ . \tag{2.127}$$

For the new timelevel, this scheme would then lead to the solution given as

$$u(x_j, t_{n+1}) = u(x_j, t_n) - \alpha(u(x_j, t_n) - u(x_{j-1}, t_n)) + \mathcal{O}(\Delta t^2, \Delta x \Delta t) \ if \lambda > 0 \ , \tag{2.128}$$

$$u(x_j, t_{n+1}) = u(x_j, t_n) - \alpha(u(x_{j+1}, t_n) - u(x_j, t_n)) + \mathcal{O}(\Delta t^2, \Delta x \Delta t) \ if \lambda > 0 \ , \tag{2.129}$$

where $\alpha \equiv \lambda(\Delta t / \Delta x)$. Figure 2.4 provides a brief schematic of the upwind scheme.

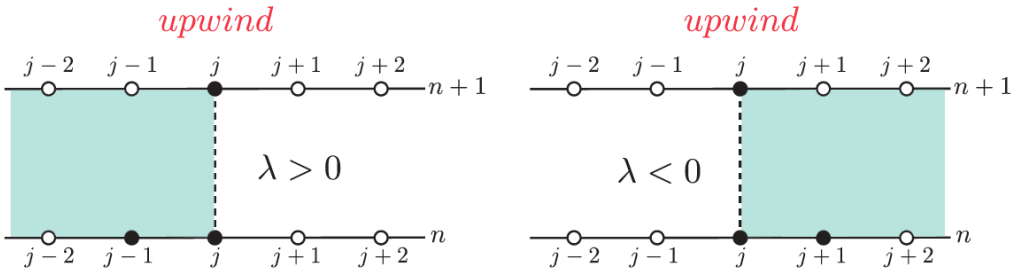

Figure 2.4: Schematic representation of the upwind scheme. Here, the dashed line represent the time step, while the filled grid-points are used by the discrete differential operator. Figure taken from [54].

2.3.3.4 Explicit and implicit schemes

Using the upwind scheme as an example, we can now define implicit and explicit schemes. An explicit scheme is a scheme for which the quantities at the $n + 1$ time step can be computed directly from combinations of the quantities at n or previous time steps. In particular

$$u(x_j, t_{n+1}) = \mathcal{F}\big(u(x_j, t_n), u(x_{j\pm1}, t_n), ..., u(x_j, t_{n-1}), u(x_{j\pm1}, t_{n-1}), ...\big) \ . \tag{2.130}$$

Whereas, an implicit scheme depends on quantites defined at the same time step or on successive time steps, for e.g.,

$$u(x_j, t_{n+1}) = \mathcal{F}\big(u(x_j, t_n), u(x_{j\pm1}, t_n), ..., u(x_j, t_{n+1}), u(x_{j\pm1}, t_{n+1}), ...\big) \ . \tag{2.131}$$

Implicit schemes prove to be advantageous since they are not necessarily required to satify the CFL stability criterion. However, they do need a general solution for evolution, which makes them computationally more expensive than explicit schemes. From definition, one can see that the upwind scheme is an explicit scheme.

2.3.3.5 Forward-time centered-space scheme (FTCS)

Starting again with the advection equation (2.122), and using Equations (2.121) and (2.126), we can arrive at the algorithm

$$u(x_j, t_{n+1}) = u(x_j, t_n) - \frac{\alpha}{2}(u(x_{j+1}, t_n) - u(x_{j-1}, t_n)) + \mathcal{O}(\Delta x^2) \ , \tag{2.132}$$

which is called as the Forward-time centered-space (FTCS) scheme. It can be shown that this scheme turns out to be unstable [54]. In particular, after performing a *Von Neumann* stability check by considering the time evolution of the eigenmode of u with the maximum amplitude, it can be noticed that this eigenmode increases exponentially in amplitude with time, resulting the numerical solution to blow up, rendering this scheme to be unfit for numerical simulations.

2.3.3.6 Leap-Frog, Lax-Friedrichs, and Lax-Wendroff schemes

The *Leap-Frog* scheme is a stable second order scheme, both in time and spatial derivatives, in which, after following the similar approach to the advection equation, we get

$$u(x_j, t_{n+1}) = u(x_j, t_{n-1}) - \alpha(u(x_{j+1}, t_n) - u(x_{j-1}, t_n)) + \mathcal{O}(\Delta x^2) \ . \tag{2.133}$$

The *Lax Friedrichs* scheme is a first order scheme, which is an improvised version of the FTCS scheme where the term u_j^n in the solution is substituted by its spatial average, so that the expression to represent the advection equation (2.122) is given as

$$u(x_j, t_{n+1}) = \frac{1}{2}(u(x_{j+1}, t_n) + u(x_{j-1}, t_n)) - \frac{\alpha}{2}(u(x_{j+1}, t_n) - u(x_{j-1}, t_n)) + \mathcal{O}(\Delta t^2, \Delta^2 x \Delta t) \tag{2.134}$$

This scheme is known to be conditionally stable which satisfies the CFL condition.

A second-order extension of the Lax-Friedrichs, the *Lax-Wendroff* scheme is an accurate two-level scheme derived by combining the Leap-Frog and the Lax-Friedrichs scheme, which can be realised in terms of two 'half-steps'. The first half-step is the Lax-Friedrichs one, for $x_{j\pm\frac{1}{2}}$ spatial positions and $t_{n+\frac{1}{2}}$ half time-level

$$u(x_{j\pm\frac{1}{2}}, t_{n+\frac{1}{2}}) = \frac{1}{2}(u(x_j, t_n) + u(x_{j\pm1}, t_n)) \mp \frac{\alpha}{2}(u(x_{j\pm1}, t_n) - u(x_j, t_n)) + \mathcal{O}(\Delta x^2) \ . \tag{2.135}$$

The second half-step is the leapfrog one, such that for the new time level t_{n+1}, we obtain the following solution, also using (2.135)

$$u(x_j, t_{n+1}) = u(x_j, t_n) - \alpha(u(x_{j+\frac{1}{2}}, t_{n+\frac{1}{2}}) - u(x_{j-\frac{1}{2}}, t_{n+\frac{1}{2}})) + \mathcal{O}(\Delta x^2) \tag{2.136}$$

$$= u(x_j, t_n) - \frac{\alpha}{2}(u(x_{j+1}, t_n) - u(x_{j-1}, t_n)) + \frac{\alpha}{2}(u(x_{j+\frac{1}{2}}, t_n) \tag{2.137}$$

$$- 2u(x_j, t_n) + u(x_{j-\frac{1}{2}}, t_n)) + \mathcal{O}(\Delta x^2) \ .$$

Therefore, the Lax-Wendroff scheme can be written as a one-level scheme as shown in the above equation, upholding the stability by successfully implementing the CFL criterion.

In Figure 2.5, we provide a schematic comparing FTCS, leap frog, Lax-Friedrichs and Lax-Wendroff schemes.

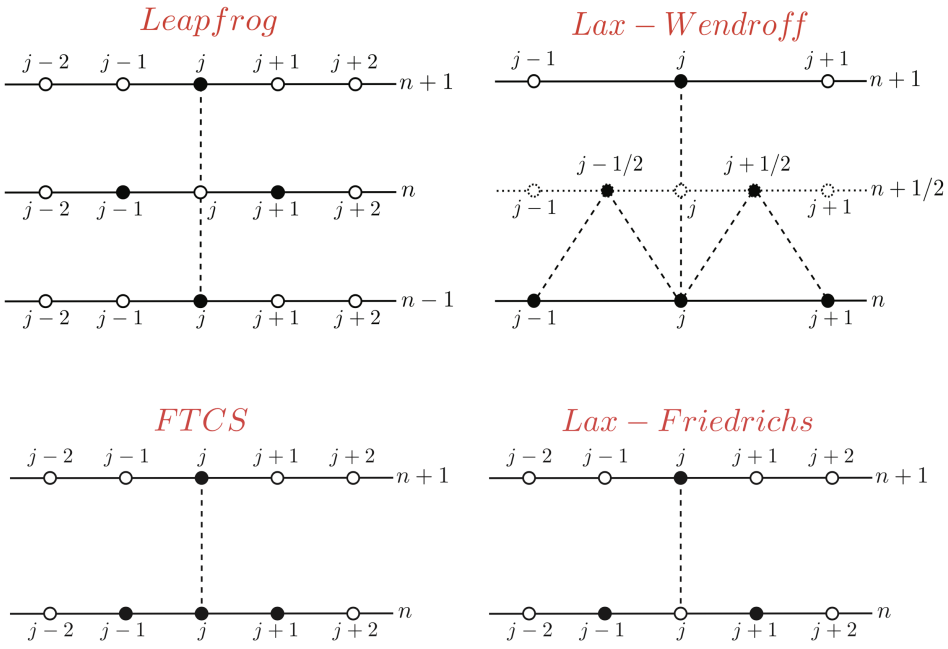

Figure 2.5: Comparison between leap-frog (top-left), Lax-Wendroff (top-right), FTCS (bottom-left) and Lax-Friedrichs (botton-right) schemes. Here, the dashed line represent the time evolution, while the filled grid-points are the ones used by the discrete differential operator. Figure adopted from [54].

2.3.4 Godunov methods

In order to deal with discontinuities efficiently, another class of methods were introduced, first by Godunov in 1959 [82]. The original approach considered approximating the continuous solutions with piece-wise constant functions, creating a series of Riemann problems (see Section 2.3.4.1 for more details) at the grid interfaces, followed by evaluating the numerical fluxes.

Let us start with considering a single computational cell of discretized spacetime and let Ω be a region of spacetime bounded by six time-like surfaces $\Sigma_{x_j-\Delta x/2}$ and $\Sigma_{x_j+\Delta x/2}$ and two space-like hypersurfaces Σ_t and $\Sigma_{t+\Delta t}$. Expressing the integral form of Equation (2.61) as

$$\int \partial_t(\sqrt{\gamma}\boldsymbol{F}^0)\mathrm{d}\Omega = \int \partial_i(\sqrt{-g}\boldsymbol{F}^i)\mathrm{d}\Omega + \int \sqrt{-g}\boldsymbol{S}\mathrm{d}\Omega \ , \tag{2.138}$$

where $\mathrm{d}\Omega \equiv \mathrm{d}t\mathrm{d}x\mathrm{d}y\mathrm{d}z$, this equation can be recast into the following form:

$$\begin{aligned}(\Delta V\bar{\boldsymbol{F}}^0)|_{t+\Delta t} - (\Delta V\bar{\boldsymbol{F}}^0)|_t = &- \int_{\Sigma_{x_j+\Delta x/2}} (\sqrt{-g}\boldsymbol{F}^x)\mathrm{d}t\mathrm{d}y\mathrm{d}z + \int_{\Sigma_{x_j-\Delta x/2}} (\sqrt{-g}\boldsymbol{F}^x)\mathrm{d}t\mathrm{d}y\mathrm{d}z \\ &- \int_{\Sigma_{y_j+\Delta y/2}} (\sqrt{-g}\boldsymbol{F}^y)\mathrm{d}t\mathrm{d}x\mathrm{d}z + \int_{\Sigma_{y_j-\Delta y/2}} (\sqrt{-g}\boldsymbol{F}^y)\mathrm{d}t\mathrm{d}x\mathrm{d}z \\ &- \int_{\Sigma_{z_j+\Delta z/2}} (\sqrt{-g}\boldsymbol{F}^z)\mathrm{d}t\mathrm{d}x\mathrm{d}y + \int_{\Sigma_{z_j-\Delta z/2}} (\sqrt{-g}\boldsymbol{F}^z)\mathrm{d}t\mathrm{d}x\mathrm{d}y \\ &+ \int \sqrt{-g}\boldsymbol{S}\mathrm{d}\Omega \ ,\end{aligned} \tag{2.139}$$

where $\bar{\boldsymbol{F}}^0$ is defined as

$$\bar{\boldsymbol{F}}^0 \equiv \frac{1}{\Delta V}\int_{\Delta V} \sqrt{\gamma}\boldsymbol{F}^0\mathrm{d}x\mathrm{d}y\mathrm{d}z \ , \tag{2.140}$$

along with

$$\Delta V \equiv \int_{x_j-\Delta x/2}^{x_j+\Delta x/2}\int_{y_j-\Delta y/2}^{y_j+\Delta y/2}\int_{z_j-\Delta z/2}^{z_j+\Delta z/2} \sqrt{\gamma}\mathrm{d}x\mathrm{d}y\mathrm{d}z \ . \tag{2.141}$$

Once the solutions to Riemann problems are derived, the numerical fluxes at the cell-interface can be computed as the time averages of the fluxes, written as

$$\bar{\boldsymbol{F}}^i \equiv \frac{1}{\Delta t}\int_t^{t+\Delta t} \sqrt{-g}\boldsymbol{F}^i\mathrm{d}t \ . \tag{2.142}$$

Dividing Equation (2.139) by ΔV and ignoring the source term, we get

$$\frac{(\bar{\boldsymbol{F}}^0)|_{t+\Delta t} - (\bar{\boldsymbol{F}}^0)|_t}{\Delta t} = \sum_{i=1,3} \frac{(\bar{\boldsymbol{F}}^i)|_{x_j-\Delta x/2} - (\bar{\boldsymbol{F}}^i)|_{x_j+\Delta x/2}}{\Delta x} \ . \tag{2.143}$$

Based on Godunov's method, the spatial fluxes can be re-written as

$$(\bar{\boldsymbol{F}}^i)|_{x_j+\Delta x/2} \approx \frac{1}{\Delta t}\hat{\boldsymbol{F}}^i(\tilde{u}(x_{j+1},t_n),\tilde{u}(x_j,t_n)) \tag{2.144}$$

$$(\bar{\boldsymbol{F}}^i)|_{x_j-\Delta x/2} \approx \frac{1}{\Delta t}\hat{\boldsymbol{F}}^i(\tilde{u}(x_j,t_n),\tilde{u}(x_{j-1},t_n)) \ , \tag{2.145}$$

where $\tilde{u}$ denotes the piecewise constant function, and the solutions to the Riemann problem are represented by $\hat{\boldsymbol{F}}(\tilde{u}(x_{j+1},t_n),\tilde{u}(x_j,t_n))$ and $\hat{\boldsymbol{F}}(\tilde{u}(x_j,t_n),\tilde{u}(x_{j-1},t_n))$, computed at the interfaces between the cells x_j, x_{j+1} and x_{j-1}, x_j, respectively.

2.3.4.1 Riemann problems

A Riemann problem consists of a specific intial value problem related to a conservative equation along with a piecewise constant initial data having a single discontinuity in the domain of interest. Discontinuities are a natural result of shocks encountered in many physical scenarios, and are expected to arise when solving nonlinear evolution equations. Furthermore, when substituting the hydrodynamical functions and spacetime terms with piecewise constant functions, we can form a series of discontinuities due to discretization. Therefore, we end up with a set of Riemann problems with discontinuous initial data. For example, for a discontinuity present at $x = 0$, the initial data for a variable $U(x, t)$ can be written as

$$U_0 = \begin{cases} U_L & \text{if} \quad x < 0 \\ U_R & \text{if} \quad x > 0 \end{cases} . \tag{2.146}$$

The solution to Riemann problems can be derived [83, 84] but even then, simplifying the evolution procedure might be non-trivial. Typically, in hydrodynamics, the solution of a Riemann problem consists of three elements: a single contact discontinuity (CD) and two waves moving away from this discontinuity. Depending on the initial conditions, the two waves moving away can either be rarefaction waves (RW) or shock waves. Figure 2.6 shows a schematic view of the solution of Riemann problem.

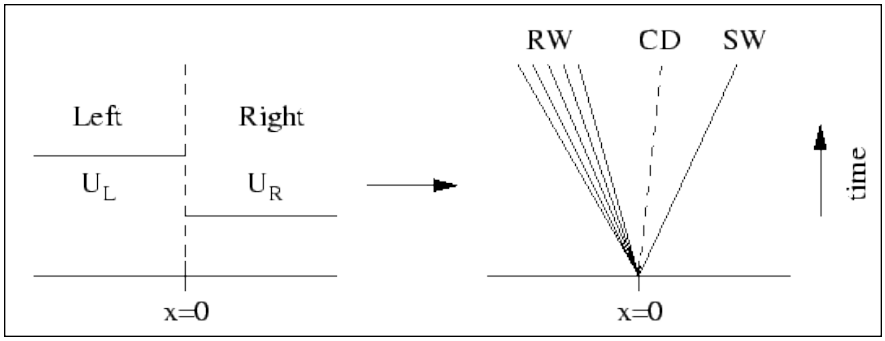

Figure 2.6: Schematic representation of a Riemann problem along with its solution. Figure taken from [85].

2.3.5 High-resolution shock capturing methods

High-Resolution Shock Capturing (HRSC) schemes are conservative numerical methods that converge to a weak solution in presence of a discontinuity, which can accurately reproduce the discontinuous features of the solution, guaranteeing the conservation of the set of conserved variables (considering sources as zero). These methods can be further divided into finite-volume conservative methods and finite difference methods, with the latter consisting of upwind and central schemes, which have been discussed in previously.

The HRSC methods used in the modern numerical codes usually follow a three step algorithm:

- implementation of a *reconstruction* method to interpolate the values to the left and right of the cell boundaries;
- employing an *approximate Riemann solver*;
- using a time-update algorithm, usually a second or higher order *Runge-Kutta* method.

2.3.5.1 Reconstruction methods

The simplest reconstruction technique is based on the Godunov scheme which replaces the function u with its spatial average inside each grid cell. However, this rough approximation leads to less accurate results, thus demanding more sophisticated methods.

Linear reconstruction

The first improvisation uses a linear function to approximate u within each cell j, such that

$$u(x_j, t_n) \approx u^n_{\rm LIN}(x) \equiv \bar{u}^n_j + m^n_j (x - x_j) \ , \tag{2.147}$$

where the slope m^n_j could be computed using, for example, a forward, backward or a centered difference scheme as

$$m^n_j = \frac{\bar{u}^n_{j+1} - \bar{u}^n_j}{\Delta x} \qquad Forward; \tag{2.148}$$

$$m^n_j = \frac{\bar{u}^n_j - \bar{u}^n_{j-1}}{\Delta x} \qquad Backward; \tag{2.149}$$

$$m^n_j = \frac{\bar{u}^n_{j+1} - \bar{u}^n_{j-1}}{2\Delta x} \qquad Centered \ . \tag{2.150}$$

The computed values of $u^n_{\rm LIN}$ at cell interfaces then serve as piecewise constant initial data for Riemann problems which could then be solved using an exact or an approximate Riemann solver. However, the presence of large gradients in u may lead to large values of the computed slope m^n_j, causing unphysical oscillations in the reconstructed function at cell boundaries. To deal with this difficulty, a *slope limiting* fix is often introduced. A common approach is to first define the *total variation* of $u^n_{\rm LIN}$ as

$$TV(u^n_{\rm LIN}) \equiv \sum_i |u^n_{\rm LIN}(x_j) - u^n_{\rm LIN}(x_{j-1})| \ , \tag{2.151}$$

which should not increase with time, following the condition

$$TV(u^{n+1}_{\rm LIN}) \leq TV(u^n_{\rm LIN}) \ , \tag{2.152}$$

Techniques that satisfy the above equation are commonly known as total-variation-diminishing (TVD). In order to fulfill this condition, the following choices for the slope m^n_j are often adopted:

- $m_j^n = \text{MINMOD}\left(\frac{\bar{u}_j^n - \bar{u}_{j-1}^n}{\Delta x}, \frac{\bar{u}_{j+1}^n - \bar{u}_j^n}{\Delta x}\right)$, where

$$\text{MINMOD}(a,b) = \begin{cases} a & \text{if} \quad |a| < |b| \text{ and } ab > 0 \\ b & \text{if} \quad |a| > |b| \text{ and } ab > 0 \\ 0 & \text{if} \quad ab < 0 \end{cases} . \tag{2.153}$$

  Here, MINMOD chooses the minimum between the forward and backward slopes ((2.148) and (2.149)) in case both have the same signs, whereas in case of opposite signs, it recovers the default Godunov scheme.

- $m_j^n = \text{MINMOD}\left(\frac{\bar{u}_{j+1}^n - \bar{u}_{j-1}^n}{\Delta x}, 2\frac{\bar{u}_j^n - \bar{u}_{j-1}^n}{\Delta x}, 2\frac{\bar{u}_{j+1}^n - \bar{u}_j^n}{\Delta x}\right)$,

  where MINMOD is extended to return the quantity whose absolute value is minimum in case all the three quantities have the same sign, while it returns zero for any other case. This technique is also called as the *monotonised central difference* method or *MC limiter*.

Piecewise-parabolic reconstruction

The *piecewise-parabolic* method (PPM) is a high-order reconstruction method which, as the name suggests, adopts a parabolic interpolation of the quantities inside a cell. Figure 2.7 shows how the values are interpolated at the boundaries (depicted in solid red boxes) via PPM, yielding the left and right states of the Riemann problem. First, we start with the spatial average of a general quantity U for $\Delta x = x_{j+\frac{1}{2}} - x_{j-\frac{1}{2}}$, given as

$$U_j^n = \frac{1}{\Delta x}\int_{x_{j-\frac{1}{2}}}^{x_{j+\frac{1}{2}}} U(x,t^n)\mathrm{d}x \ . \tag{2.154}$$

Then, introducing an interpolating parabola equation $\mathcal{P}(\alpha)$, a function of the variable α,

$$\mathcal{P}(\alpha) = a\alpha^2 + b\alpha + c \ , \tag{2.155}$$

where $\alpha = (x - x_{j-1/2})/\Delta x$ and a,b,c are vector coefficients. In order to ensure the conservative character of the reconstruction, the above equation is accompanied by a constraint equation given as

$$U_j^n = \int_0^1 \mathcal{P}(\alpha)\mathrm{d}\alpha \ . \tag{2.156}$$

These equations provide two degrees of freedom, namely U_j^- and U_j^+, which are the values of $\mathcal{P}(\alpha)$ at the left and right boundaries of the cell, which are then used in determining the vector coefficients a, b and c. Consequently, to derive these vector coefficients, we impose the condition such that they remain within the range of two adjacent values U_j^n and U_{j+1}^n, and for the smooth parts, we have the condition $U_{j+1}^- = U_j^+ = U_{j+1/2}^n$ for a continuous interpolation function at $x_{j+1/2}$, with $\mathcal{P}(\alpha)$ as a monotone in each cell.

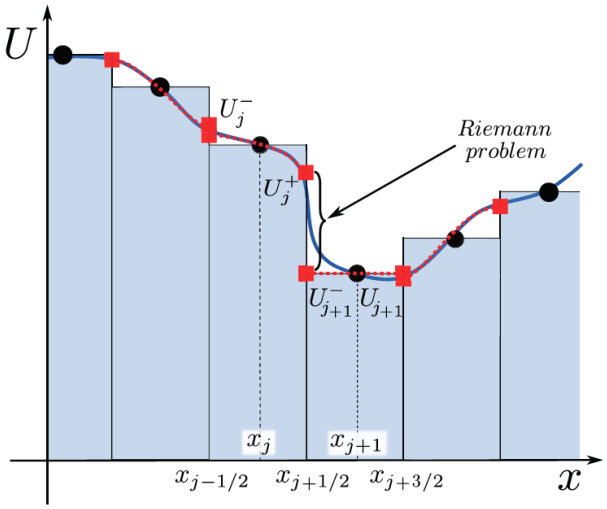

Figure 2.7: Schematic diagram representing the PPM reconstruction method. Here, the values represented by the red solid box, are extrapolated at each cell boundary, providing the left and right states of the Riemann problem. Figure taken from [54].

2.3.5.2 Approximate Riemann solvers

The Riemann problem can be numerically solved to any required accuracy, however, for very accurate or *exact* solutions, the computations turn out to be numerically expensive. Therefore, in modern day simulations, computationally less expensive and reasonably accurate *approximate Riemann solvers* are adopted. These solvers can be further classified into *complete Riemann solvers* consisting of all characteristic fields of the exact solution and *incomplete Riemann solvers*, which contain only a subset of the characteristic fields. Here, we discuss a particular incomplete Riemann solver called the *HLLE solver*, which is commonly used in state-of-the-art GRMHD codes.

HLLE

Initially introduced by Harten, Lax and van Leer (1983) [86] and later revised by Einfeldt (1988) [87], the HLLE formulation assumes a two wave-structure for the Riemann problem and after the dissolution of this local Riemann discontinuity, considers that the two waves that propagate in opposite directions with velocities v_L and v_R, with a single, constant state U^{HLLE} in between as

$$U(x,t) = \begin{cases} U_L & \text{if} \quad x/t < v_L \\ U^{HLLE} & \text{if} \quad v_L < x/t < v_R \\ U_R & \text{if} \quad x/t > v_R \end{cases} , \tag{2.157}$$

Figure 2.5 provides a better intuition of this framework. Starting with the homogeneous conservation equation $\partial_t U + \nabla F(U) = 0$, and setting $F_L = F(U_L)$ and $F_R = F(U_R)$, after a few steps of algebra, we get

$$U^{HLLE} = \frac{v_R U_R - v_L U_L + F_L - F_R}{v_R - v_L} \ . \tag{2.158}$$

By enforcing that the intial conditions propagate with a finite speed at the cell-boundaries, we can define

$$\tilde{F}_L = F_L + v_L(U^{HLLE} - U_L) \ , \tag{2.159}$$
$$\tilde{F}_R = F_R + v_R(U^{HLLE} - U_R) \ , \tag{2.160}$$
$$\tag{2.161}$$

Subsequently, by substituting one of the above two conditions into the U^{HLLE} expression, we get

$$F^{HLLE} = \frac{v_R F_L - v_L F_R + v_R v_L (U_R - U_L)}{v_R - v_L} \ , \tag{2.162}$$

where F^{HLLE} is the defined HLLE flux, which can be further used into a Godunov method as

$$F(x,t) = \begin{cases} F_L & \text{if} \quad x/t < v_L \\ F^{HLLE} & \text{if} \quad v_L < x/t < v_R \\ F_R & \text{if} \quad x/t > v_R \end{cases} \ , \tag{2.163}$$

The HLLE solver is a standard solver used in modern simulations, which is effective both for its simplistic nature and for the structure of its implementation. It has shown to work well when dealing critical sonic rarefactions, but can fall short while encountering contact discontinuities as it neglects the middle waves in the solution. Thus, it needs to be coupled with an algorithm to accurately calculate the wave speeds v_L and v_R in order to get the solution for the flux.

Lax-Friedrichs

If we assume the left and right wave speeds to be equal, i.e., $v_L = v_R = v$, the HLLE flux given by Equation (2.162) can be reduced to

$$F^{LxF} = \frac{F_R - F_L + v(U_R - U_L)}{2} \ , \tag{2.164}$$

which is called as the *Lax-Friedrichs* flux [88]. This second-order scheme is considered to be more dissipative than HLLE, however, it can be useful when dealing with very strong shocks and pressure jumps.

2.3.5.3 Time update: method of lines

The reconstruction methods ensure that a prescribed order of accuracy holds when employing the discretized representation of the spatial differential operator. However, when evolving from

one time level to another, retaining the high-order accuracy might not be trivial. To do so efficiently, the method of lines (MoL) technique [88, 89] is usually adopted. In this approach, discretization of the continuum equations is considered only in space, and the resulting set of ordinary differential equations (ODEs) are then solved numerically. This allows minimal coupling between the hydrodynamics and spacetime solvers, allowing for more independence during the implementation of different schemes.

In order to evolve the system in time, we first consider the values of conserved variables in each numerical grid point $\boldsymbol{F}^0_{i,j,k}$ to be represented as the cell average $\bar{\boldsymbol{F}}^0_{i,j,k}$ defined in Equation (2.140). The time evolution of this cell-averaged quantity can be written using Equation (2.143) as

$$\frac{\mathrm{d}\boldsymbol{F}^0_{i,j,k}}{\mathrm{d}t} = \frac{\mathrm{d}\bar{\boldsymbol{F}}^0_{i,j,k}}{\mathrm{d}t} = \sum_{l=1,3} \frac{(\hat{\boldsymbol{F}}^l)|_{x^l_{i,j,k}-\Delta x/2} - (\hat{\boldsymbol{F}}^l)|_{x^l_{i,j,k}+\Delta x/2}}{\Delta x^l} + \boldsymbol{S}_{i,j,k} \ , \tag{2.165}$$

which now also includes the source terms $\boldsymbol{S}_{i,j,k}$ to be computed from the primitive variables $\boldsymbol{U}_{i,j,k}$. This gives a system of ODEs which can now be solved with standard ODE solvers such as fourth order Runge-Kutta. For computing the right hand of the above equation, a generic algorithm followed by a GRMHD code is to separately compute the source terms $\boldsymbol{S}(\boldsymbol{U})$ from the primitives at all grid points, and side-by-side compute for each direction x^l, (i) the reconstructed quantites U_L and U_R at boudary interfaces, (ii) then derive solutions at cell interfaces using the approximate Riemann solver for Riemann problems having intial data as $U_{L,R}$, (iii) and finally, compute the flux $\hat{\boldsymbol{F}}^l$ accross these interfaces. Once the conserved variables $\boldsymbol{F}^0(\boldsymbol{U})$ are derived for the new time step, the primitive variable recovery procedure is executed to compute the primitives for this new time step, and then the stress-energy tensor is determined for use in the Einstein equations.

Chapter 3

The Spritz code

GRMHD codes provide the essential framework to study the physics of compact objects and explore the various astrophysical phenomenona related to them. In most cases, the GRMHD equations are to be evolved along with dynamical spacetimes, and a number of GRMHD codes such as `WhiskyMHD` [90], `GRHydro` [91] and `IllinoisGRMHD` [92] which work in tandem with the publicly available numerical infracture Einstein Toolkit [93, 94], have been developed over the years for this purpose. These codes have also been employed, in particular, to study compact binary mergers (e.g., [32, 95–97], JVK1) and accretion onto supermassive BHs (e.g., [71, 98–103]). In the case of compact binary mergers, GRMHD codes have been used to simulate binary neutron star (BNS) and neutron star - black hole (NSBH) mergers in order to study the effects of magnetic fields on the merger dynamics, matter ejection, jet formation, gravitational wave (GW) and electromagnetic (EM) emission (e.g., [28, 34, 35, 37, 43, 104, 105], JVK1).

In this Chapter, based on the work done in JVK2, we present our new fully GRMHD numerical code, named `Spritz`, that solves the GRMHD equations in 3D and on dynamical spacetimes. The code inherits a number of basic features from its parent code `WhiskyMHD` [90], and also takes advantage of schemes implemented and tested in the publicly available state-of-the-art codes `GRHydro` [91] and `IllinoisGRMHD` [92]. `WhiskyMHD` has already been used successfully to simulate BNS mergers [32, 34, 106–111], JVK1 and accretion onto supermassive black hole binaries [112]. However, its application has been limited to the use of simple piecewise polytropic EOS, and it also does not take into account neutrino effects (emission or absorption). Moreover, `WhiskyMHD` evolves the vector potential (instead of the magnetic field) on a non-staggered grid, resulting in undesired effects on the evolution.

The `Spritz` code can instead handle any equation of state for which the pressure is a function of rest-mass density, temperature and electron fraction, and therefore, can also use modern tabulated equations of state. This has been possible by following a similar approach used in the `GRHydro` code, which can use finite temperature tabulated EOS. However, `GRHydro` still lacks a magnetic field implementation able to handle correctly the use of mesh refinement techniques unless proper remedies (like dissipation) are applied. Whereas, `Spritz` implements a staggered version of the vector potential formulation in a formalism that recovers the original

conservative flux-CT approach implemented in the original version of `WhiskyMHD`. The use of a new equation of state driver also provides the platform to implement neutrino radiation in `Spritz` via a leakage scheme (see Chapter 4 for more details).

Here, we first start with the brief mention of the formalisms and numerical schemes used with `Spritz`. We then present a number of extensive 1D, 2D, and 3D tests, including a comparison between staggered and non-staggered schemes for the vector potential evolution, and a rather demanding 3D spherical explosion test, which `Spritz` passes successfully.

The latest version of the `Spritz` code is publicly available on Zenodo [113].

3.1 Numerical implementation

In this Section, we summarize the theoretical background and the numerical methods implemented in `Spritz`. For an extensive theoretical introduction to numerical relativity as well as relativistic hydrodynamics, we point the reader to references [54, 68, 114].

Various numerical implementations in `Spritz` are largely based on the ones employed in `WhiskyMHD` [32, 90], where the 3+1 formulation of the Einstein's equations is adopted. In this framework, the form of the line element used is given by Equation (6.3), and the coordinate setting considers $x^0 \equiv t$. `Spritz` is based on the conservative formulation described by Equations (2.61), (2.78)-(2.82), which is presented in [115] and is the GRMHD version of the original Valencia formulation [116, 117]. In order to maintain the divergence free constraint for the magnetic field (see Equation (2.75)), `Spritz` considers the evolution of the vector potential instead of the magnetic field such that the divergence free character is automatically satisfied (see Equation (2.84)) by construction. For the electromagnetic gauge (see Section 2.2.5 for more details), we have implemented both the algebraic gauge and the generalized Lorenz gauge.

`Spritz` is based on the Einstein Toolkit numerical infrastructure [93, 94] which presents a framework to automatically parallelize the code for its use on supercomputers and also provides a number of open-source code modules related to evolution of the spacetime, adaptive mesh refinement, input and output of data, checkpointing, and many others (see Section 3.1.6 for more information).

3.1.1 High resolution shock capturing schemes

In order to solve Equation (2.61), `Spritz` adopts state-of-the-art HRSC methods for efficient treatment of shocks and discontinuities. As described in Section 2.3.5, these methods are based on the choice of reconstruction algorithms which compute the values of primitive variables at the numerical cell interfaces, and of approximate Riemann solvers to finally compute the fluxes.

Our default approximate Riemann solver is based on the third-order HLLE scheme, where the computation of numerical fluxes at cell interfaces is given by Equation (2.163). As an alternative choice, we have also implemented a second-order solver based on the Lax-Friedrichs (LxF) scheme, where the fluxes instead are computed by Equation (2.164). Similarly, as for the reconstruction technique, we adopt the third-order piece-wise parabolic method (see Section 2.3.5.1 for more details) as the default one. In addition, we have also implemented the

second-order total variation diminishing (TVD) minmod method (for further details, see Section 2.3.5.1), which allows `Spritz` to deal with those cases that require more dissipative methods, for example presence of strong shocks.

3.1.2 Electromagnetic field evolution

As mentioned earlier, in `Spritz`, we evolve the vector potential $\mathbf{A}$ instead of the magnetic field variable $\mathbf{B}$, and then compute the magnetic field as the curl of the vector potential given by Equation (2.86). For the electromagnetic gauge, we can choose between algebraic and generalized Lorenz gauge, however we usually adopt the latter for our simulations unless stated otherwise.

When considering the numerical grid, within a single grid-cell, we have the fluid's state variables (e.g., ρ, p, $\boldsymbol{v}$) stored in the grid-cell's centers, whereas the electric and magnetic field variables ($\boldsymbol{E}$ and $\boldsymbol{B}$) are instead computed on cell's edges and faces respectively. Therefore, we again stress the fact that the electric and magnetic field components are not evolved variables. For storage, the staggered magnetic field variables are first linearly interpolated to cell-centers using the respective adjacent cell-face values, and then stored as grid-functions at the cell-center. The components of the vector potential are also staggered in the same fashion as the electric field, thus stored at the cell-vertices. In Figure 3.1, we show the storage location of the magnetic field variables in a grid-cell. The precise storage locations of various quantities in a grid-cell is reported in Table 3.1. When adopting the generalized Lorenz gauge, we typically

Table 3.1: Location of various quantities within an elementary grid-cell. Symbols in the left column should be considered at the code's array position (i, j, k) while the right column indicates the actual location over the grid that depends on whether the different quantities present a particular specification for the prolongation (for the components of the four-vector potential) or how they are computed within the code (for the components of the magnetic field).

Symbol	Definition	Location
α	Lapse	(i, j, k)
β^m	m–component of the shift vector	(i, j, k)
γ^{mn}	mn–component of the spatial metric	(i, j, k)
γ	Determinant of the spatial metric	(i, j, k)
ρ	Rest-mass density	(i, j, k)
p	Pressure	(i, j, k)
ϵ	Specific internal energy	(i, j, k)
v_m	m–component of fluid velocity	(i, j, k)
B^1	x–component of magnetic field	$(i+\frac{1}{2}, j, k)$
B^2	y–component of magnetic field	$(i, j+\frac{1}{2}, k)$
B^3	z–component of magnetic field	$(i, j, k+\frac{1}{2})$
A_1	x–component of vector potential	$(i, j+\frac{1}{2}, k+\frac{1}{2})$
A_2	y–component of vector potential	$(i+\frac{1}{2}, j, k+\frac{1}{2})$
A_3	z–component of vector potential	$(i+\frac{1}{2}, j+\frac{1}{2}, k)$
$\Psi_{\rm mhd}$	Scalar potential	$(i+\frac{1}{2}, j+\frac{1}{2}, k+\frac{1}{2})$

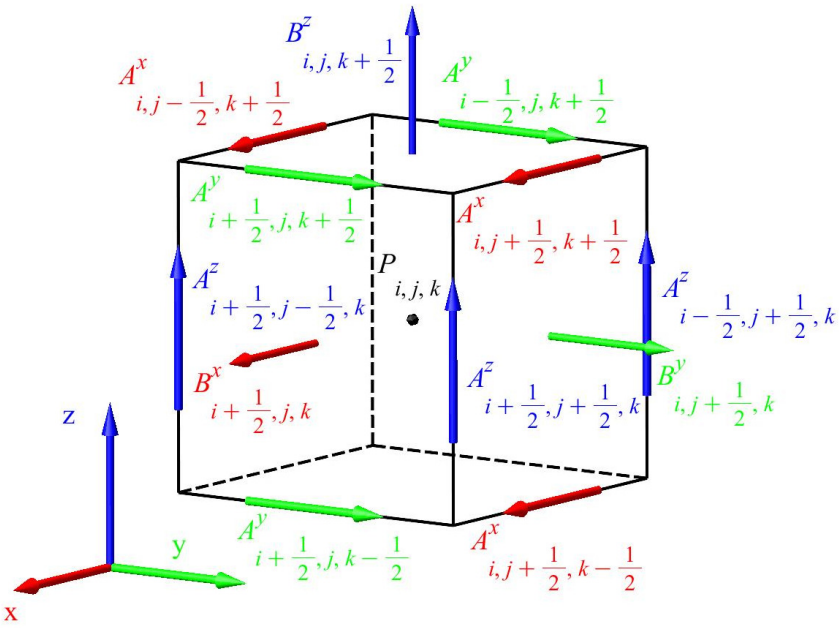

Figure 3.1: Representation of locations for magnetic field and vector potential components in our numerical code. Point $P_{i,j,k}$ represents the cell's center. Note that the magnetic field variables are eventually interpolated linearly using the two adjacent (staggered) face values of $\mathbf{B}$ and then stored at grid centers along with other hydro variables. Figure taken from JVK2.

set the damping term ξ in Equation (2.92) to $1.5/\Delta t_{\rm max}$, where $\Delta t_{\rm max}$ is the time step of the coarsest refinement level [92]. Moreover, for simplicity, we use the following definition for densitised scalar potential:

$$\Psi_{\rm mhd} \equiv \sqrt{\gamma}\Phi \ , \tag{3.1}$$

which lives at cell's vectices. Thus, when evolving with the generalized Lorenz gauge, the scalar potential $\Psi_{\rm mhd}$ should also be computed. Following [92] and using Equation (2.87), we can write the update terms for the vector potential components as well as for the scalar potential under the ideal MHD limit as follows:

$$\begin{aligned}\partial_t A_i &= -E_i - \partial_i \left(\alpha \frac{\Psi_{\rm mhd}}{\sqrt{\gamma}} - \beta^j A_j \right) \\ &= -\epsilon_{ijk} \tilde{v}^j B^k + \partial_i \left(\beta^j A_j - \alpha \frac{\Psi_{\rm mhd}}{\sqrt{\gamma}} \right) \ ,\end{aligned} \tag{3.2}$$

and

$$\begin{aligned}\partial_t \Psi_{\rm mhd} &= -\partial_j \left({F_\Psi}^j \right) - \xi \alpha \Psi_{\rm mhd} \\ &= -\partial_j \left(\alpha \sqrt{\gamma} A^j - \beta^j \Psi_{\rm mhd} \right) - \xi \alpha \Psi_{\rm mhd} \ .\end{aligned} \tag{3.3}$$

One can deduce from Equations (3.2), (3.3), and Table 3.1 that the terms on the right-hand side in general have different storage locations, and in order to perform computations correctly, we need to interpolate some of the quantities at a common point. To do so, we now implemented a new scheme briefly described below, that has shown to be numerically more accurate than the one reported in JVK2 which was prone to numerical instabilities when performing BNS merger simulations.

3.1.2.1 Evolution of the vector potential

To numerically compute the first term in the right-hand side (RHS) of Equation 3.2, i.e. $-\epsilon_{ijk}\tilde{v}^j B^k$, we employ the upwind constraint transport HRSC scheme (see Section 3.1.2.3 for more details). The second term in the RHS of Equation 3.2, i.e. $\partial_i\big(\beta^j A_j - \alpha\varphi\big)$, consists of three spatial-derivative terms along the three directions $x\ (i=1)\,,\ y\ (i=2)\,,\ z\ (i=3)$. These terms are located at the *edges* of each numerical cell, and are thus required to be evalutated at the *vertices* of each numerical cell via a centred finite differences scheme. Consider $\Delta x, \Delta y, \Delta z$ as the edge-lengths each grid-cell along the three directions x, y, z, respectively. Now, for example, along x, we can compute

$$\begin{aligned}
&\partial_x\left(\beta^j A_j - \alpha\,\frac{\psi_{\rm MHD}}{\sqrt{\gamma}}\right)|_{(i,\,j+\frac{1}{2},\,k+\frac{1}{2})} \\
&\quad\simeq \frac{\left(\beta^j A_j - \alpha\,\frac{\psi_{\rm MHD}}{\sqrt{\gamma}}\right)|_{(i+\frac{1}{2},\,j+\frac{1}{2},\,k+\frac{1}{2})} - \left(\beta^j A_j - \alpha\,\frac{\psi_{\rm MHD}}{\sqrt{\gamma}}\right)|_{(i-\frac{1}{2},\,j+\frac{1}{2},\,k+\frac{1}{2})}}{\Delta x}\,.
\end{aligned} \tag{3.4}$$

which can similarly be derived along y and z directions. Furthermore, in order to evaluate the terms $\beta^j A_j - \alpha\,\frac{\psi_{\rm MHD}}{\sqrt{\gamma}}$ at vertices, the vector potential components A_x, A_y, A_z should be interpolated from cell edges to cell vertices, whereas shift components $\beta_x, \beta_y, \beta_z$, lapse α and square-root of the 3-metric determinant $\sqrt{\gamma}$ should be interpolated from cell centers to cell vertices.

Interpolation from cell-centers to vertex

In order to interpolate a quantity from cell centers to cell vertex, we take the arithmetic mean of eight neibouring cell-centered values sharing a common vertex. interpolating some quantity from the centres of eight cells sharing one vertex to that same vertex amounts to taking a simple arithmetic mean. For example, the interpolation of the lapse function α from centers to vertex is given as

$$\begin{aligned}
\alpha|_{\left(i+\frac{1}{2},\,j+\frac{1}{2},\,k+\frac{1}{2}\right)} = \frac{1}{8}\,\big(&\alpha|_{(i,\,j,\,k)} + \alpha|_{(i,\,j+1,\,k)} + \alpha|_{(i,\,j,\,k+1)} + \alpha|_{(i,\,j+1,\,k+1)} + \\
&+\ \alpha|_{(i+1,\,j,\,k)} + \alpha|_{(i+1,\,j+1,\,k)} + \alpha|_{(i+1,\,j,\,k+1)} + \alpha|_{(i+1,\,j+1,\,k+1)}\big)\,.
\end{aligned} \tag{3.5}$$

Interpolation from cell-edges to vertex

For interpolating from cell edges to a common vertex, we again take a simple arithmetic mean. For example, the component of the vector potential along x direction, i.e., A_x can be interpo-

lated from edges to a vertex as

$$A_x|_{\left(i+\frac{1}{2},\, j+\frac{1}{2},\, k+\frac{1}{2}\right)} = \frac{1}{2}\left(A_x|_{\left(i,\, j+\frac{1}{2},\, k+\frac{1}{2}\right)} + A_x|_{\left(i+1,\, j+\frac{1}{2},\, k+\frac{1}{2}\right)}\right) \ . \tag{3.6}$$

Similarly, we can compute A_y and A_z at the same vertex.

3.1.2.2 Evolution of the scalar potential

Starting with the evolution equation of the scalar potential (3.3)

$$\partial_t \psi_{\rm MHD} = -\underbrace{\partial_i\left(\sqrt{\gamma}\,\alpha A^i\right)}_{\mathbf{i}} + \underbrace{\partial_i\left(\psi_{\rm MHD}\beta^i\right)}_{\mathbf{ii}} - \underbrace{\xi\alpha\psi_{\rm MHD}}_{\mathbf{iii}} \ , \tag{3.7}$$

we need to evaluate the three RHS terms $\mathbf{i}, \mathbf{ii}, \mathbf{i}$ at the *vertices* of each grid-cell.

i. This term can be expanded as

$$\partial_i\left(\sqrt{\gamma}\,\alpha A^i\right) = \partial_x\left(\sqrt{\gamma}\,\alpha A^x\right) + \partial_y\left(\sqrt{\gamma}\,\alpha A^y\right) + \partial_z\left(\sqrt{\gamma}\,\alpha A^z\right) \ , \tag{3.8}$$

and for each of the above three RHS terms, we apply centred finite differences to evalute them at cell-edges. For example, along x direction, we compute

$$\begin{aligned} &\partial_x\left(\sqrt{\gamma}\alpha A^x\right)|_{\left(i+\frac{1}{2},\, j+\frac{1}{2},\, k+\frac{1}{2}\right)} \simeq \\ &\qquad \frac{\left(\sqrt{\gamma}\alpha A^x\right)|_{\left(i+1,\, j+\frac{1}{2},\, k+\frac{1}{2}\right)} - \left(\sqrt{\gamma}\alpha A^x\right)|_{\left(i,\, j+\frac{1}{2},\, k+\frac{1}{2}\right)}}{\Delta x} \ , \end{aligned} \tag{3.9}$$

and follow the same procedure along y and z directions. Now, for computing the terms $\sqrt{\gamma}\alpha A^i$ at cell-edges, we follow the steps summarized below:

(a) Firstly, $\sqrt{\gamma}$ and α are interpolated from cell centers to edges.

(b) Then, we interpolate the covariant components of the vector potential. For example, components A_y located at edge $\left(i+\frac{1}{2}, j, k+\frac{1}{2}\right)$ and A_z located at edge $\left(i+\frac{1}{2}, j+\frac{1}{2}, k\right)$ are both interpolated to edge $\left(i, j+\frac{1}{2}, k+\frac{1}{2}\right)$ where A_x is situated. Similar interpolations are performed at respective locations of A_y and A_z.

(c) We also interpolate the components of the inverse spatial metric. Particulaly,

- $\gamma^{xx}, \gamma^{xy}, \gamma^{xz}$ are interpolated from cell-center to edge $\left(i, j+\frac{1}{2}, k+\frac{1}{2}\right)$ where A_x is located.
- $\gamma^{xy}, \gamma^{yy}, \gamma^{yz}$ are interpolated from cell-center to edge $\left(i+\frac{1}{2}, j, k+\frac{1}{2}\right)$ where A_y lives.
- $\gamma^{xz}, \gamma^{yz}, \gamma^{zz}$ are interpolated from cell-center to edge $\left(i+\frac{1}{2}, j+\frac{1}{2}, k\right)$ where A_z is located.

(d) Finally, we then compute the contravariant components of the vector potential. For example, the A^x component is derived as

$$A^x|_{\left(i,\, j+\frac{1}{2},\, k+\frac{1}{2}\right)} = \left(\gamma^{xx}A_x + \gamma^{xy}A_y + \gamma^{xz}A_z\right)|_{\left(i,\, j+\frac{1}{2},\, k+\frac{1}{2}\right)} \ . \tag{3.10}$$

A^y and A^z are also calculated in the same fashion.

Interpolation from cell-centers to edge

For interpolating a quantity at an edge, we simply take the average of four adjacent cell-centers. For example, the interpolation of α at the edge $\left(i, j+\frac{1}{2}, k+\frac{1}{2}\right)$ is given as

$$\alpha|_{\left(i,\, j+\frac{1}{2},\, k+\frac{1}{2}\right)} = \frac{1}{4}\left(\alpha|_{(i,\, j,\, k)} + \alpha|_{(i,\, j+1,\, k)} + \alpha|_{(i,\, j,\, k+1)} + \alpha|_{(i,\, j+1,\, k+1)}\right) \tag{3.11}$$

Interpolation from cell-edges to other edges

In order to interpolate A_y and A_z to edge $\left(i, j+\frac{1}{2}, k+\frac{1}{2}\right)$, where A_x is situated, we do

$$\begin{aligned} A_y|_{\left(i,j+\frac{1}{2},k+\frac{1}{2}\right)} =& \frac{1}{4}\Big[A_y|_{\left(i+\frac{1}{2},j,k+\frac{1}{2}\right)} + A_y|_{\left(i-\frac{1}{2},j,k+\frac{1}{2}\right)} + A_y|_{\left(i+\frac{1}{2},j+1,k+\frac{1}{2}\right)} \\ &+ A_y|_{\left(i-\frac{1}{2},j+1,k+\frac{1}{2}\right)}\Big] \,, \end{aligned} \tag{3.12}$$

$$\begin{aligned} A_z|_{\left(i,j+\frac{1}{2},k+\frac{1}{2}\right)} =& \frac{1}{4}\Big[A_z|_{\left(i+\frac{1}{2},j+\frac{1}{2},k\right)} + A_z|_{\left(i-\frac{1}{2},j+\frac{1}{2},k\right)} + A_z|_{\left(i+\frac{1}{2},j+\frac{1}{2},k+1\right)} \\ &+ A_z|_{\left(i-\frac{1}{2},j+\frac{1}{2},k+1\right)}\Big] \,. \end{aligned} \tag{3.13}$$

Interpolation of A_x and A_z to edge $\left(i+\frac{1}{2}, j, k+\frac{1}{2}\right)$ where A_y lives, and of A_x and A_y to edge $\left(i+\frac{1}{2}, j+\frac{1}{2}, k\right)$ where A_z lives, is performed following the same procedure.

ii. This term can be expanded as

$$\partial_i\left(\psi_{\rm MHD}\beta^i\right) = \partial_x\left(\psi_{\rm MHD}\beta^x\right) + \partial_y\left(\psi_{\rm MHD}\beta^y\right) + \partial_z\left(\psi_{\rm MHD}\beta^z\right) \tag{3.14}$$

where each of the three RHS terms can be considered as a shift advection term for $\psi_{\rm MHD}$. Following [92], in order to evaluate these terms at cell vertices, we employ the forward finite differences scheme. For example, to compute $\psi_{\rm MHD}\beta^x$, we have

$$\partial_x(\psi_{\rm MHD}\beta^x) \simeq \begin{cases} \frac{1}{2\Delta x}\Big[\left(\psi_{\rm MHD}\beta^x\right)|_{\left(i-\frac{3}{2},\, j+\frac{1}{2},\, k+\frac{1}{2}\right)} + \\ -4\left(\psi_{\rm MHD}\beta^x\right)|_{\left(i-\frac{1}{2},\, j+\frac{1}{2},\, k+\frac{1}{2}\right)} + \\ +3\left(\psi_{\rm MHD}\beta^x\right)|_{\left(i+\frac{1}{2},\, j+\frac{1}{2},\, k+\frac{1}{2}\right)}\Big] & \text{if } \beta^x < 0 \\ \frac{1}{2\Delta x}\Big[-\left(\psi_{\rm MHD}\beta^x\right)|_{\left(i+\frac{5}{2},\, j+\frac{1}{2},\, k+\frac{1}{2}\right)} + \\ +4\left(\psi_{\rm MHD}\beta^x\right)|_{\left(i+\frac{3}{2},\, j+\frac{1}{2},\, k+\frac{1}{2}\right)} + \\ -3\left(\psi_{\rm MHD}\beta^x\right)|_{\left(i+\frac{1}{2},\, j+\frac{1}{2},\, k+\frac{1}{2}\right)}\Big] & \text{if } \beta^x \geq 0 \end{cases} . \tag{3.15}$$

Similarly, we can calculate $\psi_{\rm MHD}\beta^y$ and $\psi_{\rm MHD}\beta^z$ as well. Note that for computing $\psi_{\rm MHD}\beta^i$ at cell vertices, β^i should first be interpolated from cell centers to vertices. This computation is already done when solving the time evolution equation for the vector potential.

iii. This consists of the damping term and does not involve any derivatives. To evaluate this term at the cell vertice, α should first be interpolated to the vertice from cell centers. This too is already done when solving the time evolution equation for the vector potential.

3.1.2.3 Computing electric field

For the first `Spritz` version as described in JVK2, the electric field is computed at cell edges using the flux-constrained transport approach as presented in the original `WhiskyMHD` paper [90]. However, we found that this implementation could lead to generation of numerical instabilities in magnetic field evolution when performing BNS merger simulations. These instabilities can be curbed by adding an appropriate amount of Kreiss-Oliger dissipation to the magnetic field variables.

In the latest development version of `Spritz`, we now compute the electric field at cell edges using the upwind constrained transport (UCT) scheme as described in [118, 119]. To compute, for example, the E_z component of the electric field on the edge $\left(i+\frac{1}{2}, j+\frac{1}{2}, k\right)$, we follow the steps summarized below:

(a) Using Equation (57) of [118], we first compute the upwind transverse transport averaged velocities, for example, on cell-face along x direction, i.e. $\left(i+\frac{1}{2}, j, k\right)$ as

$$\bar{v}^j = \frac{a^x_+ \tilde{v}^{jL} + a^x_- \tilde{v}^{jR}}{a^x_+ + a^x_-} \ , \qquad j = y, z \ . \tag{3.16}$$

where L and R stand for left and right upwind states of $\tilde{v}^i$ along an interface, $\tilde{v}^i \equiv \alpha v^i - \beta^i$, $a^x_\pm$ is defined as

$$a^x_\pm = \max\{0, \pm\lambda^{\mathrm{x}}_\pm(\mathrm{U^L}), \pm\lambda^{\mathrm{x}}_\pm(\mathrm{U^R})\} \ . \tag{3.17}$$

where $\lambda^x_\pm$ are the characteristic wave speeds calculated at both left and right states.

(b) Then, we reconstruct the quantities $\tilde{v}^x$, $\tilde{v}^y$, B^x, B^y from faces $\left(i+\frac{1}{2}, j, k\right)$ and $\left(i, j+\frac{1}{2}, k\right)$ to the edge $\left(i+\frac{1}{2}, j+\frac{1}{2}, k\right)$ using the PPM reconstruction method, following Equations (59) and (60) of [118] as

$$\begin{aligned} \bar{v}^{xL,R}|_{\left(i+\frac{1}{2},j+\frac{1}{2},k\right)} &= \mathcal{R}^{L,R}_x\left(\bar{v}^x|_{\left(i,j+\frac{1}{2},k\right)}\right), \\ B^{yL,R}|_{\left(i+\frac{1}{2},j+\frac{1}{2},k\right)} &= \mathcal{R}^{L,R}_x\left(B^y|_{\left(i,j+\frac{1}{2},k\right)}\right), \end{aligned} \tag{3.18}$$

$$\begin{aligned} \bar{v}^{yL,R}|_{\left(i+\frac{1}{2},j+\frac{1}{2},k\right)} &= \mathcal{R}^{L,R}_y\left(\bar{v}^y|_{\left(i+\frac{1}{2},j,k\right)}\right), \\ B^{xL,R}|_{\left(i+\frac{1}{2},j+\frac{1}{2},k\right)} &= \mathcal{R}^{L,R}_y\left(B^x|_{\left(i+\frac{1}{2},j,k\right)}\right), \end{aligned} \tag{3.19}$$

(c) Finally, using the above expressions, the E_z component of the electric field on the edge $\left(i+\frac{1}{2}, j+\frac{1}{2}, k\right)$ can be written using Equation (61) of [118], as

$$\begin{aligned} E_z = &- \frac{a^x_+ \bar{v}^{xL} B^{yL} + a^x_- \bar{v}^{xR} B^{yR} - a^x_+ a^x_- \left(B^{yR} - B^{yL}\right)}{a^x_+ + a^x_-} \\ &+ \frac{a^y_+ \bar{v}^{yL} B^{xL} + a^y_- \bar{v}^{yR} B^{xR} - a^y_+ a^y_- \left(B^{xR} - B^{xL}\right)}{a^y_+ + a^y_-} \ . \end{aligned} \tag{3.20}$$

In the same way, the components E_x and E_y are also derived.

As an alternative, one could use a non-staggered approach for electromagnetic field evolution where both $\boldsymbol{A}$ and $\boldsymbol{B}$ are stored at the cell centers (e.g., as done in the `WhiskyMHD` code [32]). In Figure 3.2, we provide a comparison between the staggered and non-staggered schemes through an example of a 1-dimensional shock-tube test. In this case, the staggered scheme proves to be advantageous, devoid of any post-shock oscillations.

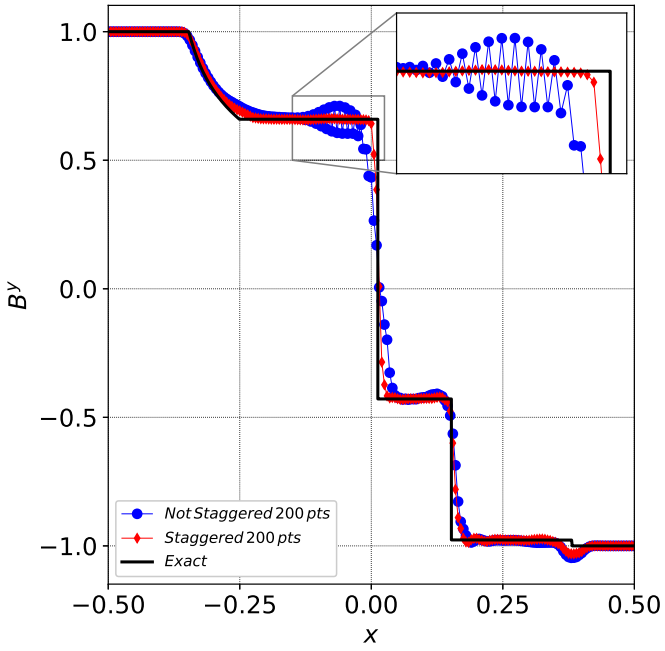

Figure 3.2: Comparing results of `Balsara 1` test (from [120]), obtained via staggered (red diamonds) and non-staggered (blue dots) vector potential. The blue curve clearly shows post-shock oscillations. Note that the non-staggered scheme is still stable since the maximum amplitude of these oscillations does not grow indefinitely during the evolution. However, in order to remove such oscillation effects, Kreiss-Oliger dissipation can be applied to the vector potential, as successfully done so in `WhiskyMHD` [32]. Figure taken from JVK2.

3.1.3 Primitive variables recovery

As previously mentioned in Section 2.2.3, flux-conservative formulation evolves a set 'conserved' variables $\mathbf{F}^0(U) = (D, S_i, \tau)$ which then need to be converted back into the fundamental 'primitive' variables $\mathbf{U} = (\rho, v^i, \epsilon)$. These primitive variables are not only necessary for data analysis but are also required at each time step in order to compute the fluxes $\mathbf{F}^i(U)$ in Equation (2.61). In GRMHD, due to the complexity of the system, there exists no analytical solution to calculate back these primitive variables. Thus, one needs to rely on root-finding algorithms to numeri-

cally retrieve these primitive variables. Such recovery procedures, also called as *Con2Prim* or *C2P* schemes, are a crucial aspect at the core of any GRMHD code. C2P is often an error-prone part of evolutionary codes, and existing state-of-the-art C2P schemes for GRMHD can possibly fail in certain regimes, for example in high magnetizations and low density regimes as shown in [21] which give a good comparative study on different C2P schemes. Most of these C2P schemes fall into two categories: (i) the first kind are based on the Newton Raphson (NR) root finding algorithms, which start from an unbounded region for computing the root but depend on initial guess as well as on EOS derivatives, and (ii) the second type are based on root-bracketing schemes which start from a bounded region known to contain the root, and might not depend on the initial guess and on EOS derivatives. In principle, the recovery problem in GRMHD is five-dimensional (5D) since obtaining the primitives $\mathbf{U}$ involves root-finding in a 5D space, assuming that magnetic field components can be recovered trivially[1]. One can also scale down this system to a smaller set of equations, i.e., reducing the dimensionality of the problem to 1D or 2D with the help of some scalar quantities proved more efficient and robust.

In the first version of the `Spritz` code as presented in JVK2, we implemented the 2D NR method presented in [115] and used in `WhiskyMHD` [90], as well as the 2D NR scheme of [121]

3.1.3.1 Noble C2P scheme

Introduced by Noble et al in 2006 [121], this scheme is based on the NR technique, and uses certain scalar quantities to reduce the dimensionality of the problem to 2D. In particular, it is based on Equations (27) and (29) of [121], which are two equations expressed in terms of unknowns v^2 and $z \equiv \rho h W^2$. Explicitly, they are written as

$$v^2(B^2+z)^2 - \frac{(B^i S_i)^2(B^2+2z)}{z^2} - S^2 = 0 \ , \tag{3.21}$$

$$\tau + D - \frac{B^2}{2}(1+v^2) + \frac{(B^i S_i)^2}{2z^2} - z + p(z,v^2) = 0 \ . \tag{3.22}$$

Here, we define S^2 using Equation (2.81) as

$$\begin{aligned} S^2 &\equiv S^i S_i \\ &= (\rho h + b^2)^2 W^4 v^2 + \alpha^2 (b^0)^2 \left[b^2(1-2W^2) - 2\rho h W^2 + \alpha^2 (b^0)^2 \right] \ . \end{aligned} \tag{3.23}$$

Moreover, one can directly compute the fluid pressure $p(z, v^2)$ in terms of z and v^2 when using a simple analytical EOS such as classical ideal-gas EOS. Once the scheme converges to the required roots, the final primitives can be obtained from the relations $\rho = D\sqrt{1-v^2}$,

$$v^i = \frac{\gamma^{ij} S_j}{z + B^2} + \frac{(B^j S_j) B^i}{z(z+B^2)} \ , \tag{3.24}$$

and using, for example, the analytical EOS, we can derive $\epsilon = \epsilon(\rho)$.

[1] Since $\tilde{B}^i = \sqrt{\gamma} B^i$ is the evolved variable, the primitive magnetic field components can simply be retrieved at each time step using $B^i = \tilde{B}^i / \sqrt{\gamma}$.

3.1.3.2 '3eqs' C2P scheme

This NR scheme is presented in [115], which also reduces the dimensionality of the recovery problem to 2D, using scalar quantities τ (see Equation (2.82)) and S^2. Again using $z = \rho h W^2$, and defining the identity

$$B^i S_i = \rho h W \alpha b^0 \ , \tag{3.25}$$

we can recast Equations (2.82) and (3.23) as

$$\left[\tau + D - z - B^2 + \frac{(B^i S_i)^2}{2z^2} + p\right] W^2 - \frac{B^2}{2} = 0 \ , \tag{3.26}$$

$$\left[(z + B^2)^2 - S^2 - \frac{2z + B^2}{z^2}(B^i S_i)^2\right] W^2 - (z + B^2)^2 = 0 \ . \tag{3.27}$$

One can employ, for example, an analytical EOS again to compute p from ρ. The unknowns here are W and z. First, the root of W is found, and then roots of $\rho = D/W$, z and p are computed. Once the algorithm converges, the final primitives are obtained from Equations (2.80)), (3.24)) and again, using the EOS, $\epsilon = \epsilon(\rho)$.

3.1.4 Atmosphere treatment

As any GRMHD grid-based code, `Spritz` cannot handle zero values for the rest-mass density. Therefore, we need to set a minimum density floor or so called *atmosphere* density value $\rho_{\rm atm}$. In case, at any grid-point, the rest-mass density ρ is computed by our C2P such that $\rho < \rho_{\rm atm}$, then the ρ value is reset to $\rho_{\rm atm}$, whereas the pressure and specific internal energy are recomputed using a polytropic EOS. Moreover, the fluid's three–velocity is set to zero. For example, in the tests presented in JVK2, unless stated otherwise, we typically set $\rho_{\rm atm} = 10^{-7}\rho_{0,\rm max}$, where $\rho_{0,\rm max}$ is the initial maximum value of the rest-mass density.

3.1.5 Equation of state

`Spritz` supports both analytic and finite-temperature composition dependent tabulated EOS. The first version of `Spritz` as reported in JVK2, provides support for only the analytic type of EOS. This was done via the `EOS_Omni` thorn provided by the Einstein Toolkit, which supports analytic EOS such as ideal fluid and piecewise polytropic ones as well as cold tabulated EOS. Moreover, a hybrid EOS can be used with `Spritz` through the `EOS_Omni` module. For more details on different types of EOS, we refer to Sections 2.2.6 and 4.1.2.

3.1.6 Einstein Toolkit infrastructure

The Einstein Toolkit [93, 94] is a community driven computational platform which provides tools to be used in research fields such as relativistic astrophysics, numerical relativity, and more. Its modular infrastructure provides basic functionality to create, run and manage numerical simulations. In particular, key components include

- the `Cactus` framework, which makes the foundation for the development of portable, independent, modular simulation codes and applications;
- the `Carpet` driver [122, 123], which is responsible for the mesh refinement, time evolution, parallelization as well as memory management operations;
- the *Simulation Factory* or *SimFactory*, a tool that incorporates a set of abstractions for tasks, related to synchronizing, configuring, building and managing simulations.

3.1.6.1 Cactus

The Cactus framework comprises modules which provide interpolators, boundary conditions, parallel drivers, coordinates, operators and efficient I/O in different data formats. Its structure consists of a core of basic pieces of code named *flesh* connected to independently developed programs, which can be split into modules called *thorns*, that can interact with one another via a common interface, both at compile- and run-time. An executable is needed to run the Cactus simulations, along with a parameter file, which provides the parameter names and desired settings within the simulation.

3.1.6.2 Carpet

The `Carpet` driver provides the adaptive mesh refinement (AMR) based on the Berger-Oliger algorithm [124]. AMR serves as an important feature in full 3D BNS merger simulations because it allows for the optimization of the number of grid points by implementing dynamic resolution, such that finer grids are used for regions requiring higher resolution, and resolution requirements are re-evaluated and updated at regular intervals during the simulations, which is called as *regridding*. While it still allows to maintain a sufficiently large computational domain to reduce any effects of external boundaries, and to allow for the extraction of gravitational wave signals far away from the source.

When using AMR with `Spritz`, special care must be taken for staggered variables, like $\boldsymbol{A}$ and $\Psi_{\rm mhd}$. Particularly, one needs to employ separate restriction and prolongation operators for such staggered variables with respect to variables located at the cell centers. Such operators are already provided by the `Carpet` driver. In Section 3.2.2, we present some tests which use AMR.

`Carpet` also supports MPI and OpenMP which are for multi-process and multi-threaded parallelisation schemes.

3.1.6.3 Thorns

Thorns performing a common task or having a common origin, are usually grouped under an *arrangement*. Here, we discuss a few important thorns that are defined in the various domains of the Einstein Toolkit:

- `CactusNumerical` : includes infrastructural thorns for interpolation, artificial dissipation, time integration, symmetry boundary conditions, and many others.

- `ADMBase` : provides grid-functions for spacetime variables based on the ADM formulation, defining the 3-metric γ_{ij}, extrinsic curvature K_{ij}, the lapse function α, the shift vector β^i, etc.
- `HydroBase` : defines the basic variables and grid functions for hydrodynamic equations, such as the rest mass density ρ, pressure P, specific internal energy ϵ, contravariant fluid three velocity v^i, contravariant magnetic field vector B^i, and temperature T.
- `TmunuBase` : provides the stress-energy tensor components, i.e., time component T_{00}, mixed components T_{0i} and spatial components T_{ij}.
- `TOVsolver` : solves the standard TOV equations for a spherically symmetric star in hydrostatic equilibrium, and provides the initial data.
- `McLachlan` : uses accurate finite differencing schemes up to eighth order for discretization of spacetime variables in the BSSNOK formulation (see Section 2.1.2 for more details on this formulation), and inter-operates between the `ADMBase` and the `TmunuBase` interfaces. Unless specified otherwise, we generally use this thorn for spacetime evolution when performing simulations with `Spritz`.
- `AHFinderDirect` : finds the apparent horizon of a black hole, given the three-metric and extrinsic curvature.
- `WeylScal4` : used to extract the Weyl scalar Ψ_4 (defined in the Newman-Penrose formalism), in order to obtain the outgoing gravitational wave radiation.

3.1.7 Boundary conditions

Since the computational domain is of finite size, there are grid points reserved at the boundaries of the grid where the boundary conditions (BC) can be applied. These outer boundary points are generally referred to as *ghost zones*. The generic `Boundary` thorn [94] from the Einstein Toolkit provides the different treatments of BCs. For example, `Spritz` works with both 'flat' and 'none' BCs. The 'flat' BC simply copies the value of each variable in the outermost grid point to the ghost zones, whereas the 'none' BC does not update the ghost zones, and keeps the value of the variables in the ghost zones constant and equal to the ones set by the initial data.

In `Spritz`, we added an additional option for treating the vector and scalar potential at the external boundary of the computational domain for the in order to compute B with better accuracy.

Following the work presented in [92], we implemented the numerical extrapolation of $\boldsymbol{A}$ and $\Psi_{\rm mhd}$ at the outer boundary using following linear extrapolation formula

$$F_i^j = \begin{cases} 2F_{i-1}^j - F_{i-2}^j & for\ i = N^j - 2, N^j - 1, N^j \\ 2F_{i+1}^j - F_{i+2}^j & for\ i = 3, 2, 1 \end{cases} , \tag{3.28}$$

where $F \in \{\boldsymbol{A}, \Psi_{\rm mhd}\}$, $j \in \{1,2,3\}$ and N is the number of grid-points in the j-direction. Typically, we use three points in the ghost zones for each direction.

`Spritz` also supports periodic BC provided by the thorn `Periodic` [94]. We show its working through the loop-advection test described in Section 3.2.2, performed using both uniform and AMR grids.

3.1.8 Spritz workflow

Here, we briefly summarize the step-by-step process followed by `Spritz` for solving the system of GRMHD equations based on the conservative formulation desribed by Equations (2.61), (2.78)-(2.82).

(i) **Initilization:** At the start of the simulation, the primitive variables $\mathbf{U} = (\rho, v^i, p, \epsilon)$ are defined at each grid point. This is done using the initial data provided by the user along with the EOS.

(ii) **Prim2Con:** After the initialization step, a *Prim2Con* or *P2C* routine is launched, which converts the primitive variables to the evolved (conserved) variables using analytic equations (2.80)-(2.82).

(iii) **Computing source terms:** Then, the sources terms $\boldsymbol{S}(\boldsymbol{U})$ in Equation (2.61) are evaluated using standard FD schemes.

(iv) **Computing flux terms:** Following that, we compute the fluxes $\boldsymbol{F^i}(\boldsymbol{U})$ in Equation (2.61) using HRSC methods. Particularly, first the reconstruction scheme (such as PPM) is implemented to compute the primitives at each cell interface, followed by a P2C routine to calculate the conserved variables at each cell interface. Finally, the fluxes are evaluated with an approximate Riemann solver (such as HLLE) using the computed values of conserved variables.

(v) **Update in time:** The flux terms $\boldsymbol{F^i}(\boldsymbol{U})$ are then subtracted from the source terms $\boldsymbol{S}(\boldsymbol{U})$. This results in time evolution equations for the conserved variables $\boldsymbol{F^0}(\boldsymbol{U})$ which are treated as ODEs and solved following the method of lines technique (provided by the `MoL` thorn of Einstein Toolkit) which uses a time integrator (such as a fourth order Runge-Kutta integrator). Thus, this computes the conserved variables for the next time step.

(vi) **Con2Prim:** Once the conserved variables are evaluated for the next time step, the Con2Prim routine is execute in order to compute the primitive variables since they would be required for computation of fluxes at this new time step.

Coupled to the above algorithm, for electromagnetic field evolution, the vector and scalar potential variables are evolved side-by-side using the schemes described in Section 3.1.2.

3.2 Test results

As already stressed earlier, the primary goal of the `Spritz` code is to perform simulations of BNS and NSBH mergers. In order to address such complex astrophysical scenarios with the necessary confidence, we first need to assess the reliability of our code in a variety of physical conditions. In this Section, we report on the results of our extensive tests performed in 1D, 2D as well as 3D, as presented in JVK2. Some of these critical tests that have been already considered in the literature in several previous studies (see, e.g., [91, 92, 120, 125] and references therein), allowing for a direct comparison with other numerical codes.

3.2.1 1D tests

Test:	1		2		3		4		5	
	L	R	L	R	L	R	L	R	L	R
ρ	1.0	0.125	1.0	1.0	1.0	1.0	1.0	1.0	1.08	1.0
p	1.0	0.1	30.0	1.0	1000.0	0.1	0.1	0.1	0.95	1.0
v_x	0.0	0.0	0.0	0.0	0.0	0.0	0.999	-0.999	0.4	-0.45
v_y	0.0	0.0	0.0	0.0	0.0	0.0	0.0	0.0	0.3	-0.2
v_z	0.0	0.0	0.0	0.0	0.0	0.0	0.0	0.0	0.2	0.2
B^x	0.5	0.5	5.0	5.0	10.0	10.0	10.0	10.0	2.0	2.0
B^y	1.0	-1.0	6.0	0.7	7.0	0.7	7.0	-7.0	0.3	-0.7
B^z	0.0	0.0	6.0	0.7	7.0	0.7	7.0	-7.0	0.3	0.5

Table 3.2: Initial data for `Balsara` relativistic shock tube tests.

In order to check the correctness of the approximate Riemann solvers and other numerical schemes implemented in the code, the first round of tests we performed with `Spritz` are those involving Riemann problems. In Figure 3.3, we show the results for 1-dimensional (1D) relativistic shock-tube problems based on the testsuite of [120]. Here, our numerical results of these tests are directly compared with the exact solutions computed via the code presented in [31]. Initial data for such tests are described in Table 3.2. For all tests, we employ an ideal fluid EOS, with $\Gamma = 2.0$ for test `Balsara 1` and $\Gamma = 5/3$ for the others. The final evolution time is considered as $t = 0.55$ for test `Balsara 5` and $t = 0.4$ for the others. We note that all tests show an excellent agreement between the numerical results and the exact solutions.

For a comparitive study, we also performed the same testsuite with the already published numerical code `GRHydro` [91], and found perfectly matching results. In Figure 3.4, we show an example of such a comparison for the `Balsara 1` shock-tube test.

Finally, in Figure 3.5, we show the results of the most demanding Balsara 3 test using different resolutions (200, 800, and 1600 grid points). Higher resolution leads to a significant increase in accuracy, which is particularly evident at the shock front (when comparing also with the exact solution in Figure 3.3).

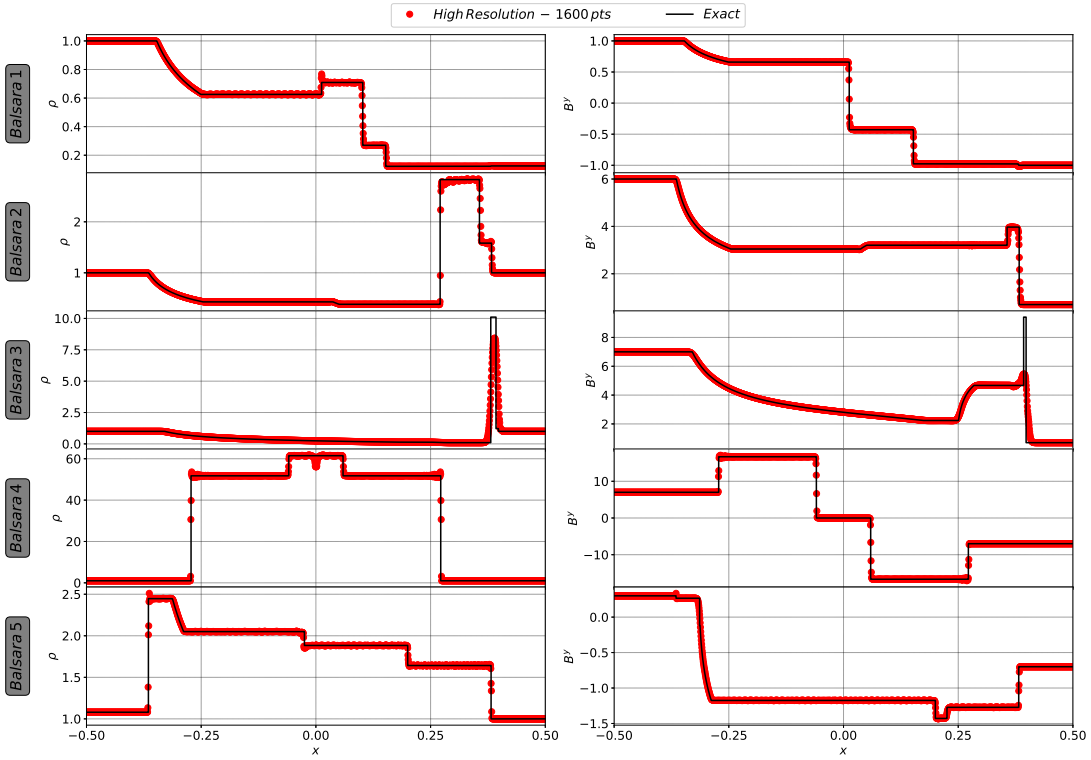

Figure 3.3: Comparison of numerical results (red dots) and exact solutions (continuous black lines) for different [120] shock-tube tests. Left and right columns show the rest-mass density ρ and the magnetic field component B^y along the direction of propogation of the shocks, i.e. x-direction, at the final time of the evolution. Here, the Balsara 1, 2, 4 and 5 tests are performed with the third order PPM method, whereas the Balsara 3 test is performed using the second order `MINMOD` method, since this test is most demanding one due to the very high jump (four orders in magnitude) in the initial pressure, thus requiring a slightly more dissipative method in order to succeed. Figure taken from JVK2.

3.2.1.1 Convergence study

To estimate the convergence order of our code, we performed the so-called Alfvén wave test, and compared our results with `GRHydro` (see [91] for details). This test considers a low-amplitude, circularly-polarized Alfvén wave advecting across the grid domain. For setting the initial conditions, we use the values provided in [91]. In particular, we set the wave amplitude to $A_0 = 1.0$, the fluid rest-mass density to $\rho = 1.0$, the fluid pressure as $p = 1.0$, the x-component of velocity as $v_x = 0.0$, and the x–component of the magnetic field to $B^x = 1.0$. For evolution, we employ a $\Gamma = \frac{5}{3}$ ideal fluid EOS, and evolve the system for 1 period.

We look for convergence considering several different resolutions along the x-axis, having number of grid points as $N_x = 8$, 16, 32, 64, 128, and 256, and using $x \in [-0.5, 2.5]$. In Figure

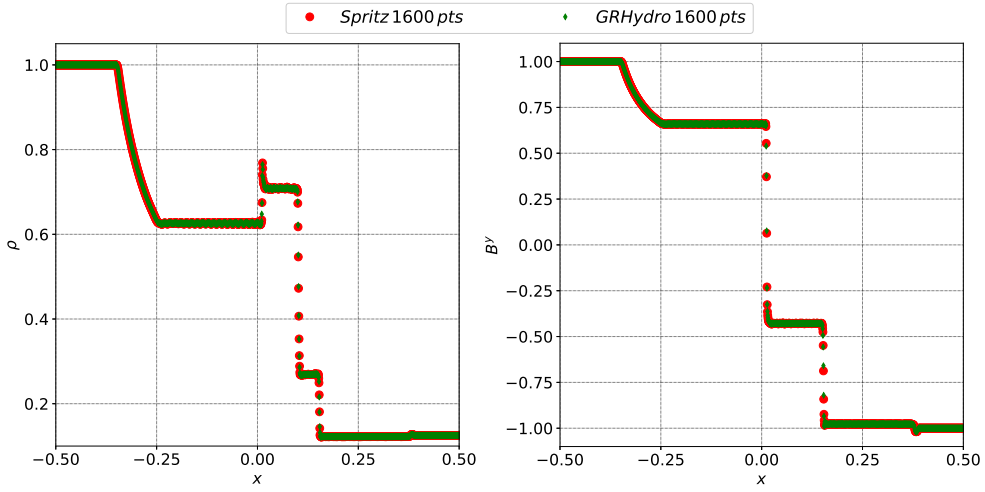

Figure 3.4: Comparison of the `Balsara 1` test results obtained with the `Spritz` code (red dots) and the `GRHydro` code (green diamonds) [91]. Figure taken from JVK2.

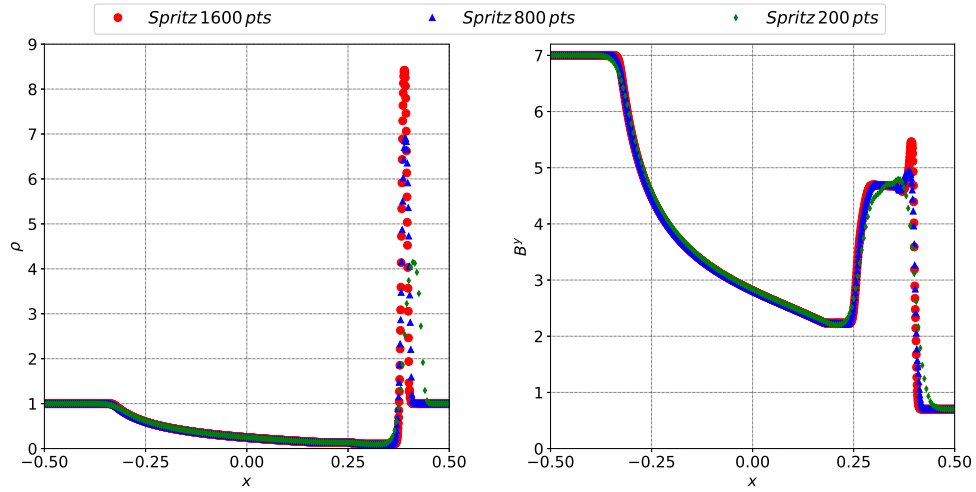

Figure 3.5: Balsara 3 test performed with the `Spritz` code using three different resolutions: low resolution (200 points - green diamonds), medium resolution (800 points - blue triangles) and high resolution (1600 points - red dots). Figure taken from JVK2.

3.6, we present the results for the $L2$-norm of the difference between the initial and final values of the y-component of the magnetic field, B^y. The initial wave is centered at $x = 0$, and the final values of B^y are compared with the initial profile. Here, we observe an overall 2nd order convergence.

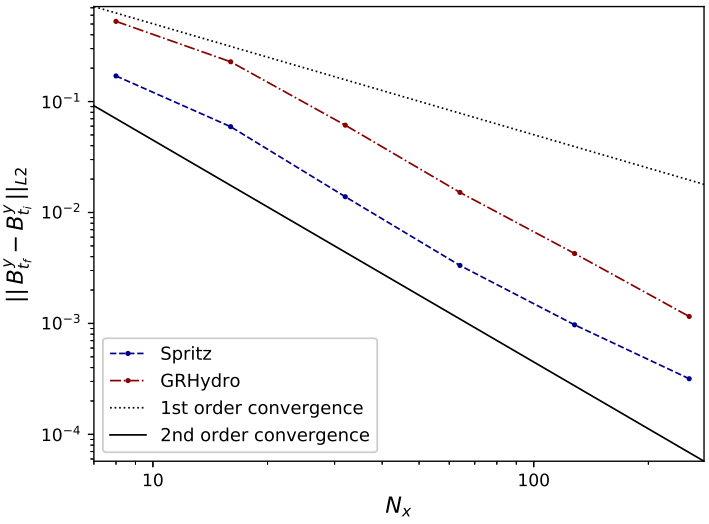

Figure 3.6: Estimating the convergence order through the 1D Alfvén wave test. The $L2$–norm of the error is plotted for both the `Spritz` code (blue–dashed line) and the `GRHydro` code (red–dot–dashed line), along with reference curves for 1st (black-dotted line) and 2nd (black-solid line) order convergence. Figure taken from JVK2.

3.2.2 2D tests

In this section, we discuss the 2D tests performed with the Spritz code. In particular, we consider three magnetized 2D tests, namely the cylindrical explosion, the magnetic rotor and the magnetic loop advection.

The cylindrical explosion test helps to check if the code can correctly follow a shock front on the equatorial plane (such as ones that are generated in BNS mergers during the very last orbit prior to merger). The magnetic rotor is a special relativistic test that examines the evolution of the magnetic field in the presence of rotation, whereas the loop advection test allows for a comparison with an exact solution as well as for checking the differences between our reconstruction schemes.

3.2.2.1 Cylindrical explosion

The cylindrical explosion (also known as the cylindrical blast wave) is a demanding multidimensional shock test, first introduced by [126], and later modified and implemented in [70, 91, 118, 125]. This test considers a uniformly magnetized domain consisting of a dense, over-pressured cylinder in the central region, expanding in a surrounding ambient medium. For the initial data, we use the parameters from the setup described in [91]. For the cylinder, we set

$$r_{\rm in} = 0.8,\ r_{\rm out} = 1.0,\ \rho_{\rm in} = 10^{-2},\ p_{\rm in} = 1.0, \tag{3.29}$$

while for the surrounding ambient medium, we consider

$$\rho_{\rm out} = 10^{-4},\ p_{\rm out} = 3 \times 10^{-5}. \tag{3.30}$$

Here, $r_{\rm in}$ and $r_{\rm out}$ are the radial parameters used for smoothing the density profile (and similarly for the smoothening of the pressure profile) considered in [91], such that

$$\rho(r) = \begin{cases} \rho_{\rm in} & for\ r \leq r_{\rm in} \\ \exp\left[\frac{(r_{\rm out}-r)\ln\rho_{\rm in}+(r-r_{\rm in})\ln\rho_{\rm out}}{r_{\rm out}-r_{\rm in}}\right] & for\ r_{\rm in} < r < r_{\rm out} \\ \rho_{\rm out} & for\ r \geq r_{\rm out} \end{cases} \tag{3.31}$$

The fluid 3-velocity is initially set to zero, while the initial magnetic field is uniformly with $B^x = 0.1$ and $B^y = B^z = 0$. For the numerical domain, we consider a 200×200 grid with x- and y-coordinates spanning over the range $[-6, 6]$. For evolution, we set the CFL factor to 0.25 and use an ideal fluid EOS with adiabatic index $\Gamma = 4/3$. For solving the numerics, second order MINMOD reconstruction method is adopted along with the HLLE flux solver and the RK4 method for time-step evolution.

The resulting structure of the blast wave is depicted in Figure 3.7 at the final time $t = 4.0$. In particular, we show the two-dimensional distribution of gas pressure p, Lorentz factor W (together with magnetic field lines), and the x– and y–components of the magnetic field, B^x and B^y. This figure shows a very similar behavior when compared to the results already presented in the literature [70, 91, 118].

In Figure 3.8, we provide instead a quantitative indication of the accuracy of our code. In this case, we depict a one-dimensional slice along $y = 0$ of the final blast wave configuration at time $t = 4.0$, in terms of rest-mass density and B^x. Particularly, two cases are considered: on the left, we compare the results obtained with low (200 grid-points) and high resolution (400 grid–points); while on the right, we compare the high resolution test results obtained with `Spritz` with those obtained with `GRHydro` [91]. The first comparison shows slight differences in the peaks of ρ due to the fact that the ability to capture the peak sharpness depends significantly on resolution. The B^x values show a much smaller deviation, due to a smoother variation in this quantity. For the second comparison, the agreement between `Spritz` and `GRHydro` appears excellent, further verifying the robustness of our code.

To validate the implementation of AMR, we carried out another simulation including an inner refined grid covering the x- and y-coordinates in the range [-3,3] with grid-spacing $\Delta x = \Delta y = 0.03$ (while the rest of the domain has double grid spacing). In Figure 3.9, we show the comparison with the uniform grid test in terms of final pressure distribution. We find no significant differences (much less than 1% in most of the region), nor specific effects at the inner grid separation boundary, demonstrating a correct implementation of the AMR infrastructure.

3.2.2.2 Magnetic rotor

Another 2D test we consider is the magnetic cylindrical rotor, originally introduced for classic MHD in [127, 128] and later employed also for relativistic MHD in [70, 129]. This test consists of

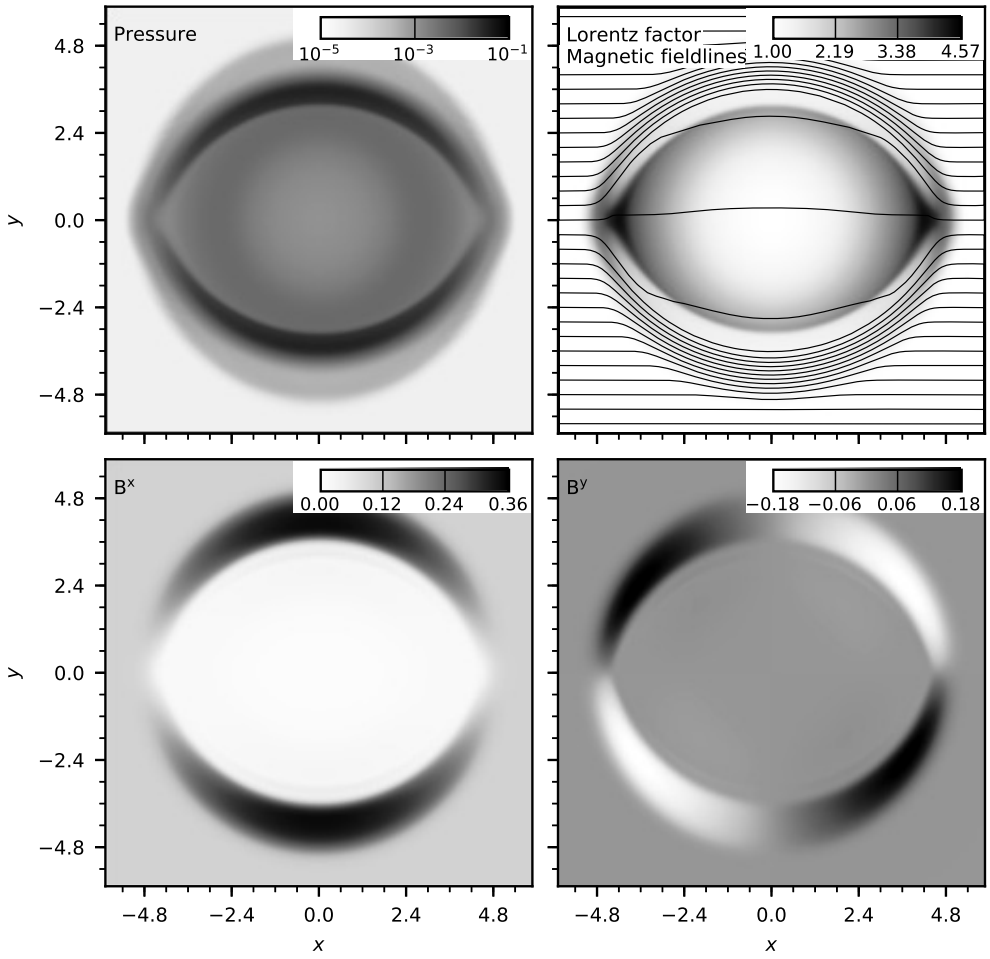

Figure 3.7: Snapshots of the cylindrical explosion test at the final evolution time $t = 4$, showing the distribution of gas pressure p (top-left), Lorentz factor W together with magnetic field lines (top-right), and x- and y-components of the magnetic field, B^x (bottom-left) and B^y (bottom-right). Adopted resolution is $\Delta x = \Delta y = 0.06$. Figure taken from JVK2.

a dense, rapidly spinning fluid at the center, surrounded by a static ambient medium, starting with a uniform magnetic field and pressure in the entire domain. For initial data, we set the radius of the inner rotating fluid as $r = 0.1$, with inner rest-mass density $\rho_{\rm in} = 10.0$, uniform angular velocity $\Omega = 9.95$, and therefore the maximum value of the fluid 3-velocity is $v_{\rm max} = 0.995$. In the outer static ambient medium, we set the rest-mass density as $\rho_{\rm out} = 1.0$. The initial the magnetic field and gas pressure are set to $B^i = (1.0, 0, 0)$ and $p_{\rm in} = p_{\rm out} = 1.0$ respectively. The numerical domain is 400×400 grid with x- and y-coordinates lying in range $[0, 1]$. Here too, we use the CFL factor to 0.25, and consider ideal fluid EOS with $\Gamma = 5/3$ for

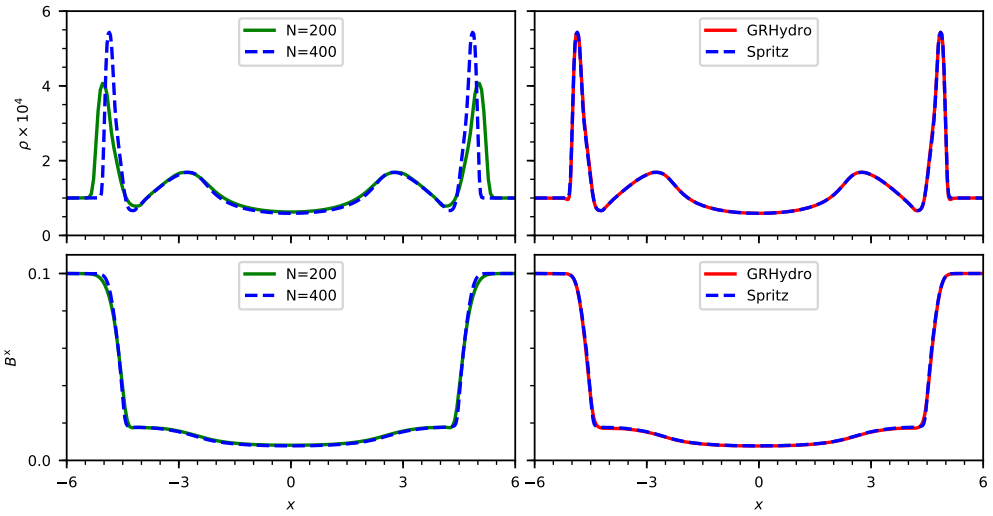

Figure 3.8: One-dimensional cut along the x-axis of the cylindrical explosion test for the final evolution time $t = 4$. Left-panels show a comparison of the rest-mass density ρ (top) and x–component of the magnetic field B^x (bottom) between low resolution test with $N = 200$ grid-points (green solid line) and high resolution test with $N = 400$ grid-points (blue dashed line. Right-panels show a comparison of the same quantities between the high resolution test performed with `Spritz` (blue dashed line) and with `GRHydro` (red solid line). Figure taken from JVK2.

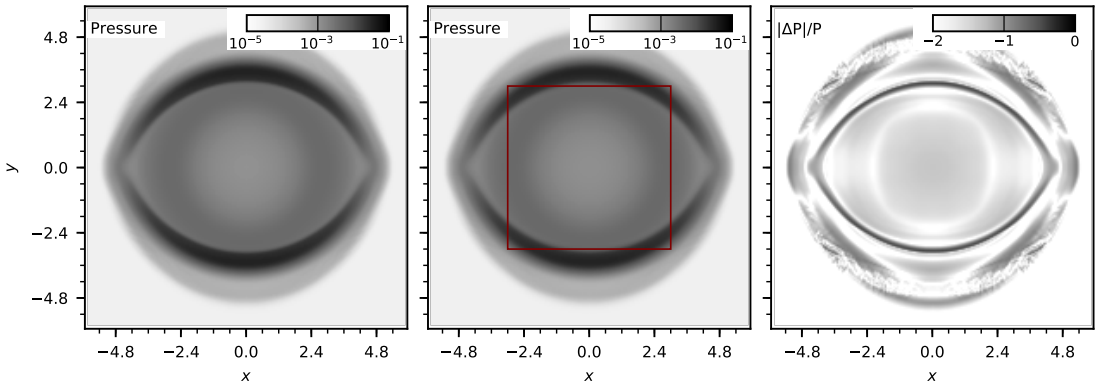

Figure 3.9: Cylindrical blast wave test with adaptive mesh refinement (AMR). Here, we compare the pressure at the final time $t = 4$ between the low resolution test (left panel) performed with uniform grid and spacing $\Delta x = \Delta y = 0.06$ and the AMR test (center panel) including a refined inner grid (red box) with double resolution (i.e., grid-spacing $\Delta x = \Delta y = 0.03$). Right panel shows the logarithmic relative differences between the two results, which are much less than 1% in most of the region, and no spurious effects are observed at the inner grid boundary. Figure adapted from JVK2.

evolution. For numerics, we use the MINMOD reconstruction, the HLLE flux solver, and the RK4 method for time-update.

Figure 3.10 depicts the 2D profiles of density ρ, gas pressure p, magnetic pressure $p_{\rm mag} = b^2/2$, and Lorentz factor W along with magnetic field lines at the final time $t = 0.4$. The

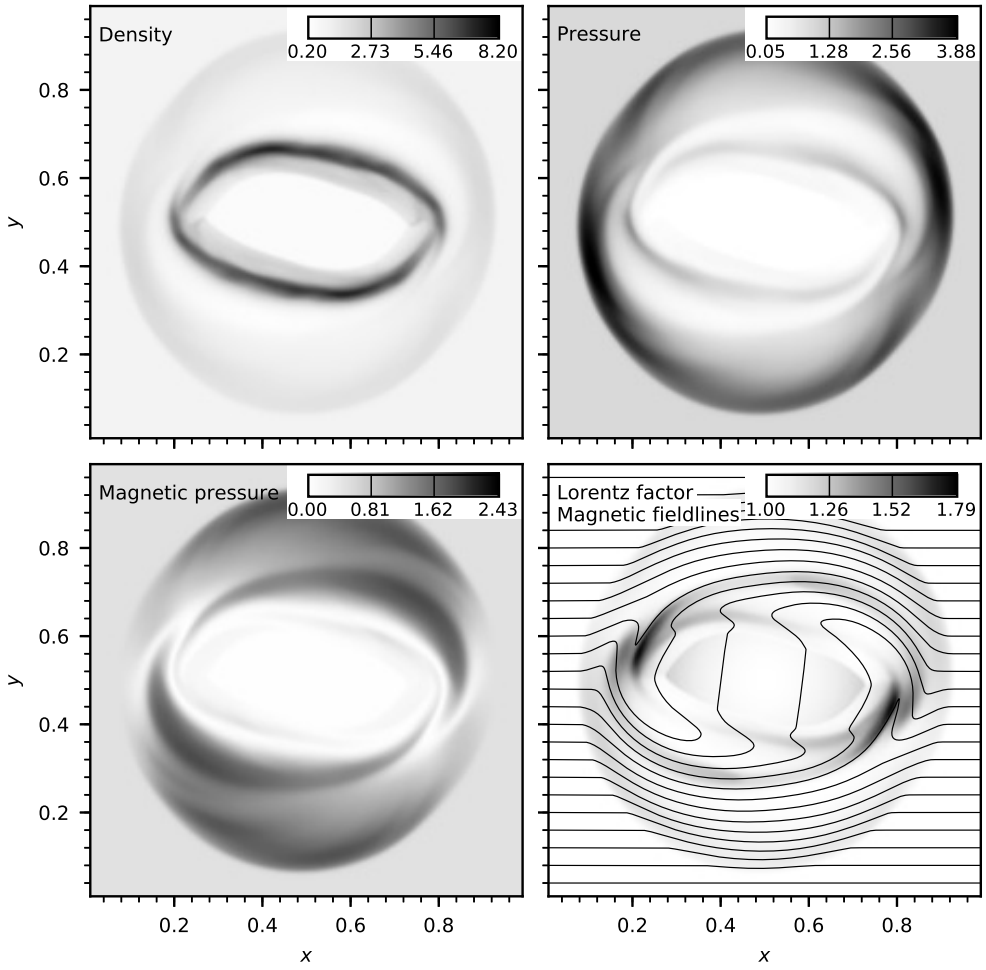

Figure 3.10: Magnetic rotor test with the following parameters shown for final evolved time $t = 0.4$: density ρ (top-left), gas pressure p (top-right), magnetic pressure $p_{\rm mag}$ (bottom-left),and Lorentz factor W together with magnetic field lines (bottom-right). The resolution considered here is $\Delta x = \Delta y = 0.0025$. Figure taken from JVK2.

rotation of the cylinder causes magnetic winding. This can be seen in the bottom-right panel of Figure 3.10, where in the central region, the field lines are twisted roughly by $\sim 90°$. This twisting of field lines could eventually slow down the rotation of the cylinder. There is also a

decrease in ρ, p, and $p_{\rm mag}$ in the central region, observed along with the formation of an oblate shell of higher density. Also for this test, the results are in good agreement with the ones in the literature [70, 91, 129].

Here too, we do a quantitative check by taking a 1D slice along $y = 0$ of the final rotor configuration at $t = 0.4$. And again, two cases are considered: (i) results comparison for the low and high resolution runs having 250 and 400 grid-points, respectively; (ii) results comparison for our high resolution test with the corresponding one preformed with `GRHydro` [91]. Figure 3.11 shows this comparison made for the two quantities ρ and B^x. For (i), as the resolution is increased, the peaks in ρ as well as B^x are better captured, showing signs of convergence towards the expected solution. For (ii), except for a minor difference in the peak values which are better captured for the `Spritz` case, the curves are comparable.

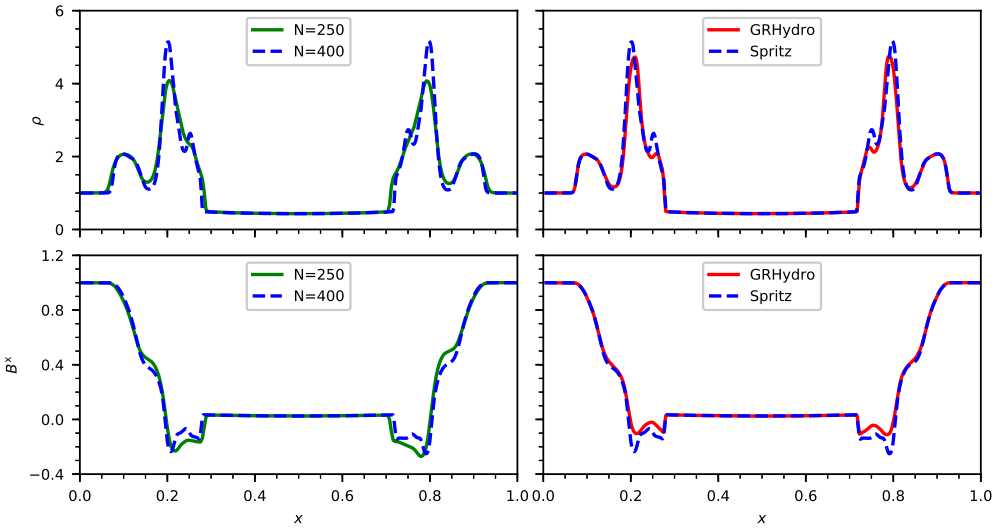

Figure 3.11: 1D cut along the x-axis for the magnetic rotor test at the final evolution time $t = 0.4$. A comparison between a low resolution test with 250 grid-points (green solid line) and a high resolution test with 400 grid-points (blue dashed line) is shown for the rest-mass density ρ and the x-component of the magnetic field B^x in the top and bottom left panels, respectively. In the top and bottom right panels, the same quantities are compared for the analogous high resolution test performed with `Spritz` (blue dashed line) and with `GRHydro` [91] (red solid line). Figure taken from JVK2.

3.2.2.3 Loop advection

The final 2D test we performed is the advection of a magnetic field loop, which was first described in [130] and later appeared in a slightly modified version (the one we consider) in [91, 125, 131, 132]. This test considers a magnetized circular field loop propagating with a constant velocity in surrounding non-magnetized ambient medium within a 2D periodic grid.

The analytical prescription for the initial magnetic field (taken from [91]) is computed as

$$B^x,\ B^y = \begin{cases} -A_{\rm loop} y/r,\ A_{\rm loop} x/r & for\ \ r < R_{\rm loop} \\ 0 & for\ \ r \geq R_{\rm loop} \end{cases} \tag{3.32}$$

where $r = \sqrt{x^2 + y^2}$ is the radial coordinate, $R_{\rm loop}$ is the loop radius, $A_{\rm loop}$ is the amplitude of the magnetic field, and B^z is set to zero. The corresponding vector potential prescription from which Equation (3.32) can be obtained is given by $\boldsymbol{A}(r) = (0, 0, \max[0, A_{\rm loop}(R_{\rm loop} - r)])$ [131].

The initial data for the density and pressure is set as $\rho = 1.0$ and $p = 3.0$ respectively throughout the computational domain. For the loop, we set $A_{\rm loop} = 0.001$ and $R_{\rm loop} = 0.3$. The fluid 3-velocity is taken as $v^i = (1/12, 1/24, 0)$ for the case with $v^z = 0$, and $v^i = (1/12, 1/24, 1/24)$ for a more generic case with a non-zero the vertical velocity, i.e., $v^z \neq 0$. We performed the test in both low resolution with a 128×128 grid and high resolution with a 256×256 grid, where the x- and y-components span the range [-0.5,0.5]. The CFL factor is 0.4 and the adiabatic index for the ideal EOS is set to $\Gamma = 5/3$. Like the previous 2D tests, we use the MINMOD reconstruction method along with the HLLE flux solver and the RK4 method for time-udpate.

In Figure 3.12, we show the outcome of the $v^z \neq 0$ test case. Here, the top row illustrates the initial configuration of the magnetic loop for the quantities B^x and $p_{\rm mag} = b^2/2$ at $t = 0$. After one entire cycle of the loop across the domain at $t = 24$, the same quantities are depicted in the middle row for low resolution run and in the bottom row for high resolution run. We notice a significant loss of magnetic pressure due to numerical dissipation for the low resolution test after one evolution cycle as also reported in [91], which is however smaller for higher resolution. Our results are comparable with the ones presented in [91]. We also point out that the expression for magnetic pressure used for Figure 3.12 is $p_{\rm mag} = b^2/2$, which differs from the expression used for Figure 10 of [91] by a factor of 1/2 (in [91] the authors actually plotted b^2).

To consider a less dissipative numerical scheme, we also perform another simulation in low resolution employing the PPM reconstruction and compare the results with those obtained with MINMOD reconstruction. This is shown in Figure 3.13, where the top and bottom panels represent the outcome of the runs with MINMOD reconstruction and PPM reconstruction, respectively. The first column depicts the initial data at $t = 0$, the second shows the loop at final time $t = 24$, while the third one shows the logarithmic values of the absolute differences between the initial and final times. As expected, we find significantly lower dissipation in the PPM case.

3.2.3 3D tests

Finally, we present the results of our 3D tests. The first test is the 3D generalisation of the cylindrical explosion test. While the second test follows the evolution of non-rotating NS in full GR, thus assessing the correctness of our code in a curved and dynamical background.

3.2.3.1 Spherical explosion

Spherical explosion is a very demanding GRMHD test, commonly performed with GRMHD codes working in spherical coordinates [133–135]. This test becomes challenging in Cartesian coordinates with the potential limitations in regions where the shock front is not parallel to the orientation of grid-cells' faces.

The test settings are an extension in spherical symmetry of the cylindrical explosion test presented in Section 3.2.2.1. Here, we consider an inner dense spherical core of radius $R_{\rm in} = 0.8$ centered in the origin with $\rho_{\rm in} = 10^{-2}$ and $p_{\rm in} = 1.0$, surrounded by a spherical shell ranging as $R_{\rm in} < r < R_{\rm out} = 1.0$, where pressure and density are characterized by an exponential decay analogous to the prescription given by Equation (3.31).

For $r > R_{\rm out}$, a low-pressure uniform fluid exists with $\rho_{\rm out} = 10^{-4}$ and $p_{\rm out} = 3.0 \times 10^{-5}$. Additionally, following [133, 134], a uniform magnetic field parallel to the z-axis is employed in the entire domain. The numerical grid extends as $[-6.0, 6.0]$ and is covered by 160 grid-cells in all directions. We evolve the system for a total time of $t_{\rm final} = 6.0$ using a CFL factor of 0.25. Also, we set a lower atmosphere density floor in this test, equivalent to $\rho_{\rm atm} = 10^{-12}$. As for the numerical schemes employed, we use MINMOD reconstruction along with the Lax-Friedrichs flux solver.

Figure 3.14 shows the snapshot on the meridional plane of gas pressure and Lorentz factor W at the final time $t = 4$ for tests performed with magnetic field strength $B^z = 0.0, 0.1$ and 1.0. At the top-right panel (Lorentz factor in the non–magnetized case), we see small deviations from spherical symmetry exactly aligned with the Cartesian axes, giving a hint of the geometrical issues brought by such a demanding test. However, despite the accumulation of errors along the diagonals due to the non-perpendicularity of the fluxes, the spherical shape of the shock front seems to be well preserved in this case, even at a relatively low resolution. In presence of a dynamically important magnetic field oriented along the z axis, the shock front deviates naturally from spherical symmetry (see middle row of Figure 3.14). Finally, when the magnetic field strength is very high (see bottom row), the central region gets completely evacuated. Even in this extreme scenario, the evolution proceeds without any problem.

3.2.3.2 TOV star

Static, spherically symmetric stars in general relativity are best described by the Tolman-Oppenheimer-Volkoff (TOV) equations [136, 137]. To further assess the stability and accuracy of our code, the next test we considered is the evolution of a non-rotating stable TOV configuration for both non-magnetised and magnetised cases. The test setup adopts the model described in [138] built using the `TOVSolver` thorn [94].The initial TOV configuration is produced using a polytropic EOS with adiabatic index $\Gamma = 2.0$, polytropic constant $K = 100$, and initial central rest-mass density $\rho = 1.28 \times 10^{-3}$. We evolve this initial configuration adopting an ideal fluid EOS with the same value for Γ. For the magnetised version, we add the magnetic field to the computed TOV configuration using the analytical prescription of the vector potential A_ϕ given by

$$A_\phi \equiv A_{\rm b} \varpi^2 \max\left(p - p_{\rm cut}, 0\right)^{n_s} \quad , \tag{3.33}$$

where ϖ is the cylindrical radius, $A_{\rm b}$ is a constant, $p_{\rm cut} = 0.04 p_{\rm max}$ determines the cutoff when the magnetic field goes to zero inside the NS, with $p_{\rm max}$ corresponding to the initial maximum gas pressure, and $n_s = 2$ sets the degree of differentiability of the magnetic field strength [32]. The value of A_b is chosen such that the maximum value of the initial magnetic field strength is set to $\approx 1 \times 10^{16}$ G. This generates a dipole-like magnetic field confined inside the NS and zero magnetic field outside.

The non-magnetised tests are run on a uniform grid with x-, y- and z-coordinates spanning over the range [0, 20] with low, medium and high resolution having $(32)^3$, $(64)^3$ and $(128)^3$ grid–cells respectively, and considering reflection symmetry with respect to every direction, i.e., the so-called octant symmetry. Furthermore, we perform two more tests for non-magnetised TOV NS in high resolution (i) employing the Cowling approximation (i.e. considering a fixed space-time) [139–141] to check the accuracy of our code by evolving just the hydrodynamical equations on a static spacetime background, and (ii) implementing a mesh refinement composed by two nested boxes centered at the origin and extending up to x, y, z =20 and 40, respectively, both having $(128)^3$ grid-cells in each direction (therefore, the inner box corresponds to the domain evolved in the unigrid run at high resolution while the outer box allows for a further out external boundary). Since Einstein Toolkit does not provide support to handle reflection symmetry for staggered variables, we perform the magnetised TOV tests in low, medium and high resolution covering the entire domain with x-, y- and z-coordinates lying in the range [-20, 20] (considering no reflection symmetries) having the same respective grid-spacing as that of the non-magnetised simulations. All test cases are simulated for 10 ms using the PPM reconstruction method, the HLLE flux solver, and the RK4 method for time stepping with a CFL factor of 0.25.

The top panel of Figure 3.15 shows the central rest-mass density $\rho_{\rm c}$ evolution for three resolutions, the high-resolution in Cowling approximation and the high-resolution with AMR, all for the non-magnetised TOV case. We note that the AMR case (orange curve) perfectly reproduces the result in high-resolution (green curve), supporting the correctness of AMR implementation within the `Spritz` code. Here, the periodic oscillations are initiated as a result of the truncation errors generated in the initial data, while the cause of dissipation is primarily due to the numerical viscosity of the finite differencing (FD) scheme [138, 142]. The results converge well after increasing the resolution, and the additional tests for the cases with Cowling approximation and AMR are also fully satisfactory. In order to further investigate the accuracy of our code, we compare the low, medium, and high resolution test results of $\rho_{\rm c}$ evolution with those obtained with `GRHydro`. As shown in the bottom panel of Figure 3.15, we observe an exact match.

The initial magnetic field configuration for the magnetised TOV test is illustrated in Figure 3.16. Here, the magnetic field strength is shown along with representative magnetic field lines. The top panel of Figure 3.17 shows the maximum rest-mass density $\rho_{\rm c}$ evolution for the magnetised TOV case, which matches almost exactly with the one for the non-magnetised case (see the top panel of Figure 3.15). This should be expected, since the imposed magnetic field represents only a small perturbation compared to the gravitational binding energy of the system. In addition, the time evolution of the maximum value of the magnetic field strength $B_{\rm max}$

is depicted in the bottom panel of Figure 3.17. While $B_{\max}$ is highly damped for the lowest resolution test with a decrease by a factor of roughly 14.75 in 10 ms, its value stabilizes with increasing resolution, as observed for ρ_c. We note again that here the damping is a numerical viscosity effect of the FD scheme.

To conclude this section, we report in Figure 3.18 the oscillation frequencies of TOV star simulations in order to validate our models with literature results. In particular, we show the results of the high-resolution simulations in pure hydrodynamics with dynamical space-time adopting both uniform grid and AMR, with the Cowling approximation (see Figure 3.18 left-panel), as well as of the high-resolution run with magnetic field (see Figure 3.18 right-panel). The power spectrum of each simulation is computed via fast Fourier transform (FFT) in order to extract the amplitudes and frequencies of the oscillations of the central rest mass density, and then the amplitudes are normalized to the maximum one for each simulation. Figure 3.18 also shows the peak frequencies of the oscillations from the literature taken from [143], which were obtained with an independent 2D code for fixed space-time and with a perturbative code in the case of hydrodynamics coupled to space-time evolution. An interesting point to note is that although the results of [143] were obtained with a polytropic EOS, our simulations with ideal gas EOS show a perfect match for the peak frequencies. The ideal gas EOS is expected to produce different results from a polytropic one only in presence of shocks, which in this case appears only on the low-density surface and therefore does not affect the oscillations at the core. Finally, we see that the peak frequencies of our non-magnetised and magnetised models are also in perfect agreement as shown by the left panel of Figure 3.18.

3.3 Summary

In this Chapter, we presented the work of JVK2, introducing a new fully general relativistic code called `Spritz`, which evolves GRMHD equations in three spatial dimensions on cartesian coordinates, and on dynamical backgrounds. This code is a considerable improvement of its parent code `WhiskyMHD` code [32, 90, 108], now providing support for handling different types of EOS (also tabulated and finite temperature), as in the `GRHydro` code [29], as well as implementing the vector potential evolution on a staggered grid, as in the `IllinoisGRMHD` code [30]. We also note that `GRHydro` does not support a vector potential formulation of the GRMHD equations, while `IllinoisGRMHD` cannot handle finite temperature tabulated EOS (at least at the time of Thesis writing).

After describing the different features and workflow of `Spritz`, we then reported on a series of tests in 1D, 2D and 3D. We started by showing the code capability of accurately solving 1D Riemann problems by comparing the numerical results with exact solutions [31]. We then described a series of special relativistic MHD tests in 2D, including the cylindrical explosion, the magnetic rotor, and the loop advection tests. All tests showed very good agreement with the exact solution (loop advection) or with the other GRMHD code `GRHydro` (cylindrical explosion and magnetic rotor). In particular, for the cylindrical explosion case, when comparing the 1D results, we found `Spritz` to capture certain features with slightly better accuracy than `GRHydro`. The same test was also used to validate the code's capability of dealing with AMR grid, and

demonstrated that using AMR has no effect in the correct evolution of MHD quantities. We then performed a demanding 3D spherical explosion test with different levels of magnetization, which produced good results as expected. We concluded our series of tests with a standard 3D evolution of a stable TOV configuration (both with and without magnetic field) in order to show the code ability to handle fully general relativistic regimes.

In the following Chapter, we describe the second version of `Spritz`, which includes support for finite temperature tabulated 3-parameter EOS, as well as the implementation of a neutrino radiation scheme.

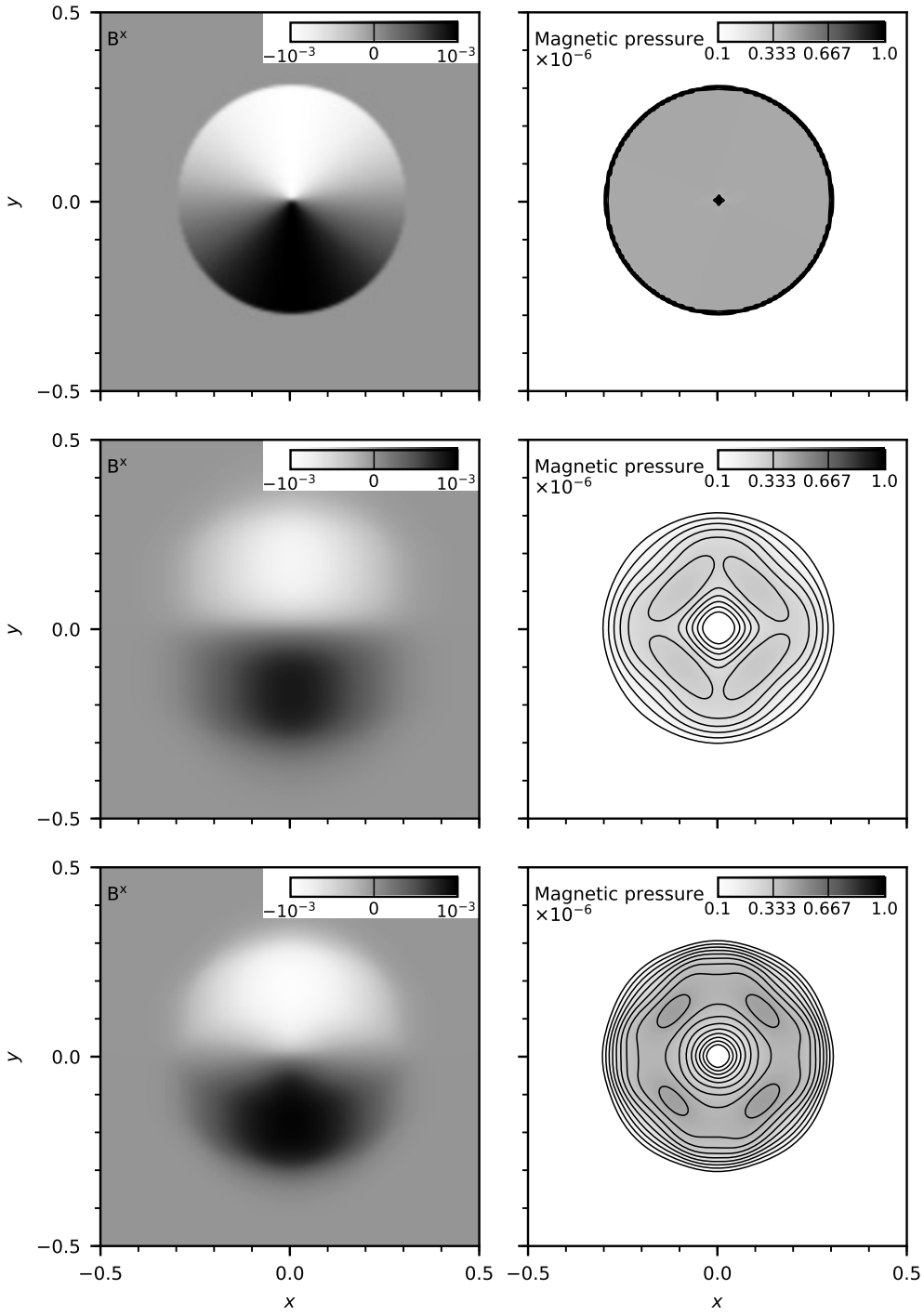

Figure 3.12: Loop advection test with $v^z = 1/24$. Left and right columns represent the x-component of the magnetic field B^x and the magnetic pressure $p_{\rm mag} = b^2/2$, respectively. The initial data for B^x and its corresponding $p_{\rm mag}$ at $t = 0$ are depicted in the top row, while middle and bottom rows represent these quantities after one periodic cycle of evolution, i.e., at $t = 24$, in low resolution ($\Delta x = 1/128$) and high resolution ($\Delta x = 1/256$), respectively. Our results show very good agreement with those reported in [91]. Figure taken from JVK2.

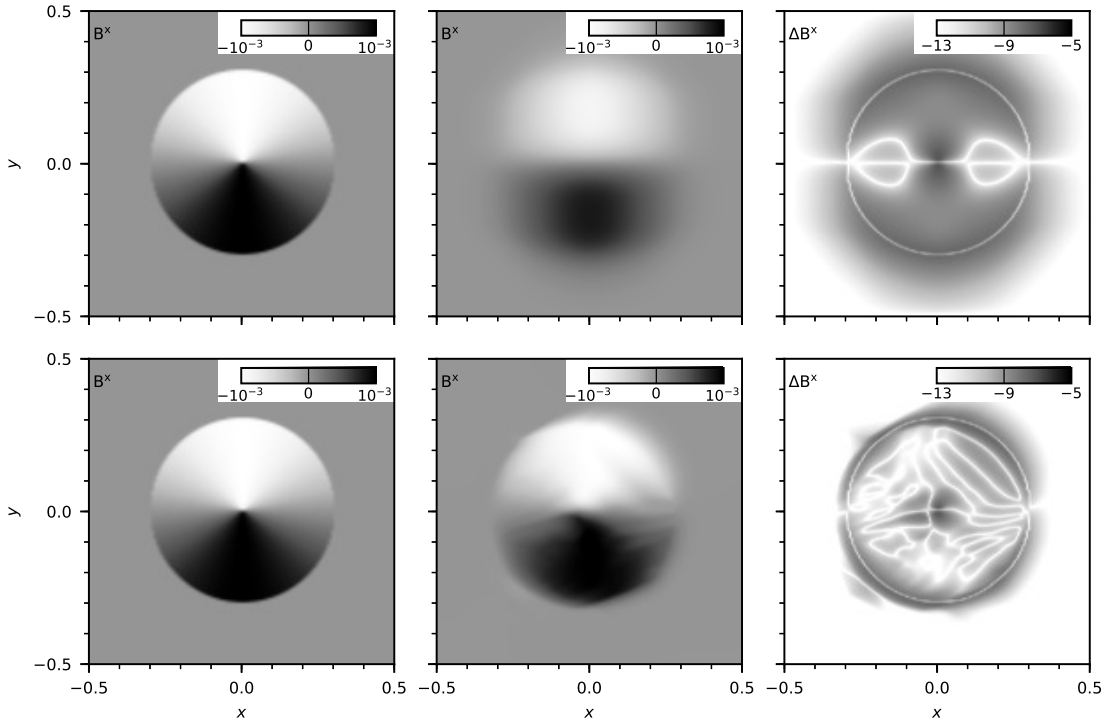

Figure 3.13: Comparison between the MINMOD and PPM reconstruction methods for the loop advection test with $v^z = 1/24$. Top and bottom rows correspond to results obtained with MINMOD and PPM respectively. First column depicts the initial configuration of the magnetic field B^x at $t = 0$, second column shows the final configuration of B^x after one periodic cycle at $t = 24$, and the third column shows the logarithmic absolute differences in B^x between the initial and final times. Figure taken from JVK2.

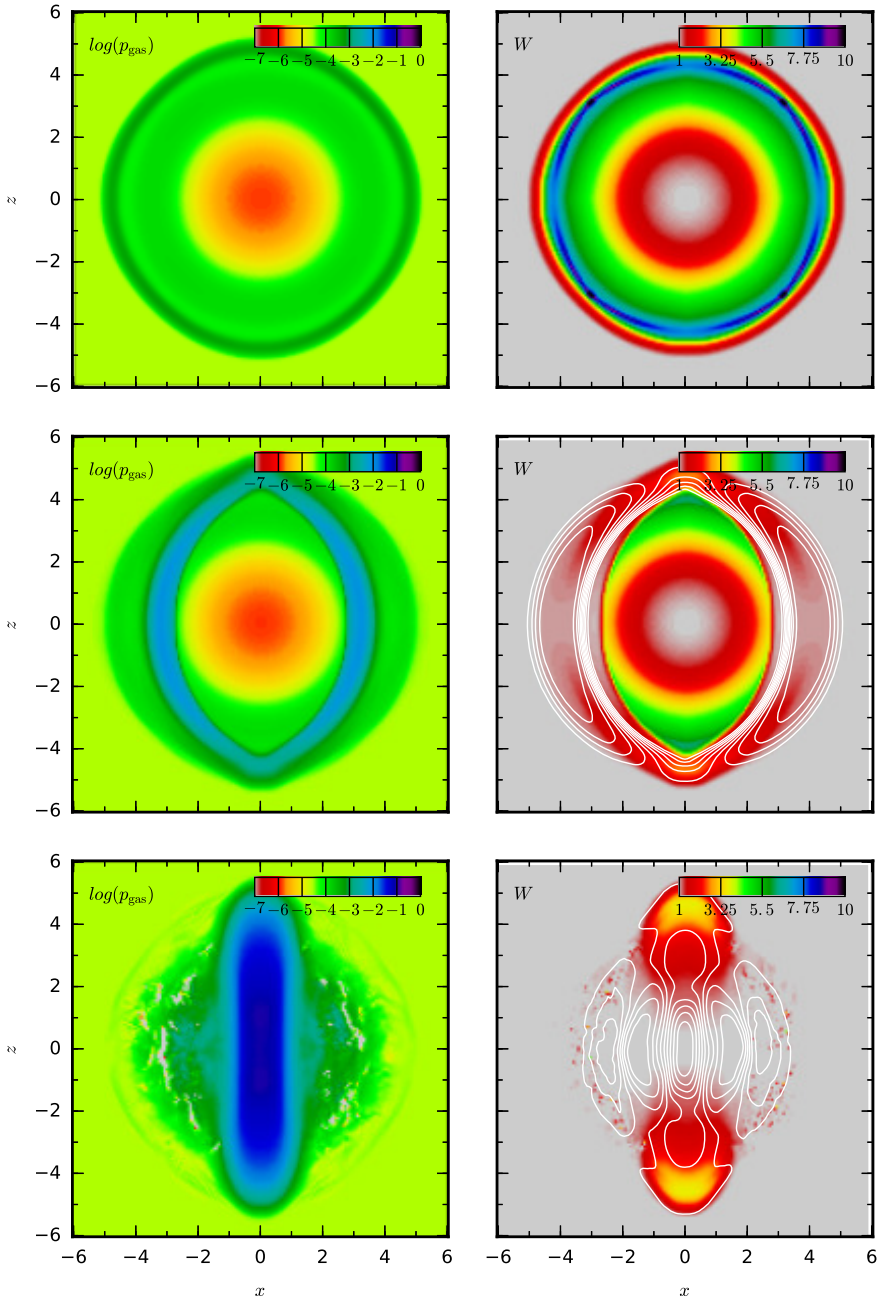

Figure 3.14: Spherical explosion test snapshots at final time $t = 4.0$. Top row shows the results for the non-magnetised case, middle row for the intermediate magnetization case with $B^z = 0.1$ while the bottom row is the strongly magnetized case with $B^z = 1.0$. The left and right columns show respectively the gas pressure and the Lorentz factor along with isodensity contour lines of $||B|| = \sqrt{B^i B_i}$. Figure taken from JVK2.

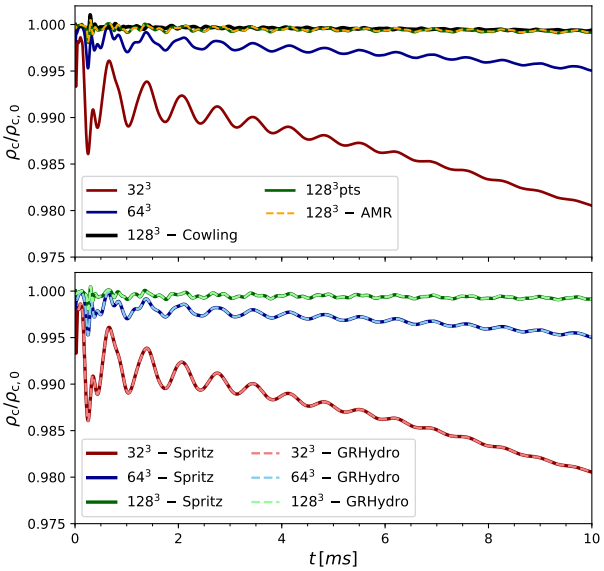

Figure 3.15: Results of the non-magnetised TOV simulations. Top: Time evolution of the normalised central rest-mass density $\rho_c/\rho_{c,0}$ for the different resolutions inclusive of cases with Cowling approximation and AMR. Bottom: Comparison of $\rho_c/\rho_{c,0}$ evolution with those obtained with `GRHydro` for low, medium, and high resolution, showing an exact match. Figure taken from JVK2.

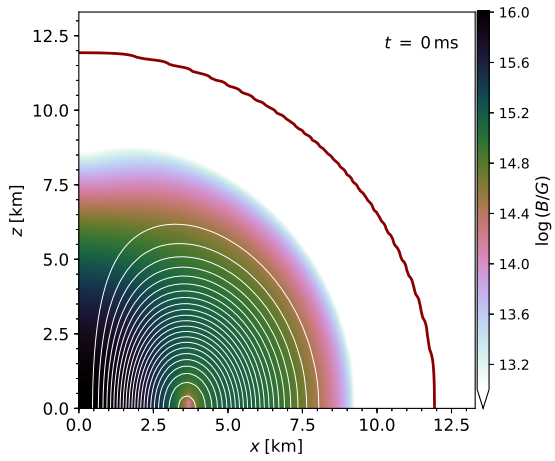

Figure 3.16: Initial internal magnetic field configuration of the magnetised TOV. Colormap indicates the strength of the magnetic field, while the contours (in white) trace a number of representative isosurfaces of the ϕ–component of the vector potential, A_ϕ. The latter contours also correspond to poloidal magnetic field lines. The red line is an approximate representation of the TOV surface, showing the iso-density contour of 5×10^5 times the assumed atmospheric floor density. Figure taken from JVK2.

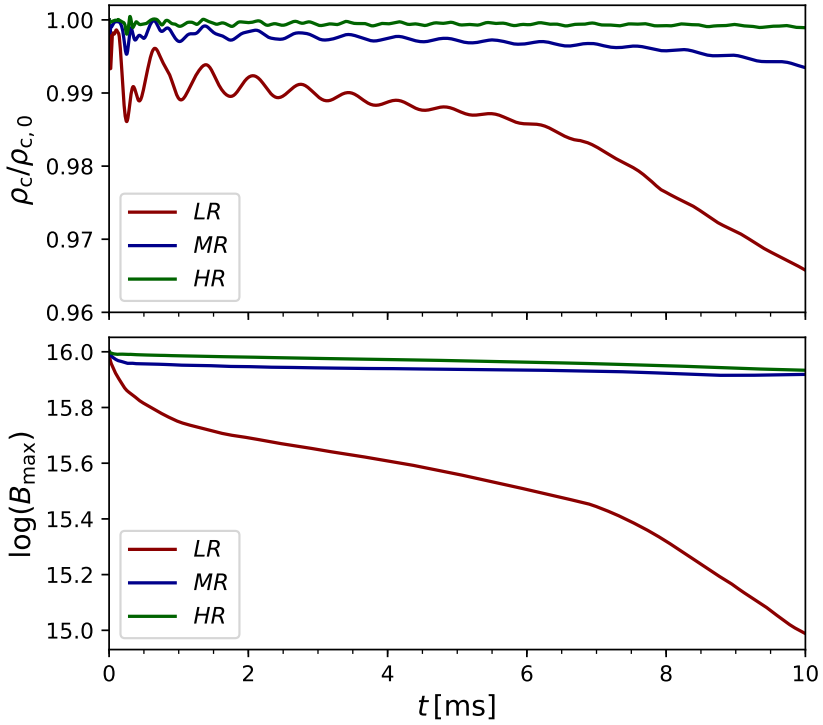

Figure 3.17: Results of the magnetised TOV simulation. Top: Time evolution of the normalised central rest-mass density $\rho_c/\rho_{c,0}$ for the different resolution runs. Bottom: Time evolution of the maximum value of the magnetic field strength for all three resolutions. Figure taken from JVK2.

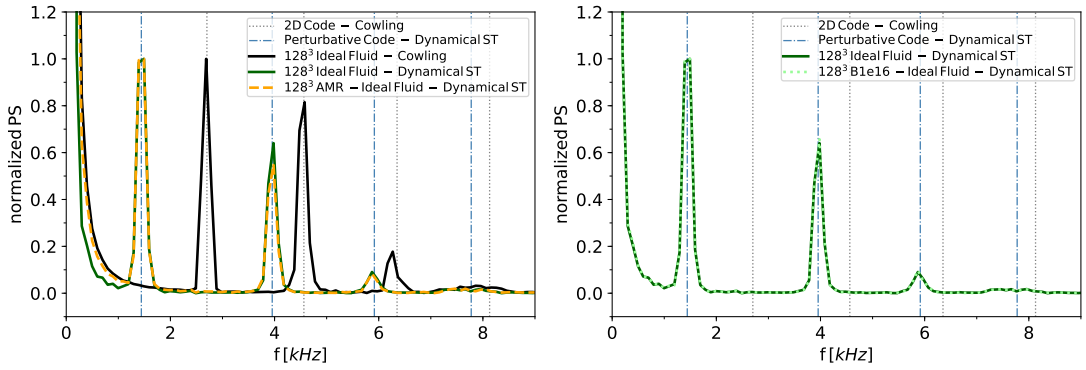

Figure 3.18: Power spectrum of the central rest-mass density evolution, normalized to maximum amplitude of the peaks of oscillations' frequencies. Left-panel shows the results from the runs without magnetic field, while right-panel also considers magnetic field. Figure taken from JVK2.

Chapter 4

Spritz with neutrinos

As mentioned before, one of the main goals of the `Spritz` code is to perform compact binary mergers simulations taking into account all key ingredients in order to study the different astrophysical mechanisms involved in such scenarios as accurately as possible. These ingredients not only include general relativistic effects and magnetic fields but also a temperature and composition dependent equation of state describing the behaviour of matter, and neutrino emission/re-absorption. For example, both magnetic fields and neutrino effects are critical (i) for accurate modelling of the BNS merger ejecta and their composition, which then affect the kilonova emission and the associated heavy element nucleosynthesis (e.g., [27, 144, 145], JVK3 and refs. therein), and (ii) for SGRB jet formation, where magnetic fields are most likely the primary driver (e.g., [42, 43, 146, 147]) whereas neutrino radiation might play a role in clearing the material along the spin axis of the merger remnant, which in turn could assist the successful propagation of the corresponding outflow (e.g., [38]). However, including all of the above elements in one code is rather challenging and only very few magnetized BNS merger simulations with neutrino treatment have been presented so far [36, 148].

In this Chapter, we describe the second version of the `Spritz` code as presented in JVK5, which now features support for finite temperature composition dependent tabulated EOS and implementation of a neutrino cooling/heating scheme. Morever, we added another C2P scheme that supports such tabulated 3-parameter EOS, and also implemented higher-order methods for hydrodynamic variables. Lastly, here we also present a large set of tests through which we validate the latest implementions in `Spritz`.

4.1 Theoretical background

We remind the reader that `Spritz` is based on the flux-conservative formalism as described in Section 2.2. Here, we focus mainly on the new additions to the code and refer to the previous chapters for more details on the equations and methods used to solve the GRMHD equations given by (2.61), (2.78-2.82). As one can see, these equations do not include the contribution of neutrino emission and reabsorption. We therefore adopt an operator-split approach such

that the GRMHD evolution step is first performed without such contribution and then the neutrino problem is solved via the leakage scheme. Finally, the variables Y_e and ϵ are updated accordingly, thus including the effects of neutrino radiation on the GRMHD evolution itself (see Sections 4.1.3 and 4.2.4 for more details).

4.1.1 Electron fraction advection

In order to incorporate the effects of neutrino emission/absorption on nuclear matter, we need to take into account the crucial role of electron fraction which can be defined as

$$Y_e \equiv \frac{n_e}{n_b} = \frac{n_e}{n_p + n_n} \ , \tag{4.1}$$

where n_e, n_p, and n_n the electron, proton, and neutron number densities respectively whereas $n_b \equiv n_p + n_n$ stands for the baryon density. The rest-mass density can be written in terms of baryon density as $\rho = m_n n_b$, where m_n is the nucleon mass considered equal for neutrons and protons (while contribution of electron masses is neglected for computing ρ). Now, for a system without weak interactions (thus, no neutrinos), there is a local conservation of the number of protons and of neutrons, therefore, guaranteeing local conservation of baryon number. In this case, the continuity equation (2.45) can be written as

$$\nabla_\mu (n_b u^\mu) = 0 \ . \tag{4.2}$$

Due to charge neutrality, this in turn assures local electron number conservation, and using the relation $n_e = Y_e n_b = Y_e \rho / m_b$, we can write

$$\nabla_\mu (Y_e \rho u^\mu) = 0 \ . \tag{4.3}$$

The above local electron number conservation together with local baryon conservation compels the local electron density $Y_e \rho$ to be advected along the fluid lines, and is thus called as *electron fraction advection* equation. This equation can then be expanded as

$$\frac{1}{\sqrt{-g}} \partial_\mu \left(\sqrt{-g} Y_e \rho u^\mu \right) = \frac{1}{\sqrt{-g}} \left[\partial_t \left(\alpha \sqrt{\gamma} Y_e \rho u^t \right) + \partial_i \left(\alpha \sqrt{\gamma} Y_e \rho u^i \right) \right] = 0 \ . \tag{4.4}$$

Using the definition $D = \rho W = \rho \alpha u^t$ and the relation between co-moving and Eulerian 3-velocities, we can recast Equation (4.4) into the hyberbolic conservative form as

$$\partial_t \left(\sqrt{\gamma} D Y_e \right) + \partial_i \left[\alpha \sqrt{\gamma} D Y_e \left(v^i - \frac{\beta^i}{\alpha} \right) \right] = 0 \ . \tag{4.5}$$

When considering the reactions involving neutrinos, the local electron number conservation equation is no longer satisfied, and a source term is added to Equation (4.5) which modifies the local electron fraction as per Equation (4.34) (see Section 4.1.3).

4.1.2 Finite temperature tabulated EOS

For accurate description of matter behavior including microphysical effects, it becomes crucial to include a proper description of matter composition as well as associated nuclear reactions to account for the precise effects on the hydrodynamic system in hand. For instance, incorporating the temperature effects on the composition becomes necessary for estimating the emission and absorption rates associated with the different processes involving neutrinos. Morever, such processes can then alter Y_e which must be estimated accurately when dealing with dynamical scenarios.

Moreover, as stated earlier in Section 2.2.6, the exact matter composition and the respective EOS for the NS core still remains unknown. Based on nuclear physics calculations, a large number of different tabulated EOS for NSs have been proposed in literature (see, for example, [41] and [73] databases for variety of such EOS). These tabulated EOS, in their standard form, are usually three-dimensional where every thermodynamic quantity is represented as a function of three variables: the rest-mass density ρ, the temperature T, and electron fraction Y_e. In particular, these tables contain quantities like the specific internal energy ϵ, gas pressure p (or P), entropy per baryon, derivatives of quantities such as $\mathrm{d}\epsilon/\mathrm{d}T$, $\mathrm{d}p/\mathrm{d}\epsilon$, $\mathrm{d}p/\mathrm{d}\rho$, speed of sound squared c_s^2, chemical potentials μ_e, μ_p, μ_n, mass fractions, mass and atomic numbers. The temperature values usually start from 0.01 MeV (for setting the atmosphere) going up to 200 MeV (allowing high temperatures during collapse to a BH or strong shocks during merger). Similarly, the rest-mass density ranges from around $10^3\,\mathrm{g/cm^3}$ (for atmosphere density floor) to $10^{16}\,\mathrm{g/cm^3}$ (here too, for instance, allowing for high density values during collapse to a BH). Range in Y_e is typically set from 0 to 0.5. Also, note that such microphysical nuclear EOS are generally constructed considering Nuclear Statistical Equilibrium (NSE) which assumes that matter is in equilibrium with respect to strong and electromagnetic interations.

In the second version of the `Spritz` code, we now provide support for handling tabulated finite-temperature and composition dependent EOS via the `EOS_Omni` thorn provided in the Einstein Toolkit.

When generating the initial data for a NS, we usually require a one-dimensional (i.e., barotropic) EOS, where P and ϵ are a function of ρ alone. Therefore, one needs to reduce the three-dimensional table having $P = P(\rho, T, Y_e)$ and $\epsilon = \epsilon(\rho, T, Y_e)$ to a simpler one-dimensional relation $P = P(\rho)$ and $\epsilon = \epsilon(\rho)$. This is done by considering two constraints on the NS matter, which we describe below.

4.1.2.1 Beta-equilibrium condition

The first constraint assumes the NS matter to be initially in β-equilibrium, which is given as

$$\mu_p + \mu_e - \mu_n - \mu_{\nu_e} = 0 \ , \tag{4.6}$$

where μ_p, μ_n, μ_e and μ_{ν_e} are the proton, neutron, electron and electron-neutrino chemical potentials. Considering that neutrinos are not trapped in the system, thus ignoring the contributions from the neutrino chemical potentials, i.e. $\mu_{\nu_e} \sim 0$, we can reformulate the (neutrinoless) beta-equilibrium constraint as a constraint on the lepton chemical potential as $\mu_l = 0$. Now, for

a given temperature T and a baryon number density ρ/m_b, it can be shown that there exists only one charge fraction of strongly interacting particles [73] such that

$$\mu_l(Y_e)|_{T,\rho} = 0 \ . \tag{4.7}$$

Using this relation along with Equation (4.6), the condition on the choice of the electron fraction, which is used for slicing the EOS table, becomes

$$(Y_e)|_{T,\rho} = Y_e \ : \ (\mu_p + \mu_e - \mu_n)|_{T,\rho} = 0 \ . \tag{4.8}$$

This allows the number of independent parameters to be reduced by one such that thermodynamic quantities like $\epsilon(\rho, T, Y_e)$ can then be expressed as $\epsilon = \epsilon(\rho, T, Y_e(\rho, T)) = \epsilon(\rho, T)$.

The β-equilibrium condition is a reasonable assumption for old NSs, such as those encountered in BNS or NSBH binary systems prior to merger.

4.1.2.2 Temperature or entropy slicing

For the second constraint, in order to reduce the independent parameters to one, we can decide to fix a constant value either for the temperature (*T-slicing* condition) or for the entropy (*S-slicing* condition).

T-slicing allows to set the an initial temperature to the lowest possible one provided by the EOS table (closest to the initial zero-temperature state for a 'cold' NS). This value is typically 0.01 MeV or 0.1 MeV. This type of slicing is typically used in BNS or NSBH merger simulations since it is reasonable to expect NSs to be cold prior to merger.

Instead of T-slicing, another possibility is to impose an isentropic constraint to obtain the 1D slice at constant specific entropy. This condition produces a temperature gradient in the NS initial data, thus allowing us to test the ability of our code in dealing with "hot" NSs.

All the simulations presented in JVK5 are performed adopting the LS220 EOS [149], which has already been employed in literature dealing with the evolution of BNS systems (e.g., [144, 150, 151]).

4.1.3 Neutrino emission and absorption

Mergers of BNS/NSBH systems can produce temperatures as high as $T \sim 10\,\mathrm{MeV} \sim 10^{11}\,\mathrm{K}$, thus also affecting the electron fraction Y_e to a great extent. In such events, in order to precisely understand the mechanisms behind the r-process nucleosynthesis taking place in the ejected matter and the subsequent production of heavy elements, one must take into account the effect of neutrinos, which play a fundamental role in both the transport of energyas well as in determining the evolution of Y_e and temperature. To do so, we need a proper estimation of the rates of the different reactions involving neutrinos for computing the nucleosythesis yields and for modelling the radiactively-powered kilonova signals accompanying such merger events (as the one already observed after GW170817; e.g., [3, 152]).

Typical timescale for weak processes involving neutrinos can be estimated from the changing electron fraction as

$$t_{\mathrm{WP}} \sim \left| \frac{Y_e}{\dot{Y}_e} \right| \ll t_{\mathrm{dyn}} \ , \tag{4.9}$$

where $t_{\rm dyn}$ represents the dynamical timescale of the simulated astrophysical event [153].

Neutrino emission can take place in a variety of ways, ranging from diffusion to free emission. Since their emission cross-sections depend directly on temperature (~ 100 MeV in BNS mergers), copious amounts of neutrinos in all flavors are emitted by the hot regions, covering the whole energy spectrum. Thus, by carrying away energy, neutrinos can significantly cool down the (meta)stable NS remnant of a BNS merger or the accretion disk around the spinning BH resulting from either a BNS or an NSBH merger (e.g., [144]). After emission, neutrino transport is further affected by different interations, scattering and absorptions, their mean free path determined by various cross-sections. For instance, a fraction of the emitted neutrinos can undergo reabsorption by the surrounding material, inducing heating and leptonization of the material itself.

The neutrino mean free path is strongly dependent on rest-mass density. Particularly, for densities higher than $10^{12}\,\mathrm{g/cm^3}$ (relating to high-density interiors of the NS), neutrinos thermalize with the surrounding matter within the so-called *neutrinosphere*[1] and diffuse out (see, for e.g., [155]), thus characterizing the *diffusive regime*. For densities much lower than $10^{12}\,\mathrm{g/cm^3}$, the neutrinos stream freely with no or minimal interaction with matter, thus carrying away energy and momentum. The intermediate regime, where neutrinos are neither free to escape nor fully trapped, is governed by the *optical depth*.

The neutrino opacity k can be defined as the inverse of its mean free path. When integrated along a path ξ, it yields the optical depth τ. The energy averaged optical depth along each path ξ followed by neutrinos can be defined as [156]

$$\tau_\xi = \int_\xi \rho(\mathbf{x}) k(\mathbf{x}) \sqrt{\gamma_{ij} dx^i dx^j} \ , \tag{4.10}$$

where $\kappa(\mathbf{x})$ is the energy averaged opacity at position $\mathbf{x}$. For a given location, the pointwise optical depth is defined by the path giving the minimum optical depth favouring neutrino escape, as

$$\tau(\mathbf{x}) = \min_{\xi\in\Xi} \tau_\xi = \min_{\xi\in\Xi} \int_\xi \rho(\mathbf{x}) \kappa(\mathbf{x}) \sqrt{\gamma_{ij} dx^i dx^j} \ , \tag{4.11}$$

where Ξ is the set of all possible paths starting from position $\mathbf{x}$.

The complexity coupled with the extremely high computational cost of solving the full neutrino transport problem via the Boltzmann radiation transport equations have been the driving factors behind the introduction of approximate schemes and simplified assumptions in modern-day codes (e.g., [157] and refs. therein). Here, we adopt a neutrino leakage scheme, already employed successfully in BNS and NSBH simulations (e.g., [148, 153, 158–160]). Particularly, we consider the leakage method presented in [156, 161], which has been implemented in the publicly available `ZelmaniLeak` code [41]. In what follows, we introduce this leakage scheme along with the basic physical assumptions. Its numerical implementation is instead discussed in Section 4.2.4.

[1] The neutrinosphere is conventionally defined as the surface of constant neutrino optical depth $\tau = 2/3$ (see e.g., [154]). This decoupling surface defines the boundary outside of which neutrinos stream freely with no or minimal interactions.

In this neutrino leakage scheme, we deal with three neutrino species: electron neutrino ν_e, electron antineutrino $\bar{\nu}_e$, and heavy-lepton neutrinos ν_x (including ν_ν, $\bar{\nu}_\mu$, ν_τ, $\bar{\nu}_\tau$). For the given cross-section σ_{ν_i}, we can first define opacities for the neutrino species ν_i as

$$\kappa_{\nu_i} = N_A \rho \sigma_{\nu_i} \ , \tag{4.12}$$

where N_A is the Avogadro number. Then, the non-energy dependent opacity can be defined as

$$\zeta_{\nu_i} \equiv \kappa_{\nu_i} / E^2_{\nu_i} \ , \tag{4.13}$$

where $E^2_{\nu_i}$ is the squared of the neutrino energy. Using this, non-energy dependent optical depth can be written as

$$\chi_\xi = \int_\xi \zeta(\mathbf{x}) \sqrt{\gamma_{ij} dx^i dx^j} \ , \tag{4.14}$$

The main driver behind neutrino opacities are the weak processes taking place in matter, which in turn depend on matter composition, rest-mass density, temperature, neutrino flavor and energy. For neutrino energies, the following isotropic Fermi-Dirac distribution is considered [2]

$$f_{\nu_i}(E_{\nu_i}) = \frac{1}{e^{\left(E_{\nu_i} - \mu_{\nu_i}\right)/k_b T} + 1} \ . \tag{4.15}$$

`ZelmaniLeak` employs the standard ansatz [162] of approximating the diffusive and free-streaming regimes, and interpolates between the two in other cases. In these regimes, two main quantities are evaluated, i.e. (i) the rate of number emission R_{ν_i}, which stands for the average number of neutrinos emitted per unit volume per unit time, and (ii) the rate of enery emission Q_{ν_i}, defined as the average energy emitted (in ergs) through neutrinos per unit volume per unit time. In the following sections, we describe these quantites for the different regimes in more detail.

4.1.3.1 Diffusive regime

The neutrino optical depths, which are important to determine the diffusive rates, are derived under the assumption that neutrinos escape along radial paths from the center, based on the ray-by-ray approach. Before describing theses diffusive rates, we first highlight the details of the opacity sources and the respective cross-sections below.

- **Neutrino-nucleon/nuclei scattering:** The first source of opacity is provided by the scattering of each neutrino species on nucleons (i.e., protons or neutrons). For the scattering reaction, $\nu_i + \{n, p\} \rightarrow \nu_i + \{n, p\}$, the interaction cross-section is given by [163]

$$\sigma_{\nu_i,\mathrm{nuc}} = \frac{1}{4} \sigma_0 \left(\frac{E_{\nu_i}}{m_e c^2} \right)^2 \ , \tag{4.16}$$

where $\sigma_0 = \frac{4 G_F^2 \left(m_e c^2\right)^2}{\pi (\hbar c^4)} \sim 1.705 \times 10^{-44}$ cm^2, and the corresponding opacity is written as

$$\kappa_{\nu_i,\{p,n\}} = X_{\{p,n\}} N_A \rho \sigma_{\nu_i,\mathrm{nuc}} \ , \tag{4.17}$$

[2] We remark that this approximation on energy distribution is made in order to avoid large computational costs, and schemes that adopt this approximation are often referred to as *gray* schemes.

where $X_{\{p,n\}}$ is the nucleon mass fraction. Similarly, neutrinos are also scattered by nuclei with the process, $\nu_i + \{A, Z\} \rightarrow \nu_i + \{A, Z\}$, having the cross section

$$\sigma_{\nu_i,\{A,Z\}} = \frac{1}{16}\sigma_0 \left(\frac{E_{\nu_i}}{m_e c^2}\right)^2 A^2 (1 - \frac{Z}{A})^2 \ , \tag{4.18}$$

where A and Z are the average heavy nucleus mass and atomic numbers respectively.

- **Neutrino-nucleon absorption:** Instead of scattering, electron and anti-electron neutrinos can get captured by the nucleons via processes, $\nu_e + n \rightarrow p + e^-$ and $\bar{\nu}_e + n \rightarrow p + e^+$, thus generating more electrons and positrons respectively. Their absorption cross-sections are given as

$$\sigma_{\nu_e,n} = \frac{1 + 3\alpha^2}{4}\sigma_0 \left(\frac{E_{\nu_i}}{m_e c^2}\right)^2 \langle 1 - f_{e^-} \rangle \ , \tag{4.19}$$

$$\sigma_{\bar{\nu}_e,p} = \frac{1 + 3\alpha^2}{4}\sigma_0 \left(\frac{E_{\nu_i}}{m_e c^2}\right)^2 \langle 1 - f_{e^+} \rangle \ , \tag{4.20}$$

where $\langle 1 - f_{e^\mp} \rangle \sim [\exp(\pm\eta_e - F_5(\pm\eta_{\nu_e})/F_4(\pm\eta_{\nu_e})) + 1]^{-1}$, are the so called fermion blocking factors, which take into account the availability of energy levels of the final states. Here, F_4 and F_5 are the Fermi integrals, defined in [164] as function of the neutrino chemical potential η, given by the general expression $F_n(\eta) \equiv \int \frac{x^n}{1+\exp(x-\eta)} dx$, which are usually computed numerically.

Using the above cross-sections, we can then compute the local spectral averaged opacity for each neutrino species as the sum of the opacities due to the scattering off nucleons, neutrino-nucleus scattering, and neutrino absorption by free nucleons (see [163] for more details). Using these mean opacities, the optical depths along each radial path are then derived. The averaged number and energy rates can then be written as [163]

$$\langle R^{\text{diff}}_{\nu_i} \rangle = \frac{4\pi c g_{\nu_i}}{(hc)^3} \frac{\zeta_{\nu_i}}{3\chi^2_{\nu_i}} T F_0(\eta_{\nu_i}) \ , \tag{4.21}$$

$$\langle Q^{\text{diff}}_{\nu_i} \rangle = \frac{4\pi c g_{\nu_i}}{(hc)^3} \frac{\zeta_{\nu_i}}{3\chi^2_{\nu_i}} T^2 F_1(\eta_{\nu_i}) \ , \tag{4.22}$$

where $i = 1, 2, 3$ and $\nu_1 = \nu_e$, $\nu_2 = \bar{\nu}_e$, $\nu_3 = \nu_x$, and the statistical weights are $g_{\nu_1} = g_{\nu_2} = 1$ and $g_{\nu_3} = 4$. Moreover, ζ_{ν_i} and χ are the non-energy dependent opacities and optical depth defined in Equations (4.13) and (4.14) respectively, with E the average neutrino energy (computed assuming a Fermi-Dirac distribution at the local temperature T). $F_0(\eta)$ and $F_1(\eta)$ are the Fermi integrals mentioned earlier.

4.1.3.2 Free-streaming regime

As mentioned earlier, in this regime, the produced neutrinos stream away freely, with no or minimal interations with the surrounding medium, thus carrying away their energy. Below we describe the implemented emission rates for the various processes in this regime.

- **Electron/positron capture:** This process produces only electron flavour neutrinos via the charged current capture reactions on nucleons. Particularly, these reactions are electron capture (EC), $e^- + p \rightarrow n + \nu_e$ and positron capture (PC), $p + e^+ \rightarrow n + \bar{\nu}_e$. Their emission rates are given as [163]

$$R_{EC} = \beta \eta_{pn} T^5 F_4(\eta_{\nu_e}) \ , \qquad Q_{EC} = \beta \eta_{pn} T^6 F_5(\eta_{\nu_e}) \ , \tag{4.23}$$

$$R_{PC} = \beta \eta_{np} T^5 F_4(\eta_{-\nu_e}) \ , \qquad Q_{PC} = \beta \eta_{np} T^6 F_5(\eta_{-\nu_e}) \ , \tag{4.24}$$

  where $\beta = \frac{\pi}{\hbar^3 c^2} \frac{1+3\alpha^2}{m_e c^2} \sigma_0$, $\eta_{pn} = \frac{n_n - n_p}{\exp(\hat{\mu}/T)-1}$, $\eta_{np} = -\eta_{pn}$, $\alpha \sim 1.25$, and $n_{\{n,p\}}$ are neutron and proton number densities.

- **Pair annihilation and plasmon decay:** This neutrino production channel which involving electron-positron annihilation, $e^- + e^+ \rightarrow \nu_i + \bar{\nu}_i$ and plasmon decay, $\gamma \rightarrow \nu_i + \bar{\nu}_i$, generates a pair of neutrino/antineutrino of every flavour. The detailed expressions of emission rates for these processes can be found in [162]. Here, we just highlight their dependence on temperature, which is given as

$$R_{ee}(\nu_i, \bar{\nu}_i) \propto T^8 \ , \qquad Q_{ee}(\nu_i, \bar{\nu}_i) \propto T^9 \ . \tag{4.25}$$

  The plasmon decay process also show the same above dependency on temperature.

- **Nucleon-nucleon Bremsstrahlung:** Through this channel, neutrinos are produced due to the interaction between two nucleons, $N + N \rightarrow N + N + \nu_i + \bar{\nu}_i$. Further details can be found in [165]. Again, here we just point out the dependency on temperature,

$$R_{\mathrm{Br}} \propto T^{5.5} \ , \qquad Q_{\mathrm{Br}} \propto T^{6.5} \ . \tag{4.26}$$

  Note that both nucleon-nucleon Bremsstrahlung rates and plasmon decay rates do not depend on the flavour of the produced neutrinos.

Finally, the actual *effective* emission rates are computed by combining the free emission and diffusive ones as follows

$$R^{\mathrm{eff}}_{\nu_i} = R^{\mathrm{free}}_{\nu_i} \left(1 + \frac{R^{\mathrm{free}}_{\nu_i}}{R^{\mathrm{diff}}_{\nu_i}} \right)^{-1} \ , \tag{4.27}$$

$$Q^{\mathrm{eff}}_{\nu_i} = Q^{\mathrm{free}}_{\nu_i} \left(1 + \frac{Q^{\mathrm{free}}_{\nu_i}}{Q^{\mathrm{diff}}_{\nu_i}} \right)^{-1} \ . \tag{4.28}$$

Using the above relations, the average neutrino energy is expressed as

$$E^{\mathrm{eff}}_{\nu_i} = \frac{Q^{\mathrm{eff}}_{\nu_i}}{R^{\mathrm{eff}}_{\nu_i}} \ . \tag{4.29}$$

For each of the three neutrino species, we can then evaluate the integrated luminosity. In particular, for a given radial direction (θ, ϕ), the isotropic-equivalent neutrino luminosity incoming from below at a distance r can be computed in the coordinate frame as

$$L^{\rm iso}_{\nu_i}(r,\theta,\phi) = 4\pi \int_0^r \left[\frac{\alpha(r',\theta,\phi)}{\alpha(r,\theta,\phi)}\right] Q^{\rm eff}_{\nu_i}(r',\theta,\phi)\alpha(r',\theta,\phi)W(r',\theta,\phi) \times [1+v^r(r',\theta,\phi)]\sqrt{g_{rr}(r',\theta,\phi)}r'^2 dr' \ , \tag{4.30}$$

where v^r is the radial velocity [3]. Here, we can also define a fluid rest frame (FRF) luminosity as

$$L^{\rm iso,FRF}_{\nu_i}(r) = \frac{L^{\rm iso}_{\nu_i}(r)}{\alpha(r)W(r)\left[1+v^r(r)\right]} \ . \tag{4.31}$$

4.1.3.3 Neutrino re-absorption

A fraction of neutrinos can undergo reabsorption by matter they encounter along their path (i.e. ν_e and $\bar{\nu}_e$ reabsorption on neutrons and protons, respectively) which eventually leads to heating as well as leptonization. This can be characterized via the local heating rate [161], given as

$$Q^{\rm heat}_{(\nu_e,\bar{\nu}_e)} = f_{\rm heat}\frac{L^{\rm iso,FRF}_{(\nu_e,\bar{\nu}_e)}}{4\pi r^2}\sigma^{\rm heat}_{(\nu_e,\bar{\nu}_e)}\frac{\rho}{m_{(n,p)}}X_{(n,p)}\left(4.275\tau_{(\nu_e,\bar{\nu}_e)}+1.15\right)e^{-2\tau_{(\nu_e,\bar{\nu}_e)}} \ , \tag{4.32}$$

where $f_{\rm heat}$ is a scaling factor of order one (we typically set $f_{\rm heat}=1$), $\sigma^{\rm heat}_{(\nu_e,\bar{\nu}_e)}$ is the reabsorption cross-section (see below), $m_{(n,p)}$ and $X_{(n,p)}$ are the neutron or proton masses and mass fractions, and the factor $e^{-2\tau_{(\nu_e,\bar{\nu}_e)}}$ is added to suppress heating at very large optical depths. And the following expression is adopted for the reabsorption cross-section [156]

$$\sigma^{\rm heat}_{(\nu_e,\bar{\nu}_e)} = \frac{1+3\alpha^2_{\rm EC}}{4}\sigma_0\frac{\langle E^2\rangle^{NS}_{(\nu_e,\bar{\nu}_e)}}{(m_e c^2)^2}\langle 1-f_{(e^-,e^+)}\rangle \ , \tag{4.33}$$

where $\alpha_{EC}=-1.25$, $\sigma_0 = 1.76\times10^{-44}\,{\rm cm}^2$, $\langle E^2\rangle^{NS}$ is the mean squared neutrino energy at the neutrinosphere, and $\langle 1-f_{(e^-,e^+)}\rangle$ are the blocking factors defined in [166].

At a given time, the full neutrino emission and reabsorption problem is solved along each radial direction by moving outwards from the center, and at each radius, we subtract the heating rates from the emission rates, i.e. $Q^{\rm eff}_{\nu_i} \to Q^{\rm eff}_{\nu_i} - Q^{\rm heat}_{\nu_i}$ and $R^{\rm eff}_{\nu_i} \to R^{\rm eff}_{\nu_i} - Q^{\rm heat}_{\nu_i}/\langle E\rangle^{NS}_{\nu_i}$, considering E_{ν_i} as the average neutrino energy at the neutrinosphere and $Q^{\rm heat}_{\nu_x}=0$.[4]

These results are then coupled with the GRMHD evolution, where the electron fraction Y_e and specific internal energy ϵ are updated as follows:

$$Y_e \to Y_e + \Delta t\frac{\partial Y_e}{\partial t} \ , \tag{4.34}$$

[3] We remark that in this expression, the time-of-flight of neutrinos is neglected. Here, neutrinos emitted at a given time and at different radial locations are collected together. However, this is only used in the region where neutrino reabsorption is relevant, and for instance, in the BNS or NSBH post-merger phase, the light travel time in such regions is much shorter than the timescale for a significant change in neutrino luminosities.

[4] As mentioned in [156], a self-consistent radiation transport treatment is necessary to have a perfect balance between emission and absorption. This is not provided by the present gray heating scheme.

where Δt the local time step, and the contribution of the aforementioned effective emission rates are included in the source term as

$$\frac{\partial Y_e}{\partial t} = \frac{R^{\rm eff}_{\bar{\nu}_e} - R^{\rm eff}_{\nu_e}}{\rho} m_n \,, \tag{4.35}$$

where m_n the rest-mass of the neutron. Similarly, for ϵ, we have

$$\epsilon \to \epsilon + \Delta t \frac{\partial \epsilon}{\partial t} \,, \tag{4.36}$$

and here too, we include the effective emission rates as

$$\frac{\partial \epsilon}{\partial t} = -\frac{\Sigma_i Q^{\rm eff}_{\nu_i}}{\rho} \,. \tag{4.37}$$

4.2 Numerical implementation

We recall that the `Spritz` code works with the Einstein Toolkit infrastructure. In Chapter 2, we described the numerical methods employed to solve the GRMHD equations. Here, we instead focus on the new additions to `Spritz` as presented in JVK5, which allow us to support the use of tabulated EOS, neutrino transport as well as higher order methods.

4.2.1 EOS driver

As already stated in Section 3.1.5, `Spritz` utilizes the `EOS_Omni` thorn provided in the Einstein Toolkit, which enables it to handle a large variety of EOS, including ideal fluid, polytropic, as well as tabulated 3-parameter ones.

Our first tests with `EOS_Omni` and tabulated EOS presented some limitations in dealing with such EOS. In particular, we noticed that for computing the temperature T from the specific internal energy ϵ, the thorn adopts a Newton-Raphson routine with a fall-back to a bisection routine in case of too many iterations, after the root is bracketed. This was not robust enough in cases when T weakly depends on ϵ, which may cause T to go out of the bounds (see [167]). We found this problem to occur especially when dealing with NS initial data which uses the lowest T available in the EOS table. Based on our suggestions, the `EOS_Omni` thorn was updated [168], now considering the fall-back to the more robust bisection scheme in such cases. In this way, we make sure that T is always contained in the range available in the EOS table. All our simulations presented in Section 4.3 use this new version of the `EOS_Omni` thorn.

4.2.2 Initial data

For computing the initial data of the NSs, the three-dimensional EOS tables should be reduced to one-dimension, which then provides pressure P is only a function of the rest-mass density ρ. To do this, we employ two constraints: (i) first, we assume matter to be in β-equilibrium (see Section 4.1.2.1), and (ii) we then apply the S-slicing or T-slicing condition (for details, see

Section 4.1.2.2. For this implementation, we wrote an algorithm which generates a 1D tabulated EOS starting from 3D ones in `.h5` format, like the ones provided in [41]. The produced 1D EOS can then be saved both in the `CompOSE` format [73] or in the `LORENE` format, both of which could be easily used with `LORENE` [169] library. The initial data used in JVK5 considers a single non-rotating NS (TOV), which was generated using the code `Nrotstar` of the `LORENE` library which can compute equilibrium solutions for non-rotating or uniformly rotating NSs. These solutions are non-magnetized, but a magnetic field can be easily added to the initial data. To read this initial data with `Spritz`, a new thorn was developed called `ID_Nrotstar` thorn to read initial data produced with `Nrotstar`, and import them in the Cartesian grid. To ensure the correct setting of β-equilibrium, an additional thorn was developed called `Spritz_SetBeta`, that performs a check at the first C2P routine execution to make sure that the code uses the same 1D EOS used to compute the initial data. After the initial data are correctly imported and conserved variables computed, the evolution starts and the full 3D EOS table is used.

Both `ID_Nrotstar` and `Spritz_SetBeta` thorns have been made publicly available as a part of the second `Spritz` code version [170].

4.2.3 1D Palenzuela C2P

The implementation of the conservative to primitive variable recovery schemes provided in the first version of the `Spritz` code (see Section 3.1.3) did not provide support when dealing with 3D tabulated EOS. In order to work with such EOS, we first implemented the 1D method C2P method presented in Palenzuela et al. [148], which is a modified version of the one already used in GRHD [167]. It consists of rewriting the conserved variables in the following way

$$q \equiv \frac{\tilde{\tau}}{D}, \quad r \equiv \frac{S^2}{D^2}, \quad s \equiv \frac{B^2}{D}, \quad t \equiv \frac{B_i S^i}{D^{\frac{3}{2}}} \ , \tag{4.38}$$

and proposes a master function $f(x)$ where $x \equiv hW$ is the independent variable. One then looks for the root of the equation $f(x) = 0$, where the master function is $f(x) = x - hW$. We do not go into the details of this algorithm and point the reader to [148] for more information. Here, we just point out that the Brent's method [171] is used for the root finding procedure, where the independent variable x should be properly bracketed, thus $x \in]x_{\rm L}, x_{\rm R}[$, with $f(x_{\rm L}) \cdot f(x_{\rm R}) < 0$. The left and right bounds can be defined in the following way (see [172]):

$$x_{\rm L} = 1 + q - s \ , \tag{4.39}$$

$$x_{\rm R} = 2 + 2q - s \ . \tag{4.40}$$

If no consistent bound is found, then the point is set to atmosphere (see Section 3.1.4). Additionally, the temperature is set to the minimum value in the table, whereas Y_e is set to 0.5.

However, in order to perform simulations where the initial temperature T is forced to be constant, the aforementioned 1D C2P scheme could not be used in such cases. Constraining the initial temperature could be useful to avoid spurious neutrino production in particular scenarios, e.g. during BNS inspiral (for some examples, see [173–175]) or when evolving a single cold NS (that may undergo a sharp initial rise of temperature due to numerical readjustment

of the initial data given by the solution of the TOV equations). Therefore, we implemented a modified version of the `3eqs` method (see Section 3.1.3.2 and [90] for details), where the $\tilde{\tau}$ variable is not used in computing the primitive variables. Particularly, we refer to Equation (45) of [90], defining the function

$$f\left(W_{\rm guess}\right) \equiv S^2 - \left[\left(\hat{Z}+B^2\right)^2 \frac{W_{\rm guess}^2-1}{W_{\rm guess}^2} - \frac{2\hat{Z}+B^2}{\hat{Z}^2}\left(B^i S_i\right)^2\right] , \tag{4.41}$$

where we have

$$\hat{Z} = W_{\rm guess}^2\left(\hat{\rho}+\hat{\rho}\hat{\epsilon}+\hat{P}\right) , \tag{4.42}$$

and $\hat{\rho} = \frac{D}{W_{\rm guess}}$, while $\hat{P}$ and $\hat{\epsilon}$ can be computed via the EOS using $\hat{\rho}$ and the constrained value of T. The algorithm workflow can be described as follows:

(i) the initial guess for the solution is assumed to be $W_{\rm guess} \in [1.0, 1.5]$, which corresponds to assuming $v \in [0.0, 0.75c]$

(ii) $\hat{\rho}$, $\hat{P}$, $\hat{\epsilon}$, and $\hat{Z}$ are computed using the EOS with the constrained value of T and the conserved variables

(iii) if, when using Equation (4.41), $f(1)\cdot f(1.5) > 0$, the point is actually set to the atmosphere

(iv) finally, the Brent's method [171] is applied to the function f defined in Equation (4.41).

The above steps are iterated until convergence. After finding the final root for W, recovery of the other primitive variables is straightforward. Note that we use Equation (45) and not Equation (46) of [90] when forcing the temperature to be constant. Therefore, we also need to update the value of $\tilde{\tau}$ after each C2P step in order to guarantee consistency between primitive and conservative variables. This is similar to what is done in other codes when using a cold EOS during the evolution.

4.2.4 Neutrino leakage

As mentioned earlier, our implementation of the neutrino leakage scheme described in Section 4.1.3 is based on the thorn `ZelmaniLeak` available on the `stellarcollapse` website [41], and firstly presented in [156]. In particular, we employ version `20161117` of this thorn. This particular version of `ZelmaniLeak` uses all the cross-sections, emission and heating rates described in Section 4.1.3. These cannot be modified by the user unless the code itself is changed. However, one can choose whether to activate neutrino emission or not. There is also a possibility to activate neutrino emission during the evolution, if not since the beginning. Moreover, one can also choose whether to activate the effect of neutrino heating (reabsorption) or not. Also, the user can freely set the number of radii across which the optical depth is to be computed.

4.2.5 Higher order methods

In the second version of `Spritz` as presented in JVK5, we also implemented high-order (HO) schemes in order to further improvise on the accuracy of the code.

4.2.5.1 Reconstruction step: WENOZ method

In order to implement a high-order scheme, we first need to choose the right reconstruction method. Here, we consider the fifth-order WENOZ algorithm [176]. In what follows, we will consider only one dimension without loss of generality: the multi-dimensional scheme is simply retrieved by considering the fluxes in each direction separately.

The fifth-order WENO scheme works with a 5-points stencil, represented by S^5, which is subdivided into three 3-points substencils, $\{S^0, S^1, S^2\}$. The polynomial approximation $f_{i+1/2}$, which is the reconstruction of the grid function f_i on the left side of the cell-interface[5], is computed via the following convex combination of the interpolated values $f^k_{i+1/2}$, that are third degree polynomials defined on each substencil S^k, $k = 0, 1, 2$:

$$f_{i+1/2} = \sum_{k=0}^{2} \omega_k f^k_{i+1/2} \ . \tag{4.43}$$

The polynomial on each substencil is given by the quadratic interpolations

$$f^0_{i+1/2} = \frac{1}{8}\left(3f_{i-2} - 10f_{i-1} + 15f_i\right) \ , \tag{4.44}$$

$$f^1_{i+1/2} = \frac{1}{8}\left(-f_{i-1} + 6f_i + 3f_{i+1}\right) \ , \tag{4.45}$$

$$f^2_{i+1/2} = \frac{1}{8}\left(3f_i + 6f_{i+1} - f_{i+2}\right) \ . \tag{4.46}$$

The weights ω_k are defined as

$$\omega_k = \frac{\alpha_k}{\sum_{j=0}^{2} \alpha_j} \ . \tag{4.47}$$

For WENOZ, the unnormalized weights α_k are given by

$$\alpha_k = d_k \left(1 + \frac{|\beta_0 - \beta_2|}{\beta_k + \epsilon}\right) \ , \tag{4.48}$$

with $\epsilon = 10^{-26}$ (to avoid a possible division by zero), and $d_k = (1/16, 10/16, 5/16)$ are the optimal weights corresponding to the weights obtained for smooth fields along with smoothness indicators, which are

$$\beta_0 = \frac{13}{12}\left(f_{i-2} - 2f_{i-1} + f_i\right)^2 + \frac{1}{4}\left(f_{i-2} - 4f_{i-1} + 3f_i\right)^2 \ , \tag{4.49}$$

$$\beta_1 = \frac{13}{12}\left(f_{i-1} - 2f_i + f_{i+1}\right)^2 + \frac{1}{4}\left(f_{i-1} - f_{i+1}\right)^2 \ , \tag{4.50}$$

$$\beta_2 = \frac{13}{12}\left(f_i - 2f_{i+1} + f_{i+2}\right)^2 + \frac{1}{4}\left(3f_i - 4f_{i+1} + f_{i+2}\right)^2 \ , \tag{4.51}$$

that measure the regularity of the k-th polynomial approximation f^k_i at the stencil S^k.

[5] $f_{i-1/2}$ is simply given by swapping the indices of the stencil: $(i-2, i-1, i, i+1, i+2) \to (i+2, i+1, i, i-1, i-2)$

Table 4.1: Coefficients of the flux function approximation $\hat{f}_{j+1/2}$.

n	d_0	d_2	d_4
2	1	0	0
4	13/12	-1/24	0
6	1067/960	-29/480	3/640

We remark that the coefficients in Equations (4.44)-(4.46) and the optimal weights d_k are taken from [177], which differ from the ones in the original work [176], because we noticed that they are better-suited for this high order scheme in combination with the derivation operation which we describe next.

4.2.5.2 Derivation operation

The derivation operation is a high-order procedure applied to obtain a high order approximation from the point value quantities calculated at the intercell location. This step is performed right after the flux computations via an approximate Riemann solver. And when employing this method, one needs to ensure that the accuracy of the spatial derivative calculations is preserved for schemes with order $n > 2$. Here too, we restrict the discussion to one dimension. The steps described below follow the one outlined in the `ECHO` paper [177]. Using these steps, we will compute the numerical flux function $\hat{f}_{i+1/2}$, given a stencil of intercell fluxes $\{f_{i+1/2}\}$.

The finite difference approximation of the first derivative at the point x_i can be written as

$$\begin{aligned} hf'(x_i) &\approx \hat{f}_{i+1/2} - \hat{f}_{i-1/2} \\ &= a(f_{i+1/2} - f_{i-1/2}) + b(f_{i+3/2} - f_{i-3/2}) + c(f_{i+5/2} - f_{i-5/2}) \ , \end{aligned} \tag{4.52}$$

where the approximation has been truncated at sixth-order, and h denotes the constant grid-spacing. Expanding both sides of the equation in Taylor series around x_i, we get

$$hf_i^{(1)} = \sum_{k=0}^{+\infty} f_i^{(k)} \frac{h^k}{k!2^k} \left[1 - (-1)^k\right] \left[a + 3^k b + 5^k c\right] \ , \tag{4.53}$$

where the corresponding order of derivation is indicated by the exponents, and the first derivative has been rewritten as $f_i^{(1)} \equiv f'(x_i)$. Here, all terms with even k vanish. For $n = 2$, where $b = c = 0$, we get $a = 1$. For $n = 4$, where $c = 0$, we find $a = 9/8$ and $b = -1/24$. Finally, for $n = 6$, the solution is $a = 75/64$, $b = -25/384$, $c = 3/640$. The next step is to write

$$\hat{f}_{i+1/2} = d_0 f_{i+1/2} + d_2(f_{i-1/2} + f_{i+3/2}) + d_4(f_{i-3/2} + f_{i+5/2}) \ . \tag{4.54}$$

Comparing this with Equation (4.53) yields the relations $d_0 = a + b + c$, $d_2 = b + c$, $d_4 = c$. The numerical values of d_0, d_2, and d_4 for the different order of approximation are given in Table 4.1. Note that for $n = 2$, one recovers $\hat{f}_{i+1/2} = f_{i+1/2}$ as expected.

This procedure essentially acts as a correction for higher than second order approximation, and in this sense, we can rewrite Equation (4.54) as

$$\hat{f}_{i+1/2} = f_{i+1/2} - \frac{1}{24}\Delta^{(2)} f_{i+1/2} + \frac{3}{640}\Delta^{(4)} f_{i+1/2} \ , \tag{4.55}$$

where only the first term is used in the case $n = 2$, the second is added for $n = 4$, and the entire expression is used for $n = 6$. For a generic index i, the second and fourth order numerical derivatives are given by

$$\Delta^{(2)} f_i = f_{i-1} - 2f_i + f_{i+1} \ , \tag{4.56}$$

and

$$\begin{aligned} \Delta^{(4)} f_i &= \Delta^{(2)} f_{i-1} - 2\Delta^{(2)} f_i + \Delta^{(2)} f_{i+1} \\ &= f_{i-2} - 4f_{i-1} + 6f_i - 4f_{i+1} + f_{i+2} \ , \end{aligned} \tag{4.57}$$

respectively.

4.3 Test results

Here, we report a number of tests (presented in JVK5) that were performed for validating the new additions to `Spritz`, focussing mainly on testing the neutrino leakage scheme and the higher-order methods. For almost all the tests presented, our reference physical system is a stable non-rotating NS (TOV). In particular, we consider a NS with mass $1.68\,\mathrm{M}_\odot$ and LS220 EOS [178], which corresponds to a coordinate radius of about 9.7 km (and the corresponding circumferential radius slightly above 12 km). Its initial data is produced using the `Lorene/Nrotstar` code, as discussed previously in Section 4.2.2. For tests involving NSs, we consider both magnetized and non-magnetized cases. For the latter, we initially add a purely poloidal magnetic field using the vector potential prescription for A_ϕ given by Equation (3.33), and the magnetic field remains initially confined within the NS because of our use of the ideal MHD approximation. The value of A_b is set such that the initial maximum magnetic field strength is set to 10^{16} G. This corresponds to the largest order of magnitude for a magnetic field that can be added to a TOV solution without introducing significant violations in the constraints of Einstein's equations. Significantly larger magnetic fields would indeed affect the structure of the star and therefore, TOV equations would not be applicable [179]. The initial and final magnetic field distribution imposed in our NS tests is depicted in Figure 4.1. All NS simulations employ AMR, utilizing 5 refinement levels. The outermost domain boundary extends to ≈ 193 km in every direction, while the innermost refinement level goes up to 13 km. The finest grid resolution used is $dx \approx 177$ m and the grid spacing is increased by a factor of two going from a refinement level to the next. The entire NS is contained within the most refined region and the NS radius is covered with about 60 points. Magnetized simulations are performed in full 3D domain, while non-magnetized simulations employ octant symmetry with reflection symmetry conditions across the $x = 0$, $y = 0$, and $z = 0$ planes. In all NS simulations, the outer boundary condition is set to 'none' for the hydro variables (i.e., values are

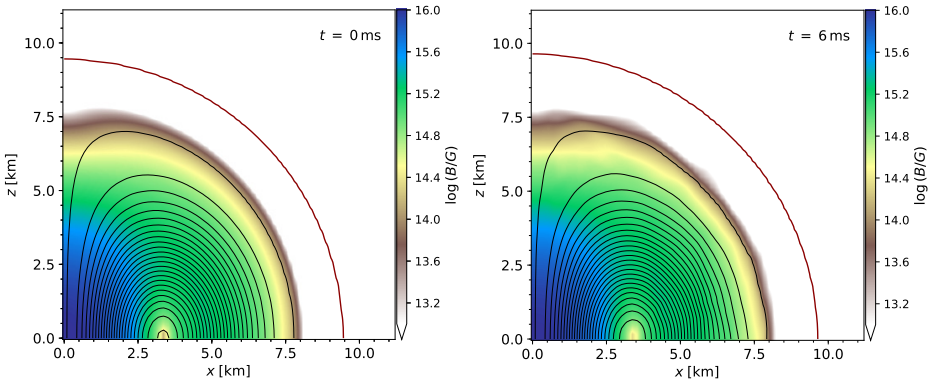

Figure 4.1: Left panel: initial magnetic field setup for simulations 13 and 14 (see Table 4.3). Black lines represent isocontours of the ϕ-component of the vector potential, while the red line is a density contour corresponding to $\rho \simeq 3 \times 10^{12}\,\mathrm{g/cm^3}$. Right panel: as in the left panel but at the end of simulation 16. Figure taken from JVK5.

Table 4.2: Initial Data used for the unmagnetised ($B = 0$) tests.

ID	Test Name	β-eq. Initial Data	ν Leakage	T evolution
01	`Spr_S_NL_NB_3D`	S-slice $1k_b$/bar	Disabled	Yes
02	`GRH_S_NL_NB`	S-slice $1k_b$/bar	Disabled	Yes
03	`Spr_S_NL_NB`	S-slice $1k_b$/bar	Disabled	Yes
04	`Spr_S_YL_NB_3D`	S-slice $1k_b$/bar	Enabled	Yes
05	`GRH_S_YL_NB`	S-slice $1k_b$/bar	Enabled	Yes
06	`Spr_S_YL_NB`	S-slice $1k_b$/bar	Enabled	Yes
07	`GRH_T_NL_NB`	T-slice 0.01 MeV	Disabled	Yes
08	`Spr_T_NL_NB`	T-slice 0.01 MeV	Disabled	Yes
09	`Spr_T1_NL_NB`	T-slice 0.01 MeV	Disabled	Yes (after $t = 2$ms)
10	`GRH_T_YL_NB`	T-slice 0.01 MeV	Enabled	Yes
11	`Spr_T_YL_NB`	T-slice 0.01 MeV	Enabled	Yes
12	`Spr_T1_YL_NB`	T-slice 0.01 MeV	Enabled (at $t = 3$ms)	Yes (after $t = 2$ms)

kept fixed to their initial one), linear extrapolation for the vector and scalar potential JVK2, and radiative boundary conditions are applied for the metric variables [93]. For the ray-by-ray calculations of the neutrino leakage scheme, we use 9 independent directions in θ and 16 in ϕ for full 3D simulations, while for cases using octant symmetry, these numbers are rescaled accordingly (i.e. 5 independent directions in both θ and ϕ).

Tables 4.2 and 4.3 summarize the number of NS tests performed, referring to non-magnetized and magnetized cases, respectively. All the simulations use `MacLachlan` thorn to evolve the spacetime in the BSSNOK formalism, and cover about 6 ms of evolution. This timescale cor-

Table 4.3: Initial Data used for the magnetized ($B \sim 10^{16}$G) tests.

ID	Test Name	β-eq. Initial Data	ν Leakage	T evolution
13	`Spr_S_NL_YB`	S-slice $1k_b$/bar	Disabled	Yes
14	`Spr_S_YL_YB`	S-slice $1k_b$/bar	Enabled	Yes
15	`Spr_T1_NL_YB`	T-slice 0.01 MeV	Disabled	Yes (after $t = 2$ms)
16	`Spr_T1_YL_YB`	T-slice 0.01 MeV	Enabled (at $t = 3$ms)	Yes (after $t = 2$ms)

responds to ~ 14 dynamical timescales, and therefore allows us to study these systems for a sufficiently long time without requiring too much computational resources. We stop these simulations manually after ~ 6 ms, and no sign of instability or numerical problem were present at the final time. In the following, we first discuss the results without neutrino leakage, testing the implementation of the tabulated EOS handling, and then those with neutrino leakage, with and without neutrino heating. Then, we also present a few tests using the higher-order schemes.

For the NS tests, we also compute the total neutrino luminosity of each neutrino species in cartesian coordinates as

$$L^{\infty}_{\nu_i} = \int_0^{\infty}\int_0^{\infty}\int_0^{\infty} Q^{\rm eff}_{\nu_i}(x',y',z') \left[\alpha^2(x',y',z')W(x',y',z') \times (1+v^r(x',y',z'))\right] \sqrt{\gamma} dx' dy' dz' \ , \tag{4.58}$$

where $v^r = (xv^x + yv^y + zv^z)/\sqrt{x^2+y^2+z^2}$.

4.3.1 Testing tabulated EOS without neutrino leakage

In order to check the implementation of the tabulated EOS handling, we here report the results of all NS simulations performed without enabling the leakage scheme, starting from either S-slicing or T-slicing initial data.

Figure 4.2 shows the results for the evolution of the maximum of ρ and T when using the S-slicing initial condition. In these models, the maximum initial temperature is located at the NS centre which does not increase more than 1% by the end of the simulation. Also, the figure shows exact matching curves for simulations 01, 02, 03, and 13, as expected (see Table 4.2 and 4.3). For a comparison study, pure-hydro simulations 02 and 03 which employ octant symmetry and are performed with the `GRHydro` and the `Spritz` codes respectively, produce the same results as adopting full-3D in simulations 01 and 13. Furthermore, the magnetic field evolution in simulation 13 is correctly handled and does not significant impact on the hydrodynamic quantities as expected (we remind that, even if large, a magnetic field of $\sim 10^{16}$ G provides a magnetic energy which is still ~ 2 orders of magnitude below equipartition). Figures 4.3 and 4.4 show similar comparison for tests starting with T-slicing initial condition. Here, the maximum of T is located near the NS surface. Simulations 09 and 15 are the most delicate to handle, since the temperature T is fixed to be constant for the first ~ 2 ms and only then allowed to evolve. When temperature evolution begins, an artificial shock is generated at the NS surface in the

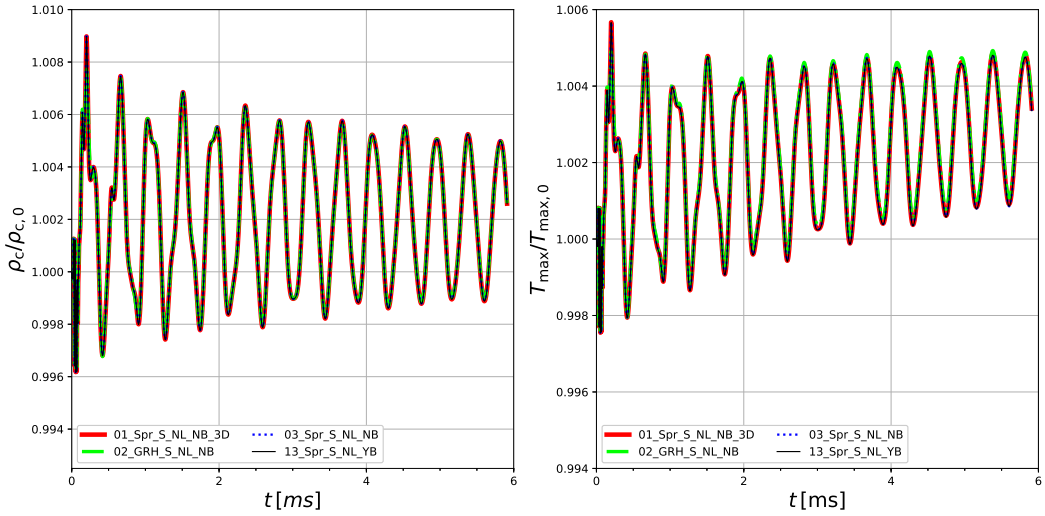

Figure 4.2: Evolution of TOV with the S-slicing condition and without neutrinos. The left panel depicts the evolution of the maximum rest-mass density normalized to its initial value, whereas the right panel is the equivalent for the maximum temperature (which is located at the NS centre). Figure taken from JVK5.

initial transient phase, however later on, the temperature evolution tends to a constant value, whereas the evolution of maximum of ρ follows closely the results given by the simulations 07 and 08, where T is evolved since the beginning. Additionally, Figure 4.4 provides perfect match between the pure-hydro simulation 09 and the magnetized simulation 15. The above results give us the confidence that the handling of the tabulated EOS has been correctly implemented, and allows us to proceed further with testing of the neutrino leakage scheme implementation.

4.3.2 Testing neutrino leakage

In this section, we discuss the results of simulations starting with either constant S or T initial data and involving neutrino leakage, reporting also the total neutrino luminosity evolution for each neutrino species, computed using Equation (4.58). We first present the results of tests performed without the heating (reabsorption), and then also including its contribution based on Equation (4.32).

4.3.2.1 Tests without neutrino heating

In Figure 4.5, we compare the tests evolving S-slicing initial data with neutrino leakage, but without neutrino reabsorption. Top panels show the usual evolution of the maxima of ρ and T normalized to their initial values, whereas the bottom panels show the evolution of neutrino luminosity of each species (electron neutrinos, electron antineutrinos, and the combined contri-

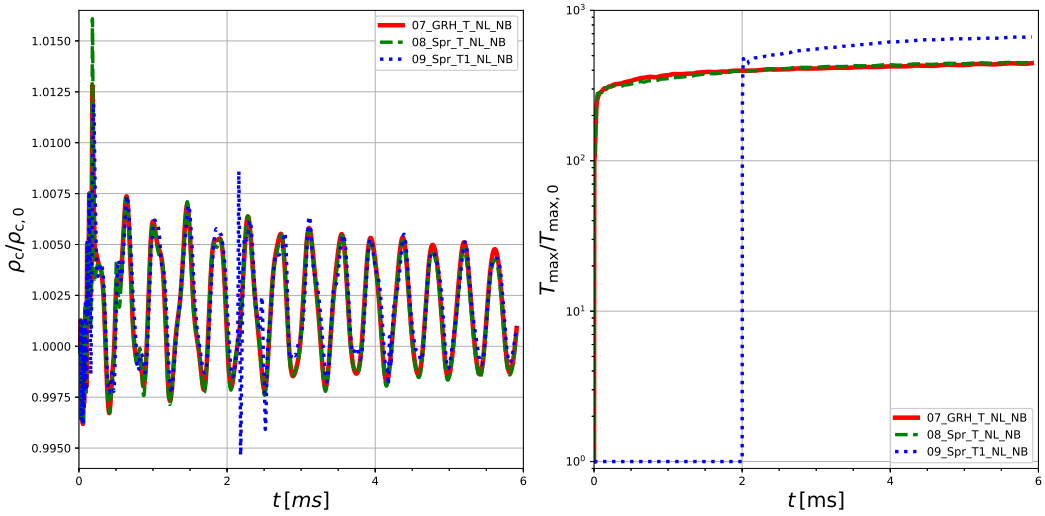

Figure 4.3: Same as Figure 4.2 but for T-slicing condition. For simulation 09, temperature evolution is activated only after 2 ms. Figure taken from JVK5.

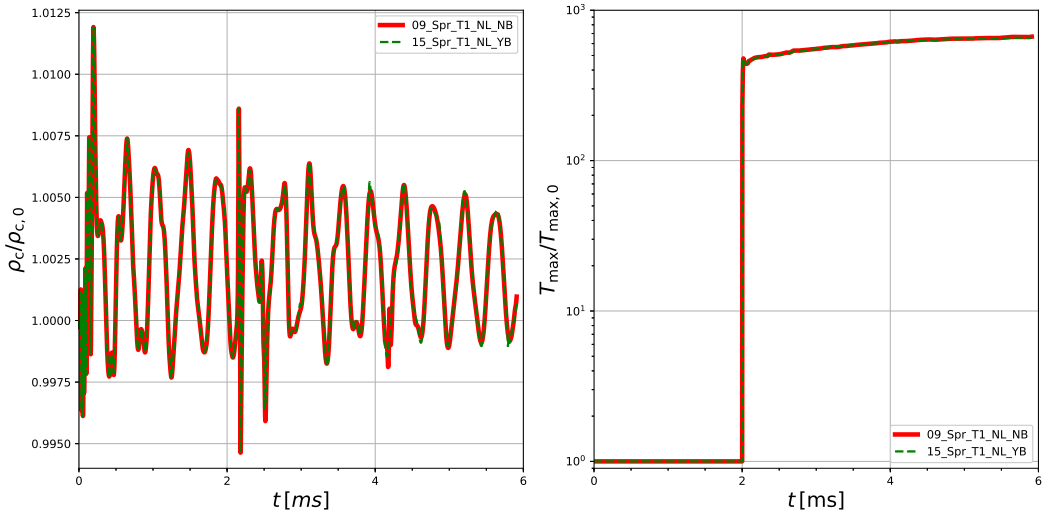

Figure 4.4: Comparison of non-magnetized and magnetized test results for T-slicing condition. In both cases, the temperature evolution is activated only after 2 ms. Figure taken from JVK5.

bution of μ and τ neutrinos and antineutrinos). Particularly, the luminosity plots demonstrate that the scenario is clearly dominated by electron capture. Here too, the maximum temperature (located at the NS center), shows an increase of less than 1%. Neutrino cooling is not effective near the stellar center which are high density regions (and thus associated with high optical

depths), and therefore, temperature evolution in such regions remains unaffected. Similarly, we

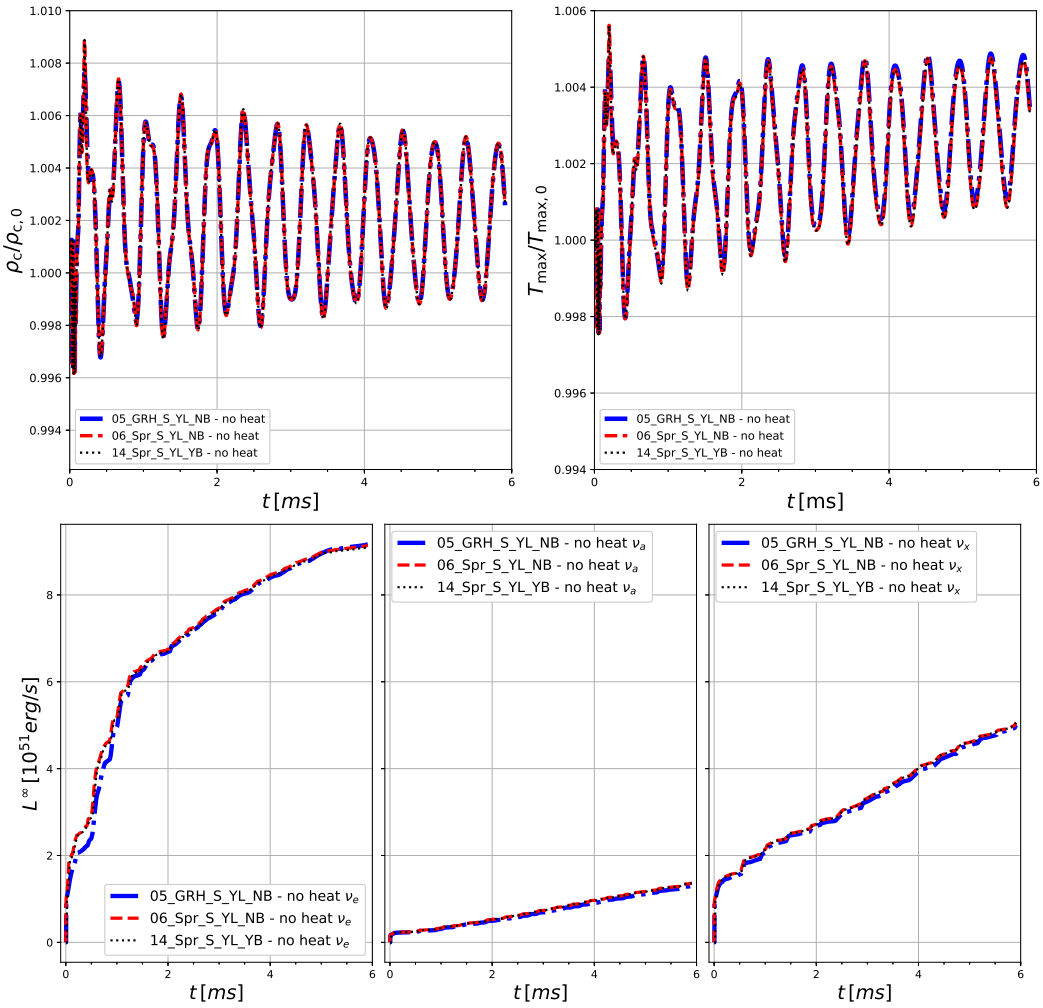

Figure 4.5: *Top panels:* Same as Figure 4.2 for S-slicing simulations now considering neutrino leakage but no heating. *Bottom panels:* Evolution of neutrino luminosities for the different neutrino species (from left to right: ν_e, $\bar{\nu}_e$ indicated here as ν_a, and ν_x). Figure taken from JVK5.

compare the results for tests starting with T-slicing initial data as shown in Figure 4.6. In this case, the maximum of the temperature is located on the NS surface and thus gets affected by any artificial shocks that develop in that region. Despite minor differences due to the different implementations in the `GRHydro` and `Spritz` codes, the results appear in good agreement.

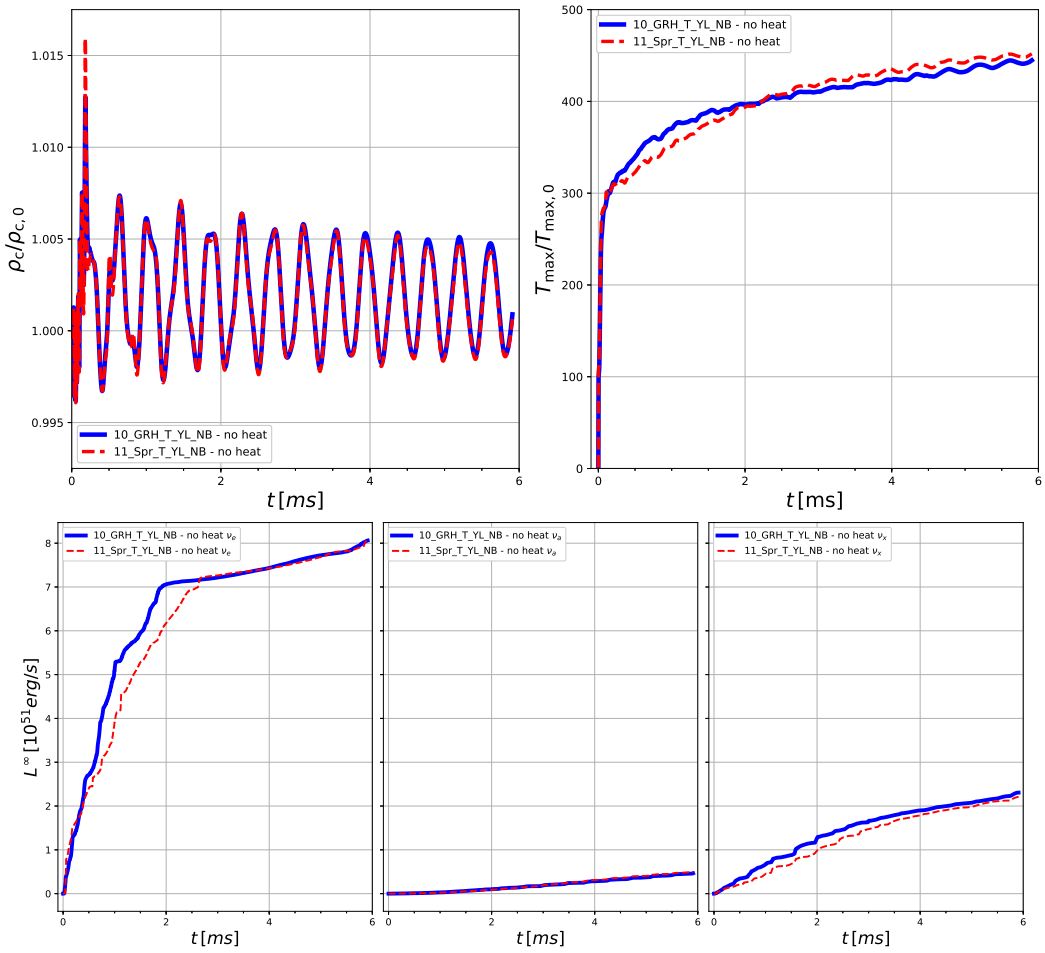

Figure 4.6: Same as Figure 4.5 but for T-slicing simulations 10 and 11, performed with `GRHydro` and `Spritz` respectively. Figure taken from JVK5.

4.3.2.2 Tests including neutrino heating

Here, we investigate how the heating contribution could alter the results of simulations. Figures 4.7 and 4.8 show the comparison between simulations with and without neutrino heating, starting with S-slicing and T-slicing initial conditions respectively. As already seen in Figure 4.3, here too, a sharp transient for the maximum of T is produced when starting with a cold initial data in the first few time steps (likely located at the NS surface for the T-slicing condition), where the NS internal temperature undergoes a re-adjustment (likely due to the production of shocks at the NS surface). This transition can affect neutrino leakage since it may produce luminosities much larger than expected. Furthermore, we recall that the heating rate given by Equation 4.32 is not self-consistent in terms of energy balance (see also Section

4.1.3.3). Therefore, when considering the heating contribution (Figure 4.8), we activated the leakage 1 ms later in order to avoid the initial transient. Figure 4.9 ilustrates results for

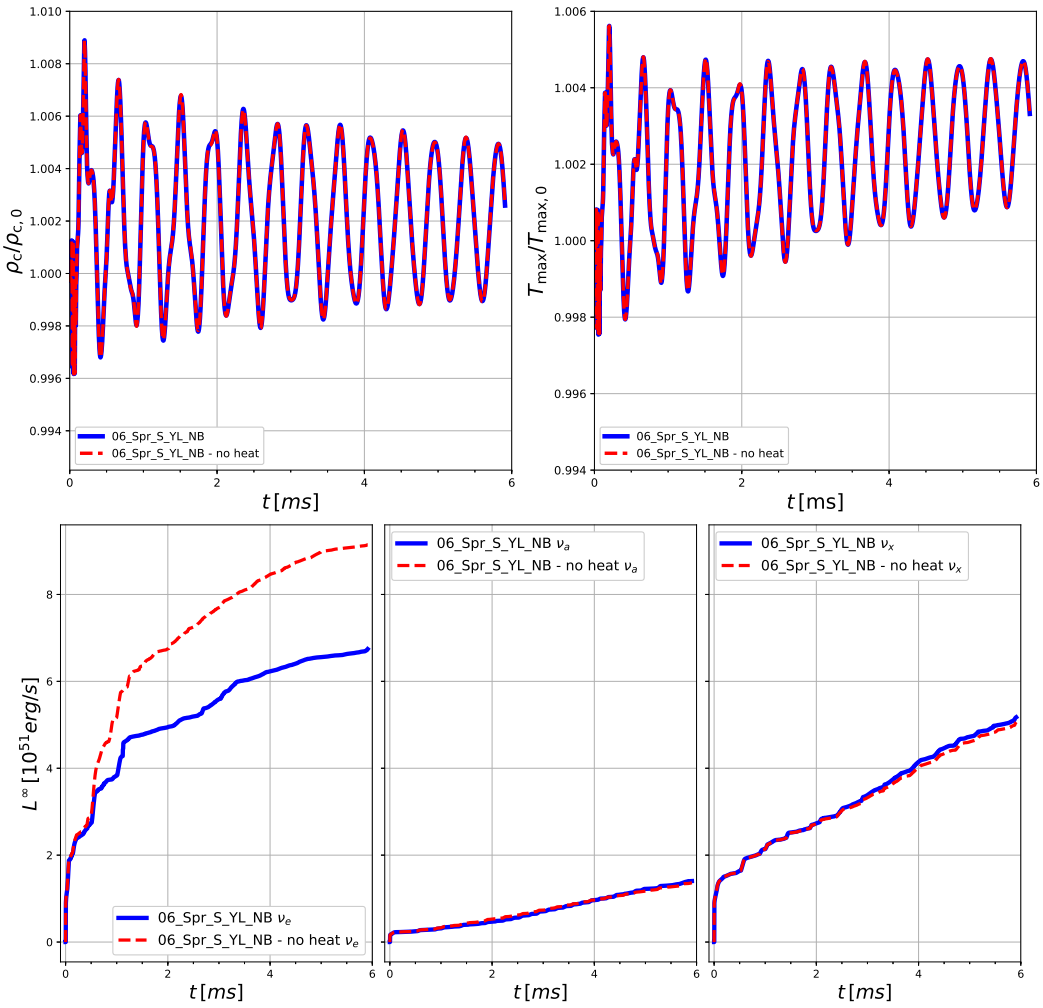

Figure 4.7: Same as Figure 4.5 but for the simulation 06 including leakage, with and without the heating contribution. Figure taken from JVK5.

S-slicing initial condition and neutrino leakage including heating. In this case, since there is no initial temperature readjustment, the heating contribution can already be activated since the beginning and not after some time. Furthermore, in Figure 4.10, we show the evolution of the maximum of magnetic field strength for the magnetized cases 13 (without leakage) and 14 (with leakage and the heating contribution), finding exactly matching curves, which suggests that neutrino leakage and heating has negligible impact on the magnetic field (and vice versa)

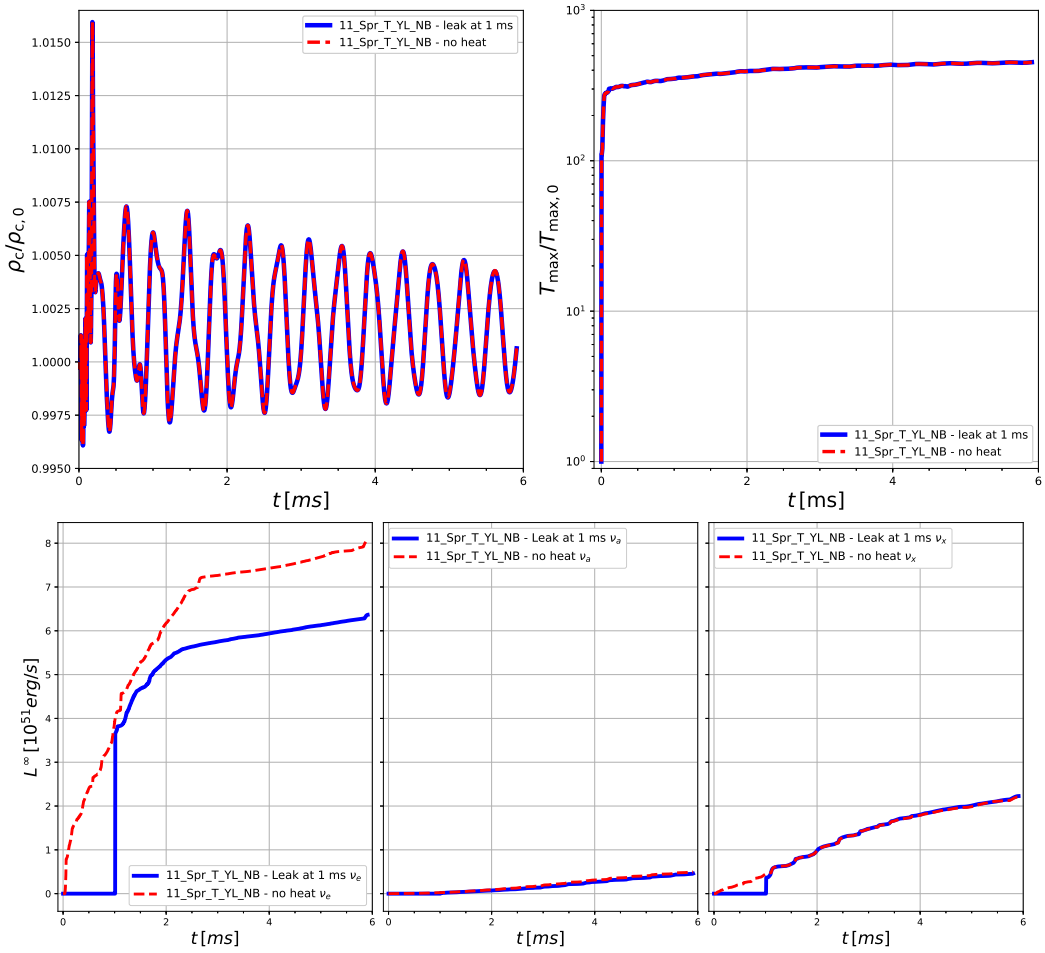

Figure 4.8: Same as Figure 4.5 but for the simulation 10 including leakage, with and without the heating contribution. When heating is considered (blue solid curve), neutrino leakage is switched on at $t = 1\,\text{ms}$ to avoid spurious effects due to the sharp initial jump in the maximum temperature. Figure taken from JVK5.

in such scenarios. Figure 4.11 compares the tests with cold NS initial data (T-slicing) and neutrino leakage including heating. For simulation 11, which considers temperature evolution since the beginning, the leakage is enabled only after 1 ms. Whereas, for simulations 12 and 16, where the temperature evolution starts only after 2 ms, we enable the leakage at 3 ms. Despite the differences in the activation times of temperature evolution and leakage, and in the presence or absence of magnetic fields, all the results show a very good agreement in the maximum rest-mass density and the late-time electron neutrino luminosities. Finally, in Figure 4.12, we look again at the maximum magnetic field evolution for simulations 15 and 16, finding per-

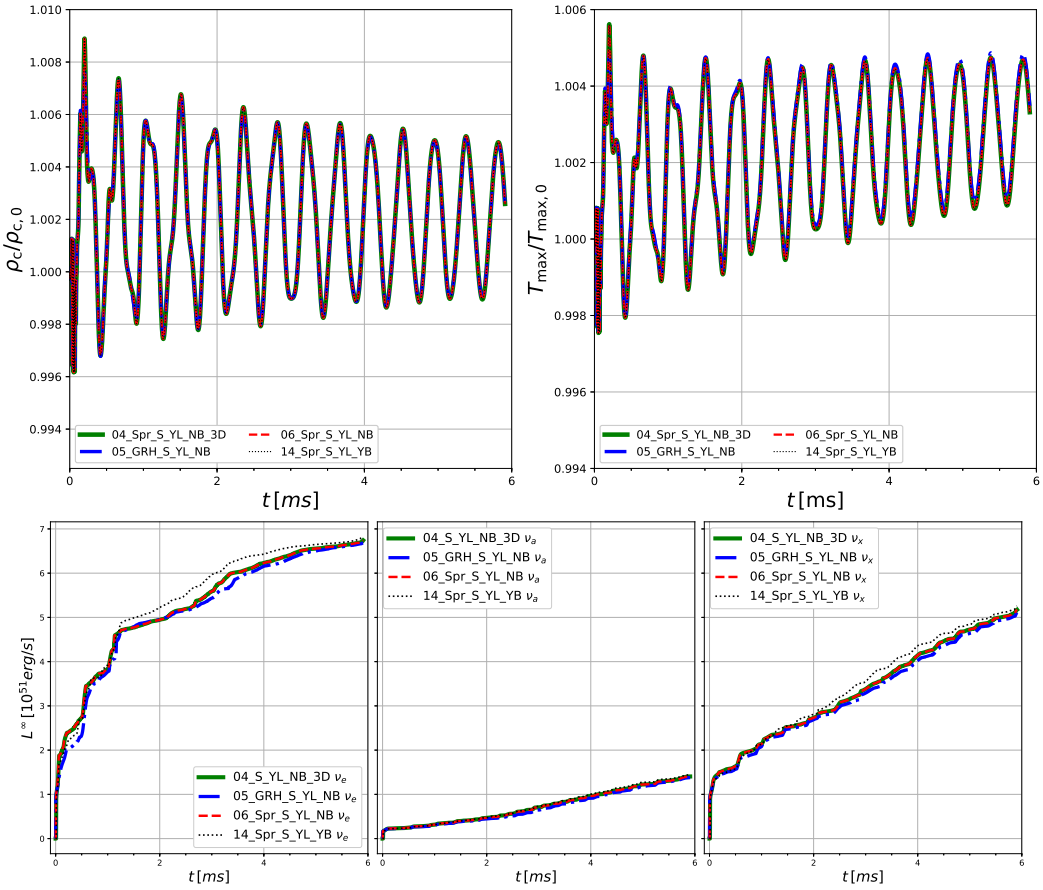

Figure 4.9: Same as Figure 4.5 but considering the neutrino heating contribution. Figure taken from JVK5.

fectly matching curves. In conclusion, all the 16 TOV simulations provide reasonable results, validating the numerical implementation of the neutrino leakage scheme, and that the code is ready to be used in more complex astrophysical scenarios, e.g., BNS/NSBH merger simulations including tabulated EOS, magnetic fields, and neutrino emission and absorption.

4.3.3 Testing higher-order schemes

After validating our implementation of the neutrino leakage scheme, we now focus on testing the implementation of higher-order methods.

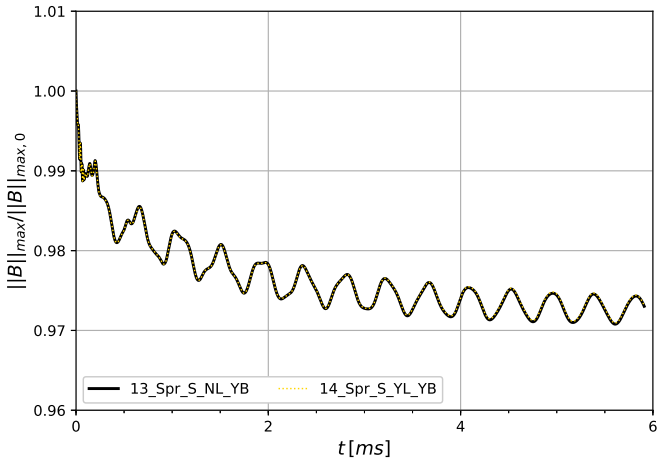

Figure 4.10: Comparison of evolution of $B_{\max}$ for tests performed with the S-slicing condition, with and without neutrino leakage and heating. Figure taken from JVK5.

4.3.3.1 Simple wave test

As a convergence test, we first consider the evolution of a relativistic simple wave [180, 181]. Particularly, we perform this test using WENOZ as the reconstruction method along with $n = 2, 4, 6$ correction to the HLLE Riemann solver (in the following, they are addressed as HLLE2, HLLE4, and HLLE6, respectively).

We set the initial data using the following conditions [182]: we choose a right-propagating simple wave with $\rho_0 = 1$ and $v_0 = 0$. Assuming a polytropic EOS with $\Gamma = 5/3$ and $K = 100$, we can compute the sound speed in the reference frame through

$$c_0^2 = \frac{K\Gamma(\Gamma-1)\rho_0^\Gamma}{(\Gamma-1)\rho_0 + K\Gamma\rho_0^\Gamma} \,, \tag{4.59}$$

obtaining $c_0 \approx 0.815$ for this specific case. Then, we perturb the velocity with a sin-like function, getting its profile as (see left panel of Figure 4.13, dashed line)

$$v = a\Theta(X - |x|)\sin^6\left[\frac{\pi}{2}\left(\frac{x}{X} - 1\right)\right] \,, \tag{4.60}$$

where $\Theta(x)$ is the Heaviside function, $a = 0.5$, and $X = 0.3$. Finally, the new sound speed is calculated according to the Riemann invariant [181]

$$c_s = \sqrt{\Gamma-1}\frac{\frac{\sqrt{\Gamma-1}+c_0}{\sqrt{\Gamma-1}-c_0}\left(\frac{1+v}{1-v}\right)^{\sqrt{\Gamma-1}/2} - 1}{\frac{\sqrt{\Gamma-1}+c_0}{\sqrt{\Gamma-1}-c_0}\left(\frac{1+v}{1-v}\right)^{\sqrt{\Gamma-1}/2} + 1} \,, \tag{4.61}$$

such that $c_s = c_0$ at $v = 0$, and $c_s \to \sqrt{\Gamma-1}$ as $v \to 1$. The other quantities can be computed

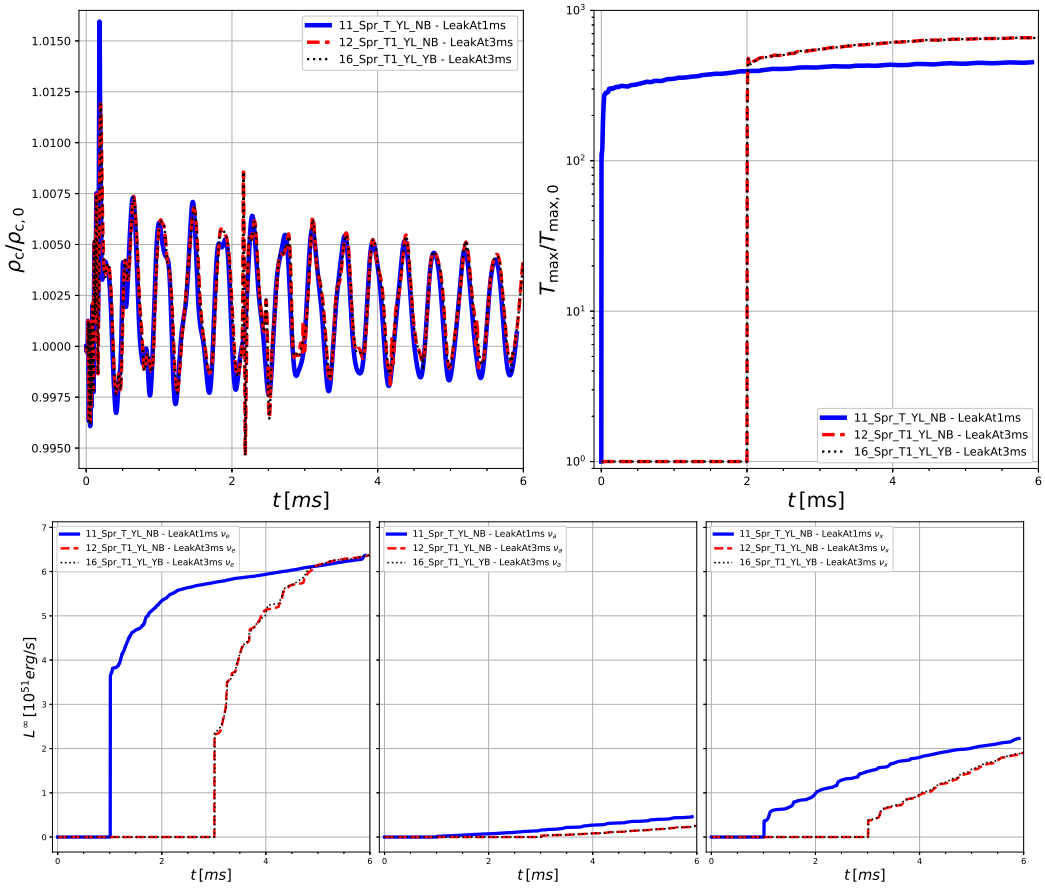

Figure 4.11: Same as Figure 4.5 but considering T-slicing cases with neutrino leakage and heating contribution, where leakage is activated 1 ms after temperature evolution is enabled (at $t = 0$ for model 11, at $t = 2$ ms for model 12, 16). Figure taken from JVK5.

from the EOS as follows:

$$\hat{\epsilon} = \frac{c_s^2}{\Gamma(\Gamma - 1 - c_s^2)}\,, \tag{4.62}$$

$$\hat{\rho} = \epsilon^{1/(\Gamma-1)}\,, \tag{4.63}$$

$$\hat{p} = \epsilon^{\Gamma/(\Gamma-1)}\,, \tag{4.64}$$

where $\hat{\epsilon}$, $\hat{\rho}$, and $\hat{p}$ stand for the specific internal energy, the density, and the pressure respectively. The tests are performed within a 1-dimensional domain $[-1.5, 1.5]$, employing RK4 integrator for HLLE2 and HLLE4, and RK65 for HLLE6[6], with a CFL factor of 0.125.

[6]We consider this choice to avoid a possible limitation on the order of convergence due to the Runge-Kutta

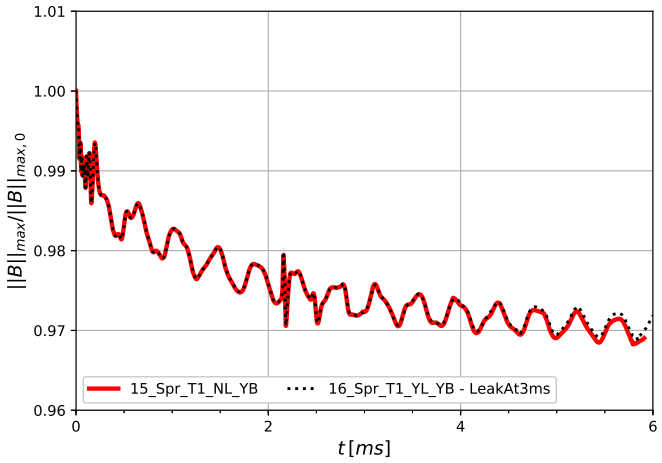

Figure 4.12: Same as Figure 4.10 but for T-slicing cases. Figure taken from JVK5.

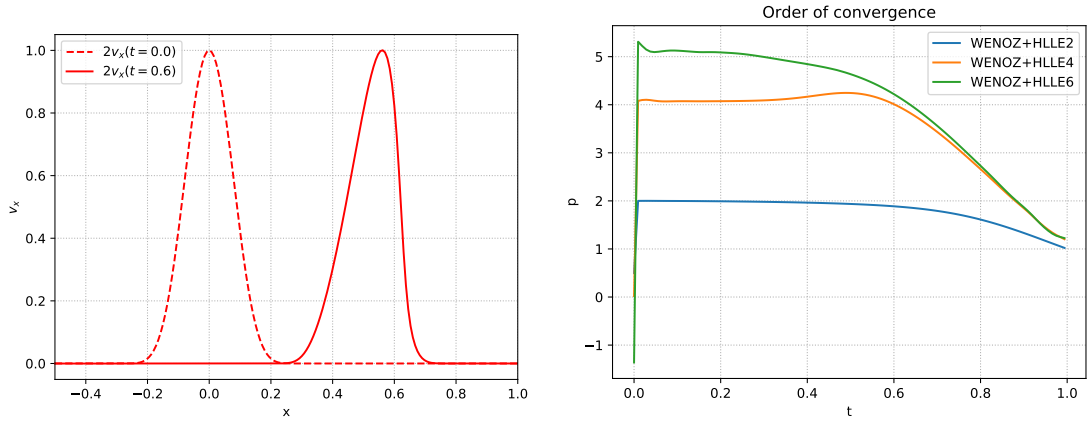

Figure 4.13: Left: Velocity solution in x-direction for the simple wave test using 400 points. Right: Self-convergence factor (see Equation 4.65), computed from three different resolutions which use 400, 800, 1600 points. Figure taken from JVK5.

During the evolution, the wave profile begins to steepen until a shock is formed at $t \approx 0.6$ (see [180]). For quantifying the convergence properties of the various schemes, we compute the self convergence factor given as

$$p \equiv \log_2 \left(\frac{||f(4\Delta x) - f(2\Delta x)||}{||f(2\Delta x) - f(\Delta x)||} \right). \tag{4.65}$$

The functions $f(\Delta x)$, $f(2\Delta x)$, and $f(4\Delta x)$ represent the numerical solutions calculated on

integrator.

uniform grids with corresponding grid spacing, and the norm computed is the L2-norm. We perform this test using three different resolutions $\Delta x = 0.0075, 0.00375, 0.001875$, corresponding to 400, 800, 1600 points respectively. As it can be seen from the right panel of Figure 4.13, the nominal convergence order is reached until the shock appears.

For both WENOZ+HLLE2 and WENOZ+HLLE4, the convergence is dominated by the order of the derivation operation, whereas for WENOZ+HLLE6, the convergence is dominated by the order of the reconstruction method, which does not allow us to reach an order of convergence beyond fifth. As expected, the convergence order goes down for all cases when the shock is formed.

4.3.3.2 Non-magnetized TOV

Next, we consider the evolution of a non-magnetized TOV star. The setup considered here is the same one adopted in JVK2. Particularly, the initial data is generated using a polytropic EOS with $\Gamma = 2.0$ and $K = 100$, and initial central rest-mass density $\rho = 1.28 \times 10^{-3}$, however no magnetic field is added. The system is then evolved using an ideal fluid EOS with $\Gamma = 2$. The physical domain is $[-20, 20]$ for x-, y-, and z-coordinates, with low, medium, and high resolution having 32^3, 64^3, and 128^3 cells, respectively. All tests are performed for 5 ms using the WENOZ reconstruction method and the three approximate Riemann solvers (HLLE2, HLLE4, and HLLE6). In the cases of HLLE2 and HLLE4, RK4 method is employed for time stepping, while RK65 is used along with HLLE6, and all cases use a CFL factor of 0.25. Here too, we see the oscillatory behavior, for example, in the central rest-mass density (see Figure 4.14), similar to the results reported in JVK2. The amplitude of these oscillations decrease with increasing resolution. In the right panels of Figure 4.14, we also notice that the density evolution shows a peculiar behavior for low and medium resolution at late times. This result can be traced back to the choice of the ideal fluid EOS in the evolution of the system. This type of evolution EOS can results in very large truncation errors, because significant unphysical shock-heating is observed at low densities [182].

To verify the convergence of the high-order methods, we compute the self-convergence factor (based on deviations of central rest-mass density with respect to the initial value), which oscillates around the value $p = 3$ for both HLLE4 and HLLE6. Such order of convergence is maintained until the aforementioned truncation errors become significant, i.e., until ~ 4 ms. Finally, Figure 4.15 reports the power spectrum of the rest-mass density evolution for the different runs, plotted in the same fashion as Figure 3.18. Here too, all simulations show a good agreement with each other as well as with the independent results. Particularly, we point out that the high-order reconstruction coupled to high-order Riemann solvers (black-dotted and green-dashed curves) is evidently capable of better resolving the overtones (i.e. the higher frequency peaks in the spectrum) with respect to the lower-order methods (red-solid and blue-dash-dotted curves).

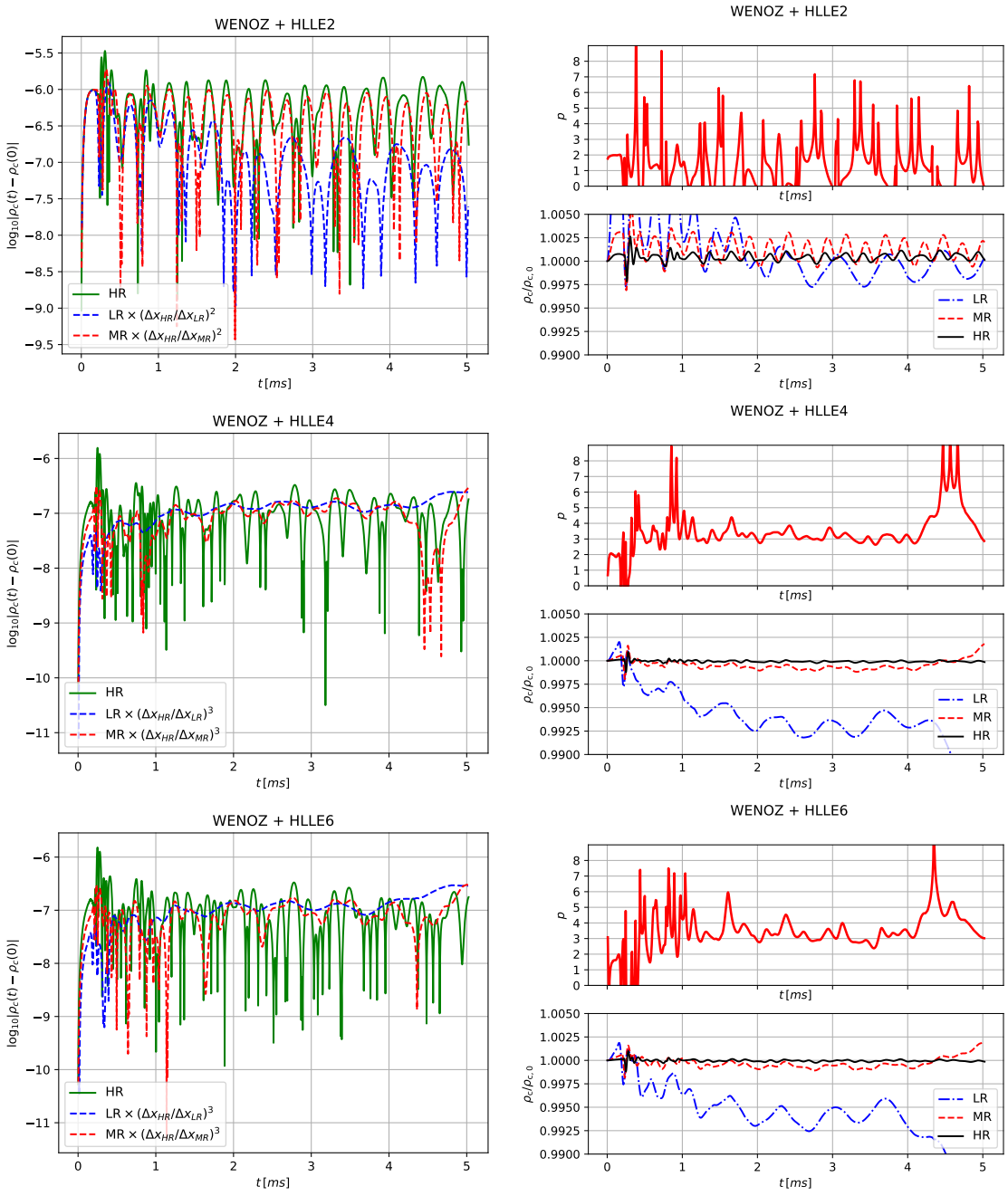

Figure 4.14: Left: Evolution of $|\rho_c(t) - \rho_c(0)|$. Right: Self-convergence factor p (top panels), computed from 3 different resolutions (32^3, 64^3, 128^3 points), and $\rho_{\max}/\rho_{\max,0}$ (bottom panels). From JVK5.

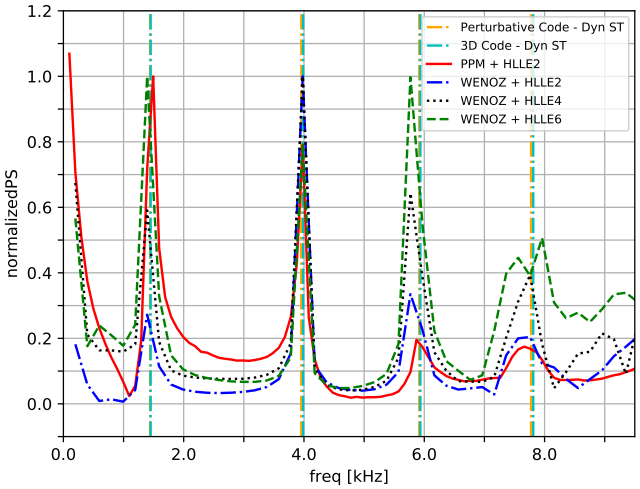

Figure 4.15: Power spectrum of the central rest-mass density evolution, normalized to the maximum amplitude of the oscillation frequency peaks. Figure taken from JVK5.

4.3.3.3 Magnetized TOV with tabulated EOS

For the last test, we perform a simulation evolving a magnetized TOV star using a tabulated EOS (LS220), with S-slicing initial condition, employing WENOZ as the reconstrunction method and the fourth order approximation for the HLLE Riemann solver (referred to as WENOZ+HLLE4). We then compare this test with the one performed using PPM reconstruction method and the 2nd order approximation to HLLE (i.e. simulation 13 of Table 4.3), denoted with PPM+HLLE2.

In the upper panels of Figure 4.16, we show the evolution of the central rest-mass density ρ_c and of the maximum of the temperature T_{max}, both normalized over their initial values. We note that the results obtained with the use of the high-order scheme, in particular the WENOZ+HLLE4 case, are more precise than the ones obtained with PPM+HLLE2, showing that high-order schemes can help to reduce the oscillations around the real value. Moreover, enabling WENOZ and the fourth-order correction to HLLE softens the slight increasing behaviour of maximum of T, as shown in the upper right panel of Figure 4.16.

The gain in accuracy is also evident in the power spectrum of the evolution of the central rest-mass density, illustrated in the lower panel of Figure 4.16. Particularly, the PPM+HLLE2 case shows a noticeable peak only for the fundamental frequency whereas the high-order upgrade is also able to resolve the first overtone with good accuracy.

4.4 Concluding remarks

In this Chapter, we described the new implementations made to our fully GRMHD `Spritz` (available on Zenodo as version 1.1.0 [170]) which now includes neutrino cooling and heating

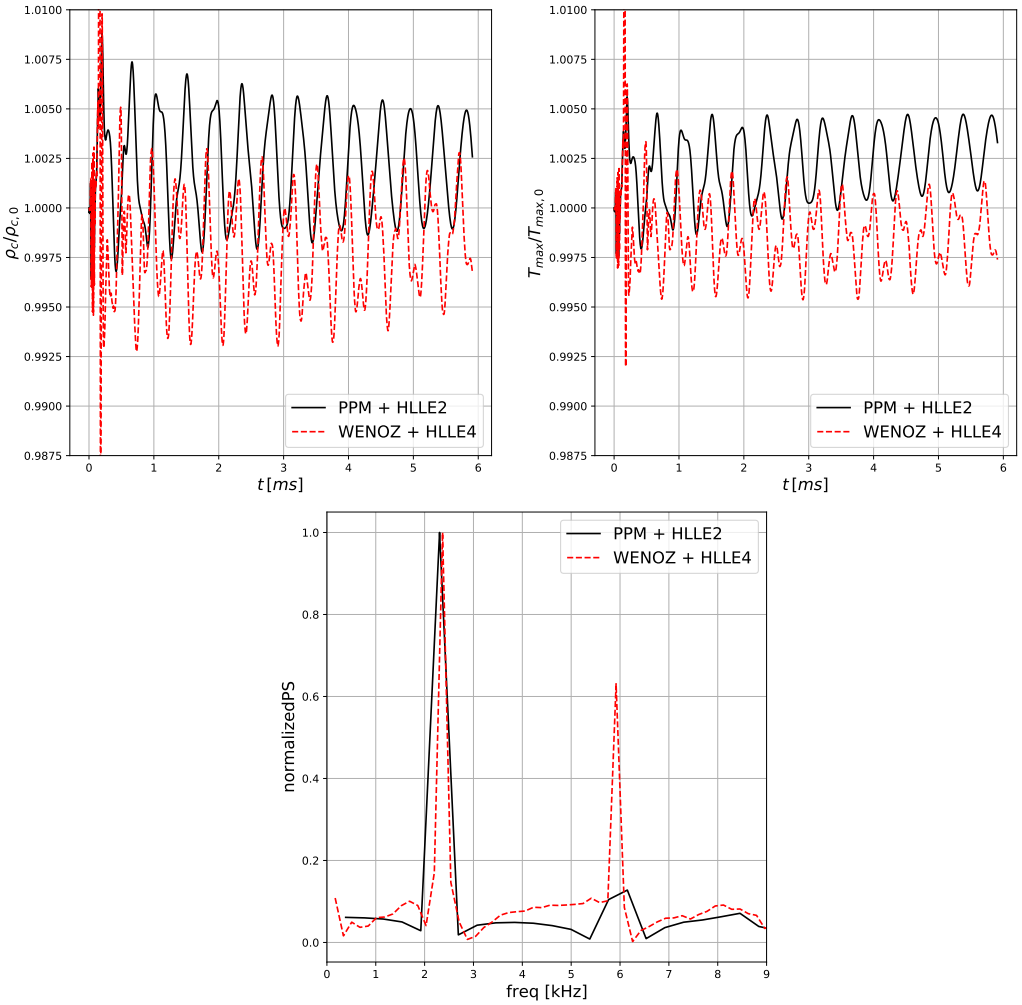

Figure 4.16: Comparison between the results obtained with and without high-order methods for a magnetized TOV evolved with the LS220 EOS. Upper panels show the evolution of the central rest-mass density (left) and the maximum of the temperature (right), both normalized to their initial values. The bottom panel depicts the normalized power spectrum of the maximum of the central rest-mass density. Figure taken from JVK5.

via the `ZelmaniLeak` code. We performed a series of TOV tests to show the robustness of the code in handling a variety of different physical scenarios, including the evolution of both “cold" and “hot" NSs with and without magnetic fields or neutrino leakage. For the cases with neutrino leakage, we also considered the effects of having neutrino heating activated or deactivated.

The `Spritz` code is currently being used to perform magnetized BNS mergers employing finite temperature tabulated EOS and including neutrino emission and reabsorption. The code has indeed all the necessary routines to evolve BNS systems during inspiral, merger and post-

merger phases. We note that the neutrino leakage scheme implemented here, which represents the first step towards a more advanced neutrino treatment, presents some limitations. First, the method adopts a ray-by-ray approach, which is well-suited for problems involving geometries that are, at first approximation, spherically symmetric (for instance, in the context of core collapse supernovae; see, e.g., [183] and references therein). For this reason, it should work reasonably well in a post-merger remnant NS phase where the latter has already achieved an approximately spherical configuration [38], but in the early post-merger or after the collapse into a BH surrounded by an accretion disk, when significant deviations from spherical symmetry are present, it would in part over-estimate the neutrino opacities used in the leakage scheme. To overcome such limitation, various groups implemented a local opacity calculation [184], which better accounts for non-spherical geometries. This different opacity calculation has been already employed in magnetized BNS mergers with neutrino leakage [36, 148], but without accounting for neutrino heating/reabsorption. These simulations represent the current state-of-the-art in the context of magnetized BNS mergers with neutrinos. A second and more general limitation, that is shared among all leakage schemes, is that neutrino energy estimates are not precise enough to provide an accurate estimate of the electron fraction in the ejecta and thus in the computation of the r-process nucleosynthesis and consequent kilonova emission (e.g., see [144]). The above limitations can be overcome by adopting more accurate neutrino transport schemes, such as the Monte-Carlo-based scheme recently adopted for the first time in (nonmagnetized) BNS merger simulations [157] or even the (much more computationally expensive) full solution of Boltzmann transport equations [185]. Future work will be devoted to improve on our current neutrino treatment, possibly following the direction suggested by [157].

We have also implemented high-order methods for the evolution of hydrodynamical quantities (see Sections 4.3.3 and 4.2.5 for details) which will allow our code to provide a better description of matter dynamics and produce also more accurate GW signals. We plan to extend the implementation of these methods also to the equations describing the evolution of magnetic fields, following an approach similar to the one discussed in [36].

Chapter 5

A new primitive variable recovery scheme for GRMHD

As discussed earlier in Sections 3.1.3 and 4.2.3, modern GRMHD codes like `Spritz`, which are based on flux-conservative formlism, require a numerical scheme based on root-finding techniques to retrieve the physical (primitive) variables from the evolved (conserved) ones. Such conservative-to-primitive variable recovery schemes, which are a critical part of any GRMHD code, are commonly referred to as Con2Prim or C2P schemes. Almost all the state-of-the-art C2P schemes investigated in [186] were shown to fail in certain problematic regimes. These schemes work well enough in most of the regimes encountered, for example, during a merger simulation, however they can still be prone to primitive variable recovery failures in astrophysically important regime of high magnetizations at moderate Lorentz factors. Additionally, some of the schemes or the evolutionary code itself could entertain evolution of invalid conserved variables due to presence of numerical errors leading to unphysical states, which needs monitoring as well as error-fixing, if required.

In order to overcome such limitations, we recently designed a new C2P scheme introduced in JVK4, and made a reference implementation publicly available [187] in form of a stand-alone C++ library named RePrimAnd (hereby referring to the scheme too as RePrimAnd, or RPA). In this Chapter, we first describe the salient features of this novel scheme, focussing on its formulation, performance and error-handling, and discuss some of the test results of the stand-alone numerical implementation. Since these stand-alone tests demonstrate robustness, efficiency, and precision, we then implemented the RePrimAnd scheme in our evolutionary code `Spritz`. A part of this Chapter is dedicated on describing this implementation along with a series of demanding 3-dimensional simulations performed in GRMHD considering different astrophysical scenarios, for validating our implementation, based on the work presented in JVK7.

5.1 Formulation of the scheme

5.1.1 Primitive variables

Here, we recap some of the definitions of the primitive variables. Using the 3-velocity v^i defined in the Eulerian frame, and the corresponding Lorentz factor W, we define a new quantity $z \equiv Wv$. We have the baryonic mass density given as $\rho = n_{\mathrm{B}} m_{\mathrm{B}}$, where n_{B} is the baryon number density in the fluid restframe and m_{B} is an arbitrary mass constant. Denoting the fluid contribution to the total energy density in the fluid restframe as e, we have the specific internal energy, given as

$$\epsilon = \frac{e}{\rho} - 1 \ . \tag{5.1}$$

Furthermore, we define $a = P/e$ where P denotes fluid pressure, and the relativistic enthalpy is written as

$$h = 1 + \epsilon + \frac{P}{\rho} = (1+\epsilon)\,(1+a) \ , \tag{5.2}$$

In terms of the Maxwell tensor, Eulerian electric and magnetic fields are $E^\mu = n_\nu F^{\mu\nu}$ and $B^\mu = n_\nu {}^*F^{\mu\nu}$ respectively, where $\mathbf{n}$ is the normal to the hypersurfaces of the foliation, and the star denotes the Hodge dual. As E^μ, B^μ are tangential to the hypersurface, they can be considered equivalent to 3-vectors E^i, B^i.

5.1.2 Equation of state

The scheme works with an EOS of the generic form $P = P(\rho, \epsilon)$. As previously mentioned in Section 4.1.2, the EOS could also depend on further variables, such as the electron fraction. Such variables, which can be evolved or computed in a trivial way, are treated as fixed parameters in the primitive recovery algorithm.

However, each EOS comes with its own specific validity range, subject to both physical and technical constraints. One such important physical constraint is the zero temperature limit for the internal energy. For a tabulated EOS, an example of a technical constraint is the limited range of values available in the table. Currently, our scheme works within an EOS-dependent validity region constrained by

$$\rho_{\min} \le \rho \le \rho_{\max} \ , \tag{5.3}$$

$$\epsilon_{\min}(\rho) \le \epsilon \le \epsilon_{\max}(\rho) \ , \tag{5.4}$$

but can easily be adapted to a more general shape in ρ, ϵ parameter space. Here, the lower validity bound $\epsilon_{\min}(\rho)$ is assumed to be the zero-temperature value at the given density. Other physical constraints like causality and thermodynamic stability require

$$0 \le c_s^2 < 1 \ , \tag{5.5}$$

where c_s is the adiabatic speed of sound, given by

$$c_s^2 = \left.\frac{\mathrm{d}\ln(h)}{\mathrm{d}\ln(\rho)}\right|_{s=\mathrm{const}} . \tag{5.6}$$

Baryon number density and specific internal energy are restricted to the limits

$$0 \leq \rho_{\min} \leq \rho\,, \qquad\qquad -1 < \epsilon_{\min}(\rho) \leq \epsilon \tag{5.7}$$

Pressure is always considered as positive[1] and further bounded by the specific internal energy, which gives

$$0 \leq a \leq 1 \tag{5.8}$$

For a given EOS, we also require a positive lower bound h_0 for the relativistic enthalpy h, such that $0 < h_0 \leq h(\rho, \epsilon)$ over the entire validity region of the EOS, and usually, h_0 is of order unity.

By design, the RePrimAnd scheme is EOS agnostic, using the information defined above, and does not make any other kind of EOS-specific distinctions or adjustments. For the purpose of testing our scheme, we use two specific EOS as examples, i.e. a hybrid EOS (see Section 2.2.6.3 for details) and a classical ideal gas EOS with $\epsilon_{\min}(\rho) = 0$ (see Section 2.2.6.2 for details). For the former, we consider the MS1 EOS from [79] (based on [188]) for the cold part and use $\Gamma_{\mathrm{th}} = 1.8$, while for the latter case, we set $\Gamma = 2$. Note that when considering the ideal gas EOS, pressure and internal energy are zero at zero temperature. Therefore, pressure is only given by thermal effects and degeneracy pressure is ignored.

5.1.3 Evolved variables

Here, we recap our definitions of the conserved variables evolved in evolutionary codes. Considering only the fluid contribution, we have

$$\bar{D} = \rho W\ , \tag{5.9}$$

$$\bar{\tau} = \bar{D}\,(hW - 1) - P\ , \tag{5.10}$$

$$\bar{S}_i = \bar{D} W h v_i\ . \tag{5.11}$$

Including also electromagnetic contributions, the evolved variables are given as

$$D = \bar{D}\ , \tag{5.12}$$

$$\tau = \bar{\tau} + \frac{1}{2}\left(E^2 + B^2\right)\ , \tag{5.13}$$

$$S_i = \bar{S}_i + \epsilon_{ijk} E^j B^k\ . \tag{5.14}$$

[1] Note that in NSs, close to saturation density, the baryonic pressure can also be negative. The EOS framework provided by the RePrimAnd library currently enforces $a > 0$, thus allowing only positive pressure values for now.

In the above equations for the evolved variables, we have left out the volume element of the spatial metric, which can be easily retrieved from spacetime evolution. Also, the magnetic field B in the Eulerian frame is considered as either an evolved variable or is reconstructed from evolved variables, such that B is known when our primitive reconstruction scheme is run. Note that our scheme works only with evolution codes that assume the ideal MHD limit, which allows computation of the electric field as

$$E^l = -\epsilon^{ljk} v_j B_k \ . \tag{5.15}$$

An additional variable $Y_e^c = DY_e$ is evolved using a conservation-law formulation corresponding to advection of the electron fraction Y_e along fluid trajectories, with additional source terms in case neutrino transport is activated.

Note that our scheme is inept for use in resistive MHD simulations. To include, for instance, the effects of resistivity, fundamentally changes the C2P problem and requires completely different C2P schemes. For further discussion, we refer to [189–192].

Furthermore, we define the following rescaled variables

$$\bar{q} = \frac{\bar{\tau}}{\bar{D}} \ , \qquad \bar{r}_i = \frac{\bar{S}_i}{\bar{D}} \ , \tag{5.16}$$

$$q = \frac{\tau}{\bar{D}} \ , \qquad r_i = \frac{S_i}{\bar{D}} \ , \tag{5.17}$$

$$b_i = \frac{B_i}{\sqrt{\bar{D}}} \ , \qquad b = \sqrt{b^i b_i} \ . \tag{5.18}$$

Here, note that b is the magnetic scale factor, and $\mathcal{O}(b) = 1$ corresponds to a very large magnetization (since pressure is typically orders of magnitude below the mass energy density). Moreover, momentum can be decomposed in to parts parallel and normal to the magnetic field

$$r^i_{\parallel} = \frac{b^l r_l}{b^2} b^i \ , \qquad r^i_{\perp} = r^i - r^i_{\parallel} \ . \tag{5.19}$$

5.1.4 Other useful relations

Let's now collect some definitions and analytic relations for later use. First two important quantities we define are

$$\mu \equiv \frac{1}{Wh} \ , \qquad x \equiv \frac{1}{1+\mu b^2} \ , \tag{5.20}$$

and they are bounded by the limits $0 < \mu \leq 1/h_0$ and $0 < x \leq 1$ respectively. For the electromagnetic part of the conserved variables, using Equation (5.15), we define

$$E^2 = x^2 \mu^2 B^2 r^2_{\perp} \ , \tag{5.21}$$

$$r^i = x r^i_{\perp} + r^i_{\parallel} \ . \tag{5.22}$$

Other relevant quantites are defined as

$$\bar{r}^2 = x^2 r_\perp^2 + r_\parallel^2 \ , \tag{5.23}$$

$$\bar{q} = q - \frac{1}{2}b^2 - \frac{1}{2}\mu^2 x^2 b^2 r_\perp^2 \ . \tag{5.24}$$

The velocity can then be expressed as $v = \mu\bar{r}$. However, this expression does not guarantee that $v < 1$ for any μ. To avoid this, we use the quantity z, as

$$v(z) = \frac{z}{\sqrt{1+z^2}} < 1 \ . \tag{5.25}$$

and arrive at an expression for the upper limit of velocity as

$$z = \frac{\bar{r}}{h} \leq \frac{r}{h} \leq \frac{r}{h_0} \equiv z_0, \qquad\qquad v \leq v_0 \equiv v(z_0) \ . \tag{5.26}$$

Once we have the velocity and Lorentz factor, rest mass density and specific internal energy can then be computed using the expressions

$$\rho = \bar{D}/W \ , \tag{5.27}$$

$$\epsilon = W\left(\bar{q} - \mu\bar{r}^2\right) + W - 1 \ . \tag{5.28}$$

If ρ and ϵ are in the validity range of the EOS, we can then compute pressure $P = P(\rho, \epsilon)$ and the enthalpy $h(\rho, \epsilon)$. Finally, we have another useful expression for μ, given as

$$\mu = \frac{1}{hW} = \frac{1}{hW\left(W^{-2} + v^2\right)} = \frac{1}{\frac{h}{W} + \frac{v^2}{\mu}} = \frac{1}{\frac{h}{W} + \bar{r}^2\mu} \ . \tag{5.29}$$

5.1.5 The master function

Since our recovery algorithm is based on a root-finding problem, we need a suitable master function of which we need to find the root. For constructing such a function, we require the function to be one-dimensional, continuous and having exactly one root, even for unphysical values of the conserved variables. It should be well-behaved in the Newtonian limit as well as for zero magnetic field. Moreover, its root should be contained in within a known interval, and the root-finding process should not depend on any EOS derivatives.

Our scheme uses μ as the independent variable to solve for, and we construct a function $f = f(\mu)$ starting with Equations (5.23) and (5.24), defining

$$\bar{r}^2(\mu) = r^2 x^2(\mu) + \mu x(\mu)\left(1 + x(\mu)\right)\left(r^l b_l\right)^2 \ , \tag{5.30}$$

$$\bar{q}(\mu) = q - \frac{1}{2}b^2 - \frac{1}{2}\mu^2 x^2(\mu) b^2 r_\perp^2 \ . \tag{5.31}$$

Functions for velocity and Lorentz factor can then be defined as

$$\hat{v}(\mu) = \min(\mu\bar{r}(\mu), v_0) \ , \qquad\qquad \hat{W}(\mu) = \frac{1}{\sqrt{1 - \hat{v}^2(\mu)}} \ , \tag{5.32}$$

where v_0 sets the upper velocity limit from Equation (5.26). Similarly, rest mass density and specific internal energy can be written according to Equations (5.27) and (5.28) as

$$\hat{\rho}(\mu) = \frac{\bar{D}}{\hat{W}(\mu)} \ , \tag{5.33}$$

$$\hat{\epsilon}(\mu) = \hat{W}(\mu)\left(\bar{q}(\mu) - \mu\bar{r}^2(\mu)\right) + \hat{v}^2(\mu)\frac{\hat{W}(\mu)^2}{1+\hat{W}(\mu)} \ , \tag{5.34}$$

defined within the validity range of the EOS. Otherwise, the density $\hat{\rho}$ is adjusted to the closest value within the validity range for ρ, and $\hat{\epsilon}$ to the closest value within the validity range for ϵ at adjusted density $\hat{\rho}$.

Now, we can also write the expression for pressure using the EOS, as

$$\begin{aligned} \hat{P}(\mu) &= P(\hat{\rho}(\mu), \hat{\epsilon}(\mu)) \ , \\ \hat{a}(\mu) &= \frac{\hat{P}(\mu)}{\hat{\rho}(\mu)(1+\hat{\epsilon}(\mu))} \ , \\ \hat{h}(\mu) &= h(\hat{\rho}(\mu), \hat{\epsilon}(\mu)) \ . \end{aligned} \tag{5.35}$$

Finally, by trial and error, using Equation (5.29), we get the master function $f(\mu)$ that is well suited to our design goals, given by

$$f(\mu) = \mu - \hat{\mu}(\mu) \ , \tag{5.36}$$

$$\hat{\mu}(\mu) = \frac{1}{\hat{\nu}(\mu) + \bar{r}^2(\mu)\mu} \ . \tag{5.37}$$

Moreover, the variable $\nu \equiv h/W$ is computed in two different ways based on Equations (5.2) and (5.8), given as

$$\nu_A(\mu) = \frac{\hat{h}(\mu)}{\hat{W}(\mu)} = (1+\hat{a}(\mu))\,\frac{1+\hat{\epsilon}(\mu)}{\hat{W}(\mu)} \ , \tag{5.38}$$

$$\nu_B(\mu) = (1+\hat{a}(\mu))\left(1 + \bar{q}(\mu) - \mu\bar{r}^2(\mu)\right) \ , \tag{5.39}$$

$$\hat{\nu}(\mu) = \max(\nu_A(\mu), \nu_B(\mu)) \ . \tag{5.40}$$

The second form ν_B helps to reduce the kink introduced by limiting $\hat{h}$, while only limiting $\hat{a}$ instead, and allowing ϵ to change further.

In Figure 5.1, we show examples for the resulting master function for different regimes. Here, we see that the master function shows almost linear behavior unless for large Lorentz factors or magnetic scale factors b, but remains well behaved even then. Note that these results are presented only within the root bracketing interval beyond which the function could have strong kinks.

5.1.6 Existence of solution

In what follows, we prove that the master function always has a root, even in the case of invalid evolved variables. We start by constructing an interval over which the master function changes

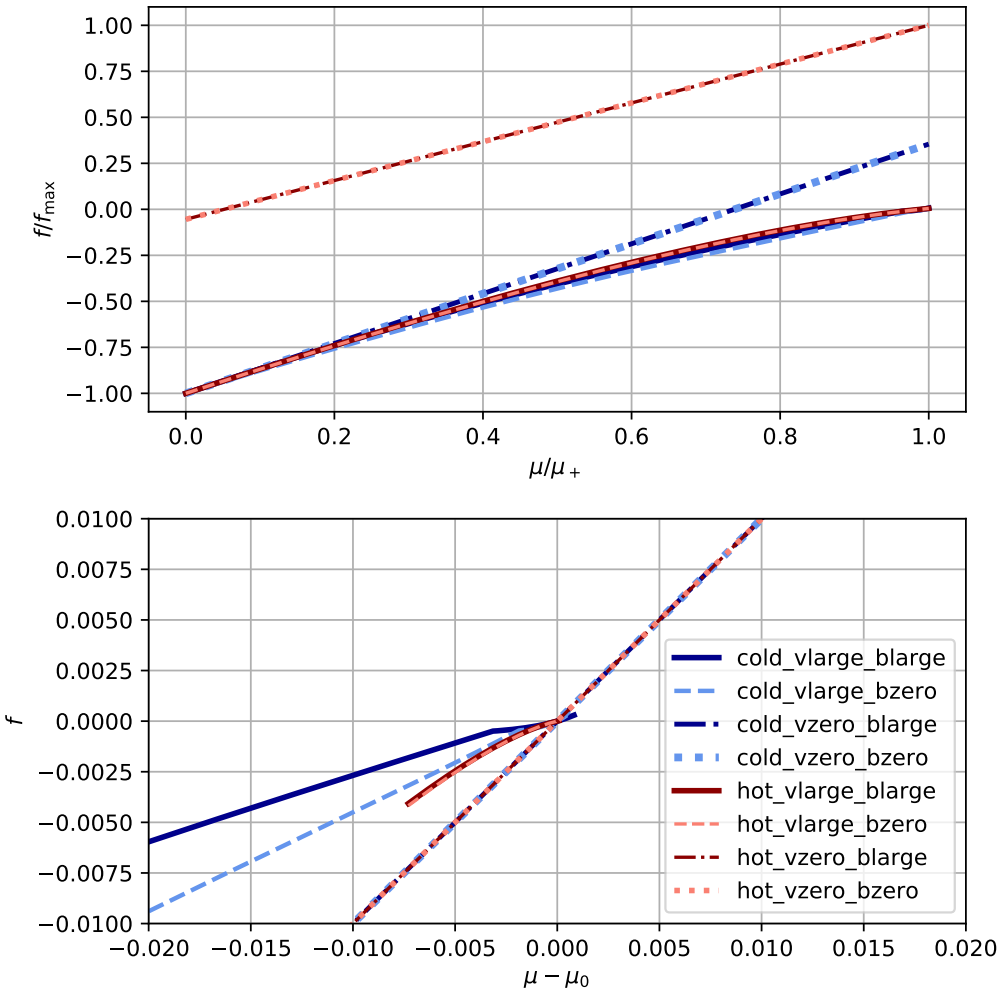

Figure 5.1: Master function f for different regimes, with cases: velocities $v = 0$ and $v = 0.99$ (vlarge), magnetic field scale $b = 0$ and $b = 2$ (blarge), specific internal energy $\epsilon_{th} = 0$ (cold) and 10 (hot), where ϵ_{th} denotes the difference to the zero temperature case. Here, velocities are considered orthogonal to the magnetic field, which is the most difficult case. Top panel shows the independent variable μ, which is scaled to the initial root bracket μ_+, and the function to the maximum value over the interval is shown. Lower panel illustrates the behavior near the root $\tilde{\mu}_0$. Figure taken from JVK4.

sign. First, we define a smooth auxiliary function

$$f_a(\mu) = \mu\sqrt{h_0^2 + \bar{r}^2(\mu)} - 1 \ . \tag{5.41}$$

This function f_a is strictly increasing, and has only one root μ_+ in the interval $(0, h_0^{-1}]$. In the following, we show that μ_+ provides an upper bound for the root of the master function f. For $f_a(\mu_+) = 0$, we get

$$\begin{aligned} \mu_+ \bar{r}(\mu_+) &= \frac{\bar{r}(\mu_+)}{\sqrt{h_0^2 + \bar{r}^2(\mu_+)}} \\ &\leq \frac{r}{\sqrt{h_0^2 + r^2}} = v_0 \ , \end{aligned} \tag{5.42}$$

using the relation $r \geq \bar{r}$ and the monotonicity of the above expression with respect to $\bar{r}$. For velocity, using Equation (5.32), we get $\hat{v}(\mu_+) = \mu_+ \bar{r}(\mu_+) \leq v_0 < 1$. Further, $f_a(\mu_+) = 0$ yields

$$\mu_+ h_0 = \sqrt{1 - \hat{v}^2(\mu_+)} = \hat{W}^{-1}(\mu_+) \ . \tag{5.43}$$

Morever, using the expression for $\hat{\nu}$, which gives $\hat{\nu} \geq \nu_A$, we can write

$$\mu_+ \hat{\nu}(\mu_+) \geq \mu_+ \frac{\hat{h}(\mu_+)}{\hat{W}(\mu_+)} \geq \mu_+ \frac{h_0}{\hat{W}(\mu_+)} \tag{5.44}$$

$$= \hat{W}^{-2}(\mu_+) = 1 - \mu_+^2 \bar{r}^2(\mu_+) \ . \tag{5.45}$$

Finally, we get

$$1 \leq \mu_+ \left(\hat{\nu}(\mu_+) + \bar{r}^2(\mu_+) \mu_+ \right) = \mu_+ / \hat{\mu}(\mu_+) \ . \tag{5.46}$$

For the master function, we find $f(\mu_+) \geq 0$, and, trivially, $f(0) < 0$. Since f is continuous, it has at least one root in the interval $(0, \mu_+]$. Using Equation (5.44), we also get that the root is strictly below μ_+ unless $\hat{h}(\mu_+) = h_0$. This interval provides a useful initial bracketing for the root finding algorithm. Although finding μ_+ requires another numerical root solving, its computation is inexpensive, and moreover, determining μ_+ is not required if $r < h_0$. In this case, $\hat{v}(1/h_0) < 1$ and $f_a(1/h_0) > 0$, the interval $(0, 1/h_0]$ can be used safely to bracket the root.

5.1.7 Uniqueness of solution

One of the desirable traits of the recovery scheme is to provide a unique solution. In that regard, we additionally require the following conditions: (i) for the valid evolved variables, the master function should not have any additional roots corresponding to invalid solutions, and (ii) the master function should still have exactly one root even for invalid evolved variables. In the following, we prove that the above conditions are satisfied.

In order to compute the derivative of the master function, we first perform differentiation

and a few straightforward algebraic computations, yielding

$$\frac{\mathrm{d}x}{\mathrm{d}\mu} = -x^2 b^2 \ , \tag{5.47}$$

$$\frac{\mathrm{d}\bar{r}}{\mathrm{d}\mu} = -\frac{(1-x)x^2}{\mu\bar{r}} r_\perp^2 \ , \tag{5.48}$$

$$\frac{\mathrm{d}\bar{q}}{\mathrm{d}\mu} = -(1-x)x^2 r_\perp^2 \ , \tag{5.49}$$

$$\frac{\mathrm{d}}{\mathrm{d}\mu}(\mu\bar{r}(\mu)) = \frac{1}{\bar{r}}\left(x^3 r_\perp^2 + r_\parallel^2\right) \geq 0 \ . \tag{5.50}$$

As $\mu\bar{r}(\mu)$ increases monotonically increasing and since, in Section 5.1.6, we show that $\mu_+\bar{r}(\mu_+) \leq v_0$, we find that for $\mu \leq \mu_+$, Equation (5.32) reduces to $\hat{v}(\mu) = \mu\bar{r}(\mu)$. This further leads to the expression

$$\frac{\mathrm{d}}{\mathrm{d}\mu}\ln(\hat{W}) = \hat{W}^2\mu\left(x^3 r_\perp^2 + r_\parallel^2\right) \ . \tag{5.51}$$

Assuming that the density $\bar{D}/\hat{W}$ is constrained within the allowed range of the EOS, we then get

$$\frac{\mathrm{d}}{\mathrm{d}\mu}\ln(\hat{\rho}) = -\frac{\mathrm{d}}{\mathrm{d}\mu}\ln(\hat{W}) \ . \tag{5.52}$$

For computing the derivative of $\hat{\epsilon}$, we use Equation (5.34) considering ϵ is in the valid range, and find

$$\frac{\mathrm{d}}{\mathrm{d}\mu}\hat{\epsilon} = \left(1 + \hat{\epsilon} - \frac{1}{\hat{W}\mu}\right)\frac{\mathrm{d}}{\mathrm{d}\mu}\ln(\hat{W}) \ . \tag{5.53}$$

At a solution, $\mu\hat{W}\hat{h} = 1$, and we get

$$\frac{\mathrm{d}}{\mathrm{d}\mu}\hat{\epsilon} = -\frac{\hat{P}}{\hat{\rho}}\frac{\mathrm{d}}{\mathrm{d}\mu}\ln(\hat{W}) = \frac{\hat{P}}{\hat{\rho}^2}\frac{\mathrm{d}}{\mathrm{d}\mu}\hat{\rho} \ . \tag{5.54}$$

This shows that when we vary μ near a solution, changes in density $\hat{\rho}$ and specific energy $\hat{\epsilon}$ are adiabatic in nature, giving the derivative of specific entropy $\hat{s}$ as zero. For the case when ϵ goes below the valid range of the EOS, $\hat{\epsilon}$ is set to the lower bound of the validity range, $\epsilon_{\min}(\hat{\rho})$, corresponding to the zero temperature limit as required. Consequently, $\hat{\rho}(\mu)$ and $\hat{\epsilon}(\mu)$ follow a curve of constant s. We can now compute the derivative of $\hat{h}$ using the adiabatic soundspeed given by Equation (5.6) and the derivative of density given by Equation (5.52), giving

$$\frac{\mathrm{d}}{\mathrm{d}\mu}\ln\hat{h} = -\hat{c}_s^2\frac{\mathrm{d}}{\mathrm{d}\mu}\ln\hat{W} \tag{5.55}$$

where $\hat{c}_s = c_s(\hat{\rho}, \hat{\epsilon})$. Morever, in both cases, we have $\hat{\nu} = \hat{\nu}_A = \hat{h}/\hat{W}$, and we then find

$$\frac{\mathrm{d}}{\mathrm{d}\mu}\ln\hat{\nu} = -\left(1 + \hat{c}_s^2\right)\frac{\mathrm{d}}{\mathrm{d}\mu}\ln\hat{W} \ , \tag{5.56}$$

Finally, at a solution, the derivative of the master function becomes

$$\begin{aligned}\frac{\mathrm{d}}{\mathrm{d}\mu}f(\mu) &= 1-\hat{v}^2+\hat{v}^2\left(1-c_s^2\right)\frac{x^3 r_\perp^2+r_\parallel^2}{\bar{r}^2}\ . \\ &\geq 1-\hat{v}^2>0\end{aligned} \tag{5.57}$$

For more details on this derivation, we refer to Appendix A of JVK4. The constraint $c_s < 1$ guarantees the uniqueness of the root for all velocities and magnetic fields.

Now, for the corner case where the specific energy goes above the valid range of the EOS, we compute $\hat{\nu}$ from Equation (5.39). We find that the uniqueness is always guaranteed (referring again to Appendix A of JVK4) under the condition that

$$\frac{A(\rho)}{1+\hat{a}}\frac{\partial a}{\partial \epsilon} \leq 1-c_s^2\ , \tag{5.58}$$

where A is a function A given by the expression

$$\frac{A(\rho)}{\rho} = \frac{\mathrm{d}}{\mathrm{d}\rho}\epsilon_{\max}(\rho) - \frac{P}{\rho^2}\ , \tag{5.59}$$

related to the change of specific entropy along the upper validity range $\epsilon_{\max}$ of the EOS. When $A = 0$, the above equation reduces to the thermodynamic condition for adiabatic change.

5.1.8 Accuracy

As the solution of the master function is numerically determined, we need to define a criterion in order to stop the iteration once the required accuracy of the root is reached. Here, we discuss this criterion based on the error propagation of the root finding accuracy in order to quantify the accuracy of the recovered primitives.

Before doing so, first we need to decide how to compute the final result based on the root found in the last iteration. The available variables $\mu, \hat{\mu}, \hat{\nu}, \bar{r}, \bar{q}, \hat{v}, \hat{W}, \hat{\rho}, \hat{\epsilon}, \hat{h}, \hat{P}$ can be used in different ways to compute the primitives, which lead to different error propagation. We found that computing $\hat{W}, \hat{\epsilon}, \hat{\rho}, \hat{P}$ directly, seems to be a good choice in terms of error propagation. Then, we can reconstruct the velocity vector using

$$\hat{v}^i = \mu\bar{r}^i = \mu x\left(r^i + \mu\left(b^l r_l\right)b^i\right)\ , \tag{5.60}$$

which avoids degeneracy for the case $b = 0$. Using the above expression, we find the Lorentz factor $W(\hat{v}^2)$ corresponding to be exactly $W(\hat{v}^2) = \hat{W}$. Since $\hat{\rho} = D/\hat{W}$, the conserved density $\hat{D} = \hat{\rho}W(\hat{v}^2)$ computed from the recovered primitive variables $\hat{\rho}, \hat{v}^i$ agrees exactly with the original one.

For detemining the accuracy, we now consider only the case when the solution is in the validity region of the EOS. For invalid solutions, the accuracy is less relevant since the results might either be corrected to the valid range or the simulation aborted.

We now define the accuracy parameter $\delta\mu$, a value up to which the root of $f(\mu)$ is numericall determined. Then, we estimate the resulting accuracy of the primitive variables to linear order,

computing, e.g., $\delta\hat{W} = \delta\mu\, \mathrm{d}\hat{W}/\mathrm{d}\mu$. Using the first derivatives at a root of f, as defined in Section 5.1.7, we find the following expressions

$$\frac{\delta\hat{W}}{\hat{W}} \leq \hat{v}^2\Delta\ , \qquad \Delta \equiv \hat{W}^2\frac{\delta\mu}{\mu}\ , \tag{5.61}$$

$$\frac{\delta\hat{z}}{\hat{z}} \leq \Delta\ , \qquad \frac{\delta\hat{v}}{\hat{v}} \leq \frac{|\delta\hat{v}^i|}{\hat{v}} \leq \frac{\Delta}{\hat{W}^2}\ , \tag{5.62}$$

$$\frac{\delta\hat{\rho}}{\hat{\rho}} \leq \hat{v}^2\Delta\ , \qquad \frac{\delta\hat{h}}{\hat{h}} \leq \hat{v}^2\Delta\ , \tag{5.63}$$

$$\frac{\delta\hat{\epsilon}}{1+\hat{\epsilon}} \leq \hat{a}\hat{v}^2\Delta\,, \qquad \frac{\delta\hat{\epsilon}}{\hat{\epsilon}} \leq (1+\hat{\epsilon})\,\frac{\hat{a}}{\hat{\epsilon}}\hat{v}^2\Delta\ , \tag{5.64}$$

$$\frac{\delta\hat{\rho_E}}{\hat{\rho_E}} \leq 2\Delta\ , \qquad \frac{\delta\hat{P}}{\hat{P}} \leq \hat{v}^2\,(1+\hat{a})\,\frac{\hat{c}_s^2}{\hat{a}}\Delta\ , \tag{5.65}$$

where $|\delta\hat{v}^i|$ represents the norm given by the 3-metric of the vector δv^i. The error in the recovered primitive variables relate to errors $\delta q, \delta S_i$ of conserved variables. In order to estimate these errors to linear order, we then insert $\hat{\rho}, \hat{h}, \hat{P}, \hat{v}^i$ into Equations (5.9, 5.14) and (5.15), and compute the first derivatives with respect to μ at the root. This gives us the following scaling

$$\frac{|\delta S_i|}{|S_i|} \leq \Delta\ , \qquad \frac{\delta(1+q)}{1+q} \leq 4v^2\Delta\ . \tag{5.66}$$

We find that the accuracy in μ required for a fixed relative error of the primitives increases with increasingly relativistic velocities, while varying the magnetic scale b has no impact on the error bounds. Note that the above error bounds do not include numerical rounding errors.

5.2 Validity

It is not uncommon to encounter invalid states at some points for evolved magnetohydrodynamic variables in numerical simulations. This could be a result of typical numerical errors but also external influences such as gauge pathologies near the center of newly formed black holes. Such errors are often harmless, to which point-wise corrections can be applied. Below we point out a few effects causing typical harmless violations:

1. Small evolution errors could drive evolved variables that correspond to a fluid energy density below the zero-temperature limit, when evolving zero-temperature initial data.

2. Mass and energy densities defined in the numerical grid points at the NS surface can drop by orders of magnitude or even become negative at a single timestep, leading to a local error which results to an invalid state for specific internal energy and velocity. Such errors lead to heating of the outermost layer of the NS surface, forming a hot atmosphere.

3. During collapse to a BH, mass density and/or temperature values might exceed the range covered by the given EOS (particularly, finite-temperature tabulated EOS), reaching a

state that is not necessarily unphysical but cannot be evolved further due to the limited range of the EOS. This could typically occur, for e.g., in region within the apparent horizon.

4. The stretching of coordinates near BH centers for gauges like the puncture gauge, coupled with under-resolved surroundings can cause numerical intabilities for the combined magnetohydrodynamical and spacetime evolution system.

5.3 Error handling

The RePrimAnd scheme, by construction, is able to deal with invalid input. As mentioned earlier in Section 5.1.5, the scheme always yields a pair $\hat{\rho}, \hat{\epsilon}$ such that $\hat{\epsilon}$ is within the validity range of the EOS at $\hat{\rho}$.

Now, the first important case we consider is when the raw value of ϵ goes below the valid range. In this case, only the recomputed conserved energy τ changes, while S and D stay the same. The adjustment of ϵ to the valid range impacts only the variable $\hat{\nu}$. For this particular case, Equation (5.40) gives $\hat{\nu} = \nu_A$. Also, the conserved energy τ is exclusively related via Equation (5.34). So if τ is adjusted such that Equation (5.34) returns the range-limited value for $\hat{\epsilon}$, we arrive at the same primitive variables without adjustment.

Now, in case the energy goes above the validity range of the EOS, all recomputed conserved variables can change. This can be prevented by always using $\hat{\nu} = \nu_A$, but not without changing the behaviorof the master function away from the solution. However, for such a case, corrections should only be allowed in specific scenarios, for example, at low-density fluid-vacuum boundaries (NS surfaces) or inside horizons.

For the treatment within BH interiors, we consider employing a more lenient error policy. Development of runaway instabilities within such regions, likely due to violations of constraint equations and gauge effects, can possibly impact the exterior. To avoid this, the energy can be limited by applying the aforementioned correction to the EOS range inside horizons even at high densities. While for momentum, one can put an upper limit to the velocities, and rescale them to stay within a given limit, as done so, for e.g., in [193].

Another correction often applied is to enforce a minimum mass density, also called artificial atmosphere. This is a common practice in order to evolve hydrodynamic evolution equations which otherwise break down in vacuum. This also allows the usage of tabulated EOS which provide only a finite range in density. Moreover, the atmosphere velocities are also usually set to zero.

5.4 Performance

Here, we subject the RePrimAnd scheme to exhaustive stand-alone numerical tests, exploring a parameter space expected to cover all scenarios arising in BNS merger simulations. Through these tests, we also aim to validate that errors produced by the RePrimAnd scheme is insignificant compared to the ones caused by modern evolution schemes.

Variables that primarily govern the behavior of the recovery scheme are Lorentz factor W, magnetic scale b, and specific energy ϵ. In our tests, we demand robustness for these variables up to values $W = 10^3$, $b \approx 100$ and $\epsilon \approx 10$ (see JVK4 for more details on these parameter choices).

In order to understand finite precision effects, we compare the accuracy provided by our stand-alone implementation to the expected accuracy derived in Section 5.1.8, using a value $\Delta = 10^{-8}$. We assume this choice in accuracy is negligible compared to the evolution error.

5.4.1 Code design

As mentioned earlier, for the recovery algorithm described in Section 5.1, we created a reference implementation in form of a C++ library named RePrimAnd which also contains an EOS framework. Figure 5.2 provides a schematic summary of the algorithm. The library provides different EOS types (not yet including fully tabulated ones) including a hybrid EOS based on a tabulated cold part. For our tests, although the MS1 variant from [79] is given analytically in form of piecewise polytropic expressions, we evaluate it as a tabulated cold part, in order to test the general purpose code intended for production runs. We set the allowed range of the EOS to $\rho_{\max} = 3 \times 10^{15}$ g/cm^3, $\epsilon_{\max} = 51$.

For root finding, our implementation uses the `TOM748` algorithm [194] provided by the `BOOST` library. This algorithm is similar to the well known Brent-Dekker schemes, but uses inverse cubic instead quadratic interpolation whenever possible, improving convergence speed near the solution. It brackets the root within a bounded region, converging in a limited amount of steps, and does not make use of function derivatives. Since tabulated EOS tend to contain very inaccurate partial derivatives which can be problematic when using a derivative-based root solver such as Newton-Raphson, our implementation therefore does not make use of the sound speed or other derivatives. The root is determined to an accuracy based on the Δ parameter defined in Equation (5.61), where the error $\delta\mu$ is taken as the size of the current tightest bracket of the root.

In case $r \geq h_0$, we compute μ_+ from the root of the auxiliary function f_a, for which we use a standard Newton-Raphson root solver, since f_a is a smooth, monotonic, analytic function.

5.4.2 Robustness and accuracy

We check for robustness and expected accuracy via our main test through sampling the primitive variable parameter space given by density, temperature/specific energy, magnetic scale b, and velocity. Particularly, we choose the following ranges: $z = Wv$ between 0 and 1000, magnetic scale b from 0 to 5, and the specific thermal energy from $\epsilon_{\text{th}} = 10^{-4}$ up to 50. For the MS1 EOS, we consider the mass density from 10^6 to 10^{15} g/cm^3, while for the ideal gas EOS, the mass density is irrelevant due to the scaling behavior of the EOS. For velocity, we consider two different orientations, i.e., parallel and orthogonal to the magnetic field. We perform the tests with both ideal gas and hybrid EOS, demanding the root finding accuracy of $\Delta = 10^{-8}$.

We find that the algorithm always recovers the correct solution for the valid input described above. To evaluate the accuracy, we first compute the conserved variables from the primitives,

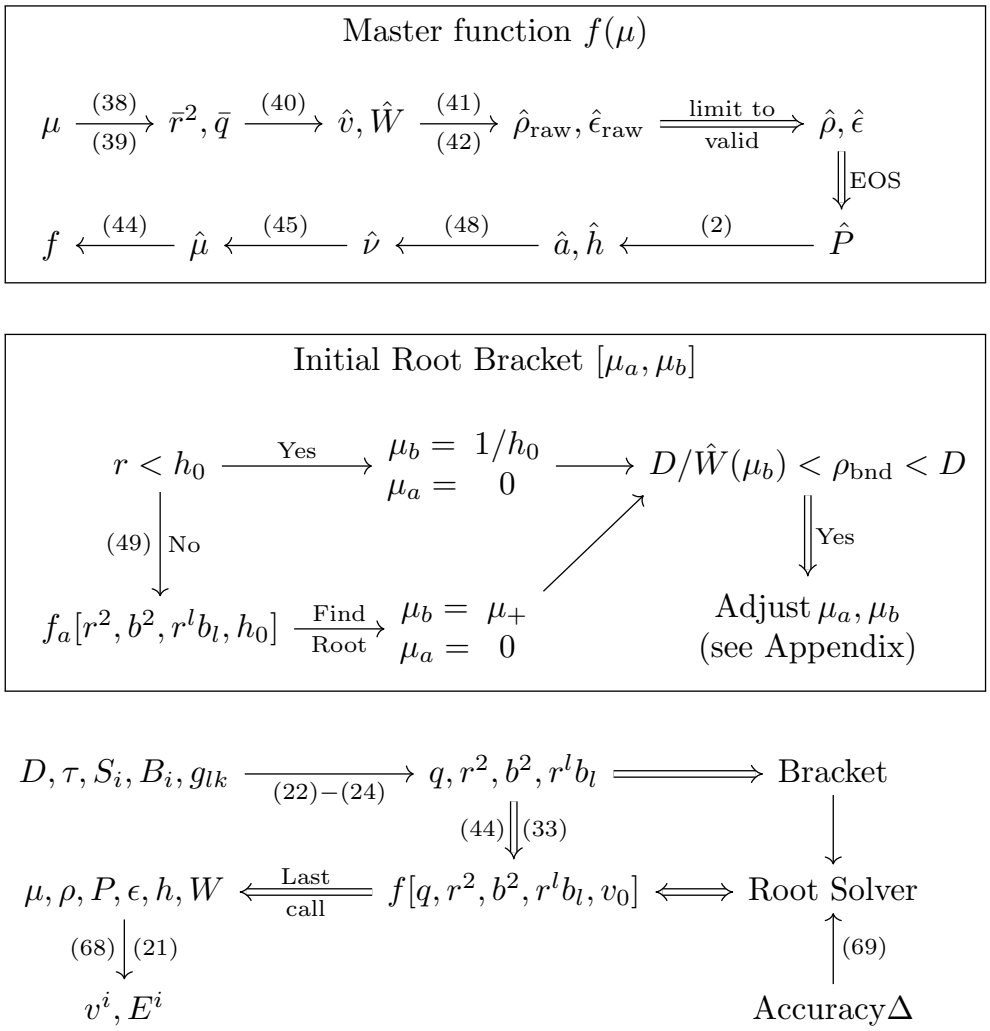

Figure 5.2: Flow diagram of the recovery algorithm along with the list of required equations. Arrows represent dependencies, double arrows are computations that require information about the EOS validity bounds, while the double arrow labeled "EOS" refers to evaluation of the EOS. Results obtained in the last root finding iteration are denoted as "Last call". Square brackets refer to fixed parameters (independent of μ) during root solving. Density $\rho_{\rm bnd}$ stands for either the upper and lower EOS validity bounds. Figure taken from JVK4.

then apply the primitive recovery algorithm, and finally compare the result to the original primitives. Furthermore, we compute the conservatives from the recovered primitives and compare to the original conservatives. Our testsuite compares the observed accuracy for each individual primitive variable to the one expected from Equation (5.61) to (5.65), and also the

accuracy of the corresponding conserved variables to Equation (5.66). In Figure 5.3, we show the recovered accuracy for the pressure as well as the boundary where the errors caused by rounding errors start exceeding those caused by root finding. In general, we find that the RePrimAnd scheme is robust in different regimes including the extreme cases, and is able to deliver the results with expected accuracy.

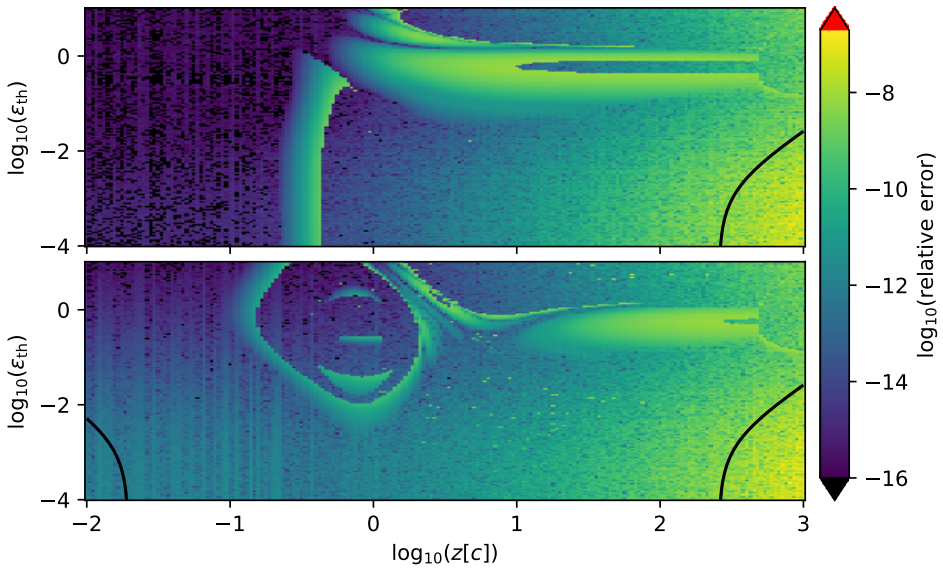

Figure 5.3: Relative error of reconstructed pressure, as a function of specific thermal energy and velocity (the latter in terms of $z = Wv$). The results were obtained for the case of the hybrid EOS, at fixed mass density 6×10^{12} g/cm^3, demanding an accuracy $\Delta = 10^{-8}$.The upper panel shows results for zero magnetic field, the lower panel for magnetically dominated case $b = 10$. The solid lines mark the regions where expected errors related to rounding start to exceed those related to root solving. Figure taken from JVK4.

5.4.3 Efficiency

In what follows, we evaluate the efficiency of our scheme on the algorithm level, while benchmarks of the execution speed of the implementation within `Spritz` is discussed in Section 5.7.1. Here, we measure the computational efficiency of our algorithm in terms of calls to the EOS. The motivation is that for a tabulated EOS including thermal and composition degrees of freedom, a single EOS call is likely more expensive than the evaluation of the analytic expressions within our recovery scheme. The worst scenario is when the EOS is tabulated with temperature as one independent variable. Each EOS call then requires an inversion step to convert from ϵ to T.

In Figure 5.4, we illustrate how the efficiency varies with specific energy and velocity, for two cases, i.e., one with zero magnetic field, and another with magnetic scale fixed to a large value of $b = 10$. These results show that the efficiency does not degrade even for Lorentz factors up 1000 and magnetic scale $b = 10$. At the density shown, $b = 10$ corresponds to extremely high magnetizations of order 10^4 (for $W = 1$) to 10^7 (for $W = 1000$).

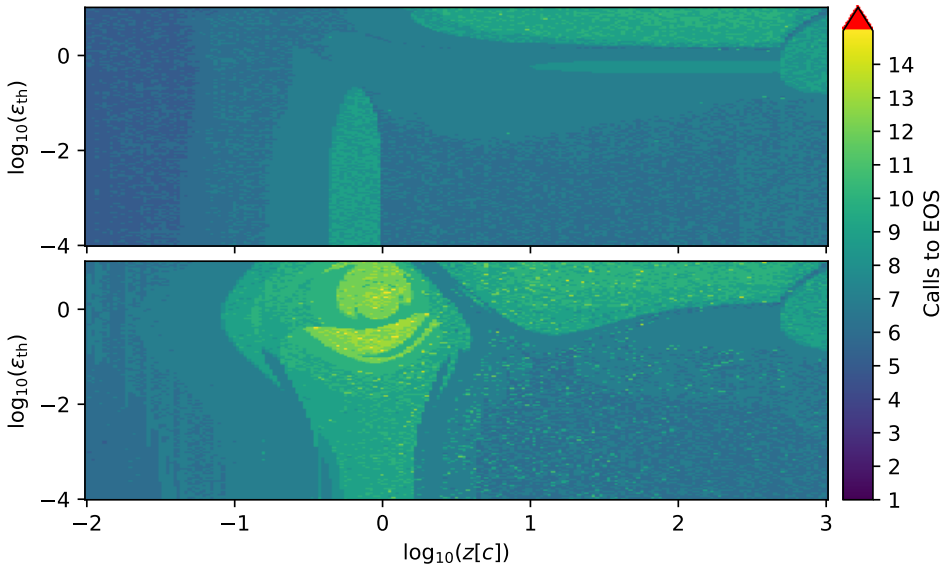

Figure 5.4: Number of calls to the EOS required to reconstruct the primitives to accuracy $\Delta = 10^{-8}$, as a function of specific thermal energy and velocity (in terms of $z = Wv$). This case uses the hybrid EOS at a mass density $\rho = 6 \times 10^{12}$ g/cm^3. The upper panel shows results for magnetic scale $b = 0$, and the lower panel for magnetically dominated case $b = 10$. Figure taken from JVK4.

When considering the whole parameter space used in the unit tests (not just the cuts shown in the plots) and both EOS types, we find a maximum number 23 of calls to the EOS required to achieve an accuracy $\Delta = 10^{-8}$. The maximum occurs for the ideal gas and only when both $\epsilon > 40$ and $b > 2$, i.e. thermal energies much larger and magnetic energies larger than the rest mass density.

Figure 5.5 shows the efficiency with respect to velocity and magnetic scale b, the latter going up to extreme values $b = 10^4$, far beyond any reasonable use case. We find that beyond $b = 10$, the efficiency gradually starts to decrease. At $b = 10^4, W = 10^3$, we require around 40 steps for $\Delta = 10^{-8}$ (which implies $\delta\mu/\mu \approx 10^{-14}$). At this point, the root solving convergence speed has decreased roughly to that of bisection. Still, we encountered no failures to converge even in this range. Note that the extremes reached in our tests are rather pathological scenarios which are rarely encountered in simulations and therefore not relevant for numerical costs of simulations. In practice, we expect an average number of required calls below 10.

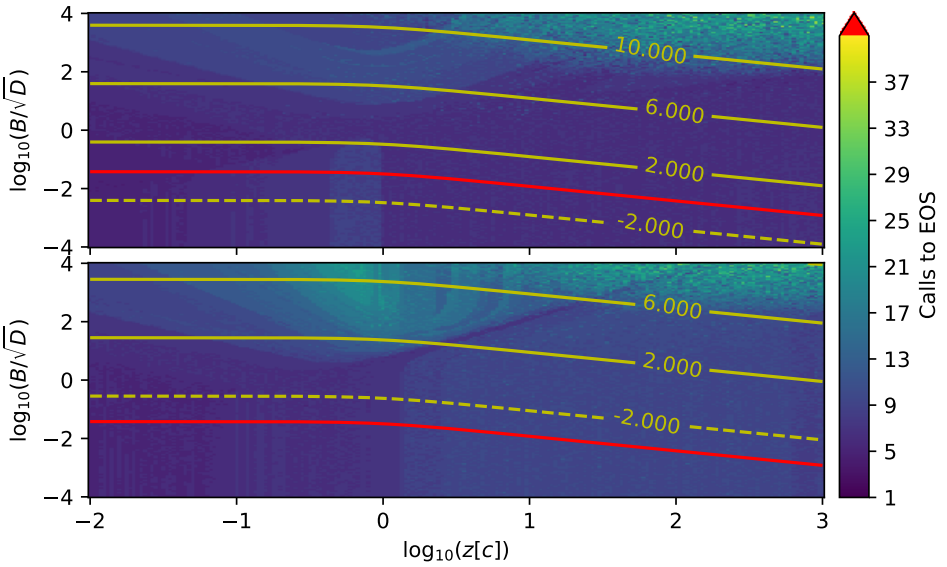

Figure 5.5: Number of calls to the EOS required to reconstruct the primitives to accuracy $\Delta = 10^{-8}$, as a function of magnetic scale b and velocity (in terms of $z = Wv$). This case stands for the hybrid EOS at a mass density $\rho = 6 \times 10^{12}$ g/cm^3. The upper panel shows results for cold matter $\epsilon_{\rm th} = 10^{-4}$, and the lower panel for very hot matter $\epsilon_{\rm th} = 10$. For comparison, we also show the magnetization as contour lines of $\log_{10}(B^2/P)$. The red line marks a magnetic field strength $B = 10^{16}$ G. Figure taken from JVK4.

5.4.4 Comparison with other schemes

Next, we turn to the comparison of our scheme to existing ones. In particular, we refer to [21] for a comprehensive review and numerical tests of previous state-of-the-art C2P schemes. The main characteristics are listed in Table 5.1. In the following, we shed light on some of the most relevant points for comparison, while for a more detailed discussion, we point the reader to JVK4.

When comparing different C2P schemes, one important difference lies in the number of independent variables. Most of the existing schemes need to solve an equation in two or three unknowns. This is a severe drawback as in such cases, it is difficult to ensure that the solution is found, and schemes based on Newton-Raphson (NR) methods might not converge. Moreover, robust but fast schemes that guarantee finding the solution in a limited number of steps only exist for one-dimensional root finding. Also, the recovery schemes based on NR require an initial guess, which is typically taken from the previous timestep during numerical evolution. This makes the methods more unpredictable and more difficult to test, as they do not depend on the conserved variables in a deterministic way. As two of the existing schemes, our scheme

Table 5.1: Main characteristics of different C2P recovery schemes. We list the independent variables used in the root finding (translated to our notation), the variables for which the EOS needs to be evaluated, whether the scheme requires derivatives of the EOS, whether the formulation allows a bound on the number of iterations needed for finding the solution, and whether the scheme requires to provide an initial guess for the solution.

Scheme	Independent variables	EOS form	EOS der.	Steps bounded	Guess needed
This work	μ	$P(\rho, \epsilon)$	No	Yes	No
Noble [195]	$(D/\mu, v^2)$	$P(\rho, h)$	Yes	No	Yes
Siegel [186]	$(D/\mu, T)$	$P(\rho, T)$	Yes	No	Yes
Duran [196]	$(W, D/\mu, T)$	$\epsilon(\rho, T)$	Yes	No	Yes
Neilsen [197, 198]	D/μ	$P(\rho, \epsilon)$	No	Yes	No
Newman [199]	P	$P(\rho, h)$	No	Yes	No

is using one-dimensional root finding. Further, it also makes use of a tight initial bracketing interval proven to contain exactly one solution, as shown in previous sections.

In [21], it is shown that all existing C2P schemes can fail for Lorentz factors 10–1000, depending on the magnetization. Figure 3 of [21] shows the number of iterations or failure to converge as function of magnetization and Lorentz factor, at fixed density 10^{11} g/cm^3 and $T = 5$ MeV (thus, $\epsilon < 1$). For our scheme, magnetic scalre factor b is the most relevant measure for the magnetic field (but not necessarily for the other schemes). Particularly, the magnetization 10^{10} covered in the figure corresponds to values up to $b \approx 10^4$. Such high values are outside the parameter space relevant for merger simulations. So in practice, failures at low velocity, but magnetization around 10^9 shown in Figure 3 of [21] are not necessarily problematic. The fact that the RePrimAnd scheme showed no failure at $b = 10^4$ for the test shown in Figure 5.5 is however reassuring regarding the numerical robustness. Failures at relativistic velocities for lower magnetization shown in Figure 3 of [21] should however be regarded as problematic. Instead, for our algorithm, the existence and uniqueness of the solution are proven analytically, and we have successfully tested our numerical implementation up Lorentz factors $W = 1000$ in the whole parameter space without encountering failures, as described in Section 5.4.2. Strong magnetization is important for studying the engine of short gamma-ray bursts (SGRBs), where ideally a very low density matter is subject to very strong magnetic fields. Moreover, such magnetized matter is expected to reach at least mildly relativistic velocities in case a magnetically powered incipient jet emerges in the post-merger phase. Such regimes are also problematic for the numerical time evolution itself. The ability of our scheme to distinguish reliably between valid and invalid evolved variables gives an important advantage.

When considering the efficiency, the different tolerance measures allow only a rough comparison, using the number of root finding iterations shown in Figures 1 and 3 of [21]. In regions where no failure occurs, we see that only the Newman scheme appears to be consistently requiring less than around 10 steps also for relativistic velocities. Other schemes need at least 30

iterations or more in certain regions of parameter space. RePrimAnd is guaranteed to converge in a finite number of steps because the root finding algorithm performs bisection steps if needed. Our stand-alone tests have shown that the efficiency does not degrade for large Lorentz factors ($W < 1000$) or strong magnetization ($b < 100$), in contrast to most other schemes. The worst case scenario for our scheme seems to be extreme values of ϵ. Even for essentially photonic states ($\epsilon = 50$), it does not require more than 23 EOS calls in the regime $b < 5, W < 1000$.

5.5 Numerical error in evolved variables

In this Section, we investigate consequences of numerical errors in the evolved variables in conjunction with the corrections applied to invalid states described in Section 5.2. Further, we identify regions in parameter space where the primitive variables are particularly sensitive to errors of the evolved ones.

5.5.1 Newtonian limit

First, we consider the the relation between evolved and primitive variables in the Newtonian limit. In this non-relativistic scenario, considering $v \ll 1, \epsilon \ll 1, a \ll 1, h \approx 1$ and $h_0 = 1$, we obtain the following expressions to leading order in v^2 and ϵ

$$x \to x_\mathrm{N} = \frac{1}{1+b^2} \ , \tag{5.67}$$

$$\bar{r}^i \to x_\mathrm{N} r^i_\perp + r^i_\parallel \ , \tag{5.68}$$

$$v^i \to \bar{r}^i \ , \tag{5.69}$$

$$\epsilon \to q - \frac{1}{2}\left(b^2\left(1+v_\perp^2\right)+v^2\right) \ . \tag{5.70}$$

Even in the Newtonian limit, b can have relatively large values, which could result in magnetic field energies that are comparable the rest mass density, which could further lead to non-relativistic velocities during the course of the evolution. Thus, in such cases, one can assume that the density of kinetic energy is not much smaller than the magnetic energy density. Setting $\mathcal{O}(b^2) \approx \mathcal{O}(v^2)$, we find $x_\mathrm{N} \approx 1$. Since $\mathcal{O}(E) = \mathcal{O}(vB)$, we can also neglect the electric contribution $b^2 v_\perp^2$ to ϵ.

Also, in the Newtonian limit, we can easily show that the master function, given by Equation (5.36), becomes a linear function (with $b^2 \ll 1$). As $x(\mu) \approx 1$, $\bar{r}(\mu)$ and $\bar{q}(\mu)$ are independent of μ and equal to the correct values. The same holds in turn for $\hat{\rho}$, $\hat{\epsilon}$, $\hat{P}$. Further, $\hat{\nu} \approx \hat{h} \approx h_0$. Since $\bar{r}^2 \ll 1$, the master function becomes $f(\mu) \approx \mu - 1$.

Now we consider the propagation of the evolution error of the variables q, r, D. We notice that both v^2 and b^2 contributions can dominate q if ϵ is even smaller. Since v is essentially computed from r, computation of ϵ from the evolved variables undergoes cancellations which

amplify evolution errors. In particular,

$$\begin{aligned}\frac{\delta\epsilon}{\epsilon} =& \frac{\delta q}{q}\left(\mathcal{O}\left(\frac{b^2}{\epsilon}\right)+\mathcal{O}\left(\frac{v^2}{\epsilon}\right)\right) \\ &+ \frac{\delta b}{b}\mathcal{O}\left(\frac{b^2}{\epsilon}\right)+\frac{|\delta r^i|}{r}\mathcal{O}\left(\frac{v^2}{\epsilon}\right) \ .\end{aligned} \tag{5.71}$$

If $\delta\epsilon/\epsilon$ becomes more than unity, reconstructing ϵ from the evolved variables might lead to larger errors than simply setting it to the zero-temperature value.

5.5.2 Magnetically dominated regime

By our definition, magnetically dominated regime refers to a regime where the magnetic pressure exceeds the fluid pressure. In such regimes, where the magnetic field dominates, the movement of matter can become constrained along the field lines. This effect can also be noticed in the equations used for primitive recovery. Considering the relation between total and fluid momentum $S_\perp$ components perpendicular to the magnetic field as $\bar{S}_\perp = xS_\perp$, where x depends only on μb^2, we find $x \ll 1$ in the limit $\mu b^2 \gg 1$. In this case, the perpendicular part of the evolved momentum is dominated by the electromagnetic part, which in turn is proportional to $v_\perp$ in ideal MHD, and also points in the same direction. So, the evolution error of the perpendicular part of momentum is not amplified by cancellations when recovering the fluid velocity orthogonal to the field. Also, since the parallel part of the evolved momentum has no electromagnetic contribution, it is also not problematic in terms of evolution errors.

Similar to the Newtonian limit case, here too, strong magnetic fields can have a detrimental impact on the accuracy of ϵ since evolution errors in B are amplified by cancellation. From Equation (5.31), we conclude that the magnetic field contribution to the energy causes strong cancellation error if $\bar{q} \ll b^2(1-v_\perp^2)$.

5.5.3 General case

In general, to evaluate the error amplification, we compute the partial derivatives of the primitive variables with respect to the conserved ones by means of finite differences. We find the specific internal energy and pressure exhibiting large error amplification in some regimes as expected, while the fluid momentum is well behaved.

For quantification of error amplification, we define certain amplication factors of specific energy error in relation to errors in the evolution of q, b, and r, as follows

$$A_q = \left.\frac{\delta\log(\epsilon)}{\delta\log(q)}\right|_{D,r,b} , \tag{5.72}$$

$$A_b = \left.\frac{\delta\log(\epsilon)}{\delta\log(b)}\right|_{D,q,r} , \tag{5.73}$$

$$A_r = \left.\frac{\delta\log(\epsilon)}{\delta\log(r)}\right|_{D,q,b} , \tag{5.74}$$

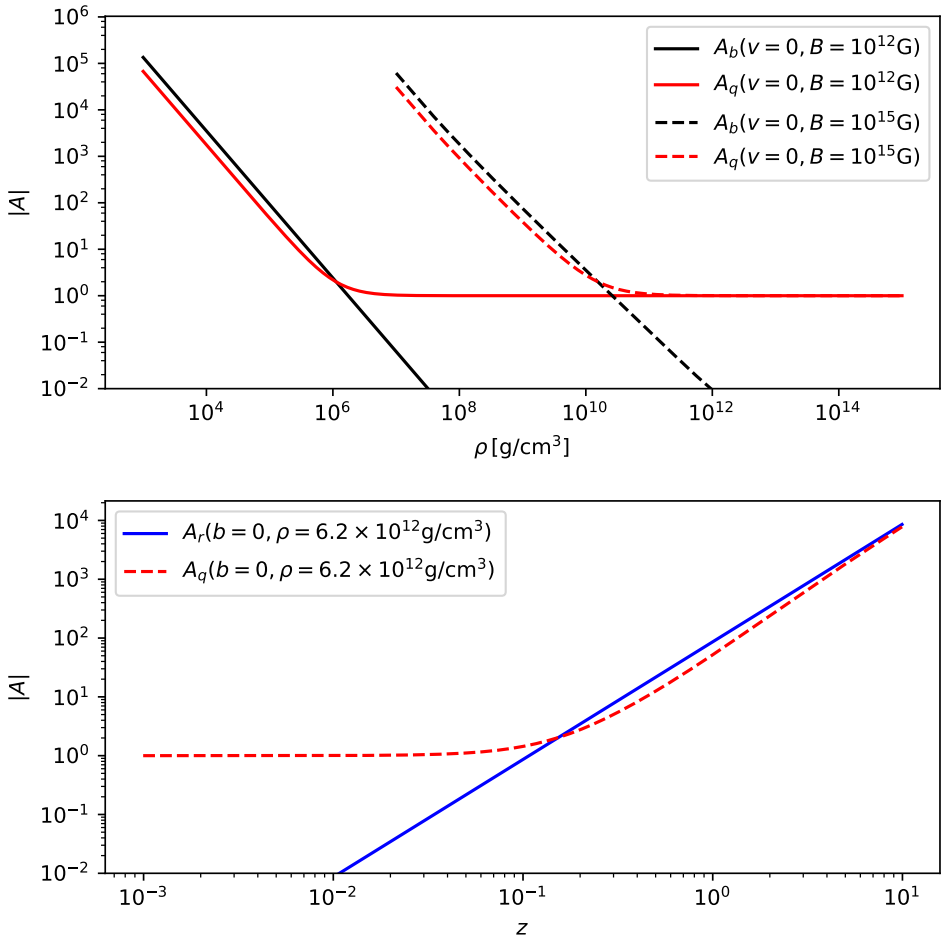

Figure 5.6: Amplification factors A_q, A_r, and A_b for the relative error of ϵ (see text for definitions), for the case considering cold matter obeying the MS1 EOS. Top panel shows the amplification as function of density, for fixed magnetic field and velocity. Bottom panel represents amplification versus velocity, for fixed density and no magnetic field. Figure taken from JVK4.

and show their behavior in Figure 5.6. We find the error in pressure to show the same qualitative behavior.

For a magnetar-strength field $B = 10^{15}$ G, a relative evolution error of $\delta b/b = 10^{-4}$ can start dominating the evolution of ϵ at densities of magnitude 10^8 g/cm^3. A similar behavior can be noticed for a relative error $\delta q/q = 10^{-4}$, since q is dominated by the b^2 contribution. Such regimes can be encountered, for example, in the engine of SGRBs, where a popular BH-disk model consists of a low-density funnel formed along the rotation axis of the BH immersed

in a strong magnetic field which is anchored in a surrounding disk. Similarly, the material surrounding a supramassive (i.e., long-lived) neutron star merger remnant could be affected.

5.5.4 Interaction with recovery corrections

Since the evolved variables are enforced to stay in the physically valid regime, applied harmless corrections close to the validity boundary can result in a drift along the boundary itself, in the worst case with a preferred direction. This can be the case when applying frequent corrections in order to limit the specific energy above the zero temperature value. For our scheme, only the specific internal energy is corrected in such cases, and the evolved momentum density in untouched.

However, limiting ϵ above the zero temperature value may result in spurious heating. The reason is that cutting the evolution error distribution from below creates a positive bias until the error distribution has little support below the cut. For the case in which the evolution errors follow a zero-mean normal distribution around the correct result, we expect the temperature to increase until the thermal energy reaches a level comparable to the width of the error distribution for total energy.

To assess the actual numerical behavior, we then employed a random walk model for different initial states, representing an evolution error, instead of performing a full evolution. After each "evolution" step, we call our recovery scheme which limited the conserved variables to the allowed regime. And we monitor the cumulative corrections applied to energy and momentum.

This allowed us to prescribe the error distribution. As a worst case example, we use a normal distribution with negative mean for the error in energy. Starting at a zero temperature state, this causes frequent corrections to the energy. For the root finding accuracy, we use four different values $\Delta = 10^{-7}, 10^{-8}, 10^{-9}, 10^{-10}$.

Our findings show that the average momentum error is orders of magnitude smaller than the limit Equation 5.66. For an initial state $v = 0.99, b = 2, \rho = 6 \times 10^{12}$ g/cm^3, the momentum errors of individual correction steps approached machine precision levels around $\Delta = 10^{-9}$. The reason behind this result is likely due to the fact that accuracy increases drastically during the final root finding step, such that the average root error is smaller than the prescribed maximum. We conclude that cumulative effects of the corrections can likely be neglected.

We also applied the random walk model to states with different combinations of $b = \{0, 2\}$, $v = \{0, 0.99\}$, $\epsilon_{\text{th}} = \{0, 10\}$, perturbing the evolved variables separately with normally distributed relative errors of order 10^{-4}. This test confirms that the implementation of the zero-temperature energy correction works as intended. We monitored the behavior of v^i, W, ϵ, P, μ for the above cases and did not encounter any problematic behavior.

5.6 Implementation in Spritz

In this Section, we describe the aspects that are relevant for the integration of the RePrimAnd scheme into the Spritz code, and the following Section focuses rather on testing this implementation with a number of demanding GRMHD tests.

As the RePrimAnd scheme is implemented as a stand-alone C++ library, in order to employ the scheme with Spritz, we created a module for the Einstein Toolkit that integrates this library, and added code to Spritz that makes use of the RePrimAnd C2P functionality. The library also includes an EOS framework that provides a fully generic interface to different types of EOS. Currently, it implements the classical ideal gas EOS and the hybrid EOS (which combines an arbitrary cold EOS with a gamma-law thermal component). The extension of this EOS framework within RePrimAnd library to support fully tabulated EOS mainly entails the handling of quality issues often encountered with nuclear physics tables, has been left for future work. In practice, the RePrimAnd scheme requires an EOS of the form $P(\rho, \epsilon, Y_e)$, where EOS that do not consider the electron fraction are emulated by treating it as a dummy variable. Furthermore, the scheme also requires a well defined validity region for the EOS in order to judge if a given combination of conserved variables is physically valid.

We also note that this new EOS framework is only used by RePrimAnd, while Spritz itself still uses the EOS framework provided by the EOS_Omni thorn of Einstein Toolkit. One reason for this is that the evolution code does not take into account any EOS validity bounds during the reconstruction step, while the RePrimAnd EOS framework strictly forbids invalid arguments. Making the reconstruction code of Spritz to work with the validity ranges would be a development task involving design decisions and tests, which is also left for future work.

As discussed in previous sections, the RePrimAnd scheme is able to distinguish reliably between valid and invalid input, and even provides more fine-grained information about which constraints on the primitives are violated, and we take advantage of this feature in our implementation in Spritz. Moreover, the scheme offers various corrections that map invalid input back onto valid input. These are optional and governed by a user-provided error policy. It should be pointed out that the error policy and corrections are completely agnostic regarding the type of EOS. Spritz makes use of those optional corrections when using the RePrimAnd scheme. The most frequent but harmless type of invalid input is given by specific internal energy that would have to be below the one for zero temperature. This could happen when evolving zero-temperature initial data. In Spritz, the policy we adopt for this case when using RePrimAnd, is to change the evolved energy to the zero-temperature value.

Another correction concerns the NS surface. When the surface is moving, e.g. during NS oscillations, the density in a numerical cell at the surface can change drastically during a single timestep, leading in rare cases to extreme velocitiesand/or internal specific energy at densities near the atmosphere cutoff. To alleviate this problem, we employ a policy that limits the velocity by means of rescaling the momentum and also limits the specific internal energy (in the NS tests using RePrimAnd presented in the next Section, we use limits $W \leq 100$ and $\epsilon \leq 50$). Since the problem should only occur near the surface of NSs but not in the interior, our policy is to treat larger values as an error if the density is above a threshold ρ_{strict} (in our tests, $\rho_{\text{strict}} = 3.95 \times 10^{13}\,\text{g/cm}^3$, a few percent of the maximum density). We emphasize that the above corrections are not required to prevent C2P failures, in particular the velocity rescaling is employed *after* the C2P solution is found.

RePrimAnd allows to specify hard limits for the magnetic scale variable $b = B/\sqrt{W\rho}$, which are treated as error when exceeded (we stress that the magnetic field is never adjusted

in any way). This merely serves as a safeguard to catch potential evolution errors that might otherwise go unnoticed, given the robustness of the C2P scheme. In our tests, we set this limit to $b_{\max} = 100.0$, since such a large value would be unexpected. The limit was indeed never reached in any of our tests.

Another optional correction is to enforce the electron fraction to stay within the EOS validity range. This option is irrelevant for our tests since we do not include neutrino reactions and use EOS for which Y_e is an unused dummy parameter.

In the following Section, we also perform tests using the already available state-of-the-art Noble scheme in `Spritz`. When using the Noble scheme instead of the RePrimAnd scheme, the above corrections are not applied. For example, the formulas defining the hybrid gamma-law or ideal gas EOS are applied to any value of specific energy when using the Noble scheme, whereas the EOS interface from the RePrimAnd library which is used in the new C2P enforces strict physical bounds even for analytic EOS. This implies that our comparisons between the two cases do not just compare the C2P scheme, but also the error policies.

A special case for corrections concerns the interior of BHs. Since the center is always severely underresolved, the numerical discretization errors can become much larger, but at the same time, their impact is limited by the presence of the horizon. When using the RePrimAnd scheme, `Spritz` is therefore employing a different, more lenient error policy near the center of BHs. In particular, if the lapse function is below a given threshold, we enforce the aforementioned speed limit at any density (and also allow effectively unlimited values for b, although we have no indication that is necessary).

An important point concerns the artificial atmosphere that is required because the evolution scheme cannot handle vacuum. We employ the standard method of forcing the density to stay above a floor density ρ_{atmo}, and set the fluid velocity to zero when the density became smaller. Further, we chose to set the temperature to zero in the atmosphere. We note that a zero-velocity artificial atmosphere also has consequences for the magnetic field evolution because of the ideal MHD condition. Taking into account the evolution equations used in `Spritz`, one can see that both vector potential and magnetic fields remain frozen in regions covered by the atmosphere. The atmosphere is enforced by the C2P schemes in essentially the same way.

Another useful feature of the RePrimAnd recovery scheme is the availability of errors bounds for all primitive variables based on a single accuracy parameter Δ, which can be prescribed by the user. The accuracy of individual primitive variables is derived by means of error propagation, given explicitly by Equations (5.61)-(5.65). However, this does not cover evolution errors. In our tests, we adopt a value $\Delta = 10^{-8}$.

5.7 Tests

In this Section, we study the interplay between the novel C2P scheme and the numerical time evolution scheme, and ascertain the correct implementation of the interface between evolution code and the RePrimAnd library. To this end, we perform a series of demanding 3D tests in GRMHD, including physical conditions encountered in highly magnetized dynamical systems

involving NSs and BHs. Those tests should be representative for BNS and NS-BH merger simulations, but are computationally less expensive.

Our tests are employing simple analytic EOS, but we stress that the RePrimAnd scheme is completely agnostic to the type of EOS, provided that it respects thermodynamic and causality constraints. This is not true for the implementation of the Noble scheme in `Spritz`, which contains different code path depending on the type of EOS. The comparisons between the two schemes will therefore not necessarily generalize to any EOS. For all tests, we employ PPM reconstruction method, HLLE flux solver, and RK4 method for time-stepping with a Courant factor of 0.25. Unless stated otherwise, we evolve the vector potential using the algebraic gauge and no dissipation, and adopt BSSNOK formulation for spacetime evolution.

5.7.1 Neutron star with internal magnetic field

Our first test consists of evolving a nonrotating NS endowed with initial magnetic field confined to the NS interior. The test setup is the same as the one adopted in JVK2. To obtain initial data, we first solve the Tolman-Oppenheimer-Volkoff (TOV) equations [136, 137] which describe the structure of a non-magnetized, static and spherically symmetric compact star in general relativity. As EOS, we use a polytrope $P(\rho) = K\rho^{\Gamma}$, with adiabatic index $\Gamma = 2$ and polytropic constant $K = 100$ (in geometric units). We consider a model with a central rest-mass density of $\rho = 8.06 \times 10^{14}\,\mathrm{g/cm^3}$. This corresponds to a star with circumferential radius of about 12 km and a gravitational mass of about $1.4\,M_{\odot}$.

The magnetic field is then imposed onto the TOV configuration using the analytical prescription for the vector potential, given by Equation (3.33), which corresponds to a field with dipolar structure confined inside the star. We chose A_b such that the maximum magnetic field strength is 10^{16} G. While this field is rather strong compared to known magnetars, it is still not strong enough to significantly deform the star, as the magnetic energy is much smaller than the NS binding energy. We therefore leave matter distribution and spacetime metric unchanged.

We perform simulations for three different grid resolutions, i.e. low (LR), medium (MR) and high resolution (HR) using $(64)^3$, $(128)^3$ and $(256)^3$ grid-cells with grid spacing dx=922 m, dx=461 m and dx=230.5 m respectively, in a uniform domain with x-, y- and z-coordinates lying in the range $[-29.5, 29.5]$ km. Each simulation covers 10 ms of evolution employing the RePrimAnd primitive recovery scheme, and an atmosphere density floor set to $6.3 \times 10^6\,\mathrm{g/cm^3}$.

For the evolution, we employ two EOS implementations compatible with the initial data. One is the classical ideal gas given by Equation (2.101) with $\Gamma = 2$. The other is the hybrid gamma-law EOS given by Equation (2.102)-(2.103), where we use the initial data polytropic EOS for the zero-temperature curves of pressure, $p_{\mathrm{gas,cold}}(\rho)$, and specific energy, $\epsilon_{\mathrm{cold}}(\rho)$, and further set $\Gamma_{\mathrm{th}} = \Gamma = 2$.

Evaluating the two expressions yields exactly the same EOS function $P(\rho, \epsilon)$, but there is a subtle difference regarding the definition of temperature and the validity range. When specifying an EOS as $P(\rho, \epsilon)$, there is an ambiguity about the definitions of entropy and temperature. We recall that for the classical ideal gas, the pressure and specific internal energy are proportional to the temperature, and the lower validity bound given by zero temperature is $\epsilon \geq 0$. For

the hybrid EOS, the zero temperature curve is the polytrope and the lower validity bound is $\epsilon \geq \epsilon_c(\rho)$. The RePrimAnd C2P scheme enforces those validity ranges for ideal gas and hybrid EOS, which might introduce small differences between simulations using the two. The Noble scheme on the other hand does not enforce EOS validity ranges.

To assess the consequences, we perform simulations of the same initial data using either the ideal gas or the equivalent hybrid EOS. As long as the C2P functions correctly, we expect identical results for the Noble scheme and RePrimAnd in conjunction with the classical ideal gas EOS (assuming that the specific energy might drop below the polytrope but still remains positive). This point is relevant because not all types of EOS can be evaluated outside the physically meaningful range, most notably fully tabulated EOS. Without an EOS-agnostic policy regarding validity ranges, C2P schemes might behave differently for different types of EOS.

Figure 5.7 shows snapshots of initial and final magnetic field strength and density contours, for the HR run with the RePrimAnd scheme.

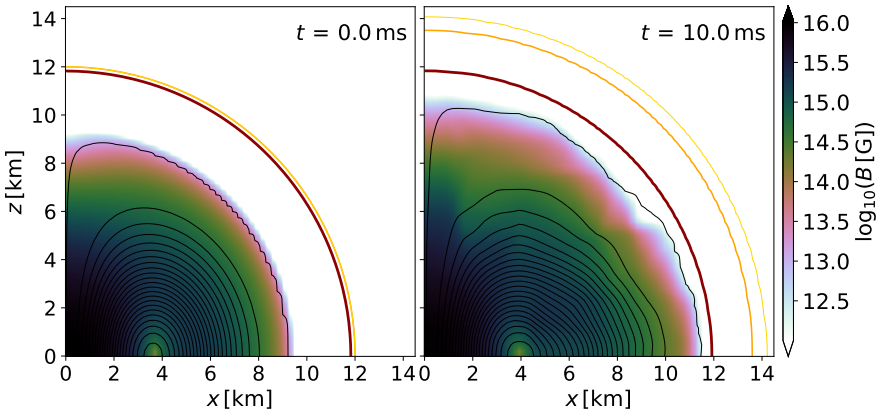

Figure 5.7: Meridional snapshots of the evolution of a magnetized nonrotating NS, where the RePrimAnd C2P scheme with ideal gas EOS is adopted. Black lines correspond to A_ϕ isocontours and reveal the geometry of the poloidal component of the magnetic field. The red line is the iso-density contour corresponding to 1% of the initial maximum density, whereas orange and yellow lines are the iso-density contours corresponding 100, and 5 times the artificial atmosphere density, respectively. The color scale indicates the magnetic field strength. Figure taken from JVK7.

The low-density region at the surface is undergoing an expansion due to spurious heating, which is a typical behavior for evolution schemes near NS surfaces. In 10 ms, the magnetic field configuration also shows some variations, in particular in the outer portion of the NS (radii above $\simeq$6 km). We note that the simulation time span is of the order of the Alfvén timescale at these field strengths and thus field readjustments can occur, possibly triggered by the known instability of purely poloidal fields (e.g., [200] and refs. therein). The evolution of the normalized maximum rest-mass density $\rho_{\max}$ and maximum magnetic field strength $B_{\max}$ is reported in the top and bottom panels of Figure 5.8, respectively, for all three resolutions. The maximum

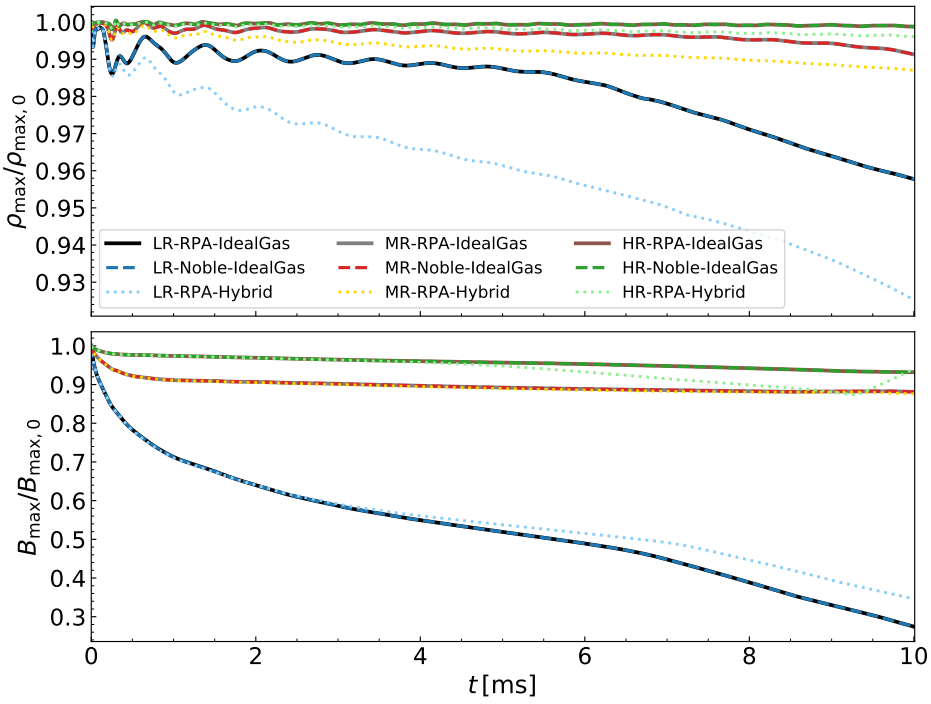

Figure 5.8: Evolution of normalized maximum rest-mass density (top) and magnetic field strength (bottom) for low (LR), medium (MR), and high resolution (HR) simulations, comparing also between the Noble C2P (dashed lines) scheme and the RePrimAnd (RPA) scheme, the latter either in conjunction with the ideal gas EOS (solid lines) or the hybrid EOS (dotted lines). Figure taken from JVK7.

density $\rho_{\max}$ shows oscillations which are decaying while the system settles toward a numerical equilibrium, similar to the behaviour noticed also, for e.g., in Figure 3.15. With increasing resolution, the initial excitation amplitude decreases. In addition, $\rho_{\max}$ and $B_{\max}$ exhibit a continuous drift, which we attribute to numerical evolution errors (compare also [138]). With increasing resolution, such a drift clearly decreases.

To assess the overall convergence behavior, we consider the time evolution of maximum density, maximum magnetic field strength, and minimum lapse function. Using the L_2 norms over time of the differences between high and medium resolution and between medium and low resolution, we find an average convergence order around 2.5 for the density, 2.7 for the magnetic field, and 3.1 for the lapse. At the finite resolutions used here, this is typical behavior for such simulations, which employ numerical schemes with different convergence orders for spacetime and magnetohydrodynamic parts.

Comparing the results obtained with the Noble scheme and the RePrimAnd scheme in conjunction with the ideal gas evolution EOS, we observe an exact match. Both schemes are equally capable to handle this test case.

Comparing between the RePrimAnd scheme with ideal gas and equivalent hybrid EOS, we find a somewhat larger drift for the latter. The only difference in the evolution is that for the hybrid EOS, the specific energy is mapped back to the value given by the polytropic cold EOS when evolution errors cause it to fall below. Hence, the correction only increases the internal energy. We conclude that on average, enforcing the validity range slightly increases the spurious heating. Enforcing the validity range might seem like a drawback, but should be weighted against consistent behavior for any type of EOS.

Since the artificial atmosphere is also handled by the C2P implementations, it is important to validate the conservation of total baryonic mass. Figure 5.9 shows the total baryonic mass, comparing the different resolutions for the RePrimAnd case, the RePrimAnd and Noble schemes at high resolution, and the RePrimAnd case with ideal gas and hybrid EOS. For completeness, we compare two different measures for the mass, including and excluding the artificial atmosphere contribution. Both the Noble and RePrimAnd implementations meet the expectations for mass conservation, and agree exactly for the case of ideal gas (for all resolutions). The enforcing of validity bounds for the hybrid EOS does not have an impact on mass conservation, as expected. Similar to Figure 3.18, here too, in Figure 5.10, we plot the power

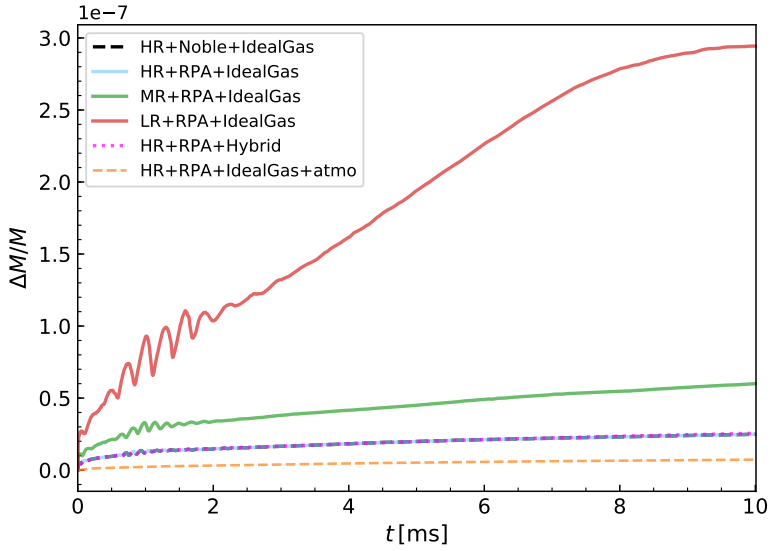

Figure 5.9: Relative change in total baryonic mass for the different tests with Noble and RePrimAnd schemes. Figure taken from JVK7.

spectrum of the maximum rest-mass density evolution. As one can see, the spectra obtained with the RePrimAnd and Noble schemes are identical. Further, the spectrum shows clear peaks that are located at frequencies of the radial NS oscillation modes, predicted in [142] using a 2D perturbative code. The oscillations of maximum density visible in Figure 5.8 thus correspond to NS oscillations excited by the deviation of initial data from equilibrium.

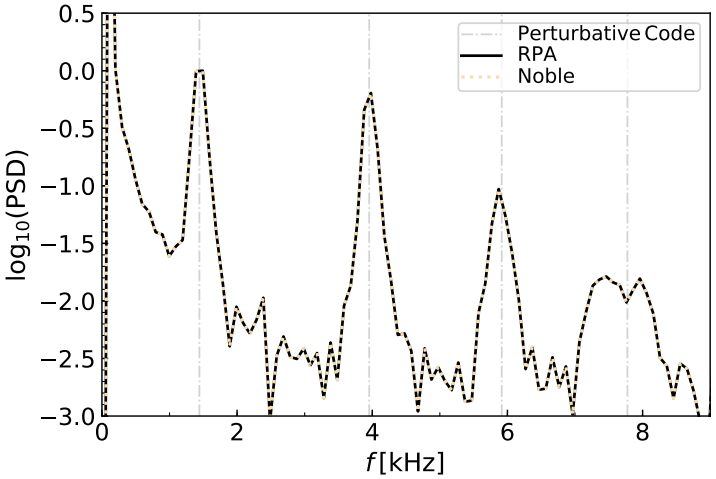

Figure 5.10: Fourier transform of the maximum rest-mass density evolution normalised to the amplitude of first frequency peak, for both the RePrimAnd and Noble schemes. The dash-dotted vertical lines represent the normal mode frequencies computed independently via a perturbative code as reported in [142]. Figure taken from JVK7.

Finally, we assess the computational costs of the two C2P implementations. Using the timing functionality available in the Einstein Toolkit, we find that both schemes use about 2.5% of the total computational time. For the test at hand, the C2P is not a computational bottleneck of the `Spritz` code, and the computational efficiency of both schemes is similar. We note that the fraction spent in the C2P might increase significantly when using a much slower type of EOS, for example an interpolation table using temperature as one independent variable.

5.7.2 Neutron star with extended dipolar magnetic field

A critical aspect for any primitive variable recovery scheme for MHD is the ability to handle high magnetizations in low density regimes. While the RePrimAnd scheme has proven to be robust and reliable when dealing with extremely high magnetisations in pointwise (i.e. single fluid element) tests, more delicate dynamical tests involving high magnetizations together with a nontrivial global evolution represent the next necessary step for a full validation in view of future BNS merger simulations.

Here, we simulate the same nonrotating NS model as reported in Section 5.7.1, but now endowed with a dipole magnetic field also extending outside its surface. In detail, the initial magnetic field is set up employing a vector potential of the form (also used in [38])

$$\begin{aligned} A_r &= A_\theta = 0, \\ A_\phi &= B_0 \frac{r_0^3}{r^3 + r_0^3} r \sin\theta, \end{aligned} \tag{5.75}$$

where $B_0 = 10^{15}\,\mathrm{G}$ (corresponding to a maximum magnetic field strength of $\simeq 6.6 \times 10^{15}\,\mathrm{G}$), and we assume $r_0 = 12\,\mathrm{km}$.

We perform a simulation using the RePrimAnd scheme together with the ideal gas EOS. The grid domain extends up to 44.3 km in all cartesian directions, with grid spacing of $dx \simeq 231\,\mathrm{m}$ (corresponding to the high resolution introduced in the previous Section). In order to make the test more demanding, we chose a very low artificial atmosphere density of $6.3 \times 10^5\,\mathrm{g/cm^3}$.

We evolved the system up to 10 ms without encountering any problems. Most importantly, the RePrimAnd C2P scheme worked robustly even in the low-density regions outside the NS, where the magnetic-to-fluid pressure ratio β reaches large values up to $\sim 10^4$. Figure 5.11 shows three snapshots of the magnetic field strength in the meridional plane, along with vector potential and rest-mass density contours. Apart from some small drift due to normal evolution errors, the field structure remains stable. When evolving the same configuration using the Noble

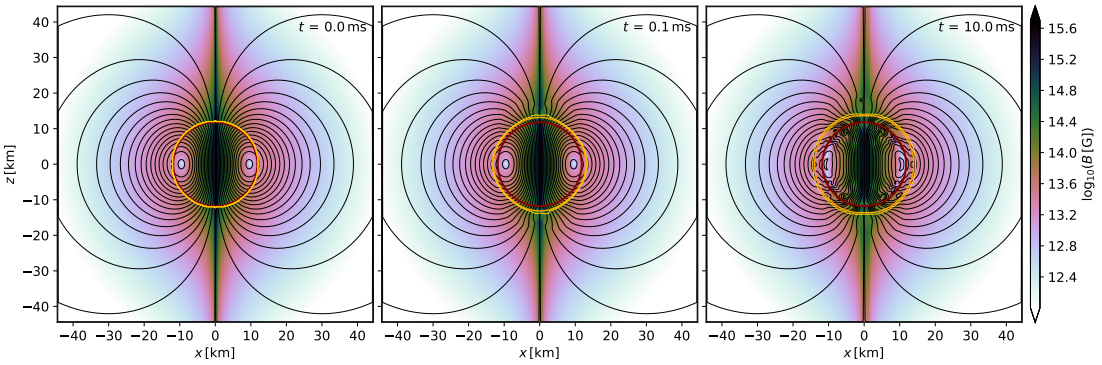

Figure 5.11: Results for the test case of a nonrotating NS endowed with an external dipolar magnetic field, evolved with the RePrimAnd C2P scheme and using a low artificial atmosphere density of $6.3 \times 10^5\,\mathrm{g/cm^3}$. The black lines are isocontours of the vector potential component A_ϕ. Rest mass density contours in red, orange and yellow are illustrated in the same fashion as done in Figure 5.7. Figure taken from JVK7.

scheme, the simulation develops strong instabilities after only $\simeq 0.1$ ms. These instabilities first appear shortly outside the NS surface in the polar region, where the magnetic field strength is largest. Subsequently, they spread around the rest of the star. As shown in the left panel of Figure 5.12, the magnetic field in the outer layers of the NS becomes highly disordered and even the density isocontours reveal a very complex, unexpected dynamics that ultimately leads to failures in spacetime evolution. The exact mechanism behind the instability is unknown. One possible explanation is that the inaccuracies of the Noble C2P solution might be larger in the parameter space of the affected regime and then interact with the evolution scheme in an unstable manner. Since the Noble scheme depends on initial guesses from the evolution, such effects would be difficult to reproduce in standalone tests such as [172].

When the atmosphere floor density is increased by a factor of 100, the simulation performs well also with the Noble scheme, as shown in the right panel of Figure 5.12. Further tests

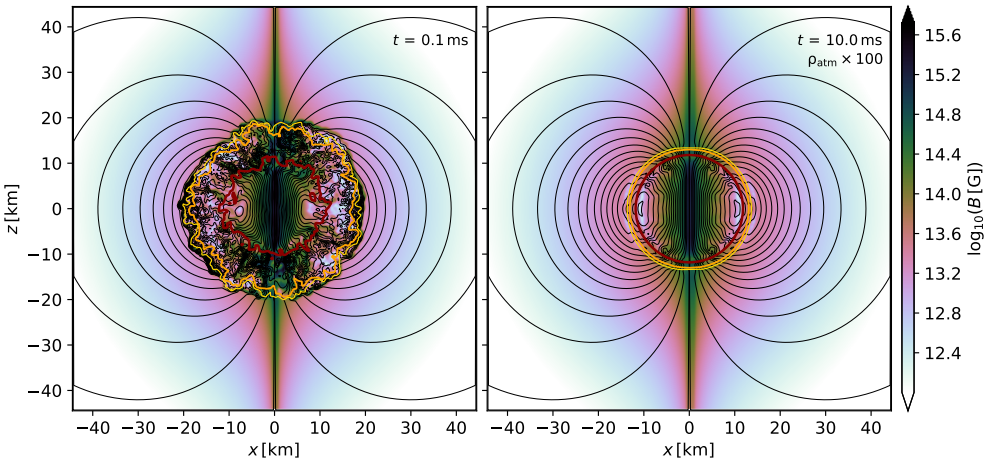

Figure 5.12: Results for the external dipole test obtained with the Noble C2P scheme. Left: Same as the middle panel of Figure 5.11, but showing the instability developing when adopting the Noble scheme. Right: Snapshot after 10 ms evolution with the Noble C2P scheme when using an artificial atmosphere density of $6.3\times10^7\,\mathrm{g/cm^3}$, enlarged by a factor 100 compared to the RePrimAnd simulation results shown in the right panel of Figure 5.11. Figure taken from JVK7.

show that increasing the atmosphere density by an intermediate factor 10 is not sufficient and still leads to an early failure. We therefore attribute the failure to the magnetization, which is maximal at lowest density and hence reduced by increasing the atmosphere density.

When using the Noble scheme with 100 times larger atmosphere, the overall results (NS surface aside) are very similar to the RePrimAnd case with the original low density atmosphere. Figure 5.13 compares the evolution of maximum rest-mass density $\rho_{\max}$ (top panel), central magnetic field strength B_{c} (middle panel), and total magnetic energy (bottom panel) for the two cases. The tests clearly show that the RePrimAnd C2P scheme increases the robustness of the `Spritz` code when dealing with magnetic-to-fluid pressure ratios at least up to $\beta\sim10^4$, compared to the Noble scheme used previously. We stress that our study is not testing the accuracy of the numerical evolution in highly magnetized low-density regions, and point out that evolving such regions more accurately might require specialized evolution schemes incorporating the force-free approximation and/or resistive MHD. However, it is already a big advantage that the presence of such regimes is not causing a failure of the whole simulation.

5.7.3 Rotating magnetized neutron star

Moving to a more demanding test, we now consider a uniformly rotating NS with magnetic field extending outside the star. The initial data are generated using the `Hydro_RNSID` module of the Einstein Toolkit. Our model employs a $\Gamma = 2$ polytropic EOS with $K = 100$ (in units $c = G = M_\odot = 1$), a central density $\rho_{\mathrm{c}} \simeq 6.87\times10^{14}\,\mathrm{g/cm^3}$ and a polar-to-equatorial radius

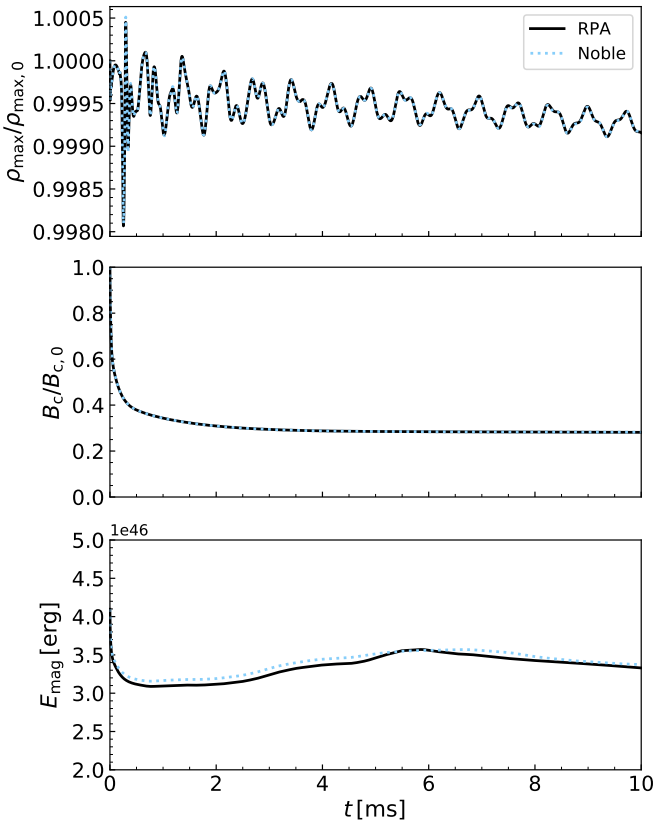

Figure 5.13: Evolution of normalized maximum rest-mass density (top), normalized magnetic field strength at the center (middle), & magnetic energy (bottom) for the case of a nonrotating NS endowed with extended dipolar magnetic field, evolved with the RePrimAnd scheme & artificial atmosphere density of $\rho_{\mathrm{atm}} = 6.3 \times 10^5\,\mathrm{g/cm^3}$ or with the Noble scheme and $\rho_{\mathrm{atm}} = 6.3 \times 10^7\,\mathrm{g/cm^3}$. From JVK7.

ratio of 0.8744. This produces a uniformly rotating NS on the stable branch with a gravitational mass of $1.4\,M_\odot$, an equatorial radius of 15.65 km, and a rotation rate of 500 Hz.

We add an extended dipolar magnetic field on the NS in the same way as done in Section 5.7.2. The magnetic dipole axis coincides with the rotational axis. Different to Section 5.7.2, we do not add the magnetic field to the initial data, but evolve the non-magnetized initial data for 10 ms before imposing the magnetic field. The motivation for this choice is to obtain a test case that is representative for the application to binary neutron star mergers using an approach similar to, e.g., [43], where the extended magnetic field is added to the NSs during the last orbits before merger.

After 10 ms of evolution without magnetic field, the NS is surrounded by a hot, low-density cloud of matter. Such diffuse halos are a typical effect of perturbations near the NS surface initially triggered by numerical evolution errors. This expansion of the outer layers, along with

the interaction with the artificial atmosphere, also leads to strong differential rotation in the corresponding regions. For the actual test, we then evolve the magnetized system for another 10 ms. The atmosphere floor density is again set to a low value of $6.3 \times 10^5\,\mathrm{g/cm^3}$.

For this test, we also use 'box-in-box' mesh refinement with four refinement levels. The coarsest(finest) computational grid extends up to $\simeq 591(74)$ km in all Cartesian directions, and the finest grid spacing is $dx = 461$ m, which is twice as large as the grid spacing used in the previous test. This setting gives about 26 grid points along the NS radius. The test allows us to validate the correct interplay between the implementation of the new C2P scheme in `Spritz` and the mesh refinement.

Figure 5.14 shows the magnetic field strength on the meridional plane along with selected isocontours of rest-mass density, both at 10 ms (time at which the field is added) and 20 ms (final simulation time). Right after the field is imposed, it starts to get distorted by the motion

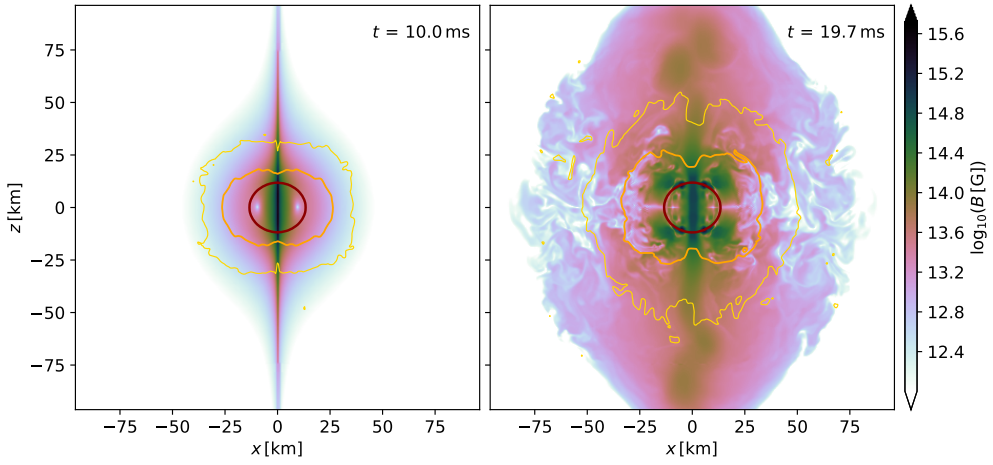

Figure 5.14: Meridional view of a magnetized rotating NS, evolved using the RePrimAnd C2P scheme. Color scale indicates the magnetic field strength and the iso-density contours are the same as in Figure 5.7. Left panel shows the time at which an extended dipolar magnetic field is imposed (10 ms), while the right panel shows the system towards the end of the simulation. Figure taken from JVK7.

of the low density material surrounding the NS bulk. Differential rotation leads to magnetic winding and the appearance of a toroidal component. The resulting magnetic pressure gradients contribute to the expansion of the outer layers of the NS and of the surrounding matter.

In Figure 5.15, we plot the field line structure close to the star towards the end of the simulation, using the visualization method developed in [34] but focusing more on the regions near the NS and rotation axis. Along the spin axis and up to about 100 km from the center, we observe the twisting of magnetic field lines[2]. At large distances, within the artificial atmosphere,

[2]Such an helical structure is also slightly bent, hinting towards the development of a kink instability (e.g., [201]). In-depth analysis of this effect is however beyond the scope of this work.

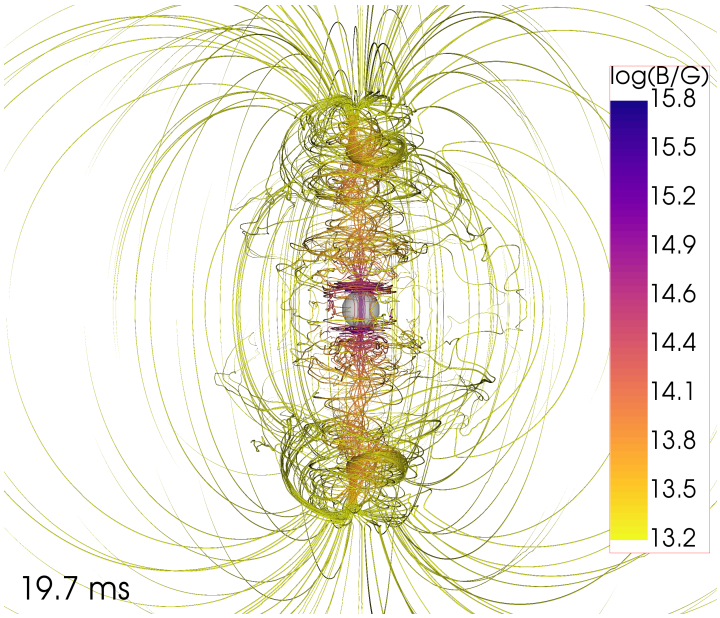

Figure 5.15: Three dimensional magnetic field structure of the system shown in right panel of Figure 5.14. A sphere of radius 10 km is added in the center to give a spatial scale reference. From JVK7.

the original dipolar structure remains frozen. We stress that a proper treatment of those outer regions would require a force-free evolution, which is not currently implemented in `Spritz`.

During the whole simulation, the RePrimAnd C2P scheme experienced no difficulties while handling the high magnetizations present in the low density regions, where the magnetic-to-fluid pressure ratio reaches $\sim 10^4$.

5.7.4 Rotating magnetized neutron star collapse

Our next test case consists of evolving the collapse of a magnetized differentially rotating hypermassive NS to a BH. Even though the gauge conditions avoid the physical singularity, the center of BHs is challenging for numerical evolution schemes. The purpose of the test is not just to demonstrate the robustness of the C2P scheme under the conditions encountered during BH formation, but also to validate that the interplay between our policy for corrections and the time evolution scheme results in a stable evolution of a BH with matter. As described in Section 5.6, we evolve the BH interior without excision, but employ a C2P policy near the center that effectively limits the velocity and specific energy. For this test, we adopt the dynamically unstable axisymmetric model A2 of [202], which consists of a hypermassive NS close to collapse. It employs a polytropic EOS with $\Gamma = 2$ and $K = 100$. The model has a gravitational mass of $M \simeq 2.228\, M_\odot$ and a central rest-mass density of $\rho_c \simeq 1.892 \times 10^{15}\, \mathrm{g/cm^3}$. The model follows the "j-constant law" of differential rotation, with differential rotation parameter $\hat{A} = 1$ (see

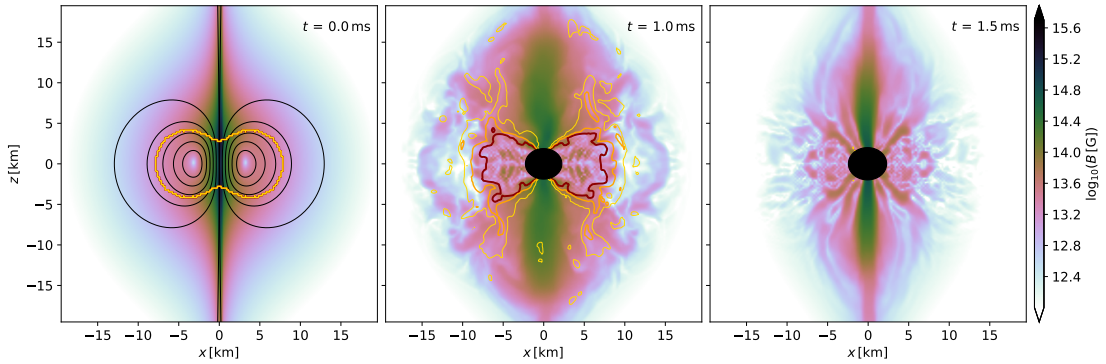

Figure 5.16: Meridional snapshots of magnetic field strength for the magnetized rotating NS collapse simulation, evolved using the RePrimAnd C2P scheme. The iso-density contours in red, orange, and yellow correspond to 5, 3 and 1.5 times the artificial atmosphere density, respectively. The left panel, referring to the initial setup, shows also the magnetic field geometry as A_ϕ isocontours (black). The middle and right panels refer to 1 and 1.5 ms of evolution, respectively. The A_ϕ isocontours are not shown in the last two panels as their disordered structure overcrowds the regions of interest we want to show. The black area marks the apparent horizon of the BH. Figure taken from JVK7.

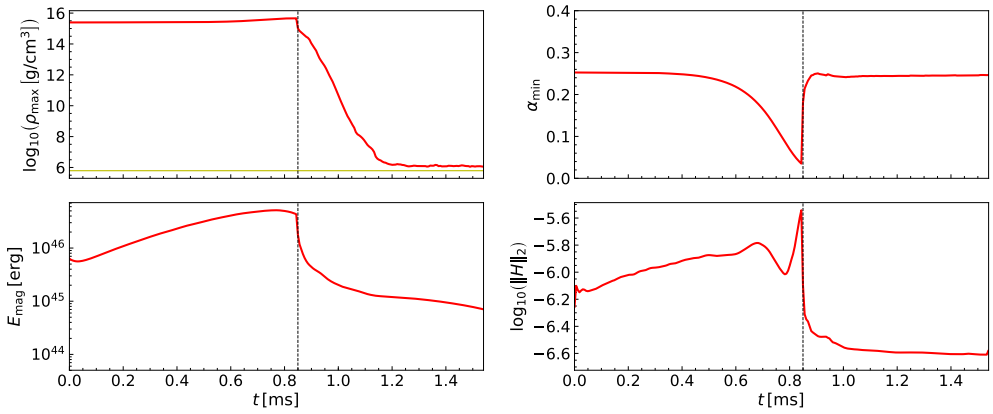

Figure 5.17: Evolution of maximum rest-mass density normalized to the initial value (top-left), total magnetic energy (bottom-left), minimum of lapse (top-right), and L2 norm of the Hamiltonian constraint (bottom-right). Once the BH is formed, the interior of the apparent horizon is excluded for the computation of these quantities. The vertical black (dashed) line in all panels marks the time at which the apparent horizon is found in the simulation, while the horizontal yellow line in the top-left panel represents the floor density. Figure taken from JVK7.

[202] for details) and central angular velocity $\Omega_c \simeq 44\,\mathrm{Rad/ms}$. The resulting ratio of the polar to the equatorial coordinate radii is $r_p/r_e = 0.33$.

The non-magnetized model is constructed using the `Hydro_RNSID` module of the Einstein Toolkit. On top of this initial configuration, we add an extended dipolar magnetic field in the same fashion as done in Section 5.7.2, with $B_0 = 10^{15}\,\mathrm{G}$. However, in this case we choose $r_0 = 4\,\mathrm{km}$.

The computational grid setup is the one described in Section 5.7.3, supplemented with an additional inner refinement level that has a grid spacing of $dx \simeq 230.5\,\mathrm{m}$ and which extends up to $[-37, +37]\,\mathrm{km}$ in all three directions. The system is evolved with `Spritz`, employing the RePrimAnd C2P scheme together with an ideal gas EOS with $\Gamma = 2$. The atmosphere floor density is again set to $6.3 \times 10^5\,\mathrm{g/cm^3}$.

We evolve the system for around 1.5 ms, which is sufficient to capture the collapse of the hypermassive star and the formation of the BH. Prior to collapse (occurring at $\simeq 0.84\,\mathrm{ms}$), the outer layers of the NS tend to expand due to spurious heating, while the central core is slightly contracting. The initially ordered and purely poloidal magnetic field is wound up by differential rotation, which creates a toroidal component and amplifies the overall field strength. At the same time, the field becomes more disordered within the expanding outer layers of the NS, due to the irregular fluid motion. After BH formation, matter is rapidly absorbed and the magnetic field is also dragged along by the in-falling material. Figure 5.16 illustrates the magnetic field strength at the initial, intermediate, and final times of the simulation. Throughout the simulation, we do not find any significant artifacts in magnetic field at the refinement level jumps.

The above dynamics is reflected in the time evolution of maximum rest-mass density $\rho_{\max}$, total magnetic energy E_{mag}, minimum lapse $\alpha_{\min}$, and L_2-norm of the Hamiltonian constraint H, which are shown in Figure 5.17. Note that once the BH has formed, the interior of the apparent horizon is excluded from those measures.

We conclude that the RePrimAnd scheme can be used for scenarios involving BH formation, most notably BNS and NS-BH mergers. Moreover, the robustness and flexibility in applying corrections allows to evolve BHs in GRMHD schemes without applying any form of excision in the center of the BH.

5.7.5 Fishbone-Moncrief BH-accretion disk

For our final test of the RePrimAnd scheme, we simulate a magnetized accretion disk surrounding a Kerr BH, based on the equilibrium torus solutions proposed by [203]. A BH-disk system is one of the typical outcomes of BNS/NS-BH mergers (e.g., [25, 35, 104, 105, 151, 204–206]) and model investigations of such systems probe the underlying mechanisms that govern the dynamics of the plasma accretion, post-merger disk winds that contribute to kilonova emission, as well as launching of relativistic jets. Such a system has also been widely used as a standard test case for different evolution codes and schemes [121, 191, 207–211]. In our case, evolving such a configuration allows another crucial check on the robustness of the RePrimAnd scheme when dealing with accretion onto a BH and MHD turbulence.

The initial data for spacetime and hydrodynamic variables is built using the Einstein Toolkit thorn `FishboneMoncriefID`, which has been adapted to work with `Spritz`. The public version

of thorn was also used, e.g., to setup the `IllinoisGRMHD` [92] simulations in the code comparison reported in [103]. For the initial data, we use a polytropic EOS with $\Gamma = 4/3$ and $K \simeq 0.156$, while for the evolution we use an ideal gas EOS with $\Gamma = 4/3$. We set the initial Kerr BH mass to $2.7\,M_\odot$ and its dimensionless spin parameter to $a = 0.9$. This results in an equatorial BH horizon radius of about 7.8 km in simulation coordinates. The inner edge of the torus is located at a coordinate radius $r_{in} \approx 24$ km, and the maximum density ($9.76\times10^{11}\,\mathrm{g/cm^3}$) is reached at coordinate radius $r_{max} \approx 48$ km. This matter configuration is then complemented by a purely poloidal magnetic field confined inside the torus, using Equation (3.33), and choosing an initial maximum magnetic field strength of 10^{14} G, which corresponds to an initial magnetic-to-fluid pressure ratio β of about 2×10^{-4}. As before, the atmosphere floor density is set to $6.3 \times 10^5\,\mathrm{g/cm^3}$ for the entire domain.

For this test, we use a fixed spacetime metric that is not evolved in time. The metric we use has a coordinate singularity at the origin. Nevertheless, we evolve the magnetohydrodynamic equations in the full domain. In order to avoid singular values, we place the numerical grid such that the origin is located at the corners of the adjacent cells on the finest refinement level, and never at a cell center. Still, the large gradients that spacetime-related variables exhibit near the origin pose a challenging test for the robustness of the code.

We employ fixed 'box-in-box' mesh refinement, using a computational grid hierarchy with five cubical refinement levels. The coarsest level extends up to 528 km and the finest one up to 33 km, with a resolution of ~ 531.6 m. For the chosen grid hierarchy, some mesh refinement boundaries are crossing the disk. This could be avoided in a production setting, but as test case facilitates the observation of potential artifacts.

Related to the potentially problematic mesh refinement boundaries and BH center, we test several evolution options. One is to employ the algebraic gauge condition [69, 70] for the vector potential, but no dissipation. Next, we use the generalized Lorenz gauge still without dissipation. Finally, we use the generalized Lorenz gauge while applying Kreiss-Oliger dissipation [212] to the evolved vector and scalar potentials[3]. In particular, we use the `Dissipation` module of the Einstein Toolkit, with dissipation order $p = 5$ and dissipation strength parameter $\epsilon_{\mathrm{diss}} = 0.1$, which is a typical value used in other works (see, for e.g., [34, 35], JVK1).

For the test case at hand, the use of the algebraic gauge leads to numerical instabilities at the mesh refinement boundaries inside the disk. This seems related solely to the evolution, whereas the C2P algorithm was not causing any problems. As an additional cross-check, we verified that the same behavior arises when using the Noble C2P scheme. The evolution using Lorenz gauge without dissipation shows high-frequency noise at the refinement boundaries, as well as numerical instabilities near the origin[4]. Again, the C2P algorithm was not causing problems.

[3] Note that this simulation was performed using the previous implementation for the evolution of electric field as described in JVK2. The latest version of `Spritz` evolves the electic field based on the upwind constrained transport scheme as described in Section 3.1.2.3, which might not require application of dissipation on magnetic field variables for such simulations.

[4] The instability near the origin is most likely caused by the particular metric used for this test. It is worth noting that it differs significantly from the one adopted in numerical merger simulations that are using the puncture gauge.

When using the Lorenz gauge with dissipation, we obtain a stable evolution without artifacts near the mesh refinement boundaries. We evolve this case for about 50 ms. The rest-mass density distribution at initial and final time is shown in Figure 5.18.

Within the first few ms, disk matter starts to fall into the BH, in part channeled along the BH spin axis, while the inner edge of the disk moves closer and closer to the horizon on the equatorial plane. At the same time, the outer layers of the disk begin to expand and the initial sharp outer edge of the disk is lost in favor of a layer of low density material gradually spreading up to larger and larger distances. At the end of the simulation (~ 50 ms), after the initial transient phase, it looks as if the system is starting to adjust towards a quasi-stationary configuration. The latter condition would however be fully achieved only via longer simulations, as reported in the literature (see, e.g., [103]).

Figure 5.19 illustrates the magnetic field strength at the initial and final time frames. For comparison, we draw the locations of the mesh refinement boundaries in one panel, illustrating that there are no significant artifacts present until the end of simulation. During the evolution, magnetic fields get dragged along with the fluid into the BH horizon as shown in the right-panels of Figure 5.19. Moreover, the magnetic field within the disk undergoes a strong amplification, particularly in the toroidal component, induced by the differential rotation and shear in the disk. The maximum magnetic field strength grows by about two orders of magnitude in 50 ms, aided by magnetic winding, and potentially the development of the magneto-rotational instability (MRI). Using $\lambda_{\rm MRI} \approx (2\pi/\Omega) \times B/\sqrt{4\pi\rho}$ as an estimate for the wavelength of the fastest growing mode, we find that at 50 ms it is resolved by 10–100 grid points in most of the disk, with local growth timescales of order 1–10 ms. Overall, magnetic energy grows by around three orders of magnitude as shown in Figure 5.20, and β increases more than the maximum field strength, reaching values up to 100. The reason is that the regions of low density above and below the disk become increasingly permeated by strong fields. The top panel of Figure 5.20 shows the mass accretion rate, computed from the mass flux penetrating the horizon (in detail, we consider the mass flow rate through a spherical surface of radius ~ 7.83 km that is slightly larger than the BH). We find that after 10–12 ms, the accretion rate starts to rapidly grow and the increase continues up to a maximum reached around 45 ms. Towards the end of the simulation, we observe first hints of saturation and what appears to be the beginning of a decreasing trend.

We note that on longer timescales, a jet might form as well. The current test should not be regarded as representative for this scenario, since it would involve magnetizations, temperatures, and velocities that exceed those reached here.

For comparison, we repeated the test with the same setup, but employing the Noble C2P implementation of the Spritz code. We observed instabilities similarly to the results shown in Section 5.7.2, as well as outright C2P failures, which occur within 1 ms. Those problems occur in a region extending outside the horizon, including the inner edge of the disk. When increasing the atmosphere density to 10 (100) times the one used for RePrimAnd test, similar failures occur within 5(11) ms.

In conclusion, our RePrimAnd scheme implementation functions well in the regimes encountered within the first 50 ms of evolution of the chosen magnetized Fishbone-Moncrief BH-

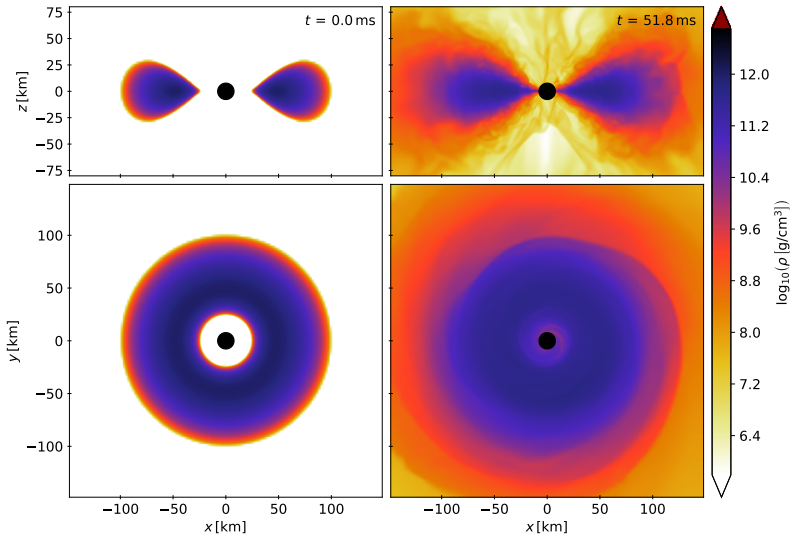

Figure 5.18: Initial and final time snapshots of the rest-mass density in the meridional (top-row) and equatorial (bottom-row) planes for the magnetized Fishbone-Moncrief BH-accretion disk test. The apparent horizon is depicted in black. Figure taken from JVK7.

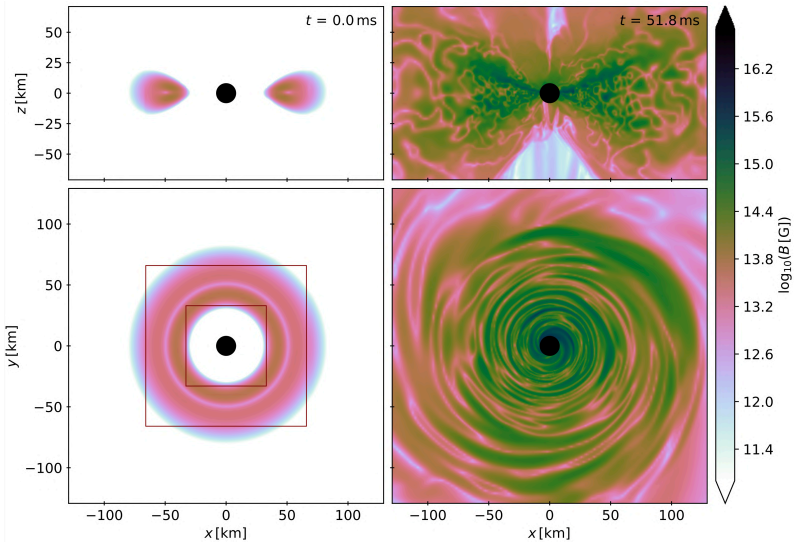

Figure 5.19: Initial and final time snapshots of the magnetic field strength within the meridional (top-row) and equatorial (bottom-row) planes, for the magnetized Fishbone-Moncrief BH-accretion disk test. The apparent horizon is depicted in black. In the lower left panel, we also highlight the mesh-refinement boundaries (red). Figure taken from JVK7.

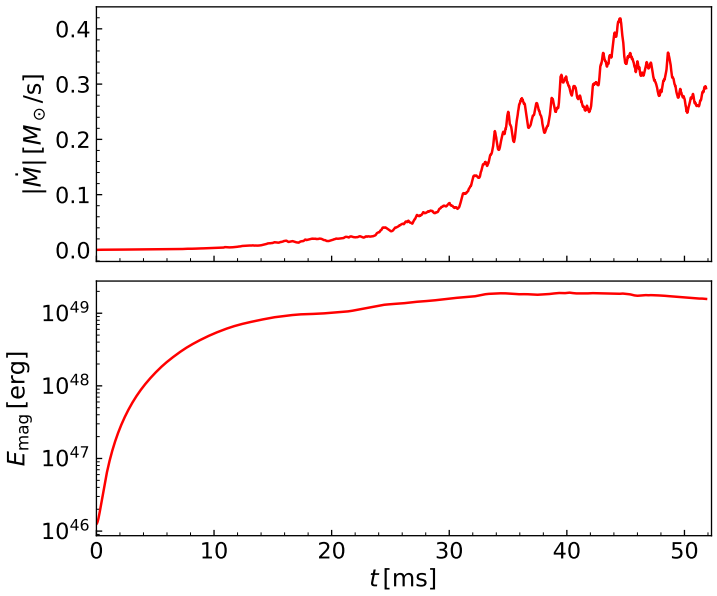

Figure 5.20: Time evolution of the mass accretion rate (top-panel) and total magnetic energy (bottom-panel) for the magnetized Fishbone-Moncrief BH-accretion disk test. Figure taken from JVK7.

accretion disk setup, for a floor density as low as $6.3 \times 10^5\,\mathrm{g/cm^3}$ and a (rather low) finest resolution of $\sim 530\,\mathrm{m}$. It is more reliable than the old C2P implementation, which failed such a test. The RePrimAnd scheme is also functioning robustly in the presence of numerical instabilities in the evolution itself, caused by other effects such as coordinate singularities. The physical setup in this test is representative for science runs involving long-term evolution of post-merger accretion disks around BHs before (or without) jet formation.

5.8 Conclusion

In this Chapter, we summarized our work presented in papers JVK4 and JVK7, introducing a new fully reliable primitive variable recovery scheme called RePrimAnd, designed for relativistic ideal magnetohydrodynamic codes, and then described its implementation in our GRMHD code `Spritz`.

For the stand-alone scheme, we first derived a mathematical proof that the algorithm always finds a valid solution, and that the solution is unique. Moreover, we derived expressions that allow us to prescribe the accuracy of the individual primitive variables. We then focussed on the describing the different features of the scheme, such as its ability to identify unphysical evolved variables, as well as the nature of the invalidity, adoption of relevant error policies and selective application of harmless corrections based on the nature of the problem.

Our reference implementation of the scheme has been made publicly available in form of a

well-documented library named RePrimAnd [187], which can be used by any evolution code. This library also comes with a generic EOS framework for using arbitrary EOS, however the C2P implementation itself is formulated in an completely EOS-agnostic manner.

We first subjected the stand-alone code to a comprehensive suite of tests, demonstrating that both the algorithm and the actual implementation are robust up to Lorentz factors and values of magnetization much larger than those relevant forBNS mergers. We also showed that the scheme is computationally efficient regarding the number of EOS evaluations (efficiency of EOS implementations aside).

As a next natural step, we added code into `Spritz` in order to import the RePrimAnd library and make use of its C2P functionality. We then performed a number of demanding 3D GRMHD tests representative for astrophysical scenarios, including binary neutron star mergers and BH formation. These tests validated the correctness of the implementation as well as the stability of the interplay of the evolution scheme with the recovery scheme. We also discuss important technical details regarding the treatment of invalid states, validity bounds of the EOS, and the evolution inside BHs without use of excision.

Through these tests, which included critical cases such as a NS collapse to a BH as well as the early evolution ($\sim 50\,\mathrm{ms}$) of a Fishbone-Moncrief BH-accrection disk system, we were able to show that the RePrimAnd scheme is able to handle magnetized, low density environments with magnetic-to-fluid pressure ratios reaching $\sim 10^4$, in situations where the previously used recovery scheme fails.

After the extensive testing, we started performing magnetized BNS merger simulations using the RePrimAnd scheme with `Spritz`. Results of these latest simulations will be presented in the upcoming work JVK9. The outcome of the first of these simulations, already completed, is discussed in Chapter 7. In the meantime, the RePrimAnd scheme has been successfully employed in BNS merger simulations using a different code, presented in the paper JVK8.

Building on the proven robustness of the RePrimAnd scheme, we are currently working on providing support for using the new scheme in `Spritz` also with a fully-tabulated, composition and temperature dependent EOS. In the near future, we plan to use this additional upgrade of the scheme to perform magnetized BNS or NS-BH merger simulations as well as long-term BH-disk simulations with microphysical EOS and including an approximate treatment of neutrino radiation.

Chapter 6

Binary neutron star mergers with WhiskyMHD

As discussed in the first introductory Chapter of this Thesis, binary neutron star (BNS) merger events provide a very rich phenomenology involving gravitational waves, electromagnetic radiation as well as microphysical effects, with the potential to answer key open questions in astrophysics and fundamental physics. BNS merger events can also be used as a laboratory to investigate the properties of nuclear matter in extreme conditions and provide constraints on the neutron star equation of state (EOS). Moreover, BNS mergers have long been considered as a very promising progenitor for short gamma-ray bursts (SGRBs). The coincident detection of GWs from the BNS merger GW170817 and the accompanying electromagnetic counterparts including an SGRB and an optical/infrared kilonova (named GRB 170817A and AT2017gfo, respectively) [2, 4, 213] confirmed the connection of BNS mergers with SGRBs and radioactively powered kilonovae and, at the same time, led to the first GW-based constraints on the NS equation of state (EOS) and the Hubble constant (e.g.,[2, 3, 9–11, 14, 15, 214, 215]; see also, e.g., [216, 217] and refs. therein). Nevertheless, this event also left behind open questions regarding the mechanisms that produced the relativisitic jet powering the SGRB, as well as the accompanying kilonova.

As mentioned in the Introduction, GRMHD simulations offer the essential infrastructure necessary to address such questions, including magnetic field effects. In this Chapter, we first start with a brief astrophysical background on NSs and BNS systems. Then, we discuss the work presented in JVK1 and JVK3, involving GRMHD simulations of BNS mergers performed using the numerical relativity code `WhiskyMHD`. In particular, JVK1 addresses, among various aspects, the question of whether a long-lived NS remnant[1] or a so-called *magnetar* can act as a central engine to power a SGRB jet, as an alternative to the standard accreting BH-disk central engine scenario (see Section 6.1.2.4, and for e.g., [17] for a recent review on different viable central engines of SGRB jets). JVK3 focusses instead on explaining the origin of the

[1] Hereafter, long-lived refers to remnants with lifetime $\gg 100\,\mathrm{ms}$.

early "blue" component of the kilonova that accompanied the GW170817 event, in terms of magnetically enhanced mass ejection occurring after merger and prior to the eventual collapse to a BH.

Note that refs. JVK1 and JVK3 are among the latest publications on BNS mergers based on the `WhiskyMHD` code. The corresponding work was conducted in parallel to the development of the new code `Spritz` (discussed in the previous Chapters 3, 4, and 5). The first BNS merger simulation results obtained with `Spritz` will be the subject of Chapter 7.

6.1 Physical background

6.1.1 Neutron stars

The theoretical prediction of the existence of neutron stars was first made by Landau in 1932 [218], and by Baade and Zwicky in 1934 [219], suggesting their origin from supernova explosions. NSs are compact stellar remnants formed by the gravitational core-collapse of high mass stars within the mass range of roughly $8-30M_{\odot}$, having masses in the range of about $1.3M_{\odot} \lesssim M < 3M_{\odot}$, radii of about $10-13$ km, and are associated with densities as high as $\sim 10^{15}$ g/cm^3.

NSs can be observed as pulsars, i.e., rapidly rotating radio emitters with very precise periodicity (with observed spins up to 716 Hz [220]), the first pulsar having been observed by Bell and Hewish in 1967 [221]. They are known to have strong dipolar magnetic fields ($B \sim 10^8-10^{15}$ G), emitting beamed EM radiation from their magnetic poles.

The first theoretical calculation of NS models was proposed by Tolman [137] and by Oppenheimer and Volkoff in 1939 [136], considering the NS matter to be composed of a very high density ideal gas of free neutrons, having its structure supported against the gravitational collapse by neutron degeneracy pressure. The EOS and the interior structure of a NS is still not well understood, making NSs extremely interesting astrophysical objects of study.

6.1.1.1 Internal structure

The internal structure of a NS can be modelled as a series of layers with different composition and thickness. Starting from the exterior, the anatomy of a NS can be described as:

- *Outer crust:* Below the atmosphere (or *the ocean*) which may be only a few cm thick plasma layer of ions and electrons, there is an outer crust where the matter density ranges from $\sim 10^7$ g/cm^3 to the neutron drip density $\rho_d \approx 4 \times 10^{11}$ g/cm^3 as we move inward. This crust is considered to be made up of a heavy nuclei lattice surrounded by an electron gas, supported by the electron degeneracy pressure. At ρ_d, the neutrons occupy all the available bound states in the nuclei, and for densities higher than ρ_d, they start to leak out (neutron drip).

- *Inner crust:* For densities between ρ_d and nuclear saturation density $\rho_0 \approx 2.67\times10^{14}$ g/cm^3, the matter is proton rich, immersed in neutron gas, and supported by the neutron degeneracy pressure. Further in, the nuclei start to deform and connect along certain directions

to form bubbles, extended tubes (*spaghetti*) and sheets (*lasagne*) of nuclear matter, also referred together as *nuclear pasta*.

- *Core:* For $\rho_0 > 2.67 \times 10^{14}$ g/cm^3, the outer core is made of a homogeneous fluid of protons, electrons and neutrons. The physics of the inner core (densities $\sim 10^{15}$ g/cm^3) is however still unclear, as those extremely high densities may lead to the formation of hyperons (e.g., Σ), boson condensates (e.g., of π or K mesons), and/or deconfined quark matter.

For such highly dense objects, we need a general relativistic treatment to describe its structure. As mentioned in previous Chapters, Tolman, Oppenheimer and Volkoff introduced a set of hydrostatic equilibrium equations for a neutron star, using the Einstein field equations for a homogeneous, spherically symmetric static star, which together with an equation of state $p = p(\rho, \epsilon)$, are known as the Tolman-Oppenheimer-Volkoff (TOV) equations [136, 137]. The TOV equations are given as

$$\frac{dm(r)}{dr} = 4\pi r^2 e \tag{6.1}$$

$$\frac{dp}{dr} = -\frac{(e+p)[m(r) + 4\pi r^3 p]}{r[r - 2m(r)]} \ , \tag{6.2}$$

where $m(r)$ and r are the enclosed mass and radius of the star respectively, having e and p as the relativistic energy density and pressure respectively, as measured by an observer in a locally inertial rest frame with respect to the fluid.

An important theorem based on the Schwarzschild solution for a homogeneous star was introduced by Buchdahl in 1959 [222], establishing a constraint between the mass and the radius such that

$$\frac{m}{r} < \frac{4}{9} \ , \tag{6.3}$$

for a static star of constant positive energy-density, where the energy density is a monotonically decreasing function of the radial coordinate, .i.e., $(de/dr) \leq 0$. This theorem is commonly known as the *Buchdahl's theorem*.

6.1.1.2 Neutron star EOS

As discussed in detail in Section 2.2.6, NSs are excellent laboratories for studying the behaviour of high-density nuclear matter. However, we still do not have a complete picture of matter behavior for supranuclear densities reached in NS cores and the corresponding EOS, which is still an active field of research. Currently, a wide collection of NS EOS candidates exists, majorly obtained from relativistic mean field theory (RMFT) and non-relativistic many body theory (NMBT) with relativistic corrections. In NMBT, an effective nuclear hamiltonian is used, which contains effective two- and three-body nucleon interaction potentials. The free parameters in these effective nuclear interactions are obtained by fitting atomic nuclei properties measurements and via results of scattering experiments, and then are extrapolated to higher nuclear densities. In RMFT, the strong nuclear interactions are modeled as a meson exchange

(in terms of scalar σ, vector ω and isovector γ) between nucleons. Here, the effective lagrangian contains the free-particle terms for each considered particle (electrons, nucleons, mesons) along with the meson-baryon interaction terms and perturbative meson self-interactions. The free parameters in this approach are also defined using the low-energy terrestrial experiments. EOS models based on these two approaches could have NS cores composed of only nucleons, or including kaon/pion condensates, hyperons, or strange quark matter.

A number of EOS candidates have been considered by [79] in their study of piece-wise polytropic representations, based on the EOS descriptions in [223, 224], covering different methods and approaches. For example, EOS considering only plain nuclear matter (n, p, e, μ) such as *MS1-2, MS1b* are based on relativistic mean field theory [225], *APR4* is based on the variational method [226], whereas *SLy* is based on the potential method [227]. For EOS models considering exotic nuclear matter (K, π, H, q), we have, for instance, *H1-7* based on RMFT with hyperons [224], *GS1-2* based on RMFT with kaons, and plenty more.

6.1.2 Binary neutron star systems

A BNS system consists of two neutron stars orbiting around their common barycenter. In 1974, Hulse and Taylor reported the first observation of such a system [228], containing a recycled pulsar along with a neutron star. Since then, several BNS systems have been reported in our galaxy. In the following, we discuss the formation and evolution of such compact BNS systems.

6.1.2.1 Binary formation

In the standard scenario, the progenitors of the compact NS binaries are a pair of main sequence stars having individual masses in the range $\sim 8-30 M_{\odot}$. Such progenitors undergo core-collapse when the fusion processes are unable to support them against their own gravity, resulting in supernova explosions. A simplistic version of the standard BNS formation channel is shown in Figure 6.1. For an asymmetric high-mass system, the more massive (primary) star evolves faster than its companion (secondary) star, forming a red-giant and eventually undergoing (assumed symmetric) supernova. If the ejected mass is more than half the total pre-supernova mass, the binary is expected to be disrupted. In practice, supernova explosions can be slightly asymmetric, providing natal 'kick' velocities to the newborn NSs. For large kicks, the binary again faces disruption, producing an isolated NS along with a runaway star. If the binary survives, the companion may also undergo transformation to a giant, overflowing its Roche lobe. This could lead to the common envelope phase, until the companion also explodes as a supernova. If it is able to sustain enough mass and has low or negligible natal kick velocity, it remains bound, forming a double NS system.

6.1.2.2 Merger dynamics

The evolution of a BNS system involves three main stages: (i) inspiral, (ii) merger, and (iii) post-merger (ringdown). The possible evolutionary channels for a BNS merger are summarized in Figure 6.2. For the inspiral phase, the binary evolves on a *radiation-reaction* time-scale, set

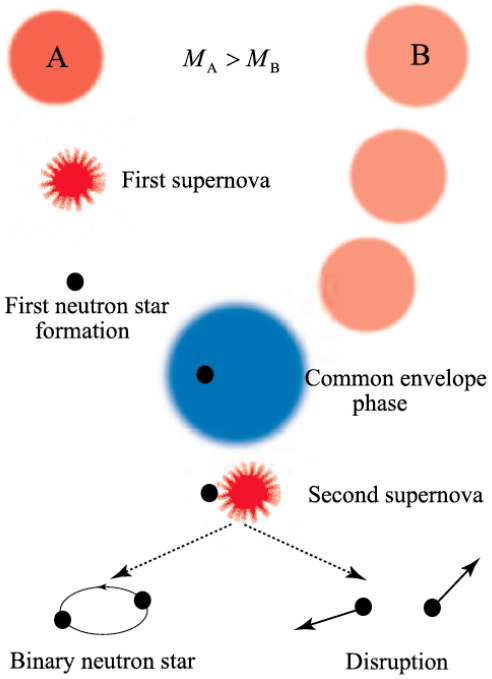

Figure 6.1: A schematic representation of a standard formation channel of a binary neutron star system. Figure taken from [68].

by the loss of energy and momentum through gravitational waves, lasting for $10^6 - 10^7$ years. When the separation reaches the order of 100 km, orbital evolution drastically increases (order of few seconds), as the binary approaches coalescence.

Few orbits before merger, tidal interactions between the two NSs become crucial, producing tidal waves. In particular, the tidal field of the companion can induce a quadrupole mass-moment, accelerating the merger process. The ratio of the quadrupole moment to the external tidal field is directly proportional to the tidal deformability, which is given as

$$\Lambda = \frac{2}{3} k_2 \left(\frac{R}{M} \right)^5 , \tag{6.4}$$

where r and m are the NS radius and mass respectively, and k_2 is the second Love number[2]. The tidal deformability thus links the NS EOS to the gravitational wave signal produced during this phase. The tidal interaction also produces small shocks which result in small matter ejections in the order of $\sim 10^{-6} - 10^{-3}\, M_\odot$.

Depending on the initial masses of two NSs and the given EOS, the merger can result in the following possibilities (see also Figure 6.2):

[2] $k_2 \simeq 0.05 - 0.15$ for realistic NSs . See [229] for a detailed description on tidal Love numbers.

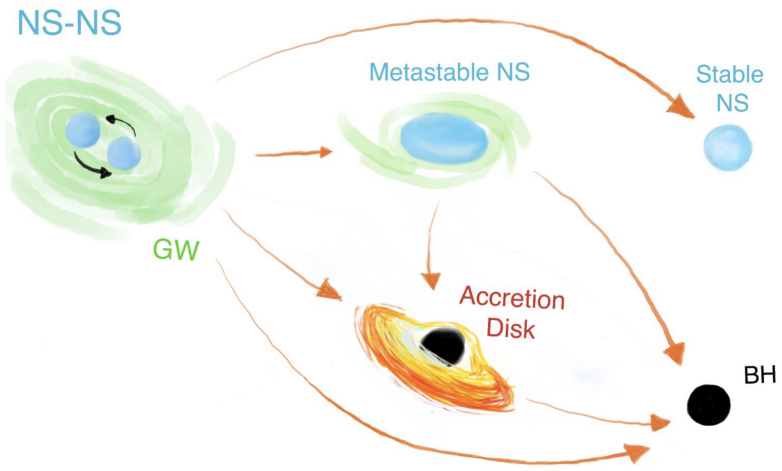

Figure 6.2: Schematic diagram representing various stages of a BNS merger. Depending on the initial NS masses and NS EOS, the post-merger remnant may promptly collapse to a BH, form a metastable NS (hypermassive or supramassive, see text for definitions) before collapsing to a BH surrounded by an accretion disk, or an indefinitely stable NS. Figure adapted from [217].

- Prompt collapse to a black hole (BH) surrounded by a torus over a time-scale of few ms. The torus eventually disappears after being accreted onto the black-hole over time-scale in the order of $1 - 100$ s or more.
- Formation of a *hypermassive* NS (HMNS), which is a NS with mass above the maximum mass for uniformly rotating configurations, believed to be supported by differential rotation. It ultimately collapses to a black hole surrounded by the torus on a time-scale of $1 - 100$ ms.
- Formation of a long-lived NS, which could be *supramassive* (SMNS), which is a NS with mass above the maximum mass for non-rotating configuration, believed to be supported by uniform rotation, that eventually collapses to a black hole on a time-scale of seconds, minutes or more. A more extreme outcome is an indefinitely stable NS.

6.1.2.3 Gravitational waves

Gravitational waves (GWs) are an emergent property of Einstein's theory of general relativity, and are considered to be perturbations in spacetime caused by accelerating objects. Predicted by Einstein in 1916 [230], the strongest of these ripples are produced by the bulk motion of massive sources, specifically from the quadrupolar (or higher multipolar) component. Propagating at the speed of light, their amplitude decays with the inverse of the distance from the source.

The quest to directly detect the GWs began in 1960s with Joe Weber's pioneering experiment using resonant bars. The first direct detection of GWs from a merger of two black holes was finally seen on September 14, 2015 by the Advanced LIGO interferometers [231]. This was followed by the recent first detection of GWs from a merger of two neutron stars by Advanced LIGO-Virgo interferometers, accompanied by the observation of electromagnetic (EM) counterparts across the entire spectrum on August 17, 2017, opening the new field of multi-messenger astrophysics with GW sources [232, 233].

In the following, we mention some of the relevant expressions related to GW radiation from a BNS merger. For further details on the formulation, we refer to, for instance, [234]. Considering a binary system with point masses m_1 and m_2, such that we have the total mass given as $M = m_1 + m_2$, and reduced mass as $\mu = m_1 m_2/(m_1 + m_2)$, in the center of mass frame, for the bodies moving in circular orbits, the amplitudes of the 'plus' and 'cross' polarizations of the GW propagating along the direction $\hat{n} = (\cos\phi \sin\theta, \sin\phi \sin\theta, \cos\theta)$ can be written as

$$h_+(t) = \frac{4}{r}\mu R^2 \omega^2 \frac{(1+\cos^2\theta)}{2}\cos(2\omega t) \tag{6.5}$$

$$h_\times(t) = \frac{4}{r}\mu R^2 \omega^2 \cos\theta \sin(2\omega t)\ , \tag{6.6}$$

where R is the relative distance between the two masses and ω is the orbital frequency, and the quadrupole radiation is emitted at 2ω. The emission of GWs carries energy away from the system, leading to shrinking of the orbit, i.e., a decrease in the value of R. A decrease in the value of R leads to an increase in the value of ω, ultimately leading to an increasing in power emission. We can therefore calculate the total power emitted by the binary system by integrating over total solid angle, which has the following expression

$$P = \frac{32}{5}\mu^2 R^4 \omega^6\ . \tag{6.7}$$

The rate of change of the GW frequency is given as

$$\dot{f}_{\rm GW} = \frac{96}{5}\pi^{8/3}\mathcal{M}_C^{5/3} f_{\rm GW}^{11/3}\ , \tag{6.8}$$

where $\mathcal{M}_C = \mu^{3/5} M^{2/3}$ is the so-called *chirp* mass, and $f_{\rm GW} = 2\omega$ is the GW frequency, which is written as

$$f_{\rm GW} = \frac{1}{\pi}\left(\frac{5}{256}\frac{1}{\tau}\right)^{3/8}\mathcal{M}_C^{-5/8}\ , \tag{6.9}$$

where τ is the time to coalescence given as $\tau = t_{\rm coal} - t$. Thus, we can see that $f_{\rm GW}$ steadily increases as we approach the merger. Finally, in terms of the chirp mass and $f_{\rm GW}$, $h_+(t)$ and $h_\times(t)$ can be written as

$$h_+(t) = \frac{4}{r}\mathcal{M}_C^{5/3}(\pi f_{\rm GW})^{2/3}\frac{(1+\cos^2\theta)}{2}\cos(2\pi f_{\rm GW} t) \tag{6.10}$$

$$h_\times(t) = \frac{4}{r}\mathcal{M}_C^{5/3}(\pi f_{\rm GW})^{2/3}\cos\theta\sin(2\pi f_{\rm GW} t)\ . \tag{6.11}$$

For a BNS system of two equal masses $m_1 = m_2 = 1.4M_\odot$ assumed to be located at a distance of 100 Mpc, a rough estimation of the order of magnitude for the amplitude of the GW signal could be

$$h \simeq \frac{2m_1^{5/3}(2\pi f_{\rm GW})^{2/3}}{r} \sim 10^{-22}\left(\frac{M}{2.8M_\odot}\right)^{5/3}\left(\frac{0.01\text{ s}}{P}\right)^{2/3}\left(\frac{100\text{ Mpc}}{r}\right)\,, \tag{6.12}$$

GW170817

The gravitational signal, named *GW170817*, detected by the LIGO-Virgo interferometers, had a duration of approximately 100 s (calculated starting from ~ 23 Hz), and had the characteristic intensity and frequency consistent with the inspiral and merger of two neutron stars. The signal was identified by matched-filtering the data against the post-Newtonian gravitational waveform models, and had a combined signal-to-noise ratio of $\sim$32.4. The post-merger signal was difficult to observe with current detector sensitivities limited by the photon shot noise. The signal lied in one of the blind-spots of Virgo, and but the data from Virgo, combined with the LIGO data, allowed a precise sky position localization of the source to an area of ~ 16 deg^2 with 90% credibility [235].

From the signal, the extracted chirp mass had the value $\mathcal{M}_C = 1.186^{+0.001}_{-0.001}M_\odot$, and using different waveform models, the total mass of the system has been constrained between 2.73 and 2.77 $M_\odot$ within 90% credible intervals. Furthermore, the component masses have been constrained as $m_1 \in (1.36, 1.60)M_\odot$ and $m_2 \in (1, 1.36)M_\odot$, having a broad range due to correlations between their uncertainties [235].

The GW signal also carries information about the neutron star EOS. More specifically, tidal deformation or the tidal deformability parameter Λ (see Section 6.1.2.2 for definition), which is an EOS-sensitive quantity, has an effect on the structure of the waveform. With an increase in $f_{\rm GW}$, the tidal effects increasingly affect the phase, becoming significant above $f_{\rm GW} \simeq 600$ Hz. For GW170817, the tidal deformability parameters Λ_1 and Λ_2 (relating to masses m_1 and m_2 respectively) were estimated from the detected GW signal using the post-Newtonian models as reported in [235]. The predictions of the tidal deformability given by a set of representative EOS (that support NSs of mass $2.01M_\odot$) are compared with Λ_1 and Λ_2 estimated from the GW signal, are shown, for instance, in Figure 1 of [6]. These results deem EOS such as APR4 (predicting smaller Λ, and therefore, a more compact NS) as favourable over EOS such as H4 or MS1, which predict larger values of Λ (and therefore, a less compact NS) that lie outside the 90% credible region. Thus, our choice of APR4 EOS for the BNS simulations (see Section 6.2.1) is consistent with these results. Using the LIGO and Virgo data, [6] also reports the measurements of the two neutron star radii as $R_1 = 10.8^{+2.0}_{-1.7}$ km for the star with mass m_1 and $R_2 = 10.7^{+2.1}_{-1.5}$ km for the star with mass m_2.

6.1.2.4 Short gamma-ray bursts

Gamma-ray bursts (GRBs) are bright, rapid flashes of radiation that peak in the gamma-ray band, with the rate of occurrence averaged to one per day at cosmological distances. Having

randomly distributed sky positions, these events can last for a duration of a fraction of a second to even hundred or thousands of seconds.

They are one of the brightest known phenomenon, with luminosities that could be as high as $\sim 10^{54}$ erg/s, and are generally characterized by a collimated relativistic jet or an outflow drilling through the interstellar medium, assumed to be powered by a central engine. This prompt phase is often followed by afterglow signals, covering a broad range of the electromagnetic spectrum (X-ray to radio waves), which could last from seconds to several months.

There exists a bimodal distribution when it comes to observing GRBs. Thus, GRBs can be classified as *short-hard* and *long-soft* bursts, based on their duration and spectral hardness. The bimodal peaks are located at $T_{90} \sim 0.2$ s and $T_{90} \sim 20$ s (divided by a boundary around $T_{90} \sim 2$ s) [236], where T_{90} is the time interval in which the cumulative counts are 90% of the total background-excluded counts, taken from 5% till 95% of the total counts.

Long GRBs (with $T_{90} > 2$ s) are generally associated with supernovae observed only in star-forming galaxies, indicating the core-collapse of massive stars to be the progenitors of these events (supported by many observations). On the other hand, according to the leading explanation, short GRBs (SGRBs) (having $T_{90} < 2$ s) are produced by the coalescence of compact binary systems composed of two neutron stars or a neutron star and a black hole (BH).

SGRB events have also been observed in regions with low or negligible star formation (such as large elliptical galaxies), disfavouring the connection with core-collapse supernovae. The merger scenario as a progenitor, has further been supported by the evidence of a possible kilonova ejection (an expected consequence of a BNS/NS-BH merger; see Section 6.1.2.5 for further details) linked to the observed short GRB 130603B as reported in [237, 238]. A gravitational wave detection from a BNS merger along with a coincident SGRB observation would indeed validate this progenitor model. The GW170817 event has proved to be a crucial episode in this case, as along with the GW signal, an SGRB signal (GRB 170817A) emerged about 1.7 s after merger with a mildly relativistic outflow, and was also accompanied by radioactively-powered kilonova event [4]. There is still an ongoing debate on whether GRB 170817A was a canonical SGRB, so we discuss a couple of possible scenarios later in this Section.

SGRB central engines

Compact binary systems (NS-NS or NS-BH) merge in dynamical timescales in the order of $\sim$ ms, generally in baryon-poor environments, thus proving to be an ideal candidate for a central engine powering the relativistic SGRB jet. However, the nature of the central engine and the jet-launching mechanism remain partially unknown. In the following, we discuss two different SGRB central engine scenarios: (i) the standard BH-accretion disk scenario, and (ii) the magnetar scenario (see [239] for a review on SGRB central engines).

(i) Black hole - accretion disk scenario

This is the standard SGRB scenario in which the binary merger results in an eventual collapse of the metastable NS remnant, forming a BH surrounded by a massive accretion disk, and the

accretion process onto the BH is thought to power the jet. In particular, the accretion disks with masses $\gtrsim 0.1\ M_\odot$ and large accretion rates ($\dot{M} \sim 0.1 - 1\ M_\odot/\mathrm{s}$) are considered favourable candidates. Two main physical mechanisms that could act as possible energy sources to launch the relativistic outflow are the (i) *neutrino-driven mechanism* and the (ii) *magnetically-driven mechanism*.

In the former case, the accretion process produces highly energetic neutrinos and anti-neutrinos copiously, especially in the inner regions of the disk. They partially annihilate above the disk, turning into $e^\pm$ pairs, $\nu + \bar{\nu} \rightarrow e^- + e^+$, and thus, deposit thermal energy at the poles of the BH. This cumulative annihilation energy is found to be in the order of $\sim 10^{49}$ erg (as shown by recent simulations [240]), which might be enough to power only relatively low luminosity jets.

To fulfill the required energy budget, magnetic fields can play a crucial role. Amongst other models, the *Blandford-Znajek* mechanism [241] seems most promising. In this mechanism, a strong magnetic field threads the accretion disk of the spinning BH, generating a Poynting-flux by tapping the rotational energy of the BH, extracted via magnetic torque, which can power a collimated relativistic outflow.

Due to the complex nature of magnetic field evolution, general relativistic magnetohydrodynamic (GRMHD) simulations are necessary to explore the potential of this mechanism to form jets in BNS as well as NS-BH mergers. Many simulations have been able to show the formation of a structured poloidal magnetic field along the BH spin axis (see [34, 242, 243]) but only [37, 43, 44] have reported a successful formation of an incipient jet for a BNS merger scenario. However, one must note that for the BNS merger case, the authors have imposed the initial fields in excess of $\sim 10^{16}\,\mathrm{G}$, but nevertheless, it is a very promising result in support of the magnetically-driven jet model.

(ii) Magnetar scenario

As discussed earlier in Section 6.1.2.2, the post-merger remnant can be a long-lived NS (stable or metastable). We now consider a SGRB scenario based on this case, the so-called the *magnetar scenario*, which is a popular alternative to the standard BH-disk scenario. Here, the incipient jet is expected to be launched by a strongly magnetized NS surrounded by an accretion disk. Specifically, the large rotational energy of the magnetar, through an efficient channeling of magnetic fields, can possibly generate a collimated Poynting-flux dominated outflow.

This model is of a particular interest as it can explain the plateau-shaped X-ray afterglows or *X-ray plateaus* that accompany a significant fraction of all the observed SGRB events (as recently reported by the Swift satellite [244]). These X-ray plateaus, lasting for timescales $\gtrsim 100 - 1000$ s, can supposedly be produced by the electromagnetic spin-down radiation of the magnetar, whereas in the BH-disk scenario, the accretion timescales are much shorter ($\lesssim 1$ s) and thus such sustained soft X-ray emission can hardly be explained.

One major drawback of this scenario is the presence of a baryon-polluted environment surrounding the merger site. The dynamical ejecta emitted during merger as well as the baryon-loaded winds produced by the differentially rotating magnetar are expected to be of higher

density as compared to the BH-disk scenario, and thus can hinder a successful jet development.

GRB 170817A

Here, we briefly discuss the case of the gamma-ray signal GRB 170817A associated with the BNS merger event GW170817.

As mentioned earlier, a gamma-ray burst was observed about ~ 1.7 s after the BNS merger of GW170817. After constraining the initial sky position of the source within 28 deg^2, an electromagnetic follow-up campaign identified a EM counterpart in galaxy NGC 4993, consistent with the distance inferred from the GW data (~ 40 Mpc). The duration and spectrum of GRB 170817A are (marginally) in agreement with those of SGRBs, which could lead to a possible interpretation which establishes the connection between BNS mergers and SGRBs. However, there were some aspects of GRB 170817A that questioned whether this event resulted in a 'canonical' SGRB.

For the approximately known distance and redshift, the observed event resulted in a much lower energy ($E_{\mathrm{iso}} \simeq 3 \times 10^{46}$ erg) and luminosity ($L_{\mathrm{iso}} \simeq 2 \times 10^{47}$ erg/s) than expected in a canonical SGRB [232]. In addition, the X-ray and radio afterglows were observed respectively about 9 and 16 days after merger and with an increasing luminosity, hinting that the ultra-relativistic flow may not be pointing towards us. Further modelling of the event suggested that the observed signal should be the outcome of a mildly relativistic outflow along the line of sight. This led to two possible interpretations:

- GRB 170817A was a canonical SGRB pointing away from us, i.e., observed off-axis by 15–30°. The low-energy gamma-ray signal detected was not produced by the jet core but the interaction with the surrounding baryon-polluted environment formed a mildly-relativistic, wide-angled cocoon. The observed gamma-rays were produced by such a cocoon moving along the line of sight, rather than by the much more energetic core of the jet (see, e.g., [245]).

- GRB 170817A resulted from a choked jet and not from a canonical SGRB. The incipient jet from the merger was not powerful enough to pierce through the baryon-polluted environment, resulting in a jet-less, wide-angled and mildly relativistic outflow.

Recently, late radio observations provided the smoking-gun evidence for the first hypothesis [246], which is now strongly favoured.

6.1.2.5 Kilonovae

Material comprising the dynamical ejecta produced during the merger as well as the post-merger baryon-loaded winds, is very hot ($T > 10^9\,\mathrm{K}$) and neutron-rich (neutron density, $n_n > 10^{22}\,\mathrm{cm}^{-3}$), providing ideal conditions for rapid neutron capture (r-process) nucleosynthesis. This can in turn produce a copious amount of heavy elements to atomic mass numbers well above A=140. The radioactive decay of the newly-formed unstable heavy nuclei can power

an EM transient called as a 'kilonova' (less commonly known as 'macronova') emerging on timescales of days to weeks.

In order to quantify the key-observables of a kilonova, i.e., its peak time-scale, effective temperature and luminosity, we require the knowledge of three key ingredients: (i) the mass and velocity of the ejecta, (ii) the opacity κ of neutron-rich matter, (iii) the different sources responsible for heating the ejecta (giving rise to different 'flavors' of kilonovae; see, e.g., [26] for a review on kilonovae).

Figure 6.3 shows the different components of the ejecta produced during a BNS merger. In the equatorial plane, tidally-driven dynamical ejecta are highly-neutron rich ($Y_e \lesssim 0.1$) and

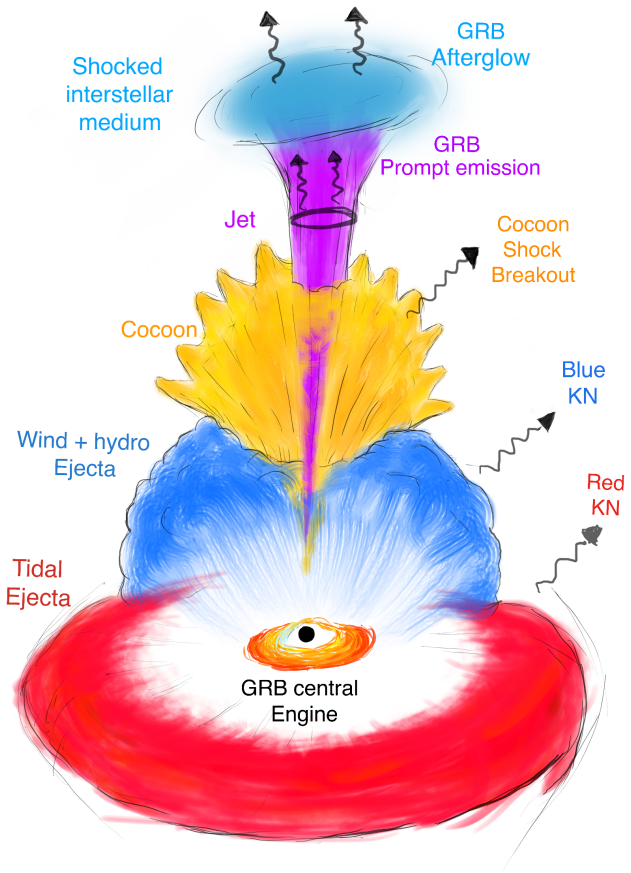

Figure 6.3: Schematic representation of the different ejecta components produced after a BNS merger. The central engine here is the BH-accretion disk, powering a relativistic jet (in purple) along the BH spin axis. The red component denotes the dynamical ejecta, while the blue component shows the hydrodynamic and wind ejecta. Ejecta matter heated by the jet (cocoon) is shown in yellow. The different components are not represented in scale. Figure taken from [217].

can go very far in producing heavier and heavier elements, including in particular, the group of lanthanides. The resulting material has high opacity ($\sim 10 - 30\,\mathrm{cm}^2/\mathrm{g}$) and results in a 'red' kilonova emission which peaks at NIR wavelengths and on a timescale of several days. In the polar directions, the mass ejected dynamically by shock heating is relatively neutron-poor ($Y_e \gtrsim 0.3$), preventing lanthanide production and leading to a lower opacity ($\sim 1\,\mathrm{cm}^2/\mathrm{g}$). In this case, a 'blue' kilonova emission emerges, peaking at optical wavelengths and on a timescale of about one day. Moreover, a UV transient may be seen due to the decay of free neutrons present in the outer layers of the polar ejecta.

A possibly dominant contribution to the ejecta comes then from the more isotropic post-merger winds, originating from the metastable massive NS (MNS) remnant prior to collapse, and by outflows from the accretion disk after BH formation. While the latter is likely a candidate contributing to a red kilonova [21], the former can act as a possible source of the blue kilonova [20]. For a longer-lived NS remnant, neutrinos emitted by the latter can increase the electron fraction of the ejecta, disfavouring lanthanide production and resulting in a bluer kilonova.

Figure 2 of [3] shows the spectral evolution of the UV/optical/IR kilonova transient from the source of the GW170817 event (officially named *AT 2017gfo*). It includes a blue component that peaks about one day after the merger between UV and blue optical wavelengths, with a maximum at 600 nm [3]. This component is characterized by a total luminosity of 3.2×10^{41} erg/s, ejecta mass of about $\sim 10^{-2} M_\odot$, expansion velocity of about $0.2\,c$, and opacity of about $0.5\ \mathrm{cm}^2/\mathrm{g}$. Therefore, this is a lanthanide-poor component which matches the properties of the shock-driven ejecta or early post-merger winds. After a few days, a second components emerges. The transient peaks in NIR, hinting towards a red-kilonova emission, with ejecta having mass of about $\sim 5 \times 10^{-2} M_\odot$ and expansion velocity of $0.1\,c$. The opacity of the transient increases with time to about $10\ \mathrm{cm}^2/\mathrm{g}$, giving a lanthanide-rich component that can be explained as associated with post-merger accretion disk winds.

6.2 First 100 ms of a long-lived magnetized neutron star formed in a BNS merger

6.2.1 Initial data and setup

In JVK1, the physical and numerical setup of the simulation is analogous to the fiducial APR4 equal-mass model discussed in [35]. To compute the initial configurations of the NSs, we use a publicly available code `LORENE` (which stands for *Langage Objet pour la RElativité NumériquE*). `LORENE` consists of a set of C++ classes to solve various problems in the field of numerical relativity. It provides a set of tools to solve partial differential equations by means of multi-domain spectral methods (briefly discussed in [247]). We use `LORENE` to generate the initial data for an equal mass (i.e. mass ratio $q = 1$) BNS system with gravitational mass of each NS set as $1.35\,M_\odot$. The initial binary system is irrotational and on a quasicircular orbit, with an initial coordinate separation of 45 km corresponding to a proper separation of ~ 59 km. The EOS employed for constructing the initial data is the piecewise-polytropic approximation

Table 6.1: Initial data parameters: mass ratio ($q = M_{\rm g}^1/M_{\rm g}^2$), total baryonic mass of the system ($M_{\rm b}^{\rm tot}$), baryonic and gravitational masses of each star at infinite separation ($M_{\rm b}$ and $M_{\rm g}$), compactness ($M_{\rm g}/R_c$, dimensionless), initial orbital frequency and proper separation (f_0 and d), initial magnetic energy ($E_{\rm mag}$), initial maximum value of magnetic field strength ($B_{\rm max}$), and A_b, the scaling parameter used in Equation (3.33) in order to fix $B_{\rm max}$.

Model	B1e16
q	1
$M_{\rm b}^{\rm tot}$ $[M_\odot]$	2.98
$M_{\rm b}$ $[M_\odot]$	1.49 – 1.49
$M_{\rm g}$ $[M_\odot]$	1.35 – 1.35
$M_{\rm g}/R_c$	0.176 – 0.176
f_0 [Hz]	283
d [km]	59
$E_{\rm mag}$ $[10^{48}$erg]	1.592
$B_{\rm max}$ $[10^{16}$G]	1.0
A_b	2587

of the corresponding nuclear physics (tabulated) APR4 EOS, taken from [110]. To maintain causality, this EOS is approximated with two additional pieces at high (core) densities (see [110] for details). During the evolution, a hybrid EOS (see Section 2.2.6.3) is employed, adding a thermal component via an ideal-fluid EOS with adiabatic index of $\Gamma = 1.8$.

The magnetic field is then added manually to the initial BNS model as `LORENE` cannot compute equilibrium configurations for magnetized binary systems. Since the magnetic field structure in actual NSs is not well-known, we use the an analytical prescription for the vector potential A_ϕ given by Equation (3.33), using $p_{\rm cut} = 0.04\ \max(p)$ and $n_s = 2$, which yields an initial dipolar magnetic field confined to the interior of the stars. The value of A_b is set such that the initial maximum magnetic field strength is $B_{\rm max} \simeq 10^{16}\,$G, corresponding to a very large initial magnetic energy of $E_{\rm mag} \simeq 1.6 \times 10^{48}\,$erg. The latter is almost an order of magnitude higher than fiducial model of [35]. The reason for this choice is that our current resolution is not sufficient to fully capture the main magnetic field amplification mechanisms that act on small scales (a common limitiation affecting all current numerical relativity simulations, e.g. [248]), which are expected to bring the field up to post-merger magnetic energies of order $10^{51}\,$ergs. Starting with a lower (and more realistic) initial magnetic energy would lead to post-merger magnetic field orders of magnitude weaker than expected. Since we want to explore more realistic post-merger magnetization levels, we compensate by starting with a higher initial field. The most relevant initial parameters of our model are summarized in Table 6.1.

For the evolution, the GRMHD equations are evolved by `WhiskyMHD`, which solves them using high-resolution shock-capturing schemes, i.e., HLLE approximate Riemann solver for flux computations along with piecewise-parabolic method (PPM) for reconstruction (see Section 2.3.5 for details), and employing '3eqs' C2P scheme (see Section 3.1.3.2), and 4th order Runge-

Kutta for time-stepping. This code is coupled with `Einstein Toolkit` (ET), in particular the `MacLachlan` code, which solves the Einstein equations using the BSSNOK formalism (see Section 2.1.2). `WhiskyMHD` evolves the vector potential and then computes the magnetic field from it, thus preserving its divergence-free character. Moreover, to avoid the spurious magnetic field effects at refinement boundaries, we use the modified Lorenz gauge (see Section 2.2.5.2). We also impose an artificial floor density of $\rho_{\rm atm} \simeq 6.3 \times 10^6\,{\rm g/cm^3}$ (as in [35]).

For the grid-setup, 'moving box' mesh refinement is implemented via the `Carpet` driver, employing 6 refinement levels. During inspiral, the two finest levels follow the NSs, while larger fixed grids replace moving grids shortly before merger. At merger, regridding is switched to fixed-mesh refinement. The grid spacing in the finest refinement is always $dx = dy = dz \approx 220$ m. Lastly, in order to save computational resources, reflection symmetry across the $z = 0$ plane is considered.

6.2.2 Merger dynamics

We evolve the system up to $\sim 95\,$ms after merger. In Figure 6.4, we show the meridional and equatorial snapshots of the rest-mass density from the merger time to the end of the simulation.

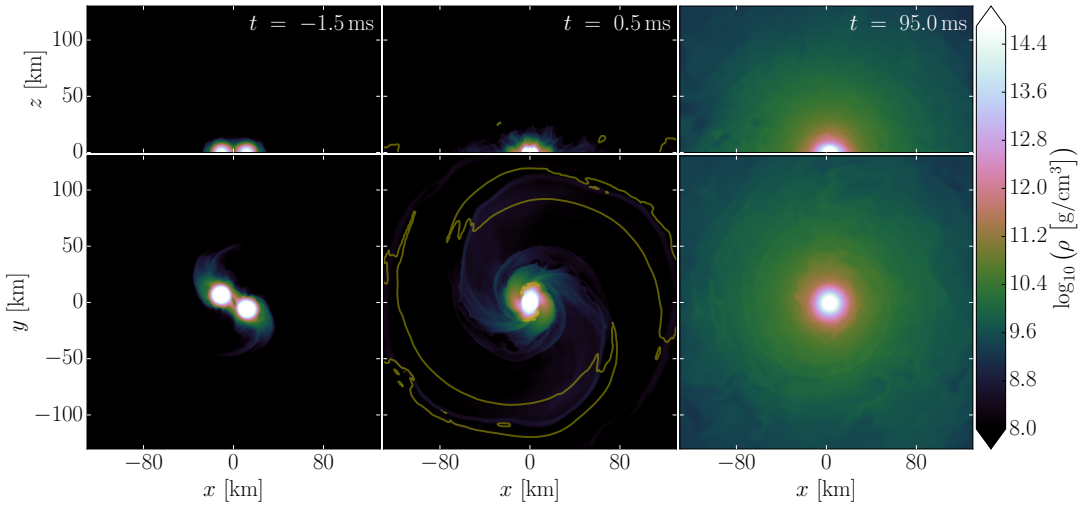

Figure 6.4: Snapshots of rest-mass density evolution in the meridional (top panels) and equatorial (bottom panels) planes. The yellow contours indicate unbound matter computed via the geodesic criterioin (see text for details). Here, $t = 0$ corresponds to the merger time. Figure taken from JVK1.

The merger produces a differentially rotating, long-lived supramassive NS remnant, which reaches a quasistationary and axisymmetric configuration in first $\sim 50\,$ms. For the next $\sim 45\,$ms of evolution, we find the density distribution to be fairly constant up to very large radii ($\sim 400\,$km), in particular along the remnant spin axis as shown in Figure 6.5. The matter distribution is also roughly isotropic for radial distances between 50 and 400 km, whereas below $r \approx 50\,$km, we find the remnant structure to be surrounded by a torus-shaped outer envelope

(Section 6.2.5 and Figure 6.16a). When comparing with the lower magnetization cases of

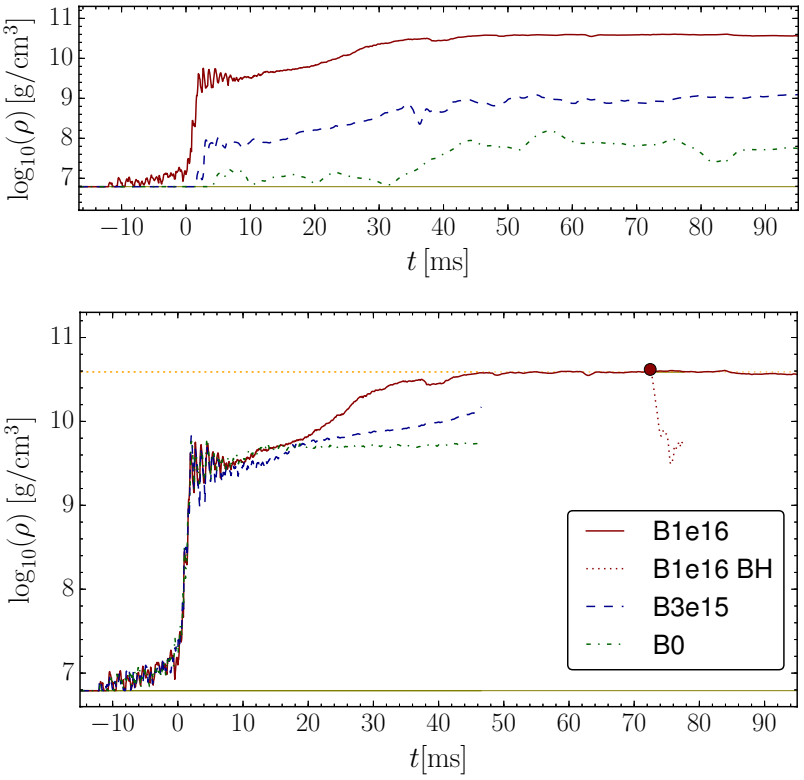

Figure 6.5: Top panel shows the rest-mass density along the orbital axis averaged over distance ranges $30-50$ km, $150-200$ km, and $400-500$ km (continuous, dashed, and dot-dashed lines). The horizontal line represents the atmosphere density floor. Bottom panel depicts rest-mass density along the orbital axis averaged in the distance range $30-50$ km for the present simulation with and without collapse ('B1e16 BH' and 'B1e16') and for the lower and zero magnetic field models in [35] ('B3e15' and 'B0'). Figure taken from JVK1.

[35], we find the remnant to be surrounded by a much denser environment, since for example, the rest-mass density close to the remnant and along its spin-axis is roughly $\sim 4\times10^{10}$ g/cm^3, about one order of magnitude higher than the non-magnetized case (Figure 6.5b). The remnant environment is thus polluted due to the post-merger baryon-loaded winds driven primarily by magnetic pressure at this high magnetization level.

This further results in a magnetized outflow spread around larger scales, consisting of a faster polar component (within $\sim40^\circ$ from the remnant spin axis) moving at a radial velocity up to 0.1 c, accompanied by a slower isotropic component with radial velocity below 0.05 c, as depicted in Figure 6.6. We estimate a cumulative mass outflow across a spherical surface of radius $r = 300$ km to be around $\sim0.1\,M_\odot$, which excludes the contribution from the tidal and

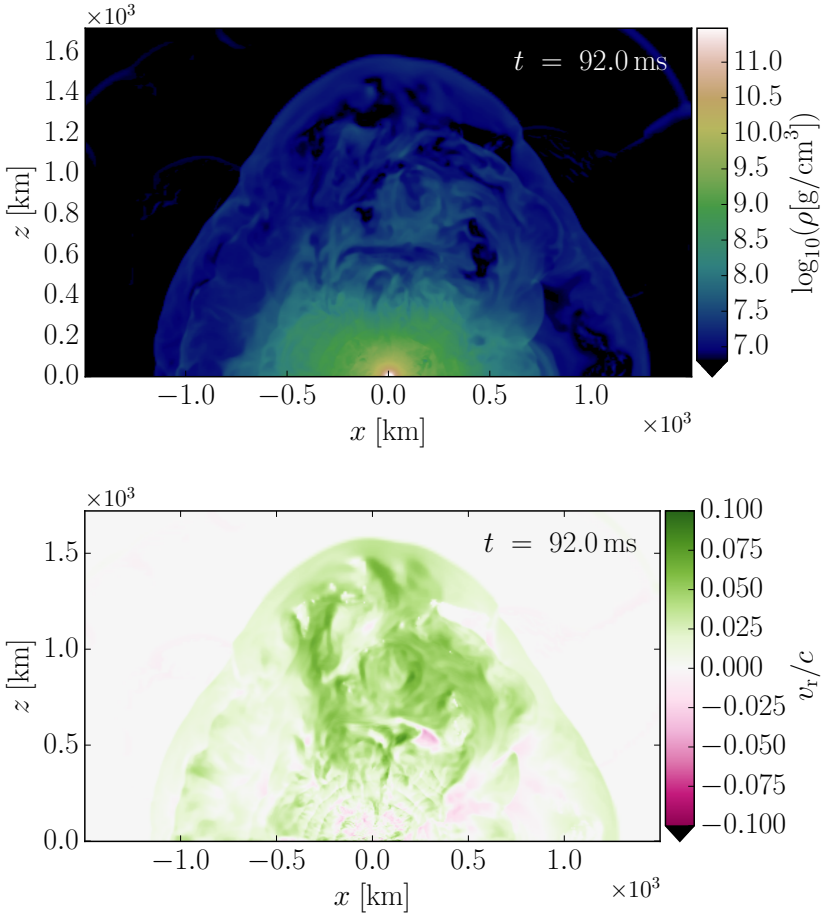

Figure 6.6: Top panel illustrates large scale meridional view of the rest-mass density towards the end of the simulation. Bottom panel shows the radial velocity of the outflowing material (positive values indicate outwards motion). Figure taken from JVK1.

shock-driven dynamical ejecta of $\simeq 0.015\, M_\odot$.

At larger distances, a significant portion of this material becomes unbound, contributing to a very massive ejecta component. The contour lines in Figure 6.4 represent the fraction of unbound matter, computed via the geodesic criterion[3]. Such magnetized post-merger outflows can possibly contribute to the early (or "blue") part of the radioactively-powered kilonova signal observed in association with GW170817 (see Section 6.3 for further discussion).

[3]The geodesic criterion is given as $u_t \leq -1$, which allows to check if the fluid element can potentially escape to infinity. Here, u_t is the covariant time component of the fluid element 4-velocity. In Newtonian limit, we have $u_t \approx -1 - \phi - v^2/2$, where ϕ is the gravitational potential. At large separation from the gravitational source, one can neglect the gravitational potential, $\phi \simeq 0$, giving $u_t \approx -1 - v^2/2 \leq -1$. Thus, the criterion imposes fluid element to have a finite velocity at infinity.

As an experiment to see how the collapse to a BH would affect the surrounding environment, we performed another simulation starting from 72 ms after merger, manually inducing the collapse by modifying the EOS parameters at supranuclear densities[4]. The collapse forms a BH near the center of the domain, and we evolved this system for another ~ 5 ms (see Figure 6.7). The final mass and dimensionless spin of the formed BH are $M_{\rm BH} \simeq 2.5\,M_\odot$ and $\chi \equiv Jc/GM^2 \simeq 0.5$. The BH begins to accrete the surrounding matter, and starts forming an accretion disk of $M_{\rm disk} \simeq 0.1\,M_\odot$, and we notice that the material along the spin axis is accreted too, creating a low density funnel. For instance, in Figure 6.7, the rest-mass density at $r = 30$ km from the center is about one order of magnitude smaller than the non-collapsing case.

When plotting the relative difference in rest-mass density between the collapsing and non-collapsing cases, as shown in Figure 6.8, we find that only the matter within ~ 200 km is affected due to BH formation, while the rest of the regions show negligible to no impact.

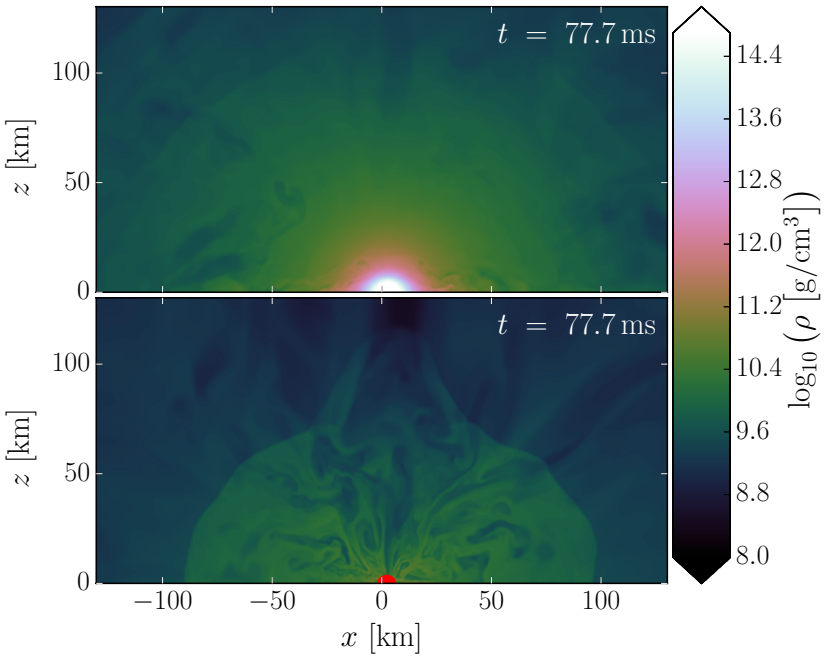

Figure 6.7: Meridional view of rest-mass density for the non collapsing (top) and collapsing (bottom) cases. Red region in the bottom panel depicts the black hole horizon. Figure taken from JVK1.

[4]To induce the collapse, we modified APR4 parameters to H4 [35] ones at $\rho > 2 \times 10^{14}\,{\rm g/cm^3}$ to obtain a less stiff EOS in the NS core. This only related a portion of the NS core which ultimately gets swallowed in the BH.

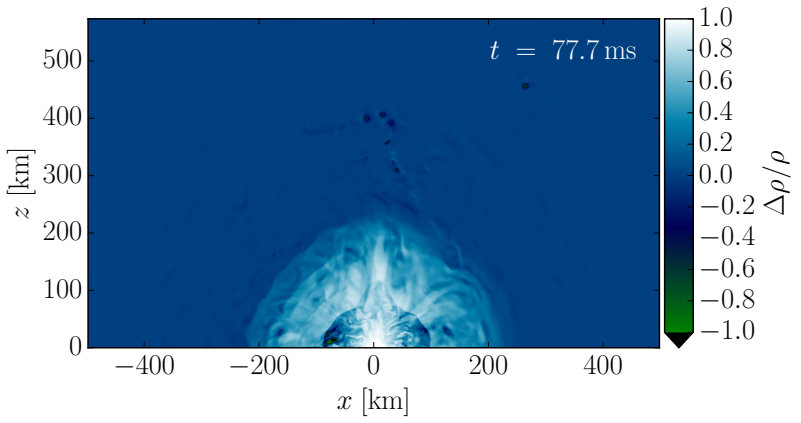

Figure 6.8: Meridional view of the relative difference in rest-mass density between the non-collapsing and collapsing cases. Figure taken from JVK1.

6.2.3 Magnetic fields

Here, we focus our attention on the magnetic field evolution for the system in hand. In Figure 6.9, we see that magnetic fields go through different stages of amplication, reaching a saturation around 50 ms after merger. Prior to merger, we observe about an order of magnitude increase in magnetic energy (from $\sim 10^{48}$ erg to $\sim 10^{49}$ erg), which could likely be caused due to the time-varying tidal deformations within during the late inspiral, converting part of the associated kinetic energy into magnetic energy. However, any unphysical causes due to, for e.g., initial data or simulation setup cannot be completely ruled out [35].

The Kelvin-Helmholtz instability (KHI) comes into play when the two NSs come into contact. In this scenario, a shear interface (or a vortex sheet) is formed where the tangential components of the velocity exhibit a discontinuity, leading to small-scale perturbations and developing KHI. This causes curling of the interface, forming a series of vortices, and eventually affecting the structure of the magnetic field lines in such localized regions. Thus, an increase in the magnetic field strength and magnetic energy is observed right after merger. However, the numerical resolution employed here (minimum grid spacing of $dx \approx 220$ m) is insufficient to fully capture the small-scale amplification due to KHI; in reality, we expect the magnetic energy to grow much faster. See [249, 250] for further discussions on the role of KHI for magnetic field amplification in BNS mergers. Later on, KHI is substituted by magnetic winding and the magnetorotational instability (MRI) as the dominant source of amplification [251–253]. Once the magnetic field reaches the final saturation level, magnetic energy is $E_{\rm mag} \simeq 2 \times 10^{51}$ erg and the magnetic field strength has a maximum of $B_{\rm max} \simeq 10^{17}$ G. To understand the possible contribution of MRI to the observed amplification, we follow the evolution of its fastest growing mode wavelength, approximately given as

$$\lambda_{\rm MRI} \approx \frac{2\pi}{\Omega} \frac{B}{\sqrt{4\pi\rho}} \ , \tag{6.13}$$

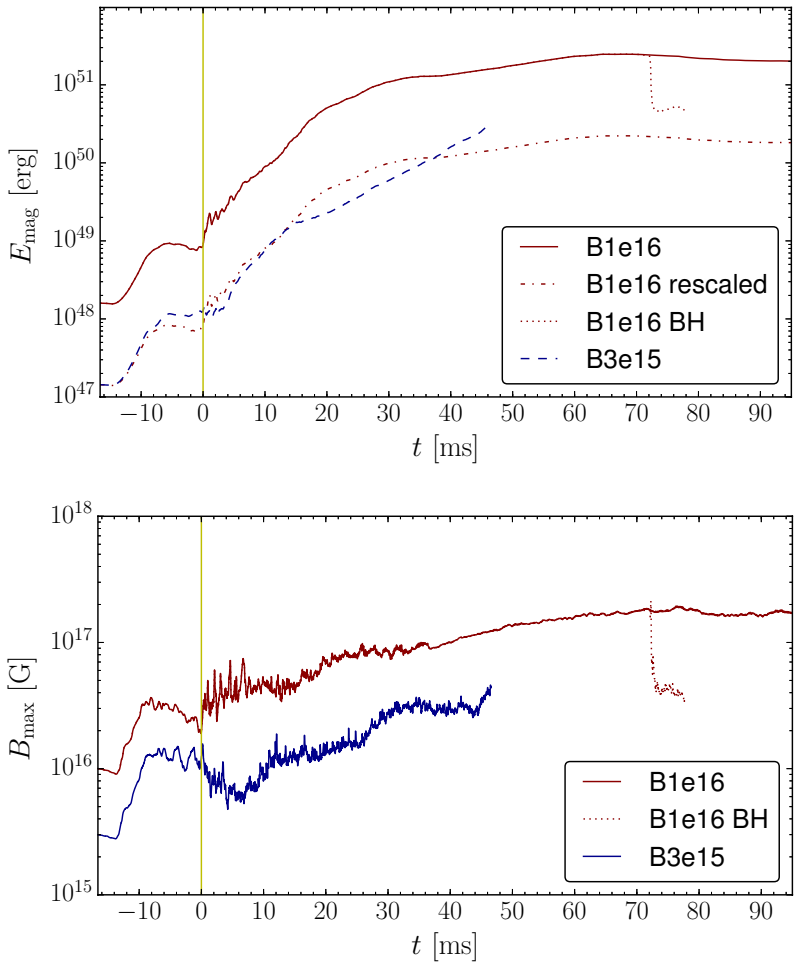

Figure 6.9: Evolution of magnetic energy (top) and maximum magnetic field strength (bottom) for the present simulation with and without collapse ('B1e16 BH' and 'B1e16') and for the lower magnetic field model in [35] ('B3e15'). Vertical line denotes the time of merger. In the top panel, we also rescaled 'B1e16' to match the initial value of model 'B3e15' for comparison. Figure taken from JVK1.

where B is the magnetic field strength and Ω is the angular velocity. This wavelength is typically much smaller than the system we consider, and in order to resolve it we require either very high initial magnetic fields or better spatial resolution (so that $\lambda_{\rm MRI}$ is covered by at least 10 grid points). Figure 6.10 shows the meridional snapshots of $\lambda_{\rm MRI}$ over the grid-spacing 10 and 30 ms after merger. At 30 ms, we notice that $\lambda_{\rm MRI}$ is covered by $10-1000$ grid points in most regions, except for the inner region enclosed in a 10 km radius. Since we require differential rotation with a negative angular velocity gradient in order to activate MRI, it does not affect the inner regions ($r < 10$ km). Overall, this result supports that MRI plays an important role

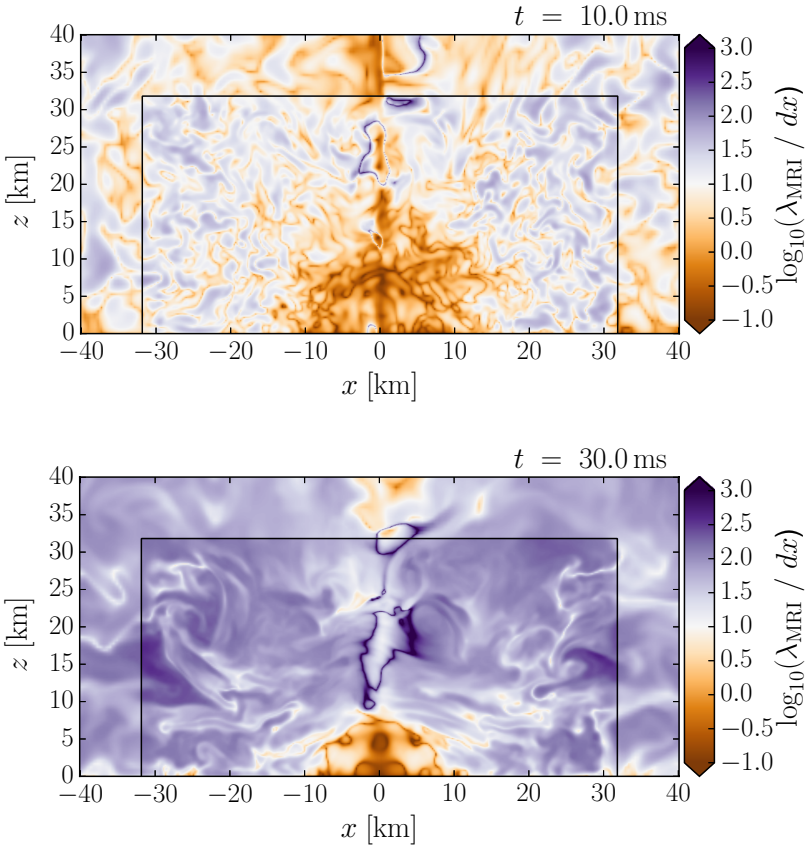

Figure 6.10: Meridional view of $\lambda_{\rm MRI}$ (see text) over the grid-spacing, 10 and 30 ms after merger. Figure taken from JVK1.

in amplifying the magnetic fields for $t \gtrsim 30\,$ms (where $t = 0$ is the merger time).

When comparing the growth in magnetic energy (Figure 6.9) with the results of [35] with a lower initial magnetization, we notice the initial evolution to be quite similar. However, about 30 ms after merger, the present simulation starts moving towards saturation whereas the results from [35] show no sign of saturation. Even though the latter simulation is not long enough to determine when saturation would begin, it is likely that the onset of saturation depends mostly on magnetic energy. We do not expect $E_{\rm mag}$ to grow much larger than $\sim 10^{51}\,$erg, also in agreement with, e.g., [249, 254], thus providing an upper limit for magnetization that realistic BNS mergers can produce (for the given mass and EOS).

In the case where a BH is formed, it rapidly accretes a large fraction of magnetized matter, thus removing the corresponding magnetic energy from the system. This drop in energy (nearly $\sim$80%) can be seen for the collapsing case in the top panel of Figure 6.9. However, after collapse, further magnetic field amplification is still possible within the accretion disk surrounding the

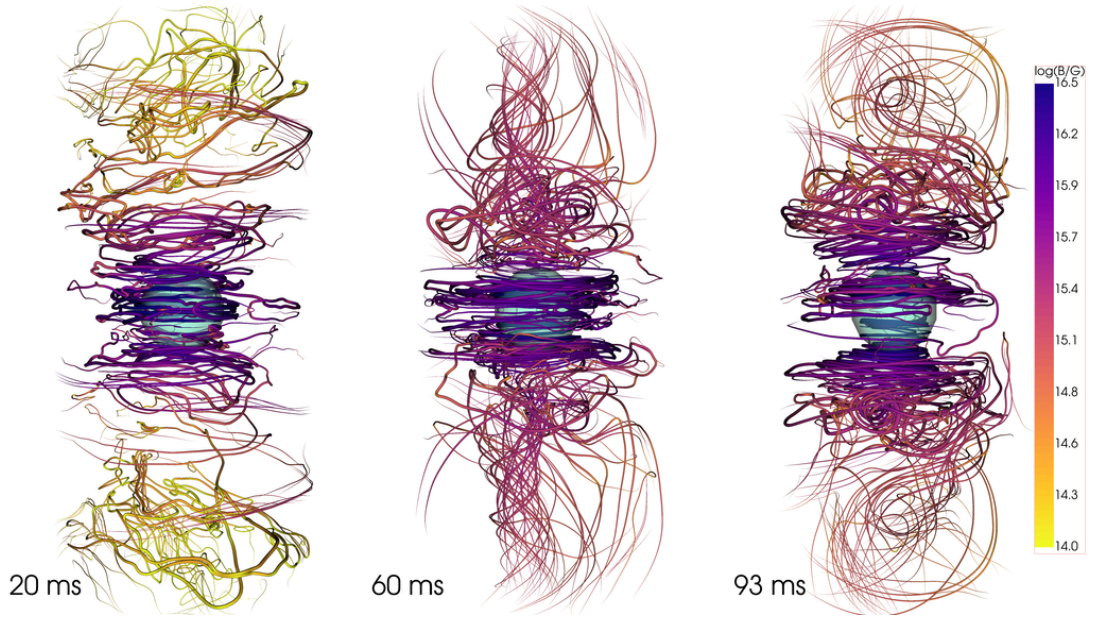

Figure 6.11: Magnetic field structure 20, 60, and 93 ms after merger. The sphere (in cyan) of radius 10 km is placed at the remnant center of mass, as scale reference. Field line colors indicate the magnetic field strength. Figure taken from JVK1.

BH.

Next, we study the structure of magnetic field lines close to the remnant as a shown in Figure 6.11. To make the plot, we employ the same technique of [34], showing only the field lines which are (on average) strongest along cones of constant angle to the rotation axis. Toroidal fields in the equatorial region get strongly amplified between 20 to 60 ms after merger, whereas along the remnant spin axis, a narrow ordered helical structure emerges. Here, the poloidal component seems to dominate, and the field strength grows from $\sim 10^{14}$ to more than 10^{15} G. Towards the end of the simulation, the helical features are replaced by a more disordered field line distribution along the axis, and the strongest field lines are predominantly toroidal up to 20 km from the remnant center.

On larger scales extending to a few hundred kilometers, the field distribution shows a mixed toroidal-poloidal character, with field lines of strength $\gtrsim 10^{15}$ G winding around the axis, roughly along a wide cone, as shown in Figure 6.12. This is indicative that at later times, a global magnetic field structure might be emerging. Since we started with the initial magnetic field confined completely inside the NSs, this emergence of a large scale field is entirely due to the dynamical and geometrical properties of the remnant. On largest scales, matter outflows shape the overall magnetic field distribution (Figure 6.13), having comparable toroidal and poloidal field components. While the toroidal component remains slightly stronger in the largest part of the volume, along the spin axis, the poloidal field strength is still almost as strong as 10^{14} G

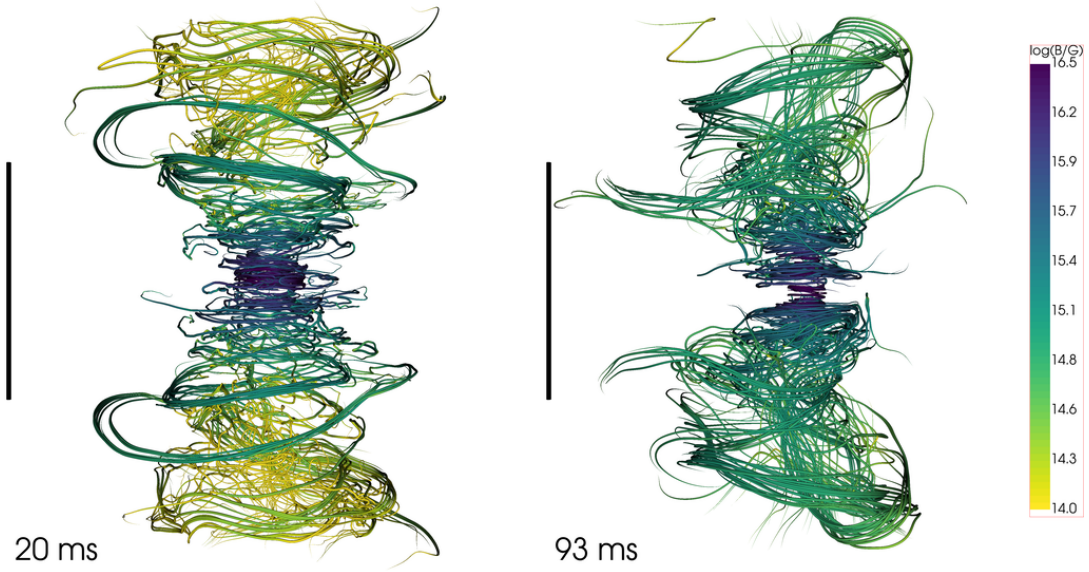

Figure 6.12: Same as Figure 6.11 at larger spatial scale. The vertical bar corresponds to 100 km. Figure taken from JVK1.

up to radii above 1000 km.

6.2.4 Short gamma-ray bursts

As stated earlier, one of the main goals of this work is to investigate whether a long-lived NS remnant could launch a jet compatible with a SGRB (and in particular GRB 170817A). Till the end of our simulation, we do not see any direct sign of jet formation. We rather observe a non-collimated, non-relativistic, and dense magnetized outflow along the polar direction, with magnetic-to-fluid pressure ratio $\beta \equiv b^2/2p$ between 0.1 and 10 in most regions as depicted in Figure 6.14. Here, $b^2 \equiv b^\mu b_\mu$, and b is the magnetic field as measured by the comoving observer (see Section 2.2.4 for details). To launch an incipient jet, the required outflow is expected to be much faster, more magnetically dominated, and with lower density (e.g. [43]). Moreover, towards the end of the simulation, we find the baryon-loaded wind to be too heavy to be accelerated up to Lorentz factors $\Gamma > 10$, as necessary for SGRB jets, and rather present as a potential obstacle for any jet launched by the remnant at later times, requiring additional energy to drill through it. In particular, the density remains too high ($\gtrsim 10^8\,\mathrm{g/cm^3}$) for distances up to $\sim$400 km (Figure 6.5), implying the jet formation timescale to be $\gg$100 ms (if any).

In order to assess the overall energy budget of the system, we compute the rotational energy (main energy reservoir in this particular scenario) according to [255, 256]

$$E_{\mathrm{rot}} = \frac{1}{2}\int d^3x\, \alpha\sqrt{\gamma}\,\Omega\, T^0_\phi \ , \tag{6.14}$$

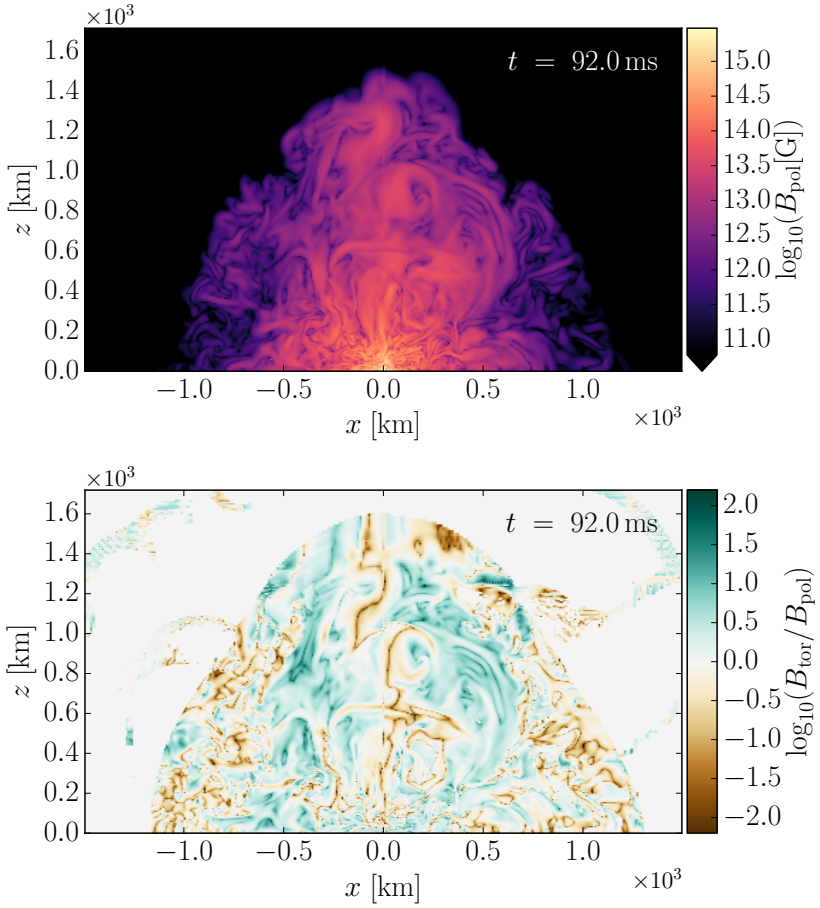

Figure 6.13: Snapshots of poloidal magnetic field strength (top) and the toroidal-to-poloidal field strength ratio (bottom) on large scales. For visualization purposes, we set the latter to zero where the rest-mass density is close to the artificial floor value ($< 1.5 \times \rho_{\rm atm}$). Figure taken from JVK1.

where α, γ, Ω, $T^{\mu\nu}$ are lapse, 3-metric determinant, angular velocity, and stress-energy tensor. In Figure 6.15, we plot evolution of $E_{\rm rot}$, which shows a linear decrease by $\Delta E_{\rm rot} \simeq 6\times10^{52}\,{\rm erg} \simeq 0.03\,M_\odot$ over the last 50 ms. This decrease is likely governed by the consumption of differential rotation over viscous timescales. Note that such timescales can be resolution dependent (see Section 6.2.5 for details). Overall, we find that $>99\%$ of $E_{\rm rot}$ is always contained within the region defined by defined by $z < 10\,{\rm km}$ and cylindrical radius $r_{\rm cyl} < 20\,{\rm km}$. Most of the above $\Delta E_{\rm rot}$ is consumed for rearranging and heating up the remnant, and only a small fraction is transferred to the surrounding matter. And at the end of our simulation, the remaining rotational energy ($\simeq 2 \times 10^{53}\,{\rm erg}$) would still be sufficient to power a SGRB jet. However, the question remains whether any mechanism would get activated at later times to convert this energy efficiently into jet energy.

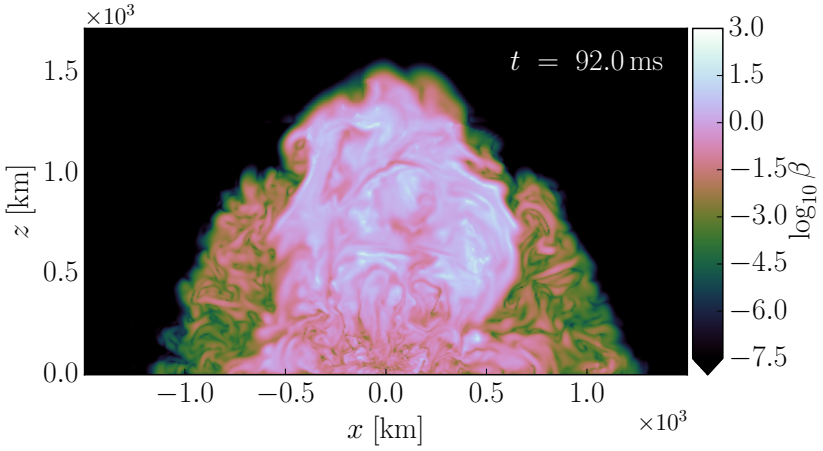

Figure 6.14: Magnetic-to-fluid pressure ratio β on the meridional plane. Figure taken from JVK1.

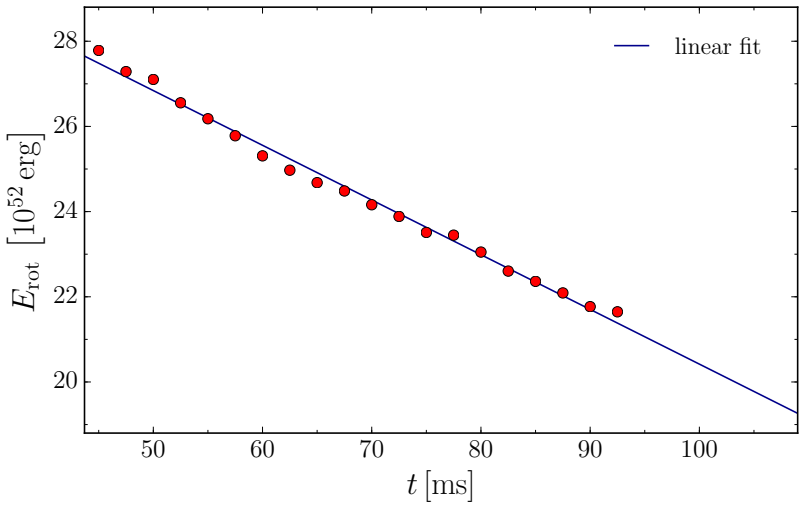

Figure 6.15: Rotational energy evolution (dots) along with a linear fit (continuous line). Merger time is $t = 0$. Figure taken from JVK1.

Moreover, assessing the system conditions, we neither have an accretion disk around the central remnant (Section 6.2.5) nor a strongly magnetized, low density funnel along the remnant axis. Therefore, even though we cannot conclusively rule out that the NS remnant could launch a jet at later times energetically compatible with GRB 170817A, our current findings point in disfavour of such a scenario. Note that our simulation neglects neutrino-radiation and its associated effects. Including such effects could possibly clean up the baryon polluted environment along the remnant spin axis, creating the right conditions to launch an incipient

jet [38]. We leave this study for future work.

We now turn to the case in which the remnant instead collapses to a BH at 72 ms after merger. Since enough matter remains outside the BH, which could form an accretion disk of $\sim 0.1\,M_\odot$ (see also Section 6.2.5), an incipient jet could possibly by launched by the resulting BH-disk system via the Blandford-Znajek mechanism [241], with power [257]

$$L_{\rm BZ} \sim 10^{52} \Big(\frac{\chi}{0.5}\Big)^2 \Big(\frac{M_{\rm BH}}{2.5\,M_\odot}\Big)^2 \Big(\frac{B_{\rm BH}}{10^{16}\,{\rm G}}\Big)^2 \ {\rm erg/s}\ .$$

In the above expression, we use the reference values from our simulation for the dimensionless BH spin χ, mass $M_{\rm BH}$, and magnetic field strength at the poles $B_{\rm BH}$.

The formed jet would still have to drill through a massive ejecta layer ($\sim 0.1\ M_\odot$), especially the regions from and above $z = 200$ km along the spin axis. This would likely result in a jet head with nonrelativistic velocities (e.g. [258]), assuming a jet half opening angle $\theta_{\rm j} \gtrsim 5^\circ$. Using Equations 3 and 4a of [258], we roughly estimate the jet breakout time as 0.01, 0.03, and 0.14 s for a constant $\theta_{\rm j}$ of 5°, 10°, and 20°, respectively, while for $\theta_{\rm j} \gtrsim 30^\circ$, the jet head would not be fast enough to ever reach the ejecta front. Therefore, one can expect a successful jet despite the heavy ejecta for a collimation of $\theta_{\rm j} \lesssim 20^\circ$ and an engine duration $\Delta t_{\rm engine} \gtrsim 0.15$ s.

Factors related to remnant life-time, initial magnetization level, NS masses and EOS, can possibly alter the above results. We leave the exploration of systems with such different properties for future work.

6.2.5 Remnant structure and rotation profile

Next, we turn our attention to the remnant properties at smaller scales. In Figure 6.16, we show the density distribution of the remnant 10 and 72 ms after merger. At 10 ms after merger, the remnant's inner core is surrounded by a torus-shaped outer envelope, a typical structure for BNS merger remnants (e.g. Figure 16 in [173]). In time, this envelope undergoes a general expansion, occupying an increasing volume while attaining a more spherical configuration. Towards the core, the change in radius becomes gradually smaller. This can be seen in Figure 6.16. However, note that our simulations do not take into account neutrino cooling effects, which might aid in maintaing a less dense environment along the remnant spin axis (see, for instance, [38]).

Following the approach of [174], we compute baryonic mass and proper volume enclosed in the surfaces of constant mass density, obtaining a gauge independent mass-inside-volume relation. We express proper volume by the radius of an Euclidian sphere of same volume. Using this technique, at the end of the simulation, we find a plateau in the mass-inside-radius relation which allows us to define a fiducial remnant baryon mass of $2.75\,M_\odot$.

In Figure 6.17, we plot the remnant's rotational profile along the equator. In general, the remnant is characterized by a slowly rotating central core (circumferential radius $r_{\rm c} \lesssim 5$ km) surrounded by a rapidly rotating outer layer. Further out, the profile becomes nearly Keplerian since the centrifugal force starts dominating over the pressure. Such differential rotation curves have already been reported in literature [35, 110, 173, 174, 259–261]. For the present simulation, we find the maximum spin frequency to be around 1.7 kHz, and the maximum is located at

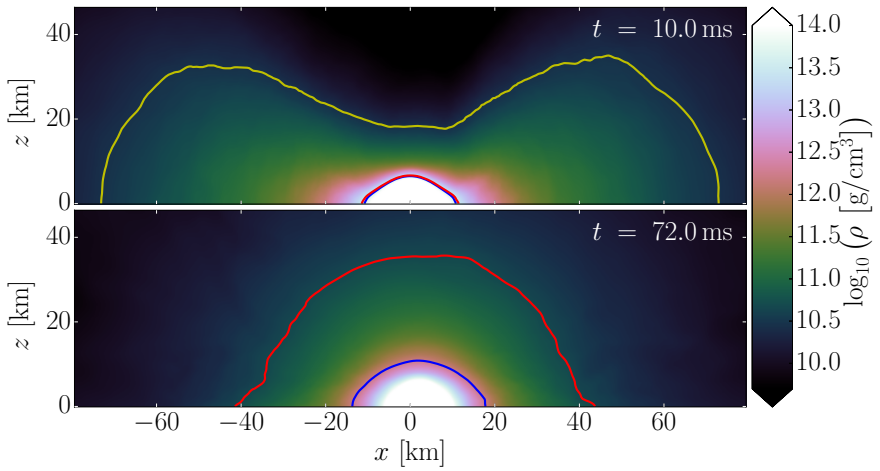

Figure 6.16: Rest-mass density distribution on small scales at 10 and 72 ms after merger. Plots are averaged over 4 ms around the given times in order to remove contributions from oscillations. Isodensity contours shown in blue, red, and yellow (visible only in top panel) contain the fiducial remnant baryon mass, 93% of the total baryon mass (red), and 98% of the total baryon mass respectively. Figure taken from JVK1.

$r_c \approx 12$ km. For comparison, we computed the properties of uniformly rotating NS obeying the same zero-temperature EOS as the initial data. In Figure 6.17, we show rotation rate and radius for a model with the baryonic mass of the fiducial remnant and its angular momentum at the end of the simulation. We find the final rotation rate for uniform rotation to be quite similar to the maximum rotation rate 80 ms after merger. Moreover, comparing to the sequence of constant baryonic mass shown in the same figure, the central rotation rate is much lower than the minimum allowed uniform rotation rate for the given mass. At the same time, the remnant extends to larger radii than possible for a uniformly rotating star.

In time, the inner core gains angular momentum at the expense of the outer envelope (top panel of Figure 6.17), moving towards uniform rotation (a flat rotation profile). The difference between maximum and central rotation frequencies, $\Delta\nu = \nu_{\rm max} - \nu_{\rm core}$, decreases from a maximum of 849 Hz at $t = 19$ ms after merger down to 340 Hz at $t = 91$ ms.

One of the reasons behind this decrease could be numerical dissipation which acts as viscosity. Other causes could be physical in nature, for instance, effective viscosity caused by strong small scale magnetic fields or turbulent motion, as well as magnetic winding (see also [261–263]). In the bottom panel of Figure 6.17, we evaluate the effect of different levels of magnetization on the same system. We find mild influence of magnetic field on the initial rotation profile, and the decrease in $\Delta\nu$ is comparable for the three cases, implying that non-magnetic effects are the major contributor towards the removal of differential rotation. However, due to insufficient resolution, our simulation does not fully capture small-scale magnetic field effects which could have a non-negligible contribution for the corresponding effective viscosity. We refer to [250] for

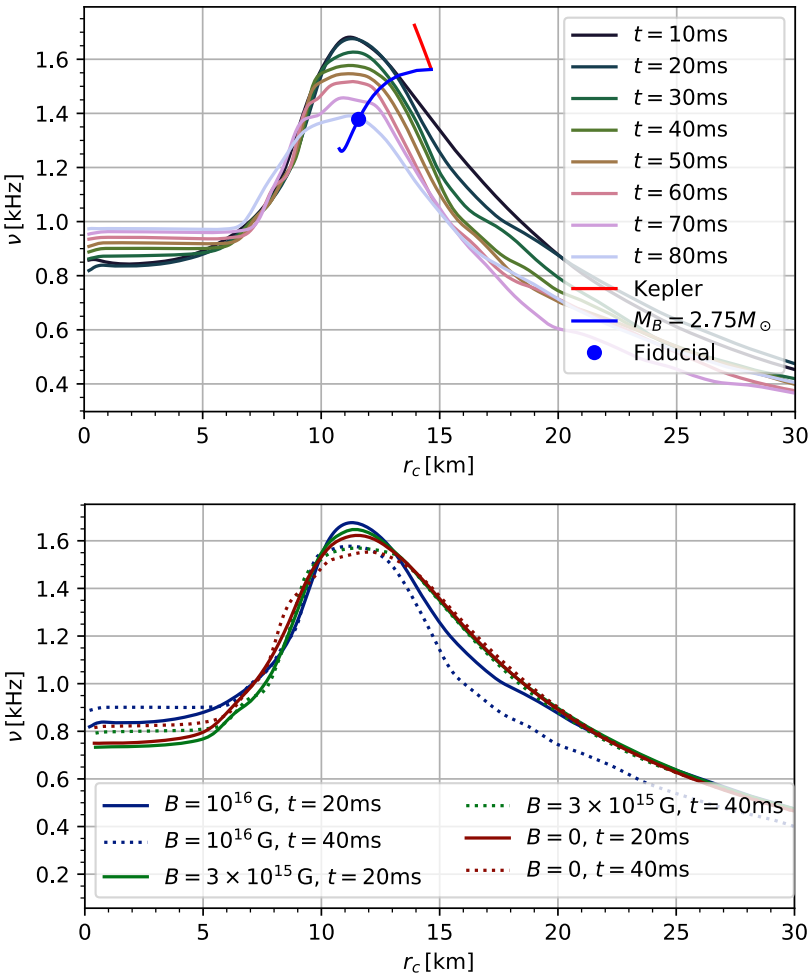

Figure 6.17: Top panel depicts the evolution of the rotation profile in the equatorial plane. Here, rotation rates averaged in ϕ-direction and over 2 ms in time versus proper circumferential radius, at different times (values relative to merger time). For comparison, we show rotation rate and circumferential radius of the uniformly rotating fiducial model (see text), the uniformly rotating sequence of constant baryon mass (blue line), and the mass shedding sequence with baryonic masses between fiducial remnant mass and total binary mass (red line). Bottom panel illustrates curves for models starting with different initial maximum magnetic field strengths at 20 and 40 ms after merger. Lower and zero magnetic field cases are taken from [35]. Figure taken from JVK1.

a detailed discussion based on simulations with much higher resolutions. However, magnetic effects do have a non-negligible impact on the outer envelope as for the present simulation, we see up to $\sim 20\%$ decrease in rotation frequency from 20 to 40 ms after merger. But note

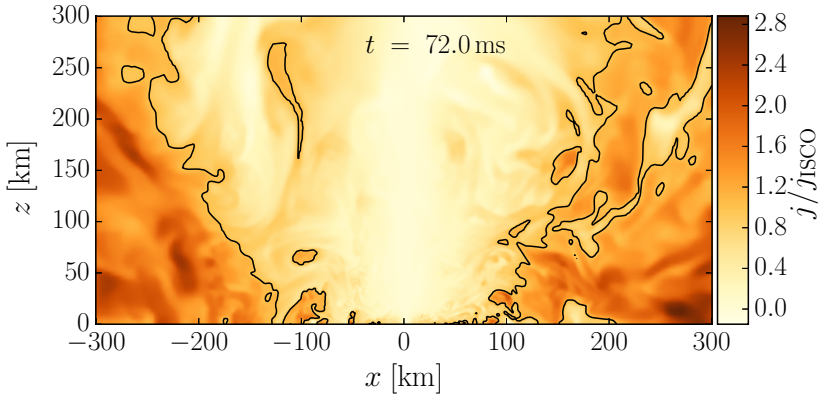

Figure 6.18: Specific angular momentum with respect to the remnant spin axis, on meridional plane, 72 ms after merger. The given values are in units of the specific angular momentum of a test particle on the innermost stable circular orbit around the BH formed in the collapsing case ($j_{\rm ISCO}$). The black contour corresponds to $j = j_{\rm ISCO}$. Figure taken from JVK1.

that simulations with weaker and zero magnetic fields show almost no effects. Our simulation suggests that above $E_{\rm mag} \sim 10^{51}$ erg, magnetic fields start to affect the outer layers within a timescale below 100 ms.

Along with differential rotation, the rotational energy also shows a decrease, as mentioned earlier. Following the discussion in Section 6.2.4, since the energy in the surrounding matter increases only slightly, most of the rotational energy is converted into potential energy and heat, which plays a role on expansion of the remnant as well.

For the collapse case instead, we focus mainly on determining the mass of the accretion disk to be formed around the BH. To do so, we use the widely adopted criterion which suggests that only the matter which fulfills $j > j_{\rm ISCO}$ before the collapse, contributes to the accretion torus, where $j_{\rm ISCO}$ is the specific angular momentum of a test particle on the innermost stable circular orbit around the newly-formed BH. Following [264], we compute $j_{\rm ISCO}c/GM \simeq 2.9$ for the BH formed in our simulation, and find that only negligible mass fraction obeys $j > j_{\rm ISCO}$ within a radius of $\simeq 50$ km, as shown in Figure 6.18. Based on the above criterion, almost all matter within 50 km from the remnant center should be directly swallowed by the BH. However, only $\lesssim 97\%$ of the corresponding baryon mass is actually swallowed. This can possibly due to the fact that part of the surrounding matter has significant outgoing velocities, deviating from the conditions for which the criterion is supposed to hold. About 3% discrepancy still allows a massive ($\sim 0.1\,M_\odot$) accretion torus and thus a potentially viable SGRB central engine.

6.2.6 Gravitational waves

In this Section, we discuss the remnant oscillations and the resulting GW signal. The GW signal from a BNS merger can be divided into inspiral, merger, and post-merger phases. In

addition to the inspiral and early post-merger phase, the present simulation allows us to study the late time behavior.

In Figure 6.19, we plot the evolution of the GW strain, obtaining a typical result as expected for a BNS system in the supramassive mass range. Since our adopted system is the same as of the equal mass APR4 model reported in [35] except for the difference in the initial magnetic field strength, and since magnetic fields are expected to have neglible impact on GW emission up to merger [106] (see also the discussions in [27]), we expect similar results up to merger as of [35]. Soon after merger, the GW amplitude decays strongly. We find the total radiated energy from 10 ms after merger onward to be only $4.6 \times 10^{-3}\, M_\odot$, which is $\sim$0.5% of the binding energy of the fiducial remnant. Also, the angular momentum is carried away by GW during this period is less than 2% of the total. Thus, the GW emission has only minor impact on the evolution of the remnant.

Comparing the evolution of GW frequency to the evolution of maximum rotation rate in the equatorial plane in Figure 6.19, we confirm that the GW frequency is indeed twice the latter for the early post-merger phase (up to around 30 ms after merger), as also reported in [35, 173, 174]. For later times, we study the numerical accuracy of oscillations with very small amplitudes, and observe a splitting of modes around 30 to 50 ms after merger. Using the formalism presented in [259], in Figure 6.19, we also plot the spectrogram of the average $m = 2$ component of the density in the equatorial plane. Here, we observe a superposition of a mode with frequency following twice the rotation rate, and a component remaining at slightly larger frequency. Consequently, the GW strain exhibits a beating phenomenon visible in the upper panel of Figure 6.19.

The reason for the split and the nature of the oscillations is currently not clear. We suspect that it might either be related to the decaying amplitude of the perturbation or to the decrease in differential rotation. In the early post-merger phase, it could be that the non-axisymmetric deformation has a nonlinear quasi-stationary nature. And with decreasing amplitude, the evolution of the remnant deformation might be governed more by linear perturbation theory, or could be linked to convective instabilities [265].

After 70 ms after merger, we notice a growing low-frequency oscillation in the GW signal, which is likely a numerical artifact since at the same frequency, we observe a growing oscillation of the coordinate system as well.

6.3 Magnetically driven baryon winds from BNS merger remnants

In this Section, we move on to discuss the results presented in JVK3 based on one of the BNS simulations performed in [147], which goes up to $\simeq 255$ ms after merger. In particular, we analyse the results of the simulation model 'B5e15' of [147], which starts with the initial maximum magnetic field strength of 5×10^{15} G. This simulation presents an interesting case since such a system launches a magnetically-driven collimated outflow emanating from a long-lived massive neutron star (MNS) remnant. Even though this outflow does not resemble a

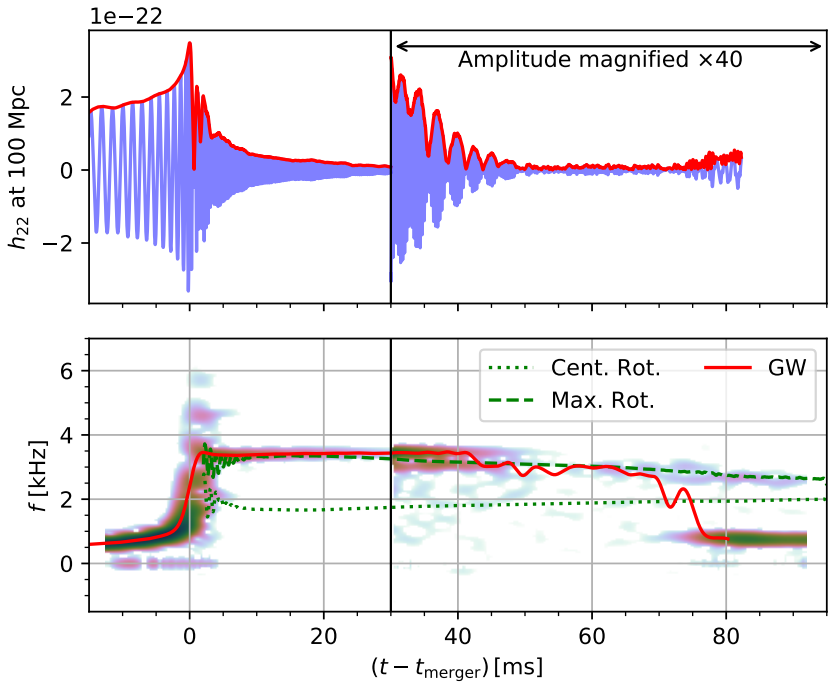

Figure 6.19: Top panels shows the GW strain $l = m = 2$ multipole coefficient (real part). The strain after $t = 30$ ms is magnified by a factor 40. In the bottom panel, the red curve shows the phase velocity of the GW strain. The green curves show twice the central (dotted) and twice the maximum rotation rates (dashed). The spectrogram (colorplot) represents the $m = 2$ component of the density perturbation in the equatorial plane averaged in the whole remnant. We use the logarithmic scale, spanning over 5 orders of magnitude, and the amplitude after $t = 30$ ms is scaled by a factor 1000. All phase velocities are smooth averages over 1 ms. Times shown are with respect to merger time (and using retarded time for the GW signal). Note the oscillation at the end of the simulation is likely an artifact. Figure taken from JVK1.

SGRB jet (see [147] for details), the associated material given out by this system can likely explain certain aspects of the kilonova AT 2017gfo that accompanied the GW170817 event. In particular, the physical origin of the ejected material responsible for the early (blue) component of this kilonova is still under debate (see discussion in Chapter 1). Through this BNS merger simulation, we demonstrate that the magnetically enhanced MNS winds appear as a promising source of this component.

In the following, we first briefly describe the adopted model along with the numerical setup, which is slightly different from the simulation described in previous sections, and then focus on the properties of the ejecta component.

6.3.1 BNS model and numerical setup

The 'B5e15' model considers the same chirp mass for the binary as inferred for the GW170817 event [214] and a mass ratio of $q \simeq 0.9$. The simulation adopts the APR4 EOS to describe the NS matter, which results in a long-lived NS remnant that survives without collapsing to a BH for the entire simulation. As mentioned earlier, this simulations starts with initial dipolar magnetic fields imposed within the two NSs with maximum field strength of 5×10^{15} G and the corresponding total magnetic energy of $E_{\rm mag} \simeq 4 \times 10^{47}$ erg.

For this simulation, the mumerical codes, methods, and setup are the same as described in Section 6.2.1, with the following exceptions. First, the computational domain is extended up to ≈ 3400 km in each direction. The artificial floor density is set to $\rho_{\rm atm} \simeq 6.3 \times 10^4$ g/cm^3 (two orders of magnitude lower than the previous simulation described in Section 6.2.1). This corresponds to a mass of $\simeq 2 \times 10^{-3}\, M_\odot$ within a sphere of radius 2360 km, which is the largest distance at which we monitor matter outflows.

In addition to this simulation, for comparison study, we performed the exact same simulation going up to ~ 160 ms after merger, but setting the magnetic field to zero (non-magnetized 'B0' model)[5].

6.3.2 MNS wind component of the ejecta

As previously mentioned, the merger product is a magnetized NS remnant which is characterized by strong differential rotation [147]. As seen in 6.2.3, here too, the magnetic fields get strongly amplified at different stages, first due to KHI soon after merger, and later via MRI and magnetic winding, eventually reaching a physical saturation around 50 ms after merger, corresponding to $E_{\rm mag} \sim 10^{51}$ erg [147]. During this phase, the build-up of magnetic pressure drives a baryon-loaded wind that pollutes the environment around the MNS. Since the overall magnetic field structure is still quite disordered, the mass outflow is nearly isotropic (Figure 6.6). At later times, the growing helical structure emerges along the remnant spin axis, which starts enhancing the outward acceleration, resulting in a faster component of outflowing material that begins to come out after ~ 100 ms post merger [147] [6].

In Figure 6.20, we can see how the faster outflow interacts with the slower and more isotropic surrounding material, and eventually forms wide angle ejecta component with a velocity profile that is maximum along the axis and declines at higher polar angles. Further mass ejection is significantly reduced near the end of the simulation, whereas the material that remained bound starts to slowly fall back towards the MNS.

[5] Results of the non-magnetized 'B0' BNS simulation were also used, serving as initial data, for a different work JVK6 which instead focussed on the long-term and large-scale evolution (performed with the special relativistic code `PLUTO`) of SGRB jets piercing through the environment material surrounding the merger remnant. Ref. JVK6 is the first study of its kind where the initial conditions for the surrounding environment were obtained by directly importing data from the outcome of an actual BNS merger simulation.

[6] This further acceleration along the spin axis is likely caused by the same mechanism as reported in [38, 201, 266–268] which instead impose by hand a strong large-scale dipolar field on a nonmagnetized differentially rotating NS. While the latter setup almost always generates a collimated outflow, the same outcome is not ubiquitous for a more realistic magnetic field evolution through the BNS merger (see discussion in [27, 147]).

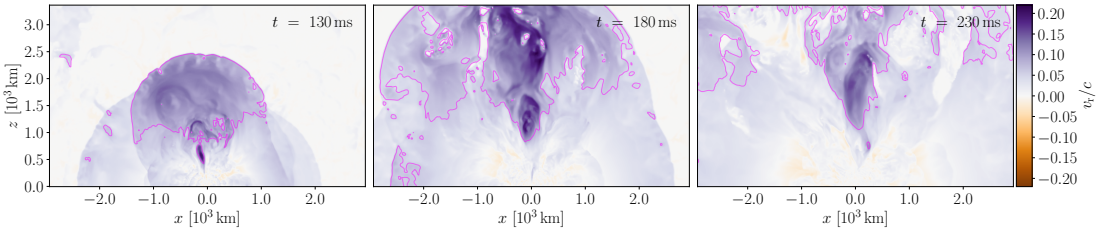

Figure 6.20: Snapshots of radial wind velocities on meridional plane at 130, 180, and 230 ms after merger. The magenta contour lines indicate unbound matter (according to the geodesic criterion $-u_t > 1$, see Section 6.2.2 for details). Figure taken from JVK3.

Figure 6.21 shows the space-time diagrams of material ejected during and after merger for the 'B5e15' (top-panel) and 'B0' models, plotted by collecting the unbound matter at regular intervals in 1D histograms binned by radial coordinate. To define the unbound mass, we adopt the conservative geodesic criterion (see Section 6.2.2). In general, the matter is ejected in a series of waves at different times. Until early post-merger phase, the main contribution in both simulations comes from the dynamical ejecta, which are not affected by the presence of magnetic field. This constitutes material ejected by tidal forces before merger, by shock waves produced during merger and by quasi-radial remnant oscillations soon after merger. At later times, we can see the substantial contribution of the magnetically driven post-merger winds for the 'B5e15' case, which is absent for the 'B0' case.

Focussing only on the magnetized 'B5e15' case, in Figure 6.22, we plot the time evolution of the mass flow rate across spherical surfaces of different radius, along with the corresponding cumulative mass. In particular, we report the result for 1180 km and 2360 km distance and for both the total mass and the unbound mass. Here too, a clear separation between the early contribution of dynamical ejecta and the MNS wind contribution can be noticed. About $\simeq 0.01\, M_\odot$ of dynamical ejecta with high velocities (ranging up to more than $0.2\, c$) is expelled within less than 10 ms after merger. However, only a fraction of this material is expected to retain low opacity (e.g., [47]), which coupled with the fact that the mass is already smaller than the expected range (i.e. $\simeq 0.015 - 0.025\, M_\odot$), acts in disfavour of dynamical ejecta being the dominant source of the blue kilonova.

The mass flow rate (total and unbound) representing the MNS wind grows in time up to a maximum and then starts declining (Figure 6.22). The final decline is quite regular and can be reproduced very well with an exponential decay. This allows us to extrapolate in time and compute the total and unbound cumulative masses in the late-time limit (assuming that no collapse to a BH occurs) for a given set of distances. The result is shown in Figure 6.23. Here, we find the total (bound plus unbound) mass to decrease with distance while the unbound mass increases. At very large distances, the two are expected to coincide since all the outflowing matter far away from the MNS is expected to be unbound. At the distance of 2360 km, the total and unbound masses provide the range of values ($M_{\rm ej,\,wind} \simeq 0.010{-}0.028\, M_\odot$) within which the final ejecta mass is contained. This considers only MNS wind and excludes the dynamical ejecta

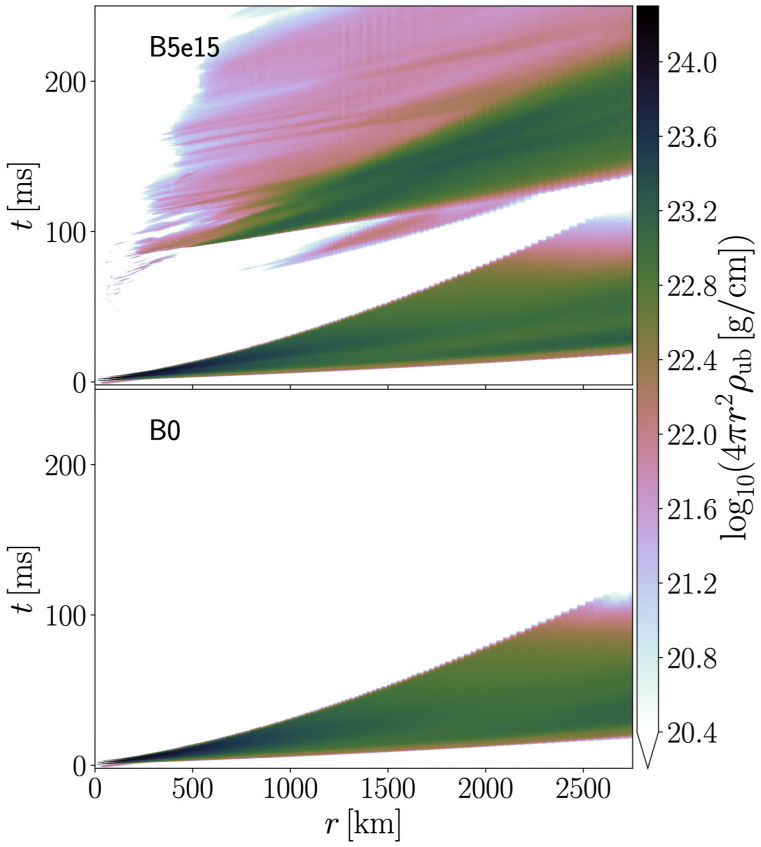

Figure 6.21: Time evolution of the radial distribution of ejecta for the magnetized 'B5e15' (top) and non-magnetized 'B0' (bottom) models. Color scale corresponds to the increase of unbound mass inside spherical surfaces per increase in radius.

contribution. The above mass would be sufficient to explain the blue kilonova in AT 2017gfo. Therefore, in terms of mass, magnetically driven MNS winds represent a valid and promising source.

In case the MNS collapses to a BH, the mass ejection process via the MNS wind is stopped. The collapse also influences the material surrounding the BH within $\approx 200-300$ km, while the rest is almost unaffected (see, for e.g., Section 6.2.2). Monitoring the cumulative mass outflow across the spherical surface of radius 300 km, we find that 90% of the mass outflow (from 5% to 95%) occurs between 54 and 189 ms after merger, while after 285 ms further outflow accounts for less than 1% of the total. Thus, a collapse occuring within about 50 ms would almost entirely suppress the MNS wind ejecta component, whereas any collapse beyond ≈ 200 ms would lead to a similar ejecta mass,

In Figure 6.20, we find MNS wind radial velocities to reach over $0.2\,c$, particularly along polar directions within $\simeq 15°$ from the the spin axis. Overall, the velocity of the unbound

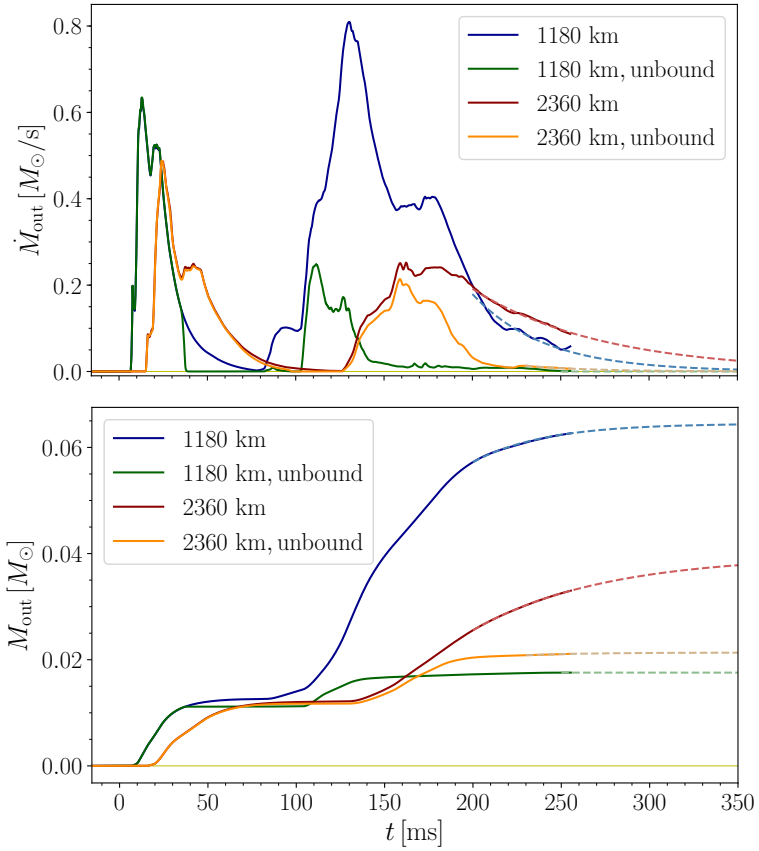

Figure 6.22: Top panel shows evolution of the mass flow rates across spherical surfaces of radius 1180 and 2360 km, considering both the total mass and the unbound mass, for the magnetized 'B5e15' simulation. Dashed lines correspond to the exponential profiles used for the extrapolation at later times. Bottom panel depicts the analogous plot for the cumulative mass flows. Figure taken from JVK3.

material lies in the range $\simeq 0.1-0.2\,c$, which is consistent with the lower end of the range inferred from observational data (i.e. $\simeq 0.2-0.3\,c$) for the blue kilonova component. Certain effects, such as presence of a relativistic jet at later times and neutrino irradiation, which are not included in our simulation, could further enhance these velocities by depositing additional kinetic energy. In addition, the artificial floor density of $\simeq 6.3\times10^4\,{\rm g/cm^3}$ imposed in our simulation could be slowing down the MNS wind in a non-negligible way (e.g., [269]).

Finally, we conclude with a note on the opacity. The presence of neutrino radiation can significantly raise the electron fraction of the MNS wind material (see, e.g., [270, 271]), leading to ejecta having $Y_{\rm e}\simeq 0.25-0.40$. Material with such electron fraction values would produce heavy elements with $A\lesssim 140$ via r-process nucleosynthesis, resulting in relatively low opacities, i.e. $\sim 0.1-1\,{\rm cm^2/g}$ (e.g., [272]). This is in agreement with the blue kilonova requirement.

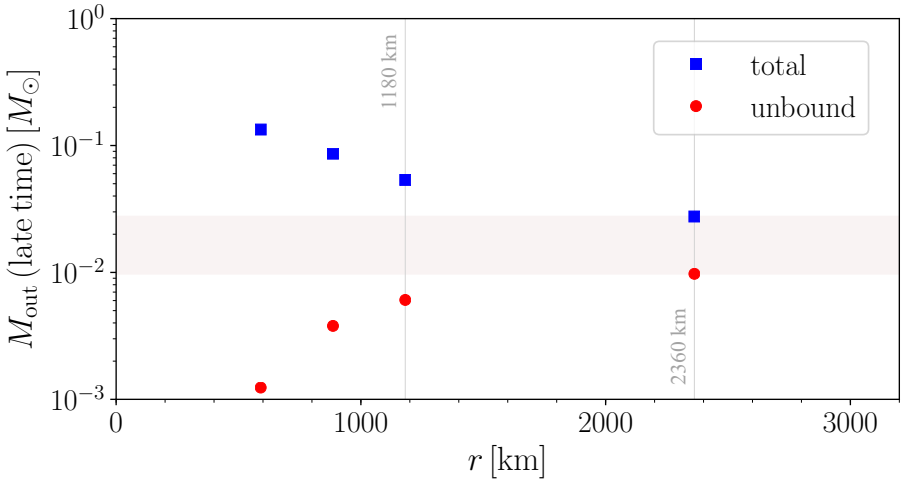

Figure 6.23: Total and unbound cumulative mass flowing across spherical surfaces of different radii in the late time limit. The value do not include contributions from dynamical ejecta, but only of MNS wind. At very large distances, the final ejecta mass should fall within the range defined by the shaded region. Figure taken from JVK3.

Putting together the above results and considerations on mass, velocity and opacity, the magnetically driven MNS wind is found as a viable explanation for the blue kilonova component of the August 2017 event.

6.4 Summary

In this Chapter, we first provided a brief astrophysical background on BNS mergers. Then, we presented the outcomes of our BNS merger simulations performed with the GRMHD code `WhiskyMHD`, which produce a long-lived NS remnant. Our simulations involved long post-merger evolution (up to $\sim 100\,$ms in JVK1, and up to $\sim 255\,$ms in JVK3) which allowed us to gain novel insights on the remnant properties over unexplored timescales.

In JVK1, we observed that the magnetic field gets amplified due to different mechanisms in action (for e.g., KHI and MRI) during the course of evolution, until it reaches a physical saturation around 50 ms after merger, corresponding to magnetic energy of the order 10^{51} erg. Following the evolution of magnetic field lines, we saw that towards the end of the simulation, a large scale magnetic field of mixed poloidal-toroidal structure emerges, with average magnetic strength reaching roughly $10^{15}\,$G. Our result supports the idea that BNS mergers can produce remnant NSs endowed with a global field of magnetar-like field strength.

Along with the dynamical ejecta, magnetically driven post-merger winds emanating from MNS remnant lead to formation of a dense environment with a nearly isotropic and steady rest-mass density distribution up to $\approx 400\,$km. The material ejected from susch winds is slow in nature ($< 0.1\,c$) and correspond to a mass loss rate of up to $\dot{M} \sim 3\,M_\odot/$s, for a total

mass of $0.1\,M_\odot$ at the end of the simulation. It is also too heavy to be accelerated up to relativistic speeds and turn into a jet. On the contrary, it acts as an obstacle for any incipient jet possibly launched by the remnant, even at later times. In conclusion, our current results seem to disfavour, but cannot rule out, a scenario in which a long-lived NS remnant acts as a SGRB central engine.

By looking at the bulk of the remnant NS, we observe an early structure composed of a nearly spherical inner core embedded in a torus-shaped outer envelope, which then evolves towards a more spherical configuration by the end of the simulation. Studying its rotation profile reveals that in general, it has a slowly rotating inner core attached to a faster rotation outer envelope. At larger distances, the profile becomes nearly Keplerian, indicating that this part of the remnant NS is centrifugally supported. In time, the core spin frequency increases at the expense of the outer envelope. We estimate that the remnant present at the end of our simulation could reach uniform rotation after a further rotational energy loss of $\approx 8 \times 10^{52}$ erg.

We also performed an additional simulation, inducing the collapse of the remnant ~ 72 ms after merger. The collapse forms a $\sim 2.5\,M_\odot$ BH with $Jc/GM^2 \simeq 0.5$ and surrounded by a $\sim 0.1\,M_\odot$ accretion torus. The presence of this accretion disk instead favours the conditions to launch a powerful SGRB jet via the Blandford-Znajek mechanism.

In JVK3, we analyzed the results of the simulation presented [147], in order to provide a viable explanation regarding the mechanism that produced the blue component of the kilonova in AT 2017gfo, in terms of the corresponding matter ejected. In particular, we considered the possibility that this kilonova component originated from magnetically driven post-merger ejecta given out by the massive NS remnant before its collapse to a BH. From our study, we found a robust estimate for the ejected mass to be in the range $\simeq 0.010 - 0.028\,M_\odot$, consistent with the blue kilonova observation of August 2017, and found radial velocities limited to a maximum of $\simeq 0.2\,$c, consistent with the lower end of the range estimated from the observations. Thus, we showed that this ejection mechanism offers a promising explanation.

Chapter 7

Binary neutron star mergers with Spritz

The coincident detection of GW170817 and GRB 170817A provided the smoking-gun evidence connecting BNS mergers as one of the progenitors of SGRBs. However, the nature of the central engine that produce this SGRB is still under active investigation (see [17]). In Chapter 6, through GRMHD simulations of BNS mergers, we explored the scenario which considers a long-lived NS remnant or the so-called 'magnetar' as the central engine of SGRBs. Our results, coupled with [147], act in disfavour of such a scenario (however, see [38]).

In this Chapter, we discuss the prelimnary results of a BNS merger simulation to be presented in the upcoming work JVK9, focussing instead on the standard 'accreting-BH' scenario as SGRB central engine. Recent studies of BNS merger simulations have already shown that such a system can power an incipient jet through the Blandford-Znajek mechanism [37, 43, 44]. Here, we employ our latest machinery in hand, with the main aim of performing the first BNS merger simulation with our `Spritz` code along with our robust RePrimAnd C2P scheme, and also attempt to reproduce the results of [43].

7.1 BNS model and setup

We consider an equal mass BNS model (mass ratio, $q = 1$) with individual NS gravitational mass of about $1.5\,M_\odot$ (i.e. large enough to form a BH soon after merger), having an equitorial radius of 13.6 km. The initial data is produced using the publicly available `LORENE` library, using the polytropic EOS with adiabatic index $\Gamma = 2.0$, and with an initial coordinate separation of 45 km. In particular, the irrotational case listed as $M/R = 0.14$ vs 0.14 (Table III, row 3) in [273] is adopted, which is also used in [43, 107]. The system is then evolved using the ideal gas EOS with adiabatic index $\Gamma = 2.0$[1]. After about two orbits ($t = t_B \approx 6\,\text{ms}$), we

[1]Since the current EOS framework of the RePrimAnd library does not provide support for tabulated finite-temperature, composition dependent EOS, we consider a simple EOS for initial data as well as for evolution in

impose a dipolar magnetic field on the two NSs, also extending outside their surfaces, using the vector potential prescription defined by Equation (5.75). For this expression, we set the parameter $B_0 = 2.6 \times 10^{15}\,\mathrm{G}$ (corresponding to an intial maximum magnetic field strength of $B_{\rm max} \simeq 10^{16}\,\mathrm{G}$, rather strong but still dynamically unimportant), and choose $r_0 = 4\,\mathrm{km}$, which results in an initial total magnetic energy of $E_{\rm mag} \simeq 10^{47}\,\mathrm{erg}$. For the reason behind this choice of high initial magnetic field strength, we refer to the discussion in Section 6.2.1. Note that we have already successfully tested the imposition of such an extended dipolar field on single NS in the tests reported in Section 5.7.

The atmosphere density floor is set to $\rho_{\rm atm} \simeq 6.3 \times 10^4\,\mathrm{g/cm^3}$. During the first two orbits, a small fraction of material is ejected due to tidal effects as well as because of the spurious heating near the NS surfaces, which spreads up to radial distances of roughly 200 km. Since `Spritz` imposes zero-velocity in the artificial atmosphere, when the dipolar magnetic fields are added, they are expected to remain frozen in the regions beyond $\approx 200\,\mathrm{km}$, where densities correspond to $\rho = \rho_{\rm atm}$. In order to make the initial magnetic field co-rotate with the system at larger distances, which would be a step closer to the realistic description of rotating magnetospheres of NSs, we add a low density gas (of total mass $< 0.001\,M_\odot$) at $t = t_B$, up to the radial distance of 950 km, which is co-rotating with the binary. Since the magnetic field (which is dynamically unimportant at this stage) follows the fluid motion in the atmosphere under the ideal MHD approximation, this results in an initial co-rotating magnetic field as well. In particular, the density distribution of the added matter is given by the following expression

$$\rho_{\rm gas} = \begin{cases} a_1 \rho_{\rm atm} & \text{if} \quad r < r_1 \\ a_1 \rho_{\rm atm} \left(\frac{r}{r_1}\right)^{n_1} & \text{if} \quad r \geq r_1 \end{cases} , \tag{7.1}$$

where $\rho_{\rm gas}$ is the density of the added gas, r is the radial distance, and we set the constant parameters to $a_1 = 10.0$, $r_1 \simeq 74\,\mathrm{km}$ and $n_1 = -0.9$ such that at 950 km, $\rho = \rho_{\rm atm}$. The pressure of this gas is computed using the polytropic EOS with polytropic constant $k = 123.6$ and $\Gamma = 2.0$. In order to make the gas co-rotate with the system, we first compute, in simulation coordinates, the angular velocity averaged along ϕ right before adding the gas, as shown in Figure 7.1 (in red). The resultant curve is then fitted partly with an exponential function and partly with a Keplerian profile, through which we obtain the angular velocity profile of the gas, given by the following expression

$$\Omega_{\rm gas} = \begin{cases} a_2 \exp\left(-b_2\,(r - r_2)\right) & \text{if} \quad r < r_d \\ a_3 \left(\frac{r}{r_3}\right)^{-n_3} & \text{if} \quad r \geq r_d \end{cases} , \tag{7.2}$$

where r_d is set to $\simeq 80\,\mathrm{km}$. For the exponential, we set the parameters $a_2 = 0.0218$, $b_2 = 0.045$ and $r_2 = 0.2$, while for the Keplerian profile, we choose $a_3 = r_3 = 0.9$, and $n_3 = 1.5$. The final rotational profile (averaged along ϕ) of the system including the co-rotating gas is shown in Figure 7.1 (black curve).

The grid-setup employs 'moving box' mesh refinement with 7 refinement levels. Two finest levels follow the NSs during inspiral, while shortly before merger, the moving grids are replaced

our present simulation.

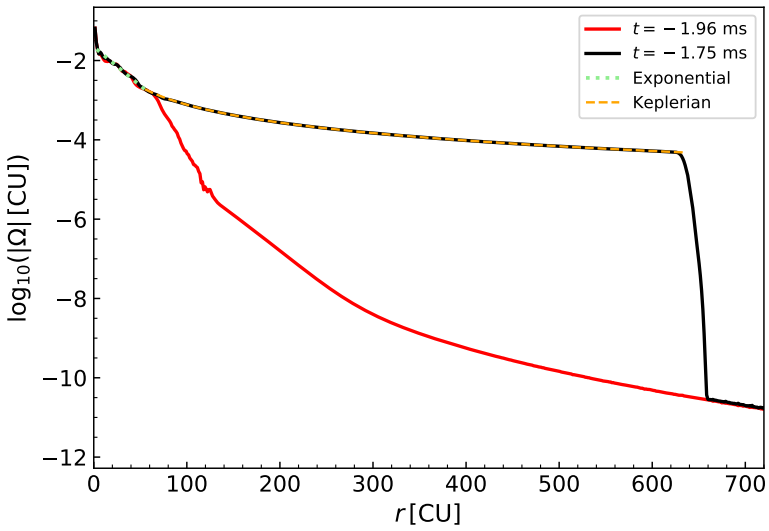

Figure 7.1: Angular velocity in the equitorial plane averaged over ϕ. Solid red curve shows the angular velocity of the system before the addition of gas (see text). Green (dotted) and orange (dashed) lines represent the exponential and Keplerian curves fitted onto the red one, which provide the parameters to define the angular velocity of the gas to be added. Solid black line represents the resulting angular velocity of the system after the addition of gas. Quantities are shown in Cactus units (CU), which consider $c = G = M_\odot = 1$.

by fixed grids. The coarsest (finest) fixed-grid extends to $\approx 2800\,\mathrm{km}$ ($\approx 22\,\mathrm{km}$) in all directions. Grid-spacing in the finest refinement level is set to $dx = dy = dz = 354\,\mathrm{m}$. Right before BH formation, we add a finer refinement level with spacing $dx = 177\,\mathrm{m}$, extending to $\approx 12\,\mathrm{km}$ in all directions. In contrast, for the entire evolution (before and after BH formation), [43] consider much higher resolution in their simulations, i.e., $dx = 227\,\mathrm{m}$ for the 'normal' case, and $dx = 152\,\mathrm{m}$ for the 'high' resolution cases.

For the evolution, we utilize our `Spritz` code to solve the GRMHD equations, and use the HLLE approximate Riemann solver along with PPM reconstruction. For spacetime evolution, we use the `MacLachlan` thorn of the Einstein Toolkit infrastructure. To evolve the vector potential, we employ the generalised Lorenz gauge based on the newly implemented technique described in Section 3.1.2.1. However, the electric field is still computed using the formulation implemented in JVK1, and not according to the one presented in Section 3.1.2.3[2]. Therefore, we add Kreiss-Oliger dissipation to the evolved vector and scalar potentials to avoid numerical instabilities during evolution. Furthermore, we use the RK4 method for time-stepping, and set the Courant factor as 0.35. RePrimAnd C2P scheme is used, setting the upper limits

[2]Implementation of the upwind constrained transport scheme to compute the electric field was still under development at the time the present simulation was performed. However, we plan to use the UCT scheme for our future simulations.

$W_{\rm max} = 100.0$, $\epsilon_{\rm max} = 10^6$, and $b_{\rm max} = 100.0$. Moreover, we set $\rho_{\rm strict} = 3.95 \times 10^{13}\,{\rm g/cm^3}$ (see Section 5.6 for parameter definitions). Inside the BH, we follow a rather linient error policy, setting $W_{\rm max} = 7.0$, $b_{\rm max} = 10^4$ and $\rho_{\rm strict} = 6.17 \times 10^{23}\,{\rm g/cm^3}$. This allows us to run the simulation till the end without applying any form of excision near the BH center.

7.2 Results

During the inspiral, the binary loses energy and angular momentum via GWs, and after about three orbits ($t = t_{\rm merge} \approx 7.89\,{\rm ms}$), the two NSs merge to form a differentially rotating metastable hypermassive NS (HMNS)[3]. The HMNS survives against collapse, for instance, via the redistribution of angular momentum. However, after losing further angular momentum via GWs, the HMNS collapses to a BH (at $t = t_{\rm BH} \approx 14.7\,{\rm ms}$), thus surviving for about 6.8 ms. Whereas, in [43], the HMNS survives for about 18 ms and 31.5 ms for the normal and high resolution cases respectively. The difference in the HMNS survival time is likely due to the differences in the grid resolution, as noted in previous studies (see, for e.g., [43] and refs. therein).

We evolve the system up to $\sim 49.8\,{\rm ms}$ after merger (i.e, $t - t_{\rm merge} = 49.8\,{\rm ms}$ and correspondingly $t - t_{\rm BH} = 43\,{\rm ms}$). About 2.5 ms after BH formation, the BH has a mass $M_{\rm BH} = 2.91\,M_\odot$ and spin $J/M^2 = 0.8$, and it is surrounded by a hot and dense accretion disk (Figure 7.2, left-panel) with mass $M_{\rm disk} \approx 0.06\,M_\odot$. Due to accretion, a low density funnel starts to form around the same time along the BH axis. At the end of the simulation, both the BH mass

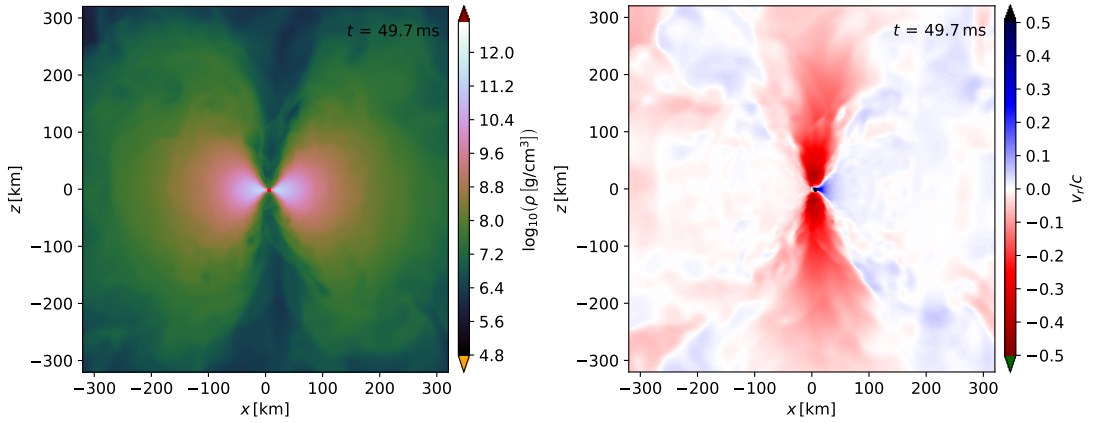

Figure 7.2: Meridional view of the rest-mass density (left) and radial velocity (right) at $\sim 49.7\,{\rm ms}$ after merger.

and spin increase to $M_{\rm BH} = 2.93\,M_\odot$ and $J/M^2 = 0.82$ respectively, with remaining disk mass $M_{\rm disk} \approx 0.03\,M_\odot$. At this point, the system has already reached steady state accretion with

[3]For the ideal gas EOS with $\Gamma = 2.0$, the maximum mass of a HMNS is $\sim 2.1\,M_\odot$.

accretion rate of roughly $\dot{M} = 0.11\,M_\odot/\mathrm{s}$, which implies that the disk would be fully accreted on a timescale $\Delta t \sim M_{\rm disk}/\dot{M} \sim 0.27\,\mathrm{s}$. We find these values to be quite similar to the ones reported in [107].

Until the end of simulation, the funnel along the BH spin axis still remains rather low in density (Figure 7.2, left-panel), providing favourable conditions in case a relativistic jet is to be launched. However, we do not observe any outflow of matter along this funnel. In the right-panel of Figure 7.2, we illustrate the radial velocities obtained at the final time, which shows that the matter persistently falls back due to rapid accretion along BH poles, increasing the ram pressure which counteracts jet formation. This result is in contrast with the one reported in [43], where outward fluid velocities are observed along the BH spin axis starting from about 30 ms after BH formation, followed by a well-developed incipient jet about 42 ms after BH formation for their normal-resolution case.

Next, we focus our attention to magnetic fields, which play a key role in driving relativistic jets. Figure 7.3, we show the evolution of total magnetic energy for the present simulation. After the magnetic fields are activated (at $t - t_{\rm merge} = -1.8\,\mathrm{ms}$), they undergo pre-merger

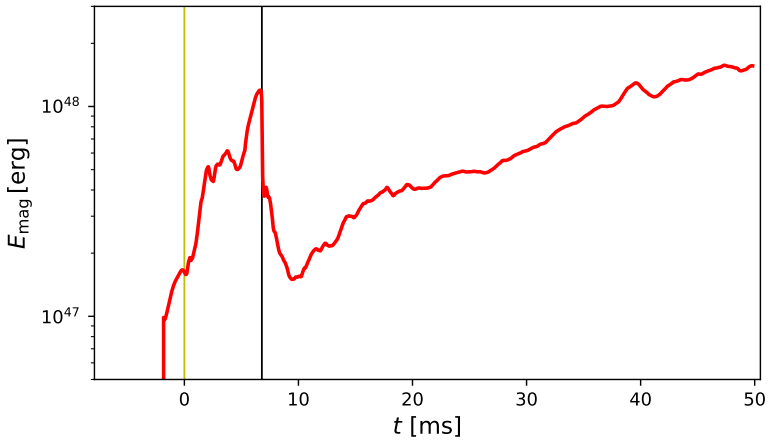

Figure 7.3: Evolution of total magnetic energy for the present simulation. Vertical yellow line stands for the time of merger $t_{\rm merge}$. Black line denotes the time of collapse to BH $t_{\rm BH}$.

amplification, likely due to the reasons explained in Section 6.2.3. The left-panel of Figure 7.4 shows the magnetic field line structure (plotted using the technique employed in [34]) soon after the dipolar fields are imposed on the two NSs. As shown in this Figure, close to the NSs, the magnetic field gets slightly distorted due to the turbulent motion of the low density material surrounding the binary system, while at large distances, the original dipolar geometry is retained. Note that we would require a force-free evolution for a proper treatment of the outer regions, which is not currently implemented in `Spritz`.

At merger, KHI develops in the shear layer when the two NS cores come in contact, raising the magnetic energy at least by a factor of 5, as seen in Figure 7.3. Note that small-scale

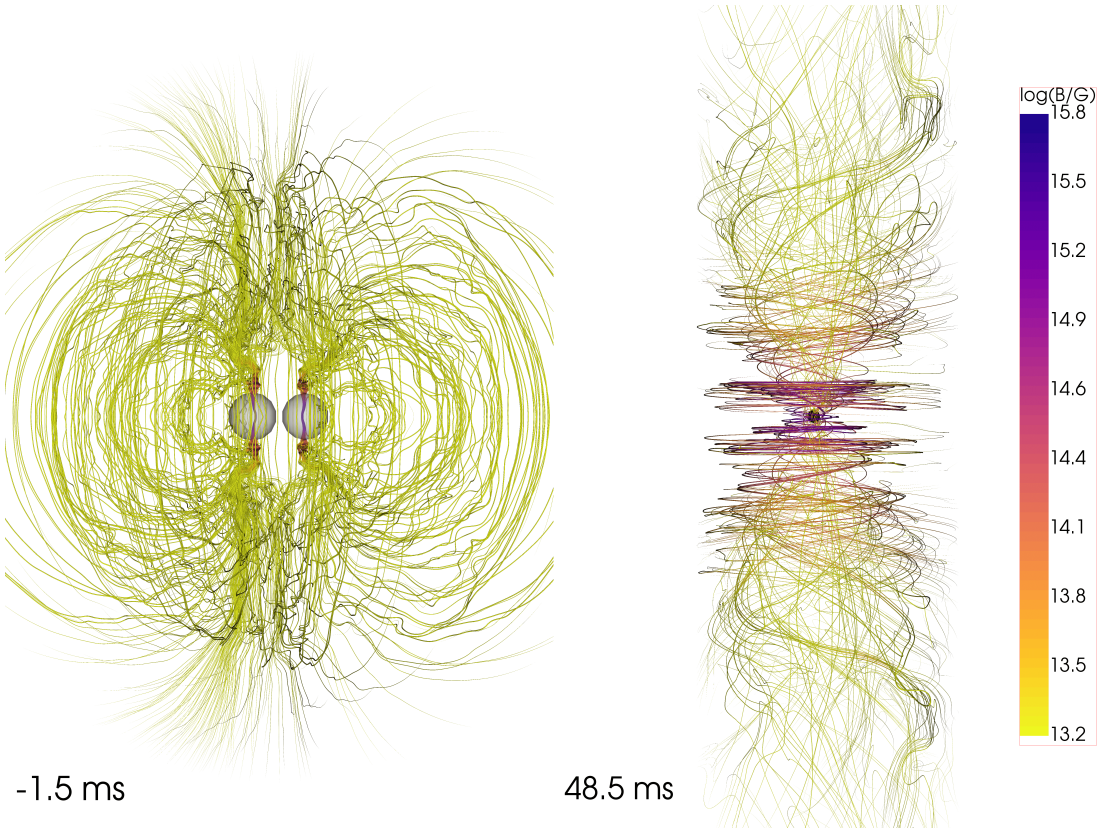

Figure 7.4: Magnetic field structure soon after field activation (left-panel) and at final simulation time (right-panel). On left, the spheres (in grey) of radius 10 km are placed at the positions of the two NSs, as scale reference. On right, the black sphere of radius 2.7 km is place at the BH center. Field line colors indicate the magnetic field strength.

turbulence effects due to KHI are not fully captured in our simulation due to the lack in resolution, which are expected to amplify the magnetic fields to much higher strengths, as also mentioned in Section 6.2.3. A few milliseconds after merger, effects of magnetic winding and development of MRI around the HMNS remnant start taking over KHI as the dominant amplification mechanism, increasing the magnetic energy to roughly 10^{48} erg, which is an order of magnitude higher than the initial magnetic energy of 10^{47} erg. This gain in magnetic energy is soon lost when the HMNS collapses to a BH, engulfing the surrounding matter, especially along its rotation axis. The resultant drop in magnetic energy is clearly visible in Figure 7.3. However, in next few tens of milliseconds, we again see a rise in magnetic energy, which is rather gradual until the end of the simulation. This growth is likely caused by effects of magnetic winding as well as the developing MRI in action, leading to the formation of a strong toroidal field in the torus surrounding the BH. At final time, we find the fastest growing MRI

mode wavelength $\lambda_{\rm MRI}$, given by Equation (6.13), to be covered by at least 10 points in part of regions within 50 km radius, suggesting that MRI contributes at least partially in amplifying the magnetic fields.

Figure 7.4 (right-panel) illustrates the magnetic field structure surrounding the BH remnant at final time. The growth in the toroidal component of the magnetic field near the equatorial plane is evident. Along the BH spin axis, we also notice the formation of helical structures extending up to a few hundreds of kilometers. Such a configuration looks promising as it might eventually support jet production at later times.

The magnetic energy reaches the value of $\approx 1.5 \times 10^{48}$ erg towards the end of the simulation, but is still slowly growing, implying that it has not reached its saturation limit. However, its current value is likely insufficient to power a relativistic jet. In contrast, previous studies which start with initial magnetic energy as high as 10^{49} erg report nearly saturated magnetization levels after merger, leading to post BH-formation magnetic energies of the order $10^{50} - 10^{51}$ erg [37], are able to successfully produce an incipient jet. Moreover, the longer surviving time of the HMNS (roughly 20-30 ms) in [37, 43] allows for additional magnetic field amplification via MRI before collapse, which does not occur in our case since the remnant collapse within 7 ms after merger.

Computing the magnetic-to-fluid pressure ratio β, we find its initial value to be around 1.7×10^{-5} at the center of the NSs at the time when magnetic field is initialized. This is roughly 200 times lower than the initial $\beta = 3.125 \times 10^{-3}$ at the stellar center used in [43]. Figure 7.5 shows the β distribution on the meridional plane at final time for the present simulation, with the maximum value achieved as 0.03. Whereas [43] show that β can reach values higher than 100 within the jet funnel. Clearly, our results imply that the system in hand is fluid pressure dominated, since by the end of the simulation we do not reach high enough magnetization levels required to power a SGRB jet, and we would require a much longer simulation to produce a jet at later times (if any).

7.3 Summary and outlook

In this Chapter, we described some of the prelimnary results of the upcoming work JVK9 based on the first successful BNS merger simulation performed with our GRMHD code `Spritz` employing our robust RePrimAnd C2P scheme. In our simulation, we were able to correctly activate and evolve the dipolar magnetic fields in the two NSs, initially extending also outside their surfaces. At larger distances, the magnetic field was able to co-rotate along with the system during inspiral, thanks to the low-density, co-rotating gas added to the system. The BNS merger first produced a HMNS which soon collapsed to a BH surrounded by an accretion disk. We evolved this system up to 43 ms after BH formation, and showed that our code can handle evolution of such a scenario up to final time, rather well, without requiring any kind of excision near the BH center. Finally, we also showed that magnetic fields can form helical structures along the BH spin axis, creating a favourable site for jet formation at later times.

Even though these first results are promising, our simulation was not able to reproduce the results of [43]. At final time, we found the low-density funnel along the BH spin axis to be dom-

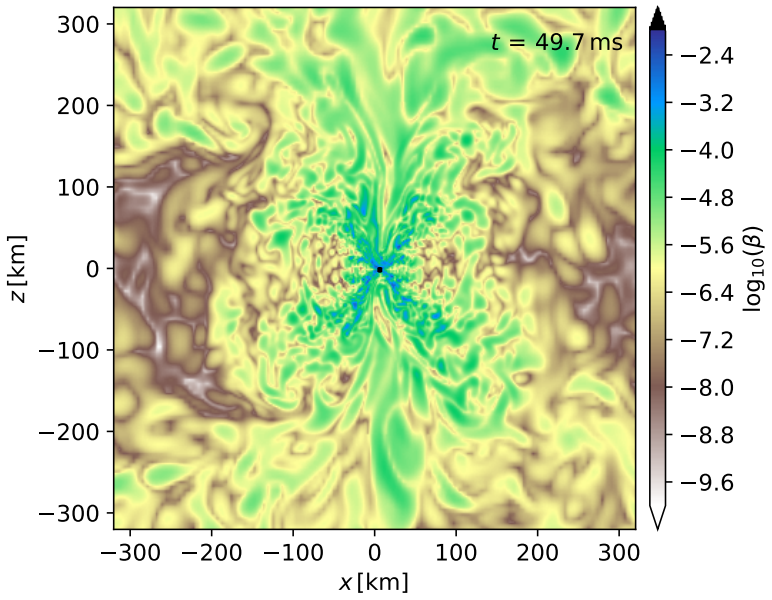

Figure 7.5: Magnetic-to-fluid pressure ratio β on the meridional plane at $\sim 49.7\,\mathrm{ms}$ after merger.

inated by fluid pressure with radial velocities always pointing inward. Furthermore, our initial magnetic energy and magnetic-to-fluid pressure β were quite too low for the given resolution as compared to the ones used in [43], which did not allow us to reach the magnetization levels expected to produce a SGRB jet. Another caveat involves the use of Kreiss-Oliger dissipation on magnetic field variables which may have possibly reduced the amount of amplification attained.

In the near future, we plan to perform similar simulations to be included in JVK9 with initial magnetic energies and β values comparable with those used in [43]. Moreover, we would employ the upwind constrained transport scheme to compute electric field, which would allow to correctly evolve the magnetic fields without any kind of dissipation.

Chapter 8

Conclusions

Since the multimessenger observation of gravitational wave event GW170817 together with a short gamma-ray burst GRB 170817A and a kilonova AT2017gfo, binary neutron stars mergers have come under the limelight in the astrophysics community. To provide a more realistic description of such events, there is a strong ongoing effort by various numerical relativity groups to accurately model these systems to probe the different physical mechanisms involved as well as to generate gravitational waveforms.

Moving along this direction, as a part of this Thesis work, we have developed a new fully general relativistic magnetohydrodynamic code called `Spritz` JVK2, based on flux-conservative formalism of GRMHD equations and on the use of HRSC schemes. `Spritz` has been adopted from its parent code `WhiskyMHD` which has already proven to be fundamental in performing magnetized BNS merger simulations in recent years. The newly implemented algorithm in `Spritz` evolves the vector potential at staggered positions of the grid and then computes the magnetic field, ensuring its divergenceless character by construction. Moreover, we added support for different types of EOS by coupling `Spritz` with the `EOS_Omni` module of the Einstein Toolkit infrastructure. For a quantitative validation our implementation, we subjected `Spritz` with the 1D Balsara shock-tube testsuite, and matched the results with exact solutions provided by [31], and also compared them with the outcome of another state-of-the-art GRMHD code `GRHydro`. `Spritz` was also assessed with a number of 2D and 3D tests including a successful evolution of a magnetized TOV star in full 3D.

Along with magnetic fields, incorporation of neutrino effects are crucial for accurate modeling of the BNS merger ejecta. For neutrino treatment, we implemented an approximate neutrino leakage scheme in `Spritz` JVK5, which takes into account both neutrino emission (cooling) as well as reabsorption (heating). Furthermore, we added support for finite temperature, composition dependent tabulated EOS which would allow us to follow evolution of temperature and electron fraction in future BNS merger simulations. Additionally, we implemented higher order methods for the evolution of hydrodynamical quantities, further enhancing the accuracy of our solutions JVK5. A series of tests were then performed to show the robustness of the code in handling a variety of different physical scenarios, including the evolution of both "cold"

and "hot" NSs with and without magnetic fields or neutrino leakage. For the cases with neutrino leakage, we also considered the effects of having neutrino heating activated or deactivated. However, note that the present leakage scheme comes with some limitations. Since it is based on a ray-by-ray approach, it works best for configurations which are, at first approximation, spherically symmetric. In presence of any significant deviations from spherical symmetry, it would in part over-estimate the neutrino opacities, for instance in the early post-merger or after the collapse into a BH surrounded by an accretion disk. Such limitations can be overcome by adopting more accurate neutrino transport schemes, such as the Monte-Carlo-based scheme [157] or courageously attempt to compute the full solution of Boltzmann transport equations which could be computationally much more expensive.

A long-standing technical problem currently faced by modern day GRMHD codes is to reliably recover the fundamental 'primitive' variables from the evolved 'conserved' ones. We tackled this problem by introducing a new conservative-to-primitive variable recovery scheme JVK4, and provided the proof for the existence and uniqueness of a solution. We also derived expressions of the analytic bounds for the accuracy of the computed primitives. Our scheme is also able to identify unphysical evolved variables, as well as the nature of the invalidity, and also allows to prescribe an error policy and selectively apply harmless corrections, wherever necessary. The reference implementation of our scheme has been made publicly available in the form of a well-documented library named 'RePrimAnd', which also contains a generic interface for using arbitrary EOS. Note that our recovery algorithm is implemented in a completely EOS-agnostic manner. We validated the stand-alone version of the scheme via a comprehensive suite of tests, demonstrating that both the scheme and the actual implementation are robust and accurate up to Lorentz factors and values of magnetization much larger than those relevant for BNS mergers. We also showed that the scheme is computationally efficient based on the number of EOS evaluations. As a matter of course, we implemented the scheme in `Spritz`, followed by a number of demanding GRMHD tests in full 3D in order to assess its correct implementation JVK7. Our tests, including the critical ones such as NS collapse to BH as well as evolution of a BH-disk system, showed that the RePrimAnd can robustly handle magnetized, low-density regimes with magnetic-to-fluid pressure ratio as high as $\sim 10^4$. The stand-alone RePrimAnd library is now also available within the latest Einstein Toolkit 'Johnson' (`ET_2021_11`) release [274], and has already been used successfully for magnetized BNS mergers in a different evolutionary code [275], JVK8.

At the time when `Spritz` was being developed, we parallely extended the investigations of [35] by performing a single BNS merger simulation using WhiskyMHD, going up to $\sim 100\,\mathrm{ms}$ after merger (longest simulation of its kind at that time) JVK1. The merger outcome was a differentially rotating, metastable long-lived NS remnant expected to survive much longer than the simulation timescale. Probing unexplored timescales, we were able to study different properties of the system in hand including magnetic field evolution and its dynamical impact, remnant structure and its rotation profile, as well as matter ejection. Moreover, we showed that the conditions found at the end of our simulation disfavoured the massive NS remnant as the central engine as a SGRB central engine, and further supported the standard 'BH-disk' scenario instead. This result was further strengthened by the latest work of [147] which reported

a similar BNS merger simulation extending up to $\sim 250\,\mathrm{ms}$ after merger. In this Thesis work, we also further analyzed the results of the latter simulation, showing that magnetically driven post-merger ejecta emanating from the MNS remnant before its collapse to a BH, with mass $\simeq 0.010 - 0.028\,M_{\odot}$ and radial velocities reaching up to $\simeq 0.2\,\mathrm{c}$, can possibly act as a viable source for the puzzling blue component of the kilonova observed in August 2017 JVK3. Finally, the outcome of an additional non-magnetized BNS merger simulation I performed, based on a similar setup, was used as input for the jet propagation study presented in JVK6. This was the first investigation of its kind based on initial data for the surrounding environment (through which the jet is to propagate) that were directly imported form the results of an actual general relativistic BNS merger simulation.

Our ongoing research entails performing magnetized BNS merger simulations with `Spritz` along with RePrimAnd C2P scheme. In this Thesis, we reported the first of such simulations, where the merger product was a HMNS which eventually collapsed to a BH surrounded by an accretion disk. We successfully followed the evolution of this system until final time without facing any problems. However, in contrast to the results of [43], our system did not produce an incipient jet until the simulation final time, likely due to the fact that we started with comparatively much lower initial magnetization levels for the grid resolution employed. Our next simulations will be based on the same setup but starting with higher initial magnetizations JVK9.

For the future, in terms code development, we plan to extend support of finite-temperature, composition-dependent tabulated EOS in `Spritz` when using the RePrimAnd C2P scheme. Another task which needs addressing is the extension of higher order methods for the magnetic field variables in `Spritz`. Since JVK8 delivered promising results, we also plan to adopt its sub-grid modeling technique within `Spritz`. Moreover, the current version of `Spritz` is designed to work efficiently on CPUs alone, hence, we also aim to provide support for running it on GPU infrastructures as well.

In terms of application to astrophysical scenarios, we plan to perform magnetized BNS as well as NSBH merger simulations employing all the latest machinery in hand i.e., using `Spritz` with RePrimAnd C2P, adopting different microphysical EOS, using higher order schemes, as well as activating neutrino leakage. Moving towards a more realistic description, our goal would be to provide better answers to some of the important open questions as well as revisit some of the old ones, in this field of research.

On the whole, we hope that `Spritz` will serve as a useful tool for the astrophysical community in the coming years, and also pave the way to unravel mysteries of some of the most extraordinary objects in the Universe.

Bibliography

1. Abbott, B. P., Abbott, R., *et al.* GW170817: Observation of Gravitational Waves from a Binary Neutron Star Inspiral. *Phys. Rev. Lett.* **119,** 161101. arXiv: 1710.05832 [gr-qc] (2017).
2. Abbott, B. P. *et al.* Gravitational Waves and Gamma-Rays from a Binary Neutron Star Merger: GW170817 and GRB 170817A. *Astrophys. J. Lett.* **848,** L13. arXiv: 1710.05834 [astro-ph.HE] (Oct. 2017).
3. Pian, E. *et al.* Spectroscopic identification of r-process nucleosynthesis in a double neutron-star merger. *Nature* **551,** 67–70. arXiv: 1710.05858 [astro-ph.HE] (2017).
4. Abbott, B. P. *et al.* Multi-messenger Observations of a Binary Neutron Star Merger. *Astrophys. J. Lett.* **848,** L12. arXiv: 1710.05833 [astro-ph.HE] (Oct. 2017).
5. Margalit, B. & Metzger, B. D. Constraining the Maximum Mass of Neutron Stars from Multi-messenger Observations of GW170817. *The Astrophysical Journal Letters* **850,** L19. arXiv: 1710.05938 [astro-ph.HE] (Dec. 2017).
6. Abbott, B. P. *et al.* GW170817: Measurements of Neutron Star Radii and Equation of State. *Phys. Rev. Lett.* **121,** 161101. arXiv: 1805.11581 [gr-qc] (2018).
7. Raithel, C. A. Constraints on the neutron star equation of state from GW170817. *European Physical Journal A* **55,** 80. arXiv: 1904.10002 [astro-ph.HE] (May 2019).
8. Nicholl, M. *et al.* Tight multimessenger constraints on the neutron star equation of state from GW170817 and a forward model for kilonova light-curve synthesis. *Monthly Notices of the Royal Astronomical Society* **505,** 3016–3032. arXiv: 2102.02229 [astro-ph.HE] (Aug. 2021).
9. Mooley, K. P. *et al.* Superluminal motion of a relativistic jet in the neutron-star merger GW170817. *Nature* **561,** 355–359. arXiv: 1806.09693 [astro-ph.HE] (Sept. 2018).
10. Lazzati, D. *et al.* Late Time Afterglow Observations Reveal a Collimated Relativistic Jet in the Ejecta of the Binary Neutron Star Merger GW170817. *Phys. Rev. Lett.* **120,** 241103. arXiv: 1712.03237 [astro-ph.HE] (June 2018).
11. Ghirlanda, G. *et al.* Compact radio emission indicates a structured jet was produced by a binary neutron star merger. *Science* **363,** 968–971. arXiv: 1808.00469 [astro-ph.HE] (2019).

12. Lazzati, D. Short Duration Gamma-Ray Bursts and Their Outflows in Light of GW170817. *Frontiers in Astronomy and Space Sciences* **7,** 78. arXiv: 2009.01773 [astro-ph.HE] (Nov. 2020).

13. Arcavi, I. *et al.* Optical emission from a kilonova following a gravitational-wave-detected neutron-star merger. *Nature* **551,** 64–66. arXiv: 1710.05843 [astro-ph.HE] (Nov. 2017).

14. Kasen, D., Metzger, B., Barnes, J., Quataert, E. & Ramirez-Ruiz, E. Origin of the heavy elements in binary neutron-star mergers from a gravitational-wave event. *Nature* **551,** 80–84. arXiv: 1710.05463 [astro-ph.HE] (2017).

15. Abbott, B. P. *et al.* A gravitational-wave standard siren measurement of the Hubble constant. *Nature* **551,** 85–88. arXiv: 1710.05835 (Nov. 2017).

16. Abbott, B. P. *et al.* Tests of General Relativity with GW170817. *Physical Review Letters* **123,** 011102. arXiv: 1811.00364 [gr-qc] (July 2019).

17. Ciolfi, R. Short gamma-ray burst central engines. *Int. J. Mod. Phys. D* **27,** 1842004. arXiv: 1804.03684 [astro-ph.HE] (2018).

18. Cowperthwaite, P. S. *et al.* The Electromagnetic Counterpart of the Binary Neutron Star Merger LIGO/Virgo GW170817. II. UV, Optical, and Near-infrared Light Curves and Comparison to Kilonova Models. *Astrophys. J. Lett* **848,** L17. arXiv: 1710.05840 [astro-ph.HE] (Oct. 2017).

19. Villar, V. A. *et al.* The Combined Ultraviolet, Optical, and Near-infrared Light Curves of the Kilonova Associated with the Binary Neutron Star Merger GW170817: Unified Data Set, Analytic Models, and Physical Implications. *Astrophys. J. Lett* **851,** L21. arXiv: 1710.11576 [astro-ph.HE] (Dec. 2017).

20. Metzger, B. D., Thompson, T. A. & Quataert, E. A Magnetar Origin for the Kilonova Ejecta in GW170817. *The Astrophysical Journal* **856,** 101. arXiv: 1801.04286 [astro-ph.HE] (Apr. 2018).

21. Siegel, D. M. & Metzger, B. D. Three-dimensional GRMHD Simulations of Neutrino-cooled Accretion Disks from Neutron Star Mergers. *Astrophys. J.* **858,** 52. arXiv: 1711.00868 [astro-ph.HE] (2018).

22. Kawaguchi, K., Shibata, M. & Tanaka, M. Radiative Transfer Simulation for the Optical and Near-infrared Electromagnetic Counterparts to GW170817. *Astrophys. J. Lett* **865,** L21. arXiv: 1806.04088 [astro-ph.HE] (Oct. 2018).

23. Nedora, V. *et al.* Spiral-wave Wind for the Blue Kilonova. *Astrophys. J. Lett* **886,** L30. arXiv: 1907.04872 [astro-ph.HE] (Dec. 2019).

24. Siegel, D. M. GW170817 -the first observed neutron star merger and its kilonova: Implications for the astrophysical site of the r-process. *European Physical Journal A* **55,** 203. arXiv: 1901.09044 [astro-ph.HE] (Nov. 2019).

25. Shibata, M. & Hotokezaka, K. Merger and Mass Ejection of Neutron Star Binaries. *Annual Review of Nuclear and Particle Science* **69,** 41–64. arXiv: 1908.02350 [astro-ph.HE] (2019).

26. Metzger, B. D. Kilonovae. *Living Reviews in Relativity* **23,** 1. arXiv: 1910.01617 (Dec. 2019).

27. Ciolfi, R. The key role of magnetic fields in binary neutron star mergers. *Gen. Rel. Grav.* **52,** 59. arXiv: 2003.07572 [astro-ph.HE] (June 2020).

28. Ruiz, M., Shapiro, S. L. & Tsokaros, A. Multimessenger Binary Mergers Containing Neutron Stars: Gravitational Waves, Jets, and γ-Ray Bursts. *Frontiers in Astronomy and Space Sciences* **8,** 39 (2021).

29. Mösta, P. *et al.* GRHydro: a new open-source general-relativistic magnetohydrodynamics code for the Einstein toolkit. *Classical and Quantum Gravity* **31,** 015005. arXiv: 1304.5544 [gr-qc] (Jan. 2014).

30. Etienne, Z. B., Paschalidis, V., Haas, R., Mösta, P. & Shapiro, S. L. IllinoisGRMHD: an open-source, user-friendly GRMHD code for dynamical spacetimes. *Classical and Quantum Gravity* **32,** 175009. arXiv: 1501.07276 [astro-ph.HE] (Sept. 2015).

31. Giacomazzo, B. & Rezzolla, L. The exact solution of the Riemann problem in relativistic magnetohydrodynamics. *Journal of Fluid Mechanics* **562,** 223–259 (2006).

32. Giacomazzo, B., Rezzolla, L. & Baiotti, L. Accurate evolutions of inspiralling and magnetized neutron stars: Equal-mass binaries. *Physical Review D* **83,** 044014 (2011).

33. Palenzuela, C. *et al.* Effects of the microphysical equation of state in the mergers of magnetized neutron stars with neutrino cooling. *Phys. Rev. D* **92,** 044045. arXiv: 1505.01607 [gr-qc] (Aug. 2015).

34. Kawamura, T. *et al.* Binary neutron star mergers and short gamma-ray bursts: Effects of magnetic field orientation, equation of state, and mass ratio. *Phys. Rev. D* **94,** 064012. http://link.aps.org/doi/10.1103/PhysRevD.94.064012 (6 2016).

35. Ciolfi, R. *et al.* General relativistic magnetohydrodynamic simulations of binary neutron star mergers forming a long-lived neutron star. *Phys. Rev. D* **95,** 063016. arXiv: 1701.08738 [astro-ph.HE] (Mar. 2017).

36. Most, E. R., Papenfort, L. J. & Rezzolla, L. Beyond second-order convergence in simulations of magnetized binary neutron stars with realistic microphysics. *Mon. Not. R. Astron. Soc.* **490,** 3588–3600. arXiv: 1907.10328 [astro-ph.HE] (Dec. 2019).

37. Ruiz, M., Tsokaros, A., Paschalidis, V. & Shapiro, S. L. Effects of spin on magnetized binary neutron star mergers and jet launching. *Physical Review D* **99,** 084032 (2019).

38. Mösta, P., Radice, D., Haas, R., Schnetter, E. & Bernuzzi, S. A Magnetar Engine for Short GRBs and Kilonovae. *Astrophys. J. Lett.* **901,** L37. arXiv: 2003.06043 [astro-ph.HE] (Oct. 2020).

39. East, W. E., Lehner, L., Liebling, S. L. & Palenzuela, C. Multimessenger signals from black hole-neutron star mergers without significant tidal disruption. *arXiv:2101.12214* (2021).

40. Most, E. R., Papenfort, L. J., Tootle, S. D. & Rezzolla, L. On accretion discs formed in MHD simulations of black hole–neutron star mergers with accurate microphysics. *Monthly Notices of the Royal Astronomical Society* **506,** 3511–3526. ISSN: 0035-8711. eprint: https://academic.oup.com/mnras/article-pdf/506/3/3511/39354872/stab1824.pdf. https://doi.org/10.1093/mnras/stab1824 (July 2021).

41. *Stellar Collapse, https://stellarcollapse.org/* https://stellarcollapse.org/.

42. Just, O., Obergaulinger, M., Janka, H. T., Bauswein, A. & Schwarz, N. Neutron-star Merger Ejecta as Obstacles to Neutrino-powered Jets of Gamma-Ray Bursts. *Astrophys. J. Lett.* **816,** L30. arXiv: 1510.04288 [astro-ph.HE] (Jan. 2016).

43. Ruiz, M., Lang, R. N., Paschalidis, V. & Shapiro, S. L. Binary Neutron Star Mergers: A Jet Engine for Short Gamma-Ray Bursts. *Astrophys. J. Lett.* **824,** L6. arXiv: 1604.02455 [astro-ph.HE] (June 2016).

44. Ruiz, M., Tsokaros, A. & Shapiro, S. L. Jet launching from merging magnetized binary neutron stars with realistic equations of state. *Physical Review D* **104,** 124049. arXiv: 2110.11968 [astro-ph.HE] (Dec. 2021).

45. Bauswein, A., Goriely, S. & Janka, H. T. Systematics of Dynamical Mass Ejection, Nucleosynthesis, and Radioactively Powered Electromagnetic Signals from Neutron-star Mergers. *The Astrophysical Journal* **773,** 78. arXiv: 1302.6530 [astro-ph.SR] (Aug. 2013).

46. Hotokezaka, K. *et al.* Remnant massive neutron stars of binary neutron star mergers: Evolution process and gravitational waveform. *Physical Review D* **88,** 044026. arXiv: 1307.5888 [astro-ph.HE] (Aug. 2013).

47. Radice, D. *et al.* Dynamical mass ejection from binary neutron star mergers. *Monthly Notices of the Royal Astronomical Society* **460,** 3255–3271 (2016).

48. Arnowitt, R., Deser, S. & Misner, C. W. Dynamical structure and definition of energy in general relativity. *Physical Review* **116,** 1322 (1959).

49. Nakamura, T., Oohara, K. & Kojima, Y. General relativistic collapse to black holes and gravitational waves from black holes. *Progress of Theoretical Physics Supplement* **90,** 1–218 (1987).

50. Shibata, M. & Nakamura, T. Evolution of three-dimensional gravitational waves: Harmonic slicing case. *Physical Review D* **52,** 5428 (1995).

51. Baumgarte, T. W. & Shapiro, S. L. Numerical integration of Einstein's field equations. *Physical Review D* **59,** 024007 (1998).

52. Alcubierre, M. *Introduction to 3+ 1 numerical relativity* (Oxford University Press, 2008).

53. Anile, A. Relativistic Fluids and Magneto-Fluids, Cambridge Monographs on Mathematical Physics (1989).

54. Rezzolla, L. & Zanotti, O. *Relativistic hydrodynamics* (Oxford University Press, 2013).

55. Alcubierre, M. *et al.* Towards a stable numerical evolution of strongly gravitating systems in general relativity: The conformal treatments. *Physical Review D* **62,** 044034 (2000).

56. Alcubierre, M. *et al.* Gauge conditions for long-term numerical black hole evolutions without excision. *Physical Review D* **67,** 084023 (2003).

57. Sarbach, O., Calabrese, G., Pullin, J. & Tiglio, M. Hyperbolicity of the Baumgarte-Shapiro-Shibata-Nakamura system of Einstein evolution equations. *Physical Review D* **66,** 064002 (2002).

58. Bona, C., Ledvinka, T., Palenzuela, C. & Žáček, M. Symmetry-breaking mechanism for the Z4 general-covariant evolution system. *Physical Review D* **69,** 064036 (2004).

59. Nagy, G., Ortiz, O. E. & Reula, O. A. Strongly hyperbolic second order Einstein's evolution equations. *Physical Review D* **70,** 044012 (2004).

60. Alcubierre, M., Allen, G., Brügmann, B., Seidel, E. & Suen, W.-M. Towards an understanding of the stability properties of the 3+ 1 evolution equations in general relativity. *Physical Review D* **62,** 124011 (2000).

61. Font, J. A., Miller, M., Suen, W.-M. & Tobias, M. Three-dimensional numerical general relativistic hydrodynamics: Formulations, methods, and code tests. *Physical Review D* **61,** 044011 (2000).

62. York Jr, J. W. Kinematics and dynamics of general relativity. *Sources of gravitational radiation,* 83–126 (1979).

63. Bona, C., Masso, J., Seidel, E. & Stela, J. New formalism for numerical relativity. *Physical Review Letters* **75,** 600 (1995).

64. Alcubierre, M. & Brügmann, B. Simple excision of a black hole in 3+ 1 numerical relativity. *Physical Review D* **63,** 104006 (2001).

65. Wendroff, B. L. P. Systems of conservation laws. *Commun. Pure Appl. Math.* **13,** 217–237 (1960).

66. Hou, T. Y. & LeFloch, P. G. Why nonconservative schemes converge to wrong solutions: error analysis. *Mathematics of computation* **62,** 497–530 (1994).

67. Font, J. A. Numerical hydrodynamics and magnetohydrodynamics in general relativity. *Living Reviews in Relativity* **11,** 1–131 (2008).

68. Shibata, M. *Numerical relativity* (World Scientific, 2015).

69. Etienne, Z. B., Paschalidis, V., Liu, Y. T. & Shapiro, S. L. Relativistic magnetohydrodynamics in dynamical spacetimes: Improved electromagnetic gauge condition for adaptive mesh refinement grids. *Physical Review D* **85,** 024013 (2012).

70. Etienne, Z. B., Liu, Y. T. & Shapiro, S. L. Relativistic magnetohydrodynamics in dynamical spacetimes: A new adaptive mesh refinement implementation. *Physical Review D* **82,** 084031 (2010).

71. Farris, B. D., Gold, R., Paschalidis, V., Etienne, Z. B. & Shapiro, S. L. Binary Black-Hole Mergers in Magnetized Disks: Simulations in Full General Relativity. *Phys. Rev. Lett.* **109,** 221102. `http://link.aps.org/doi/10.1103/PhysRevLett.109.221102` (22 2012).

72. P, H. G. *Polytropes: applications in astrophysics and related fields* ((Springer Science & Business Media), 2004).

73. *CompOSE, https://compose.obspm.fr/home/* `https://compose.obspm.fr/home/`.

74. Baym, G., Pethick, C. & Sutherland, P. The ground state of matter at high densities: equation of state and stellar models. *The Astrophysical Journal* **170,** 299 (1971).

75. Negele, J. W. & Vautherin, D. Density-matrix expansion for an effective nuclear Hamiltonian. II. *Physical Review C* **11,** 1031 (1975).

76. Tsang, M. *et al.* Constraints on the symmetry energy and neutron skins from experiments and theory. *Physical Review C* **86,** 015803 (2012).

77. Lattimer, J. M. & Prakash, M. The equation of state of hot, dense matter and neutron stars. *Physics Reports* **621,** 127–164 (2016).

78. Oertel, M., Hempel, M., Klähn, T. & Typel, S. Equations of state for supernovae and compact stars. *Reviews of Modern Physics* **89,** 015007 (2017).

79. Read, J. S., Lackey, B. D., Owen, B. J. & Friedman, J. L. Constraints on a phenomenologically parametrized neutron-star equation of state. *Physical Review D* **79,** 124032 (2009).

80. Richtmyer, R. D. & Morton, K. W. Difference methods for initial-value problems. *Malabar, Fla.: Krieger Publishing Co., 2nd ed.* (1994).

81. Courant, R., Friedrichs, K. & Lewy, H. On the partial difference equations of mathematical physics. *IBM journal of Research and Development* **11,** 215–234 (1967).

82. Godunov, S. & Bohachevsky, I. Finite difference method for numerical computation of discontinuous solutions of the equations of fluid dynamics. *Matematičeskij sbornik* **47,** 271–306 (1959).

83. Wendroff, B. The Riemann problem for materials with nonconvex equations of state I: Isentropic flow. *Journal of Mathematical Analysis and Applications* **38,** 454–466 (1972).

84. Wendroff, B. The Riemann problem for materials with nonconvex equations of state: II: General Flow. *Journal of Mathematical Analysis and Applications* **38,** 640–658 (1972).

85. *The Riemann problem* `https://www.uv.es/astrorela/simulacionnumerica/node31.html`.

86. Harten, A., Lax, P. D. & Leer, B. v. On upstream differencing and Godunov-type schemes for hyperbolic conservation laws. *SIAM review* **25,** 35–61 (1983).

87. Einfeldt, B. On Godunov-type methods for gas dynamics. *SIAM Journal on Numerical Analysis* **25,** 294–318 (1988).

88. Toro, E. F. *Riemann solvers and numerical methods for fluid dynamics: a practical introduction* (Springer Science & Business Media, 2013).

89. Laney, C. B. *Computational gasdynamics* (Cambridge university press, 1998).

90. Giacomazzo, B. & Rezzolla, L. WhiskyMHD: a new numerical code for general relativistic magnetohydrodynamics. *Classical and Quantum Gravity* **24,** S235 (2007).

91. Mösta, P. *et al.* GRHydro: a new open-source general-relativistic magnetohydrodynamics code for the Einstein toolkit. *Classical and quantum gravity* **31,** 015005 (2013).

92. Etienne, Z. B., Paschalidis, V., Haas, R., Mösta, P. & Shapiro, S. L. IllinoisGRMHD: an open-source, user-friendly GRMHD code for dynamical spacetimes. *Classical and Quantum Gravity* **32,** 175009 (2015).

93. Löffler, F. *et al.* The Einstein Toolkit: a community computational infrastructure for relativistic astrophysics. *Classical and Quantum Gravity* **29,** 115001 (2012).

94. Babiuc-Hamilton, M. *et al.* The Einstein Toolkit. *Zenodo* (2019).

95. Liu, Y. T., Shapiro, S. L., Etienne, Z. B. & Taniguchi, K. General relativistic simulations of magnetized binary neutron star mergers. *Phys. Rev. D* **78,** 024012. arXiv: 0803.4193 (July 2008).

96. Anderson, M. *et al.* Magnetized neutron-star mergers and gravitational-wave signals. *Physical Review Letters* **100,** 191101 (2008).

97. Kiuchi, K., Kyutoku, K., Sekiguchi, Y. & Shibata, M. Global simulations of strongly magnetized remnant massive neutron stars formed in binary neutron star mergers. *Physical Review D* **97,** 124039 (2018).

98. Palenzuela, C., Lehner, L. & Liebling, S. L. Dual jets from binary black holes. *Science* **329,** 927–930 (2010).

99. Giacomazzo, B., Baker, J. G., Miller, M. C., Reynolds, C. S. & van Meter, J. R. General relativistic simulations of magnetized plasmas around merging supermassive black holes. *The Astrophysical Journal Letters* **752,** L15 (2012).

100. Gold, R. *et al.* Accretion disks around binary black holes of unequal mass: General relativistic MHD simulations of postdecoupling and merger. *Physical Review D* **90,** 104030 (2014).

101. Kelly, B. J., Baker, J. G., Etienne, Z. B., Giacomazzo, B. & Schnittman, J. Prompt electromagnetic transients from binary black hole mergers. *Physical Review D* **96,** 123003 (2017).

102. d'Ascoli, S. *et al.* Electromagnetic emission from supermassive binary black holes approaching merger. *The Astrophysical Journal* **865,** 140 (2018).

103. Porth, O. *et al.* The event horizon general relativistic magnetohydrodynamic code comparison project. *The Astrophysical Journal Supplement Series* **243,** 26 (2019).

104. Paschalidis, V., Ruiz, M. & Shapiro, S. L. Relativistic simulations of black hole–neutron star coalescence: the jet emerges. *The Astrophysical Journal Letters* **806,** L14 (2015).

105. Ruiz, M., Paschalidis, V., Tsokaros, A. & Shapiro, S. L. Black hole-neutron star coalescence: effects of the neutron star spin on jet launching and dynamical ejecta mass. *Physical Review D* **102,** 124077 (2020).

106. Giacomazzo, B., Rezzolla, L. & Baiotti, L. Can magnetic fields be detected during the inspiral of binary neutron stars? *MNRAS* **399,** L164–L168. arXiv: 0901.2722 [gr-qc] (Oct. 2009).

107. Rezzolla, L. *et al.* The missing link: merging neutron stars naturally produce jet-like structures and can power short gamma-ray bursts. *The Astrophysical Journal Letters* **732,** L6 (2011).

108. Giacomazzo, B. & Perna, R. Formation of stable magnetars from binary neutron star mergers. *The Astrophysical Journal Letters* **771,** L26 (2013).

109. Giacomazzo, B., Zrake, J., Duffell, P. C., MacFadyen, A. I. & Perna, R. Producing magnetar magnetic fields in the merger of binary neutron stars. *The Astrophysical Journal* **809,** 39 (2015).

110. Endrizzi, A., Ciolfi, R., Giacomazzo, B., Kastaun, W. & Kawamura, T. General relativistic magnetohydrodynamic simulations of binary neutron star mergers with the APR4 equation of state. *Classical and Quantum Gravity* **33,** 164001 (2016).

111. Ciolfi, R. *et al.* General relativistic magnetohydrodynamic simulations of binary neutron star mergers forming a long-lived neutron star. *Physical Review D* **95,** 063016 (2017).

112. Giacomazzo, B, Baker, J. G., Miller, M. C., Reynolds, C. S. & van Meter, J. R. General Relativistic Simulations of Magnetized Plasmas around Merging Supermassive Black Holes. *ApJ Letters* **752,** L15. arXiv: 1203.6108 [astro-ph.HE] (2012).

113. Giacomazzo, B. *et al. The Spritz Code* version 1.1.0. Dec. 2020. https://doi.org/10.5281/zenodo.4350072.

114. W, B. T. & L, S. S. *Numerical relativity: solving Einstein's equations on the computer* ((Cambridge University Press), 2010).

115. Antón, L. *et al.* Numerical 3+ 1 general relativistic magnetohydrodynamics: a local characteristic approach. *The Astrophysical Journal* **637,** 296 (2006).

116. Banyuls, F., Font, J. A., Ibáñez, J. M., Martí, J. M. & Miralles, J. A. Numerical {3+ 1} general relativistic hydrodynamics: A local characteristic approach. *The Astrophysical Journal* **476,** 221 (1997).

117. Martí, J. M., Ibánez, J. M. & Miralles, J. A. Numerical relativistic hydrodynamics: Local characteristic approach. *Physical Review D* **43,** 3794 (1991).

118. Del Zanna, L, Zanotti, O, Bucciantini, N & Londrillo, P. ECHO: a Eulerian conservative high-order scheme for general relativistic magnetohydrodynamics and magnetodynamics. *Astronomy & Astrophysics* **473,** 11–30 (2007).

119. Mignone, A. & Del Zanna, L. Systematic construction of upwind constrained transport schemes for MHD. *Journal of Computational Physics* **424,** 109748 (2021).

120. Balsara, D. Total variation diminishing scheme for relativistic magnetohydrodynamics. *The Astrophysical Journal Supplement Series* **132,** 83 (2001).

121. Noble, S. C., Gammie, C. F., McKinney, J. C. & Del Zanna, L. Primitive Variable Solvers for Conservative General Relativistic Magnetohydrodynamics. *Astrophys. J.* **641,** 626–637. arXiv: `astro-ph/0512420 [astro-ph]` (Apr. 2006).

122. *Carpet, https://carpetcode.org/* `https://carpetcode.org/`.

123. Schnetter, E., Hawley, S. H. & Hawke, I. Evolutions in 3D numerical relativity using fixed mesh refinement. *Classical and quantum gravity* **21,** 1465 (2004).

124. Berger, M. J. & Oliger, J. Adaptive mesh refinement for hyperbolic partial differential equations. *Journal of computational Physics* **53,** 484–512 (1984).

125. Beckwith, K. & Stone, J. M. A second-order Godunov method for multi-dimensional relativistic magnetohydrodynamics. *The Astrophysical Journal Supplement Series* **193,** 6 (2011).

126. Komissarov, S. A Godunov-type scheme for relativistic magnetohydrodynamics. *Monthly Notices of the Royal Astronomical Society* **303,** 343–366 (1999).

127. Balsara, D. S. & Spicer, D. S. A staggered mesh algorithm using high order Godunov fluxes to ensure solenoidal magnetic fields in magnetohydrodynamic simulations. *Journal of Computational Physics* **149,** 270–292 (1999).

128. Tóth, G. The nabla · B= 0 constraint in shock-capturing magnetohydrodynamics codes. *Journal of Computational Physics* **161,** 605–652 (2000).

129. Del Zanna, L, Bucciantini, N & Londrillo, P. An efficient shock-capturing central-type scheme for multidimensional relativistic flows-II. Magnetohydrodynamics. *Astronomy & Astrophysics* **400,** 397–413 (2003).

130. DeVore, C. R. Flux-corrected transport techniques for multidimensional compressible magnetohydrodynamics. *Journal of Computational Physics* **92,** 142–160 (1991).

131. Gardiner, T. A. & Stone, J. M. An unsplit Godunov method for ideal MHD via constrained transport. *Journal of Computational Physics* **205,** 509–539 (2005).

132. Stone, J. M., Gardiner, T. A., Teuben, P., Hawley, J. F. & Simon, J. B. Athena: a new code for astrophysical MHD. *The Astrophysical Journal Supplement Series* **178,** 137 (2008).

133. Cerdá-Durán, P., Font, J. A., Antón, L. & Müller, E. A new general relativistic magnetohydrodynamics code for dynamical spacetimes. *Astronomy & Astrophysics* **492,** 937–953 (2008).

134. Cerdá-Durán, P., Font, J. A. & Dimmelmeier, H. General relativistic simulations of passive-magneto-rotational core collapse with microphysics. *Astronomy & Astrophysics* **474,** 169–191 (2007).

135. Mewes, V. *et al.* Numerical relativity in spherical coordinates: A new dynamical spacetime and general relativistic MHD evolution framework for the Einstein Toolkit. *Phys. Rev. D* **101,** 104007. arXiv: `2002.06225 [gr-qc]` (May 2020).

136. Oppenheimer, J. R. & Volkoff, G. M. On Massive Neutron Cores. *Physical Review* **55,** 374–381. https://link.aps.org/doi/10.1103/PhysRev.55.374 (4 1939).

137. Tolman, R. C. Static solutions of Einstein's field equations for spheres of fluid. *Physical Review* **55,** 364 (1939).

138. Baiotti, L. *et al.* Three-dimensional relativistic simulations of rotating neutron-star collapse to a Kerr black hole. *Physical Review D* **71,** 024035 (2005).

139. Cowling, T. G. The non-radial oscillations of polytropic stars. *Monthly Notices of the Royal Astronomical Society* **101,** 367 (1941).

140. Lindblom, L. & Splinter, R. J. The accuracy of the relativistic Cowling approximation. *The Astrophysical Journal* **348,** 198–202 (1990).

141. Thorne, K. S. Nonradial pulsation of general-relativistic stellar models. IV. The weakfield limit. *The astrophysical journal* **158,** 997 (1969).

142. Font, J. A., Stergioulas, N. & Kokkotas, K. D. Non-linear hydrodynamical evolution of rotating relativistic stars: numerical methods and code tests. *Monthly Notices of the Royal Astronomical Society* **313,** 678–688 (2000).

143. A, F. J. *et al.* Three-dimensional numerical general relativistic hydrodynamics. II. Long-term dynamics of single relativistic stars. *PRD* **65,** 084024 (2002).

144. Foucart, F. *et al.* Impact of an improved neutrino energy estimate on outflows in neutron star merger simulations. *Phys. Rev. D* **94,** 123016. arXiv: 1607.07450 [astro-ph.HE] (2016).

145. Radice, D. *et al.* Binary Neutron Star Mergers: Mass Ejection, Electromagnetic Counterparts and Nucleosynthesis. *Astrophys. J.* **869,** 130. arXiv: 1809.11161 [astro-ph.HE] (2018).

146. Perego, A., Yasin, H. & Arcones, A. Neutrino pair annihilation above merger remnants: implications of a long-lived massive neutron star. *J. Phys. G Nucl. Phys.* **44,** 084007. arXiv: 1701.02017 [astro-ph.HE] (Aug. 2017).

147. Ciolfi, R. Collimated outflows from long-lived binary neutron star merger remnants. *Mon. Not. R. Astron. Soc. Lett.* arXiv: 2001.10241 [astro-ph.HE] (Apr. 2020).

148. Palenzuela, C. *et al.* Effects of the microphysical equation of state in the mergers of magnetized neutron stars with neutrino cooling. *Phys. Rev. D* **92,** 044045 (2015).

149. Lattimer, J. M. & Swesty, F. D. A generalized equation of state for hot, dense matter. *Nucl. Phys. A* **535,** 331–376 (1991).

150. Radice, D., Perego, A., Bernuzzi, S. & Zhang, B. Long-lived remnants from binary neutron star mergers. *Mon. Not. R. Astron. Soc.* **481,** 3670–3682. ISSN: 0035-8711. eprint: https://academic.oup.com/mnras/article-pdf/481/3/3670/25838737/sty2531.pdf. https://doi.org/10.1093/mnras/sty2531 (Sept. 2018).

151. Bernuzzi, S. Neutron star merger remnants. *Gen. Rel. Grav.* **52,** 108. ISSN: 1572-9532. https://doi.org/10.1007/s10714-020-02752-5 (2020).

152. Smartt, S. *et al.* A kilonova as the electromagnetic counterpart to a gravitational-wave source. *Nature* **551,** 75–79 (2017).

153. Sekiguchi, Y. Stellar Core Collapse in Full General Relativity with Microphysics: Formulation and Spherical Collapse Test. *Prog. Theor. Phys.* **124,** 331–379 (2010).

154. Rosso, A. G., Mascaretti, C., Palladino, A. & Vissani, F. Introduction to neutrino astronomy. *Eur. Phys. J. Plus* **133,** 267 (2018).

155. Ruffert, M, Janka, H.-T., Takahashi, K & Schäfer, G. Coalescing neutron stars–a step towards physical models. *Astron. Astrophys.* **319,** 122 (1997).

156. O'Connor, E. & Ott, C. D. A new open-source code for spherically symmetric stellar collapse to neutron stars and black holes. *Class. Quantum Grav.* **27,** 114103 (2010).

157. Foucart, F. *et al.* Monte-Carlo Neutrino Transport in Neutron Star Merger Simulations. *Astrophys. J. Lett.* **902,** L27. arXiv: `2008.08089 [astro-ph.HE]` (Oct. 2020).

158. Deaton, M. B. *et al.* Black hole-neutron star mergers with a hot nuclear equation of state: outflow and neutrino-cooled disk for a low-mass, high-spin case. *Astrophys. J.* **776,** 47 (2013).

159. Foucart, F. *et al.* Neutron star-black hole mergers with a nuclear equation of state and neutrino cooling: dependence in the binary parameters. *Phys. Rev. D* **90,** 024026 (2014).

160. Radice, D. *et al.* Dynamical mass ejection from binary neutron star mergers. *Mon. Not. R. Astron. Soc.* **460,** 3255–3271 (2016).

161. Ott, C. D. *et al.* General-relativistic simulations of three-dimensional core-collapse supernovae. *Astrophys. J.* **768,** 115 (2013).

162. Ruffert, M., Janka, H.-T., Takahashi, K. & Schaefer, G. Coalescing neutron stars – a step towards physical models, II. Neutrino emission, neutron tori, and gamma-ray bursts. *Astron. Astrophys.* **319,** 122–153 (1997).

163. Rosswog, S. & Liebendörfer, M. High-resolution calculations of merging neutron stars—II. Neutrino emission. *Mon. Not. R. Astron. Soc.* **342,** 673–689 (2003).

164. Takahashi, K, El Eid, M. & Hillebrandt, W. Beta transition rates in hot and dense matter. *Astron. Astrophys.* **67,** 185–197 (1978).

165. Burrows, A., Reddy, S. & Thompson, T. A. Neutrino opacities in nuclear matter. *Nuclear Physics A* **777,** 356–394 (2006).

166. Ruffert, M, Janka, H.-T. & Schaefer, G. Coalescing neutron stars-a step towards physical models. I. Hydrodynamic evolution and gravitational-wave emission. *Astron. Astrophys.* **311,** 532–566 (1996).

167. Galeazzi, F., Kastaun, W., Rezzolla, L. & Font, J. A. Implementation of a simplified approach to radiative transfer in general relativity. *Phys. Rev. D* **88,** 064009 (2013).

168. *ETK Turing* `http://lists.einsteintoolkit.org/pipermail/users/2020-May/007449.html`.

169. *Lorene, https://lorene.obspm.fr/* https://lorene.obspm.fr/.

170. *the Spritz Code, https://doi.org/10.5281/zenodo.3689751* https://doi.org/10.5281/zenodo.3689751.

171. Brent, R. P. *Algorithms for minimization without derivatives* (Courier Corporation, 2013).

172. Siegel, D. M., Mösta, P., Desai, D. & Wu, S. Recovery schemes for primitive variables in general-relativistic magnetohydrodynamics. *Astrophys J.* **859,** 71 (2018).

173. Kastaun, W., Ciolfi, R. & Giacomazzo, B. Structure of stable binary neutron star merger remnants: A case study. *Physical Review D* **94,** 044060 (2016).

174. Kastaun, W., Ciolfi, R., Endrizzi, A. & Giacomazzo, B. Structure of stable binary neutron star merger remnants: Role of initial spin. *Physical Review D* **96,** 043019 (2017).

175. Martin, D, Perego, A, Kastaun, W & Arcones, A. The role of weak interactions in dynamic ejecta from binary neutron star mergers. *Class. Quantum Grav.* **35,** 034001 (2018).

176. Borges, R., Carmona, M., Costa, B. & Don, W. S. An improved weighted essentially non-oscillatory scheme for hyperbolic conservation laws. *J. Comp. Phys.,* 3191–3211 (2008).

177. Del Zanna, L., Zanotti, O., Bucciantini, N. & Londrillo, P. ECHO: a Eulerian conservative high-order scheme for general relativistic magnetohydrodynamics and magnetodynamics. *Astron. Astrophys.* **473,** 11–30. arXiv: 0704.3206 [astro-ph] (Oct. 2007).

178. Lattimer, J. M. & Swesty, D. F. A generalized equation of state for hot, dense matter. *Nucl. Phys. A* **535,** 331–376 (Dec. 1991).

179. Bocquet, M., Bonazzola, S., Gourgoulhon, E. & Novak, J. Rotating neutron star models with magnetic field. *Astron. Astrophys.* **301,** 757. arXiv: gr-qc/9503044 (1995).

180. Liang, E. Relativistic simple waves: shock damping and entropy production. *Astrophys. J.* **211,** 361–376 (Jan. 1977).

181. Anile, A. *Relativistic Fluids and Magneto-fluids* 348. ISBN: 0521304067 (Cambridge University Press, 1990).

182. Bernuzzi, S. & Dietrich, T. Gravitational waveforms from binary neutron star mergers with high-order weighted-essentially-nonoscillatory schemes in numerical relativity. *Phys. Rev. D* **94,** 064062. arXiv: 1604.07999 [gr-qc] (Sept. 2016).

183. Ott, C. *et al.* Correlated gravitational wave and neutrino signals from general-relativistic rapidly rotating iron core collapse. *Phys. Rev. D* **86,** 024026 (2012).

184. Neilsen, D. *et al.* Magnetized neutron stars with realistic equations of state and neutrino cooling. *Phys. Rev. D* **89,** 104029. arXiv: 1403.3680 [gr-qc] (May 2014).

185. Shibata, M., Nagakura, H., Sekiguchi, Y. & Yamada, S. Conservative form of Boltzmann's equation in general relativity. *Phys. Rev. D* **89,** 084073 (2014).

186. Siegel, D. M., Mösta, P., Desai, D. & Wu, S. Recovery Schemes for Primitive Variables in General-relativistic Magnetohydrodynamics. *Astrophys. J.* **859,** 71. arXiv: 1712.07538 [astro-ph.HE] (May 2018).

187. Kastaun, W. *RePrimAnd: Version 1.1* version v1.1. Oct. 2020. https://doi.org/10.5281/zenodo.4075317.

188. Müller, H. & Serot, B. D. Relativistic mean-field theory and the high-density nuclear equation of state. *Nuclear Physics A* **606,** 508–537. eprint: nucl-th/9603037 (Feb. 1996).

189. Palenzuela, C., Lehner, L., Reula, O. & Rezzolla, L. Beyond ideal MHD: towards a more realistic modelling of relativistic astrophysical plasmas. *Monthly Notices of the Royal Astronomical Society* **394,** 1727–1740 (2009).

190. Dionysopoulou, K., Alic, D., Palenzuela, C., Rezzolla, L. & Giacomazzo, B. General-relativistic resistive magnetohydrodynamics in three dimensions: Formulation and tests. *Phys. Rev. D* **88,** 044020. arXiv: 1208.3487 [gr-qc] (2013).

191. Ripperda, B. *et al.* General-relativistic resistive magnetohydrodynamics with robust primitive variable recovery for accretion disk simulations. *The Astrophysical Journal Supplement Series* **244,** 10 (2019).

192. Wright, A. J. & Hawke, I. A resistive extension for ideal magnetohydrodynamics. *Monthly Notices of the Royal Astronomical Society* **491,** 5510–5523. arXiv: 1906.03150 (Feb. 2020).

193. Galeazzi, F., Kastaun, W., Rezzolla, L. & Font, J. A. Implementation of a simplified approach to radiative transfer in general relativity. *Phys. Rev. D* **88,** 064009. arXiv: 1306.4953 [gr-qc] (Sept. 2013).

194. Alefeld, G. E., Potra, F. A. & Shi, Y. Algorithm 748: Enclosing Zeros of Continuous Functions. *ACM Trans. Math. Softw.* **21,** 327–344. ISSN: 0098-3500. https://doi.org/10.1145/210089.210111 (Sept. 1995).

195. Noble, S. C., Gammie, C. F., McKinney, J. C. & Zanna, L. D. Primitive Variable Solvers for Conservative General Relativistic Magnetohydrodynamics. *Astrophys. J.* **641,** 626–637. https://doi.org/10.1086%2F500349 (2006).

196. Cerdá-Durán, P., Font, J. A., Antón, L. & Müller, E. A new general relativistic magnetohydrodynamics code for dynamical spacetimes. *Astron. Astrophys.* **492,** 937–953. arXiv: 0804.4572 [astro-ph] (Dec. 2008).

197. Neilsen, D. *et al.* Magnetized neutron stars with realistic equations of state and neutrino cooling. *Phys. Rev. D* **89,** 104029. https://link.aps.org/doi/10.1103/PhysRevD.89.104029 (10 2014).

198. Palenzuela, C. *et al.* Effects of the microphysical equation of state in the mergers of magnetized neutron stars with neutrino cooling. *Phys. Rev. D* **92,** 044045. https://link.aps.org/doi/10.1103/PhysRevD.92.044045 (4 2015).

199. Newman, W. I. & Hamlin, N. D. Primitive Variable Determination in Conservative Relativistic Magnetohydrodynamic Simulations. *SIAM J. Sci. Comput.* **36,** B661–B683 (2014).

200. Ciolfi, R., Lander, S. K., Manca, G. M. & Rezzolla, L. Instability-driven Evolution of Poloidal Magnetic Fields in Relativistic Stars. *Astrophys. J. Lett.* **736,** L6. arXiv: 1105.3971 [gr-qc] (July 2011).

201. Kiuchi, K., Kyutoku, K. & Shibata, M. Three-dimensional evolution of differentially rotating magnetized neutron stars. *Phys. Rev. D* **86,** 064008. arXiv: 1207.6444 (2012).

202. Giacomazzo, B., Rezzolla, L. & Stergioulas, N. Collapse of differentially rotating neutron stars and cosmic censorship. *Phys. Rev. D* **84,** 024022. https://link.aps.org/doi/10.1103/PhysRevD.84.024022 (2 2011).

203. Fishbone, L. G. & Moncrief, V. Relativistic fluid disks in orbit around Kerr black holes. *The Astrophysical Journal* **207,** 962–976 (1976).

204. Foucart, F. *et al.* Numerical simulations of neutron star-black hole binaries in the near-equal-mass regime. *Phys. Rev. D* **99,** 103025. arXiv: 1903.09166 [astro-ph.HE] (2019).

205. Bernuzzi, S. Neutron star merger remnants. *General Relativity and Gravitation* **52,** 108. arXiv: 2004.06419 [astro-ph.HE] (2020).

206. Kastaun, W. & Ohme, F. Numerical Inside View of Hypermassive Remnant Models for GW170817. *arXiv preprint arXiv:2103.01586* (2021).

207. Gammie, C. F., McKinney, J. C. & Tóth, G. HARM: A Numerical Scheme for General Relativistic Magnetohydrodynamics. *Astrophys. J.* **589,** 444–457. arXiv: astro-ph/0301509 [astro-ph] (2003).

208. Noble, S. C., Krolik, J. H. & Hawley, J. F. Direct Calculation of the Radiative Efficiency of an Accretion Disk Around a Black Hole. *Astrophys. J.* **692,** 411–421. arXiv: 0808.3140 [astro-ph] (2009).

209. Porth, O. *et al.* The black hole accretion code. *Computational Astrophysics and Cosmology* **4,** 1. arXiv: 1611.09720 [gr-qc] (May 2017).

210. Janiuk, A., Sapountzis, K., Mortier, J. & Janiuk, I. Numerical simulations of black hole accretion flows. *arXiv e-prints,* arXiv:1805.11305. arXiv: 1805.11305 [astro-ph.HE] (2018).

211. Murguia-Berthier, A. *et al.* HARM3D+NUC: A new method for simulating the post-merger phase of binary neutron star mergers with GRMHD, tabulated EOS and neutrino leakage. *arXiv e-prints.* arXiv: 2106.05356 [astro-ph.HE] (2021).

212. Kreiss, H.-O. & Oliger, J. *Methods for the approximate solution of time dependent problems* **10** (International Council of Scientific Unions, World Meteorological Organization, 1973).

213. Abbott, B. P. *et al.* GW170817: Observation of Gravitational Waves from a Binary Neutron Star Inspiral. *Phys. Rev. Lett.* **119,** 161101. arXiv: 1710.05832 [gr-qc] (Oct. 2017).

214. Abbott, B. *et al.* Properties of the binary neutron star merger GW170817. *Physical Review X* **9,** 011001 (2019).

215. Abbott, B. P. *et al.* Model comparison from LIGO–Virgo data on GW170817's binary components and consequences for the merger remnant. *Class. Quantum Grav.* **37,** 045006. https://doi.org/10.1088%2F1361-6382%2Fab5f7c (2020).

216. Ciolfi, R. Binary neutron star mergers after GW170817. *Front. Astron. Sp. Sci.* **7,** 27. arXiv: 2005.02964 [astro-ph.HE] (June 2020).

217. Ascenzi, S., Oganesyan, G., Branchesi, M. & Ciolfi, R. Electromagnetic counterparts of compact binary mergers. *Journal of Plasma Physics* **87,** 845870102. arXiv: 2011.04001 [astro-ph.HE] (Feb. 2021).

218. Landau, L. D. On the theory of stars. *Phys. Z. Sowjetunion* **1,** 152 (1932).

219. Baade, W. & Zwicky, F. On Super-novae. *Proceedings of the National Academy of Science* **20,** 254–259 (May 1934).

220. Hessels, J. W. T. *et al.* A Radio Pulsar Spinning at 716 Hz. *Science* **311,** 1901–1904. arXiv: astro-ph/0601337 [astro-ph] (Mar. 2006).

221. Hewish, A., Bell, S. J., Pilkington, J. D. H., Scott, P. F. & Collins, R. A. Observation of a Rapidly Pulsating Radio Source. *Nature* **217,** 709–713 (Feb. 1968).

222. Buchdahl, H. General relativistic fluid spheres. *Physical Review* **116,** 1027–1034 (1959).

223. Lattimer, J. & Prakash, M. Neutron star structure and the equation of state. *The Astrophysical Journal* **550,** 426 (2001).

224. Lackey, B. D., Nayyar, M. & Owen, B. J. Observational constraints on hyperons in neutron stars. *Physical Review D* **73,** 024021 (2006).

225. Mueller, H. & Serot, B. D. Relativistic mean-field theory and the high-density nuclear equation of state. *Nuclear Physics A* **606,** 508–537 (1996).

226. Akmal, A., Pandharipande, V. R. & Ravenhall, D. G. Equation of state of nucleon matter and neutron star structure. *Phys. Rev. C* **58,** 1804–1828. https://link.aps.org/doi/10.1103/PhysRevC.58.1804 (1998).

227. Douchin, F & Haensel, P. A unified equation of state of dense matter and neutron star structure. *Astronomy & Astrophysics* **380,** 151–167 (2001).

228. Hulse, R. A. & Taylor, J. H. Discovery of a pulsar in a binary system. *The Astrophysical Journal* **195,** L51–L53 (1975).

229. Hinderer, T. Tidal Love numbers of neutron stars. *The Astrophysical Journal* **677,** 1216 (2008).

230. Einstein, A. Approximative integration of the field equations of gravitation. *Sitzungsber. Preuss. Akad. Wiss. Berlin (Math. Phys.)* **1916,** 688–696 (1916).

231. Abbott, B. P. *et al.* Observation of gravitational waves from a binary black hole merger. *Physical review letters* **116,** 061102 (2016).

232. Abbott, B. P. *et al.* GW170817: Observation of gravitational waves from a binary neutron star inspiral. *Physical Review Letters* **119,** 161101 (2017).

233. Abbott, B. *et al.* Multi-messenger observations of a binary neutron star merger. *Astrophysical Journal Letters* **848,** L12 (2017).

234. Maggiore, M. *Gravitational waves: Volume 1: Theory and experiments* (OUP Oxford, 2007).

235. Abbott, B. P., Abbott, R., Abbott, T. D., Acernese, F., *et al.* Properties of the Binary Neutron Star Merger GW170817. *Phys. Rev. X* **9,** 011001. `https://link.aps.org/doi/10.1103/PhysRevX.9.011001` (1 2019).

236. Kouveliotou, C. *et al.* Identification of two classes of gamma-ray bursts. *The Astrophysical Journal* **413,** L101–L104 (1993).

237. Tanvir, N. *et al.* A 'kilonova'associated with the short-duration γ-ray burst GRB 130603B. *Nature* **500,** 547 (2013).

238. Berger, E., Fong, W & Chornock, R. An r-process kilonova associated with the short-hard GRB 130603B. *The Astrophysical Journal Letters* **774,** L23 (2013).

239. Ciolfi, R. Short gamma-ray burst central engines. *International Journal of Modern Physics D,* 1842004 (2018).

240. Just, O., Obergaulinger, M., Janka, H.-T., Bauswein, A. & Schwarz, N. Neutron-star merger ejecta as obstacles to neutrino-powered jets of gamma-ray bursts. *The Astrophysical Journal Letters* **816,** L30 (2016).

241. Blandford, R. D. & Znajek, R. L. Electromagnetic extraction of energy from Kerr black holes. *Monthly Notices of the Royal Astronomical Society* **179,** 433–456 (1977).

242. Kiuchi, K., Kyutoku, K., Sekiguchi, Y., Shibata, M. & Wada, T. High resolution numerical relativity simulations for the merger of binary magnetized neutron stars. *Physical Review D* **90,** 041502 (2014).

243. Dionysopoulou, K., Alic, D. & Rezzolla, L. General-relativistic resistive magnetohydrodynamic simulations of binary neutron stars. *Physical Review D* **92,** 084064 (2015).

244. Gehrels, N. *et al.* The Swift gamma-ray burst mission. *The Astrophysical Journal* **611,** 1005 (2004).

245. Lazzati, D. *et al.* Late time afterglow observations reveal a collimated relativistic jet in the ejecta of the binary neutron star merger GW170817. *Physical Review Letters* **120,** 241103 (2018).

246. Mooley, K. *et al.* Superluminal motion of a relativistic jet in the neutron star merger GW170817. *Preprint arXiv:1806.09693* (2018).

247. Gourgoulhon, E., Grandclement, P., Taniguchi, K., Marck, J.-A. & Bonazzola, S. Quasiequilibrium sequences of synchronized and irrotational binary neutron stars in general relativity: Method and tests. *Physical Review D* **63,** 064029 (2001).

248. Kiuchi, K., Cerdá-Durán, P., Kyutoku, K., Sekiguchi, Y. & Shibata, M. Efficient magnetic-field amplification due to the Kelvin-Helmholtz instability in binary neutron star mergers. *ArXiv e-prints.* arXiv: `1509.09205 [astro-ph.HE]` (Sept. 2015).

249. Kiuchi, K., Cerdá-Durán, P., Kyutoku, K., Sekiguchi, Y. & Shibata, M. Efficient magnetic-field amplification due to the Kelvin-Helmholtz instability in binary neutron star mergers. *Physical Review D* **92,** 124034 (2015).

250. Kiuchi, K., Kyutoku, K., Sekiguchi, Y. & Shibata, M. Global simulations of strongly magnetized remnant massive neutron stars formed in binary neutron star mergers. *Phys. Rev. Lett.* **97,** 124039. arXiv: 1710.01311 [astro-ph.HE] (2018).

251. Balbus, S. A. & Hawley, J. F. A powerful local shear instability in weakly magnetized disks. I - Linear analysis. II - Nonlinear evolution. *ApJ* **376,** 214–233 (July 1991).

252. Duez, M. D., Liu, Y. T., Shapiro, S. L., Shibata, M. & Stephens, B. C. Collapse of Magnetized Hypermassive Neutron Stars in General Relativity. *Phys. Rev. Lett.* **96,** 031101. eprint: arXiv:astro-ph/0510653 (Jan. 2006).

253. Siegel, D. M., Ciolfi, R., Harte, A. I. & Rezzolla, L. Magnetorotational instability in relativistic hypermassive neutron stars. *Phys. Rev. D R* **87,** 121302. arXiv: 1302.4368 [gr-qc] (June 2013).

254. Giacomazzo, B., Zrake, J., Duffell, P., MacFadyen, A. I. & Perna, R. Producing Magnetar Magnetic Fields in the Merger of Binary Neutron Stars. *Astrophys. J.* **809,** 39. arXiv: 1410.0013 [astro-ph.HE] (2015).

255. Shibata, M., Baumgarte, T. W. & Shapiro, S. L. The Bar-Mode Instability in Differentially Rotating Neutron Stars: Simulations in Full General Relativity. *Astrophys. J.* **542,** 453–463. arXiv: astro-ph/0005378 [astro-ph] (Oct. 2000).

256. Corvino, G., Rezzolla, L., Bernuzzi, S., De Pietri, R. & Giacomazzo, B. On the shear instability in relativistic neutron stars. *Class. Quantum Grav.* **27,** 114104. arXiv: 1001.5281 [gr-qc] (June 2010).

257. Thorne, K. S., Price, R. H. & MacDonald, D. A. *Black holes: The membrane paradigm* (1986).

258. Bromberg, O., Nakar, E., Piran, T. & Sari, R. The Propagation of Relativistic Jets in External Media. *Astrophys. J.* **740,** 100. arXiv: 1107.1326 [astro-ph.HE] (2011).

259. Kastaun, W. & Galeazzi, F. Properties of hypermassive neutron stars formed in mergers of spinning binaries. *Phys. Rev. D* **91,** 064027. http://link.aps.org/doi/10.1103/PhysRevD.91.064027 (6 2015).

260. Hanauske, M. *et al.* Rotational properties of hypermassive neutron stars from binary mergers. *Phys. Rev. D* **96,** 043004. arXiv: 1611.07152 [gr-qc] (Aug. 2017).

261. Radice, D. General-relativistic Large-eddy Simulations of Binary Neutron Star Mergers. *The Astrophysical Journal* **838,** L2. https://doi.org/10.3847%2F2041-8213%2Faa6483 (2017).

262. Shibata, M., Kiuchi, K. & Sekiguchi, Y.-i. General relativistic viscous hydrodynamics of differentially rotating neutron stars. *Phys. Rev. D* **95,** 083005. https://link.aps.org/doi/10.1103/PhysRevD.95.083005 (8 2017).

263. Duez, M. D., Liu, Y. T., Shapiro, S. L., Shibata, M. & Stephens, B. C. Evolution of magnetized, differentially rotating neutron stars: Simulations in full general relativity. *Phys. Rev. Lett.* **73,** 104015. eprint: astro-ph/0605331 (May 2006).

264. Bardeen, J. M., Press, W. H. & Teukolsky, S. A. Rotating Black Holes: Locally Nonrotating Frames, Energy Extraction, and Scalar Synchrotron Radiation. *Astrophys. J.* **178,** 347–370 (Dec. 1972).

265. De Pietri, R. *et al.* Convective Excitation of Inertial Modes in Binary Neutron Star Mergers. *Phys. Rev. Lett.* **120,** 221101. arXiv: 1802.03288 [gr-qc] (June 2018).

266. Shibata, M., Suwa, Y., Kiuchi, K. & Ioka, K. Afterglow of a binary neutron star merger. *The Astrophysical Journal Letters* **734,** L36 (2011).

267. Siegel, D. M., Ciolfi, R. & Rezzolla, L. Magnetically driven winds from differentially rotating neutron stars and X-ray afterglows of short gamma-ray bursts. *The Astrophysical Journal Letters* **785,** L6 (2014).

268. Ruiz, M., Shapiro, S. L. & Tsokaros, A. GW170817, general relativistic magnetohydrodynamic simulations, and the neutron star maximum mass. *Physical Review D* **97,** 021501 (2018).

269. Martin, D, Perego, A, Kastaun, W & Arcones, A. The role of weak interactions in dynamic ejecta from binary neutron star mergers. *Classical and Quantum Gravity* **35,** 034001 (2018).

270. Perego, A. *et al.* Neutrino-driven winds from neutron star merger remnants. *Monthly Notices of the Royal Astronomical Society* **443,** 3134–3156 (2014).

271. Fujibayashi, S., Kiuchi, K., Nishimura, N., Sekiguchi, Y. & Shibata, M. Mass ejection from the remnant of a binary neutron star merger: viscous-radiation hydrodynamics study. *The Astrophysical Journal* **860,** 64 (2018).

272. Tanaka, M. *et al.* Properties of kilonovae from dynamical and post-merger ejecta of neutron star mergers. *The Astrophysical Journal* **852,** 109 (2018).

273. Taniguchi, K. & Gourgoulhon, E. Quasiequilibrium sequences of synchronized and irrotational binary neutron stars in general relativity. III. Identical and different mass stars with γ=2. *Physical Review D* **66,** 104019. arXiv: gr-qc/0207098 [gr-qc] (Nov. 2002).

274. Brandt, S. R. *et al. The Einstein Toolkit* version The "Katherine Johnson" release, ET_2021_11. To find out more, visit http://einsteintoolkit.org. Dec. 2021. https://doi.org/10.5281/zenodo.5770803.

275. Aguilera-Miret, R., Viganò, D., Carrasco, F., Miñano, B. & Palenzuela, C. Turbulent magnetic-field amplification in the first 10 milliseconds after a binary neutron star merger: Comparing high-resolution and large-eddy simulations. *Phys. Rev. D* **102,** 103006. arXiv: 2009.06669 [gr-qc] (Nov. 2020).